

THESIS

FAULTING IN THE FOAM CREEK STOCK, NORTH CASCADE MOUNTAINS, WASHINGTON

Submitted by

Adrian Walter Kahn

Department of Geosciences

In partial fulfillment of the requirements

For the Degree of Master of Science

Colorado State University

Fort Collins, Colorado

Fall 2017

Master's Committee:

Advisor: Jerry Magloughlin

John Ridley

John van de Lindt

Copyright by Adrian Walter Kahn 2017

All Rights Reserved

ABSTRACT

FAULTING IN THE FOAM CREEK STOCK, NORTH CASCADE MOUNTAINS, WASHINGTON

The Foam Creek Stock (FCS) is a tonalite pluton in the northwestern part of the Nason Terrane in Washington state, a region that has experienced a wide range of structural regimes. Faults cutting the FCS have been studied through field, microscope, fluid inclusion, and geochemical methods. The purpose of this study is to understand the nature of these faults, and their place in the regional tectonic history.

The FCS is cut by two populations (P1 and P2) of small-scale faults that share similar orientations but are microstructurally and geochemically distinct. P1 faults are generally E-dipping and host a distinct, bleached alteration halo and a thin, highly altered fault core containing the secondary minerals adularia (K-feldspar), chlorite, albite, and actinolite, and remnant host minerals quartz and altered plagioclase. P1 fault cores are thin (<1 mm) and display small apparent offsets (<2 cm). P2 faults cut P1 faults, dip N, S, and E, have generally steeper dips and greater displacements (average 14.1 cm apparent offsets) than P1 faults, and host predominantly secondary adularia and fractured host rock within thicker (~3 cm), more well-developed cataclastic fault cores.

P1 faults show microstructural evidence of grain boundary bulging in quartz, along with seams that are interpreted to have hosted diffusive mass transfer (DMT) within the cataclastic fault core, suggesting a component of aseismic deformation accommodated some of the strain. In contrast, P2 fault cores range from random fabric to weakly foliated cataclasite, and host aseismic DMT and coseismic pseudotachylyte, indicating strain was accommodated across a wide range of strain rates.

Kinematic analysis using both outcrop and microscale observations indicates that P1 faults are reverse, whereas P2 faults are normal and sinistral.

Chemical analyses of the fault cores of the two populations, using a portable XRF reveal geochemical changes accompanying faulting. The most significant changes include P1 faults are enriched in Pb (~100%), and depleted in Ti (~50%), Ca, Sr, and Zn, whereas P2 faults are enriched in K (~40%) and Rb, and depleted in Fe (~30%), Mn, Ca, Sr and Zn.

Interpretation of textural relationships between primary and secondary minerals suggests the fluids that migrated through both fault populations may have been initially sodic, and a shift in composition produced a sequence of alteration reactions with the host FCS tonalite. The final product of this changing fluid-rock system was adularia precipitation within fault cores, which in turn served to strengthen the faults. Mechanical strengthening likely inhibited reshear of faults, and thus additional strain of the pluton was accommodated along newly nucleated fault planes through slip delocalization.

Fluid inclusion microthermometry, combined with observed deformation mechanisms and secondary mineral assemblages, allowed for estimation of temperature of trapping of the fluids, and revealed temperature conditions of $\sim 289 \pm 24^\circ\text{C}$ during P1 faulting, and $\sim 262 \pm 23^\circ\text{C}$ during P2 faulting. When combined with T-t curves constructed using K-Ar and Ar-Ar data from previous studies, the estimated age of the faults is $\sim 71.9 \pm 3.5$ Ma for P1 and 69.2 ± 3.5 Ma for P2. Using these ages, it is proposed that Late Cretaceous deformation of the FCS observed in this study records relative counterclockwise rotation of the converging Farallon Plate. The resultant shift from E-W compression to dextral transpression was locally expressed as reverse P1 faults followed by N-S P2 extension with a sinistral component during regional post-metamorphic uplift and dextral shear.

ACKNOWLEDGMENTS

Many thanks go to my advisor, Dr. Jerry Magloughlin, for the inspiration for this project and the introduction to the North Cascades, for the advice as I came across stumbling blocks and forks in the road, and for the lively discussions about this project, geology in general, and numerous other topics. Under your guidance, I have learned to become a better scientist. Thank you as well to my committee, John Ridley and John van de Lindt, whose time and input have greatly improved this document, and whose questions have improved the scope of my research. Thank you to my field assistant, Russell Thomas, who, at the last minute, accepted my desperate request for help and spent the next three weeks in the wilderness of the Pacific Northwest. To the friends I made at CSU: Kate, Katharine, Tucker, Dominic, Chris, and many others, you have been an invaluable support system as we navigated graduate school and other trials together. Finally, I would like to thank my family, and Demi, for their unwavering support.

TABLE OF CONTENTS

ABSTRACT.....	ii
ACKNOWLEDGEMENTS	iv
1. INTRODUCTION.....	1
1.1. PURPOSE.....	1
1.2. GEOLOGIC SETTING	2
1.2.1. ACCRETIONARY TECTONICS AND AN EVOLVING PLATE MARGIN....	2
1.2.2. BAJA BC.....	4
1.2.3. THE NORTH CASCADES CRYSTALLINE CORE	5
1.2.4. THE NASON TERRANE	6
1.2.5. THE FOAM CREEK STOCK.....	8
2. METHODS.....	17
2.1. FIELD WORK	17
2.2. PETROGRAPHY	21
2.3. SEM	21
2.4. GEOCHEMICAL METHODS	21
2.4.1. BULK ROCK GEOCHEMISTRY	21
2.4.2. PXRF	22
2.5. FLUID INCLUSION ANALYSIS	23
3. DATA AND OBSERVATIONS.....	28
3.1. FIELD OBSERVATIONS	28
3.1.1. FOAM CREEK STOCK.....	28
3.1.2. POPULATION 1.....	29
3.1.3. POPULATION 2.....	30
3.1.4. STRUCTURAL RELATIONSHIPS BETWEEN FAULT POPULATIONS ..	31
3.2. PETROGRAPHIC OBSERVATIONS.....	42
3.2.1. FOAM CREEK STOCK.....	42
3.2.2. POPULATION 1.....	47
3.2.3. POPULATION 2.....	55
3.3. FAULT KINEMATICS	72
3.4. GEOCHEMICAL DATA.....	79
3.4.1. POPULATION 1.....	80
3.4.2. POPULATION 2.....	81
3.4.3. POPULATION 1 ALTERATION HALO	83
3.5. FLUID INCLUSIONS	89
3.5.1. FLUID INCLUSION PLANE ORIENTATIONS	89
3.5.2. MICROTHERMOMETRY	90
3.5.2.1. POPULATION 1	90
3.5.2.2. POPULATION 2	90
4. INTERPRETATION AND DISCUSSION	100
4.1. HOST ROCK FEATURES	100
4.1.1. FOLIATION.....	100
4.1.2. MAGMATIC EPIDOTE AND CLINOZOISITE	100
4.2. DEFORMATION MECHANISMS IN THE FCS.....	101

4.2.1. CATACLASIS.....	101
4.2.2. DIFFUSIVE MASS TRANSFER	103
4.2.3. PSEUDOTACHYLYTE.....	104
4.2.4. BULGING IN QUARTZ.....	105
4.2.5. IMPLICATIONS OF DEFORMATION MECHANISMS IN THE FCS	106
4.3. FLUID ROCK REACTIONS	106
4.3.1. CHLORITE.....	107
4.3.2. ALBITE	108
4.3.3. ADULARIA.....	109
4.3.4. SERICITE	110
4.3.5. AMPHIBOLE.....	111
4.3.6. INTERPRETATION OF GEOCHEMICAL DATA.....	113
4.3.6.1. POPULATION 1	113
4.3.6.2. POPULATION 2	114
4.3.7. FLUID HISTORY MODEL	114
4.4. NATURE AND COMPOSITION OF FLUID INCLUSIONS IN THE FCS.....	122
4.4.1. COMPOSITION OF THE AQUEOUS COMPONENT	122
4.4.2. COMPOSITION OF THE VAPOR COMPONENT	123
4.4.3. POSSIBLE SOURCES OF FLUIDS	126
4.4.4. IMPLICATIONS OF HOMOGENIZATION TEMPERATURE.....	127
4.4.5. ESTIMATION OF PRESSURE FROM FLUID INCLUSIONS.....	127
4.5. CONDITIONS DURING FAULTING.....	132
4.6. REGIONAL SIGNIFICANCE OF FAULTS IN THE FCS.....	138
4.6.1. ESTIMATED TIMING OF FAULTS.....	138
4.6.2. P1 FAULTS.....	139
4.6.3. P2 FAULTS.....	139
4.6.4. BAJA BC.....	141
4.7. EVOLUTION OF FAULTS IN THE FCS.....	143
4.7.1. EFFECTS OF FLUIDS ON FAULT STRENGTH	143
4.7.2. FAULT EVOLUTION MODEL.....	144
4.7.3. LACK OF REACTIVATION OF POPULATION 1 FAULTS	146
5. CONCLUSION AND FUTURE WORK	149
5.1. CONCLUSION.....	149
5.2. SUGGESTIONS FOR FUTURE WORK.....	152
REFERENCES	154
APPENDICES.....	172

1. Introduction

1.1. Purpose

The objective of this research is to gain a better understanding of processes associated with a previously unstudied brittle fault network within the Late Cretaceous Foam Creek Stock (FCS), located within the northwestern part of the Nason Terrane, North Cascade Mountains, Washington. The Nason Terrane, along with the entire Pacific Northwest, has witnessed a long and complex geologic past. The FCS intrudes the Nason Terrane and likely deformed by a number of structural events that left their mark on the area, and thus the results of this study may help understand the structural marks left by tectonic events in this region.

Analysis of faults in granitoid rocks has become a preferred practice because homogenous composition, relatively isotropic rheology, and minimal metamorphic overprinting provide a natural laboratory for the study of fault rocks (e.g. Di Toro & Pennacchioni 2004; Pennacchioni *et al.*, 2006; Griffith *et al.*, 2008; and many others). As a biotite tonalite, the FCS falls within this category, and in addition is relatively well exposed. Goals of this study include characterization of the fault rocks from the outcrop to SEM scale, analysis of fluids associated with faulting, and connecting the fault populations to tectonic events affecting the Pacific Northwest.

Gaining a better understanding of the nature of these faults requires various observations and tests. Interpretation of outcrop scale observations, including cross-cutting relations and orientations, aids in understanding how structures within the FCS fit in a regional strain framework. Extremes of topography (including extensive vertical rock walls) limited work to only a portion of the pluton. Thorough kinematic analysis was not always possible owing to glacially polished outcrops; this was partially redressed using oriented samples, by using offset indicators in thin section combined with field data. Additional microstructural observations allow for a better understanding of conditions during deformation.

Mineralogical and textural analysis of FCS fault rocks gives insights into the structural processes that formed them, and their general geologic significance. Comparative geochemical analysis using X-ray fluorescence data, and fluid inclusion studies, were undertaken to determine heterogeneity among the fault rocks and characterize their associated fluids. This helped establish a window for pressure, temperature, and metasomatic conditions accompanying faulting. These analyses were synthesized to create a multi-tiered story involving structural and chemical interpretations of the fault rocks with a goal of unlocking the geologic importance of the faults in the FCS on different scales.

Questions to be addressed by this study:

- How many generations of faults cut the FCS?
- What geochemical changes accompanied faulting of the FCS?
- How did fluids associated with faults play a role in FCS alteration?
- What is the rheological evolution of the faults?
- Under what temperature conditions did faulting occur?
- What is the regional significance of the faults, their orientations, and kinematics?

1.2. Geologic Setting

1.2.1. Accretionary Tectonics and an Evolving Plate Margin

The Pacific Northwest tells a geologically and tectonically complex story. Multiple episodes of terrane accretion in the Mesozoic, and subsequent shearing, resulted in a complicated geology that is still not fully understood. As part of the North American Plate, the region currently sits atop the subducting oceanic Juan de Fuca Plate. However, this margin has hosted various tectonic regimes (Dickinson, 2004) and is still evolving. To further complicate the geology of the area, numerous magmatic events occurred over at least 90 million years.

Western North America grew by the progressive accretion of exotic or tectonostratigraphic terranes, geologic provinces whose paleogeographic origins prior to emplacement are commonly

unknown (Fig. 1.1; Coney *et al.*, 1980; Monger *et al.*, 1982; Saleeby 1983; Paterson *et al.*, 1989; Dickinson 2004). They are defined by internal consistency, stratigraphic continuity, and commonly an oceanic affinity (Tabor *et al.*, 1989). These terranes can be identified by fault-bounded lithological changes in the continental crust (Coney, 1989). As subduction and accretion continued, margin-parallel magmatic arcs intruded into previously accreted terranes (Paterson and Tobisch, 1988). Importantly, these terranes are bounded by faults or shear zones that reveal a structural history of reactivations during collision and by post-collision tectonics (Coney, 1989).

The driving force behind the accretionary tectonics of the Pacific Northwest is the convergent ocean-continent North America-Farallon Plate system (Dickinson, 2004). As Pangaea began to rift at approximately 205 Ma, the western margin of North America changed from passive to convergent or transform (Engebretson *et al.*, 1985). The subducting Farallon slab was responsible for the eastward transport of oceanic island arcs and fragments of continental crust which accreted onto the North American plate (Coney *et al.*, 1980; Monger *et al.*, 1982; Brown, 1987). These fragments of exotic origin were originally referred to as “suspect terranes” (Coney *et al.*, 1980), now most commonly ‘terranes’, and they form much of the bedrock geology of the Pacific Northwest.

Convergent tectonics and subduction continued to consume vast amounts of the oceanic lithosphere through the Mesozoic (Engebretson *et al.*, 1985). As the terranes collided with the western portion of the continent in the middle Cretaceous, a ~1500 km long margin-parallel orogenic arc known as the Coast Plutonic Complex (CPC) formed (Fig. 1.2.; Monger *et al.*, 1982). The CPC extends from northern Washington state to the Yukon, and is made up of a collection of metamorphosed terranes, intrusive magmatic bodies (including the Foam Creek Stock of this study), and extrusive volcanic rocks (Brown *et al.*, 2000).

The CPC displays extensive evidence for middle to late Cretaceous (~90 Ma) crustal shortening accommodated by a regional west-verging thrust fault system, associated with collision and accretion of terranes (Rubin *et al.*, 1990). An episode of abundant pluton

emplacement accompanied convergence. As the plate margin evolved in the Late Cretaceous, transitioning from E-W compression to dextral transpression and then Eocene transtension (Engebretson *et al.*, 1985; Doubrovine & Tarduno 2008), thrusting was succeeded by large-scale strike-slip motion as large, margin-parallel shear zones propagated along terrane boundaries and offset the CPC by up to 100s of kilometers (Paterson *et al.*, 2004; Wyld *et al.*, 2006). This evolution of the nature of the plate boundary is hypothesized to have contributed to the northward transport of terranes, an idea termed the “Baja BC Hypothesis”.

1.2.2. Baja BC

Large-scale northward translation and rotation of terranes has been prevalent throughout the Pacific Northwest, as demonstrated by observations of dextral shear present along many terrane boundaries (Fig. 1.3.; Wells & Heller 1988; Wyld *et al.*, 2006). The term “Baja-BC” refers to terranes that originated and/or accreted along the latitude of present-day Baja California, and were subsequently transported northward to the general latitude of present-day British Columbia, Canada (Housen *et al.*, 2003). This northward transport was driven by the change of the convergence vector from perpendicular to oblique, according to a tectonic model proposed by Engebretson *et al.* (1985) of counter-clockwise Farallon plate rotation relative to the North American plate.

Many researchers have built upon the Engebretson model. Wells & Heller (1988) combined paleomagnetic data with geologic relationships to constrain the model of dextral block transport and rotation. Hundreds of kilometers of dextral slip are accommodated on various northwest-southeast trending faults in British Columbia and northern Washington, including the Nason Terrane-bounding Straight Creek Fault. Wyld *et al.* (2006) hypothesized that the Farallon plate's oblique slip boundary with North America was a driving force for dextral shear, and offset was accommodated by several large faults along the margin (Fig. 1.3.). Wyld *et al.* assigned 110 km of right lateral displacement between 100 and 50 Ma to the Straight Creek Fault, and proposed ~1000 km of total northward translation between accretion and current latitude. A greater

magnitude of translation was proposed by Housen *et al.* (2003) in a study of paleomagnetism of the Mount Stuart Batholith in the southern Nason Terrane, who concluded that the terrane underwent 3040 ± 630 km of northward transport and $\sim 20^\circ$ of clockwise vertical axis rotation since 91 Ma.

Alternatively, these paleomagnetic results are possible through large-scale block tilting. A moderate translation model between endmember tilting and translation was introduced in a study by Butler *et al.* (2001; Fig. 1.4.) in a region located between two major dextral shear zones believed to have contributed to northward terrane transport similar to the Straight Creek Fault. Regional normal faulting and the presence of numerous transform faults in the area possibly accommodated tilting and uplift, resulting in paleomagnetic inclination, while minimizing the effects of northward translation.

1.2.3. The North Cascades Crystalline Core

The North Cascades Crystalline Core (NCCC, Misch 1966) is the southernmost extent of the CPC, offset ~ 110 km from the rest of the arc by the \sim N-S, margin-parallel dextral Straight Creek-Fraser fault (Fig. 1.2.; Dickinson 2004). The NCCC is bounded by two major right-lateral shear zones: the Straight Creek fault to the west and the Ross Lake fault zone to the east (Brown and Talbot, 1989; Miller and Bowring, 1990). Rocks in the NCCC are primarily metamorphosed Paleozoic to Mesozoic terranes of oceanic and island-arc origin (Tabor *et al.*, 1989), sutured together during collision (Monger *et al.*, 1982). P-T-t analysis of the NCCC indicate peak metamorphic conditions corresponding to burial depths locally exceeding 40 km and temperatures up to 750°C between 96 and 68 Ma, coincided with SW-NE convergence and crustal thickening (Whitney *et al.*, 1999; Valley *et al.*, 2003). Peak metamorphism in the NCCC was generally synchronous with the emplacement of numerous tonalite to granodiorite plutons (Brown & Walker 1993; Miller *et al.*, 2009), including the FCS of this study.

Within the NCCC, the Entiat Fault is a NNW-trending Tertiary high-angle fault that displays evidence of 30 km of dextral strike slip motion, and minor normal slip (Fig. 1.5; Tabor *et al.*, 1989).

It postdates metamorphism and divides the NCCC into the western Wenatchee block and the eastern Chelan block (Valley *et al.*, 2003). These blocks had distinct magmatic and metamorphic histories. While the entire NCCC was host to shortening, deep burial, and plutonism, magmatism and metamorphism in the Wenatchee block ceased after ~84 Ma (Miller *et al.*, 1993). The Chelan Block underwent late Cretaceous magmatism as well, and continued to host pulses of intrusions and metamorphism into the Eocene. It displays younger, higher grade metamorphism and magmatic events that resulted in pluton emplacement up to ~45 Ma (Haugerud *et al.*, 1991; Miller *et al.*, 1993). Faults with top-to-north extensional shear sense have been observed in the Chelan block, likely associated with unroofing and exhumation of the NCCC that accompanied all stages of Late Cretaceous-Eocene deformation after shortening ceased (Paterson *et al.*, 2004).

1.2.4. The Nason Terrane

The Wenatchee block is comprised of multiple terranes, all linked by similar metamorphic and magmatic histories. The dominant member of the Wenatchee block is the fault-bounded Nason Terrane, primarily composed of the semi-pelitic to metapelitic Chiwaukum Schist, believed to have been deposited in a deep marine environment (Tabor *et al.*, 1989; Magloughlin 1993). During peak metamorphism in the Late Cretaceous the terrane underwent regional amphibolite facies conditions (Brown and Walker, 1993; Magloughlin, 1993).

Peak metamorphic pressures in the Nason Terrane, and indeed the entire Wenatchee block, increase from ~3 kb in the south to >9 kb in the north (Magloughlin, 1993). These conditions are concomitant with Late Cretaceous pluton emplacement: the Mount Stuart Batholith along the southern Nason Terrane-Ingalls Complex boundary crystallized at 2-4 kb, while plutons in the northeastern Napeequa Complex, including the Tenpeak Pluton and Sulphur Mountain Pluton, were emplaced at greater depths, between 7-10 kb (Matzel *et al.*, 2006; Miller *et al.*, 2009). Additionally, the Tenpeak and Sulphur mountain plutons contain magmatic epidote and clinozoisite, and indicator of >6 kb emplacement depth (Zen and Hammarstrom, 1984; Zen, 1985).

The Nason Terrane has recorded a number of deformational episodes associated with evolving regional tectonics. To the south, the Jurassic ophiolitic Ingalls Complex overthrust the older Chiwaukum Schist along the Windy Pass thrust fault, causing southwest-verging NW-SE trending folds and compressional ductile shearing within the Nason Terrane and accommodating regional Cretaceous shortening and crustal thickening (Miller *et al.*, 2006). The steeply dipping, generally reverse-sense White River Shear Zone bounds the Nason Terrane to the northeast, separating it from the older Napeequa Complex (Magloughlin, 1993; Miller and Paterson, 2001; Raszewski, 2005). The large-offset, dextral Eocene Straight Creek Fault to the west is the most kinematically significant bounding fault of the Nason Terrane (Tabor *et al.*, 1989).

Extensional detachment faulting is also present in the region, in the form of reactivated Cretaceous compression-related thrusts, and the Tertiary dextral-normal Entiat Fault (Coney, 1989; Miller and Paterson, 2001). This shift from compression to extension was related to the evolving Farallon-North American plate boundary (Engebretson *et al.*, 1985). Even during the transpressional period following compression, a shift in relative plate motions allowed for local extension through gravitational collapse of over-thickened crust (Coney, 1987; Fossen and Tikoff, 1998; Liu, 2001). Additional evidence for extension in the NCCC are NE-SW mineral stretching lineations, perpendicular to the maximum shortening direction, believed to have formed 85-45 Ma, during oblique collision (Brown and Talbot, 1989).

The dominant foliation in the Nason Terrane is NW-SE and steeply dipping. The foliation is believed to be the result of regional tectonic activity. Two models have been proposed for foliation development: NE-SW shortening during contraction or transpression (Brown & Talbot 1989; Paterson *et al.*, 2004), or regional shear strain during unroofing (Magloughlin, 1993). Folding and ductile shear along the terrane boundaries either accompanied or followed the development of regional foliations, also associated with NE-SW shortening. There is minor evidence for brittle shear associated with this deformation event.

Brittle faulting in the northern Nason Terrane has been observed in widespread cataclasite and pseudotachylyte-bearing faults in the Chiwaukum Schist, post-dating ductile folding and shear (Magloughlin, 1989, 1993). The faults are typically oriented parallel to, and commonly reactivated along, the regional foliation (Magloughlin, 1989, 1992, 1993, 2011). Kinematics of these brittle faults indicate they were commonly sinistral. Major dextral motion along terrane boundary faults (e.g. Straight Creek Fault) may have resulted in block rotation, and internal left-lateral Riedel shear, proposed by Magloughlin (1993) (Fig. 1.6).

1.2.5. The Foam Creek Stock

The Foam Creek Stock of this study (Fig. 1.7) was emplaced 89 Ma, and is believed to be associated with the cluster of deeply-emplaced plutons in the Napeequa Complex (e.g. Tenpeak, Sulphur Mountain), though it is the sole member of the group to have intruded the Chiwaukum Schist of the Nason Terrane (White *et al.*, 1988; Ford, *et al.*, 1988a; Ford *et al.*, 1988b; Tabor *et al.*, 2002a). Along with the other plutons in this group like the nearby Tenpeak Pluton (Raszewski, 2005), the FCS intruded along White River Shear Zone which serves as the Napeequa-Nason boundary, and is elongated parallel to the NW-SE shear zone, suggesting possible synkinematic emplacement.

K-Ar thermochronology of the FCS by Engels *et al.* (1976) shows muscovite cooling ages of $77.58 \text{ Ma} \pm 2.1 \text{ Ma}$, and $71.11 \text{ Ma} \pm 2.1 \text{ Ma}$ for biotite. K-Ar cooling dates of hornblende, muscovite, and biotite of nearby rocks, including the Tenpeak and Sulphur Mountain plutons, from the same study can be found in Appendix D and agree with the cooling rates of the FCS. More recent Ar-Ar cooling dates of hornblende and biotite in the Tenpeak pluton by Matzel (2004) agree with the data from Engels, and can also be found in Appendix D.

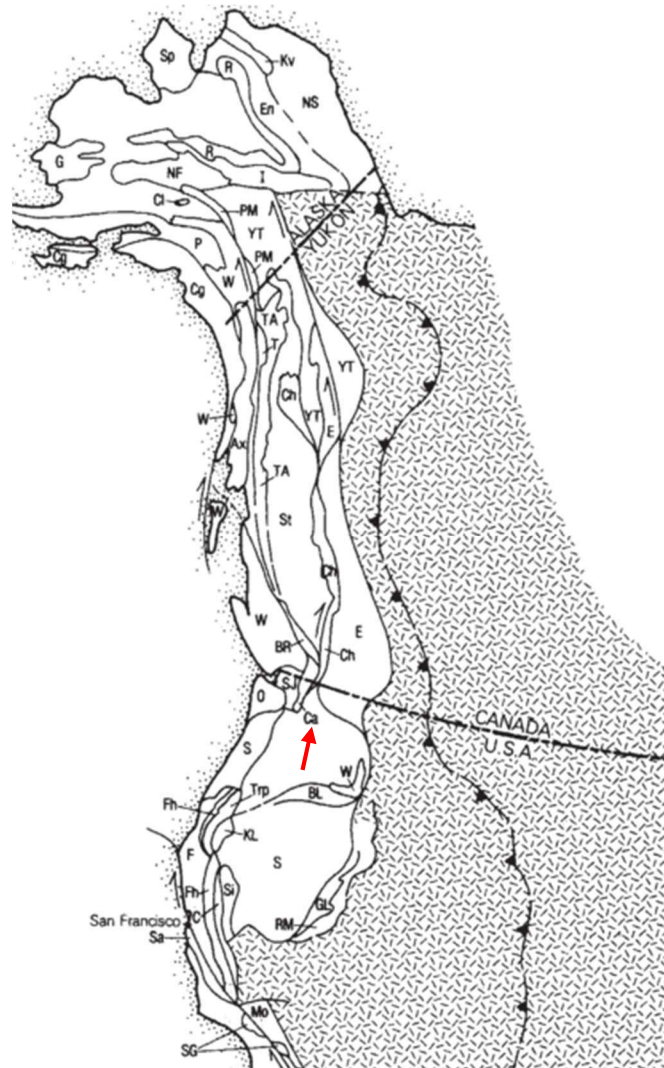


Figure 1.1. Overview of the patchwork of terranes along the western United States. The North Cascades (Ca) is marked by a red arrow. The line spanning from Texas to the northern Alaska-Yukon border is the eastern limit of Cordilleran Mesozoic-Cenozoic deformation. The gray, dashed pattern in the continent represents the North American craton. From Coney *et al.*, 1980.

Sp: Seward Peninsula; Ns: North Slope; Kv: Kagvik; En: Endicott; R: Ruby; I: Innoko; NF: Nixon Fork; G: Goodness; Cl: Chulitna; PM: Pingston & McKinley; YT: Yukon-Tanana; W: Wrangellia; P: Peninsular; Cg: Chugach; Ax: Alexander; T: Taku; TA: Tracy Arm; Ch: Cache Creek; BR: Bridge River; St: Stikine; E: Eastern; SJ: San Juan; Ca: Northern Cascades; O: Olympic; BL: Blue Mountains; Fh: Foothills; S: Lower Cenozoic volcanics; Trp: Triassic and Palaeozoic of Klamath Mountains; KL: Eastern Klamath Mountains; Si: Northern Sierra; C: Calaveras; F: Franciscan; Sa: Salinia; SG: San Gabriel; OR: Orocopia; Mo: Mohave; B: Baja; V: Vizcaino; S: Sonomia; GL: Golconda; RM: Roberts Mountains.

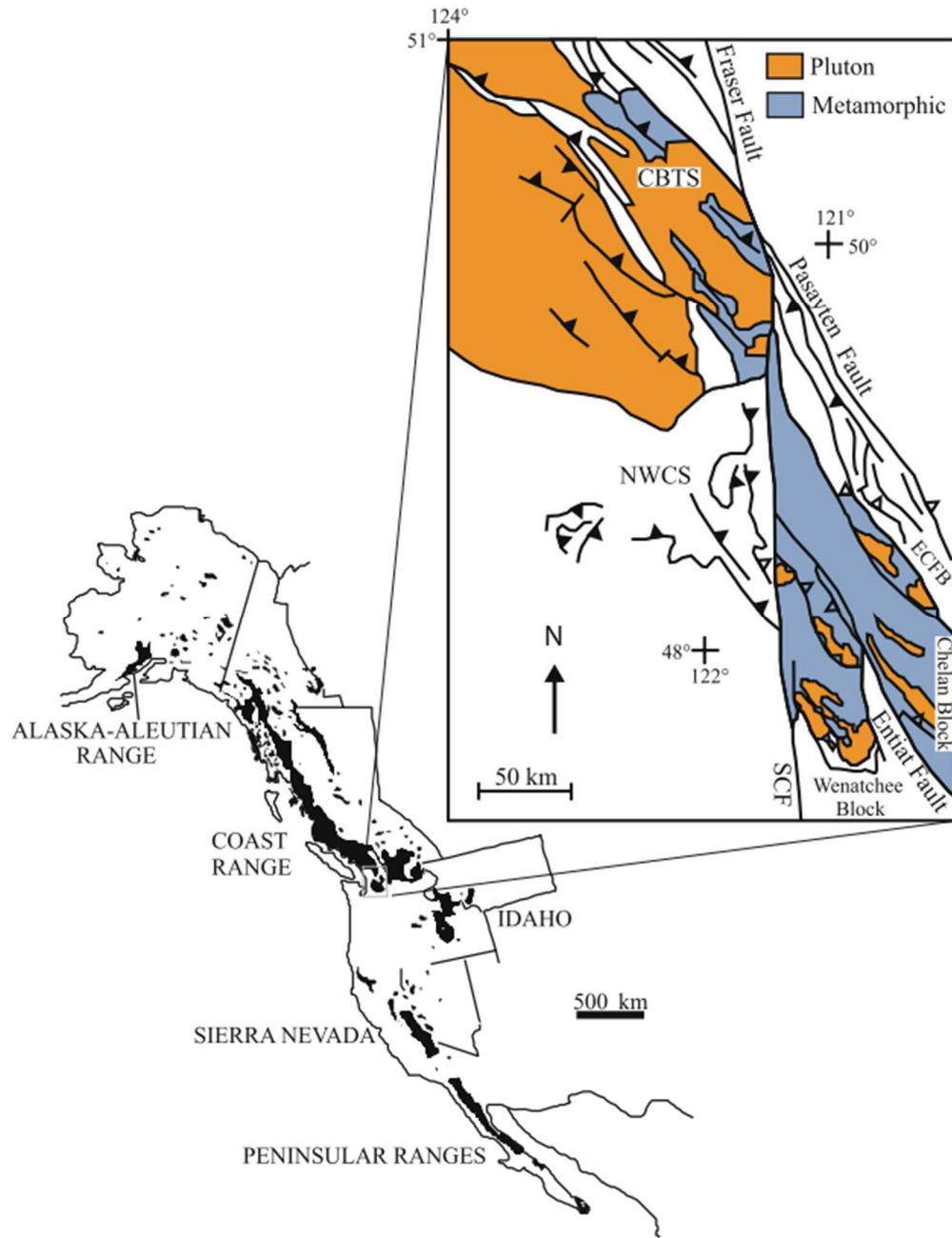


Figure 1.2. Maps showing the CPC and other margin-parallel arcs along the Farallon-North America boundary. Inset shows the southernmost extent of the CPC, offset right-laterally by the Straight Creek Fault (SCF). The metamorphic complex along the fault offset portion to the east is the NCCC. The NCCC is divided into the Wenatchee and Chelan blocks by the Entiat Fault. (CBTS: Coast Belt Thrust System; NWCS: Northwest Cascades System; ECFB: Eastern Cascades Fold Belt). From Miller *et al.*, 2009.

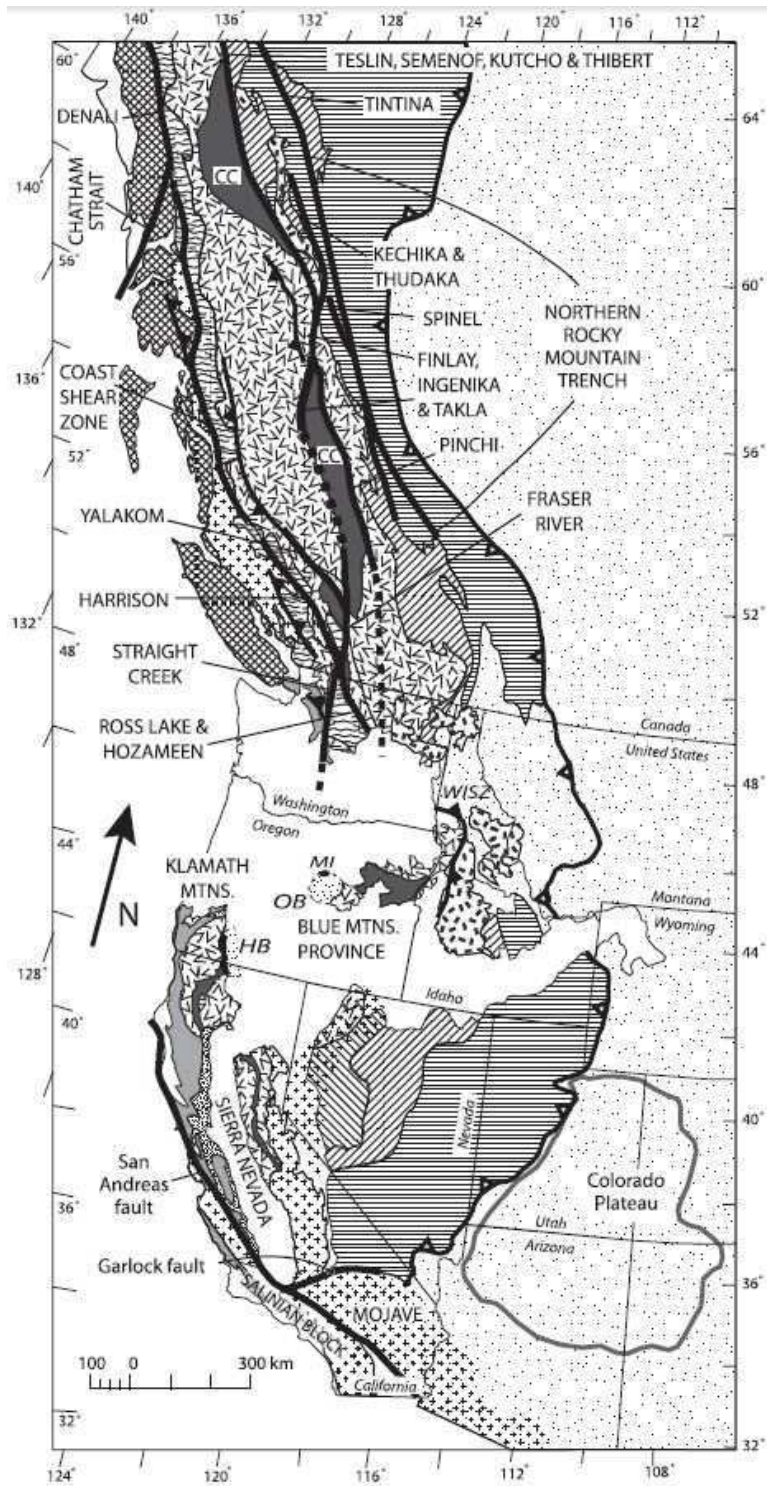


Figure 1.3. Overview of the western North American continent. Thick black lines indicate major faults in the North American Cordillera that accommodated northward transport of terranes post-accretion. From Wyld *et al.*, 2006.

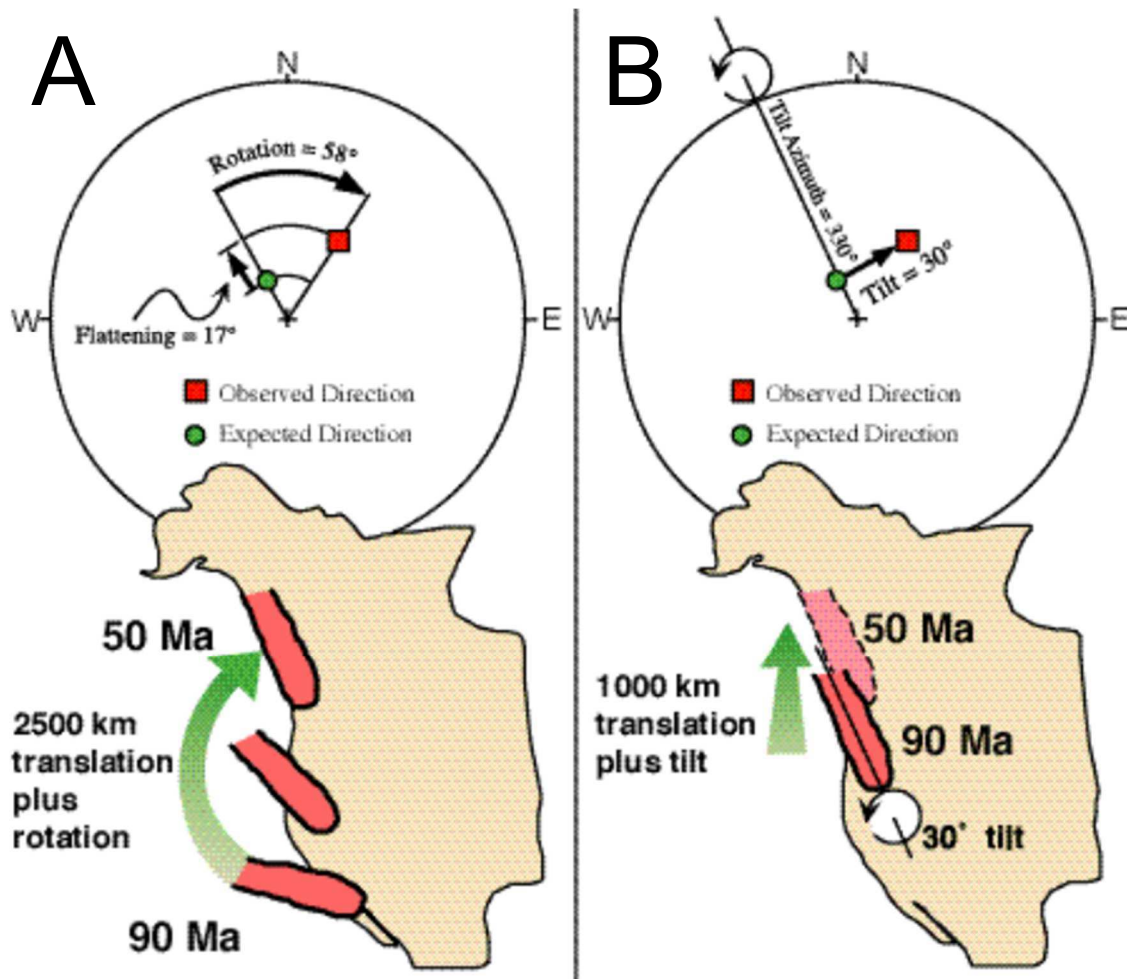


Figure 1.4. Two models for terrane transport along the western North American margin, in the scope of the Baja BC hypothesis. The models are based on observed versus expected paleomagnetic directions, and show two paths toward the same endmember. Model “A” shows a translation and rotation model for terrane transport. To accommodate the discrepancy between observed and expected paleomagnetic direction, the rocks translated 2500 km north, and rotated 58° on a vertical axis. Model “B” shows a tilt and translation model. This model still incorporates northward translation, though a lesser magnitude, 1000 km northward transport. The remaining paleomagnetic discrepancy is accounted for through 30° of tilt along a horizontal axis with an azimuth of 330°. From Butler *et al.*, 2001. As discussed in the text, there are possible intermediate models involving varying amounts of tilt and translation, though an element of northward transport is widely accepted, and supported by the presence of large dextral shear zones like the Straight Creek Fault.

(Continued from previous page)

BC: Buck Creek Pass pluton; BP: Beckler Peak stock; BR: Bearcat Ridge Orthogneiss; CH: Chaval pluton; CS: Chiwaukum Schist; CZ: Cenozoic undifferentiated; DF: Dirtyface pluton; HP: High Pass pluton; MC: Marble Creek pluton; NQ: Napeequa unit; RRC: Railroad Creek pluton; RLFZ: Ross Lake fault zone; RP: Riddle Peaks pluton; SC: Sloan Creek plutons; SM: Sulphur Mountain pluton; SZ: shear zone; WPT: Windy Pass thrust; WRG: Wenatchee Ridge Orthogneiss. From Miller *et al.*, 2009.

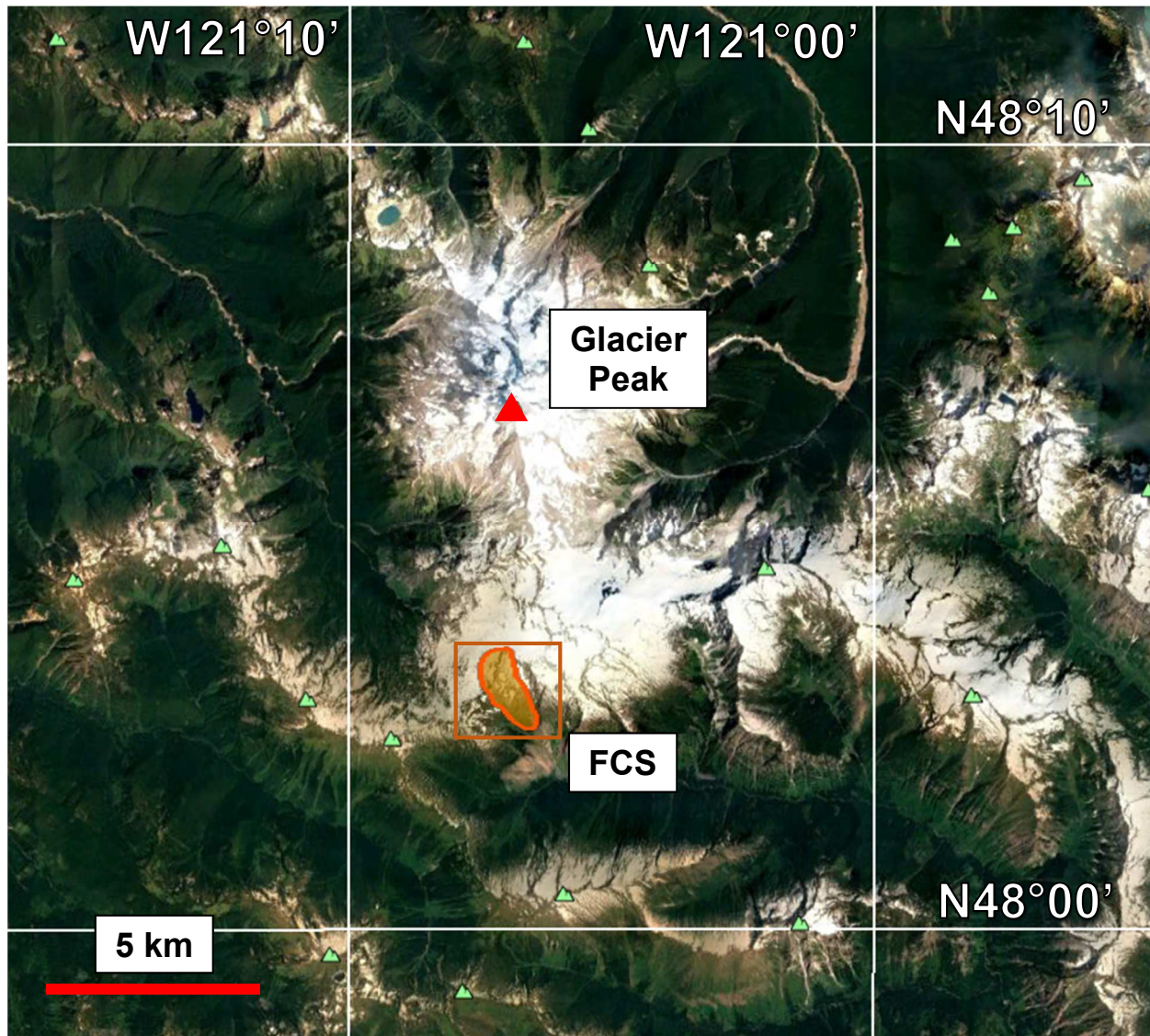


Figure 1.6. Satellite image of the Foam Creek Stock (outlined in orange), in relation to the Glacier Peak stratovolcano (red). The location of the FCS is the defined by Tabor et al., (2002b). The area within the orange outline is represented in Figure 2.3.

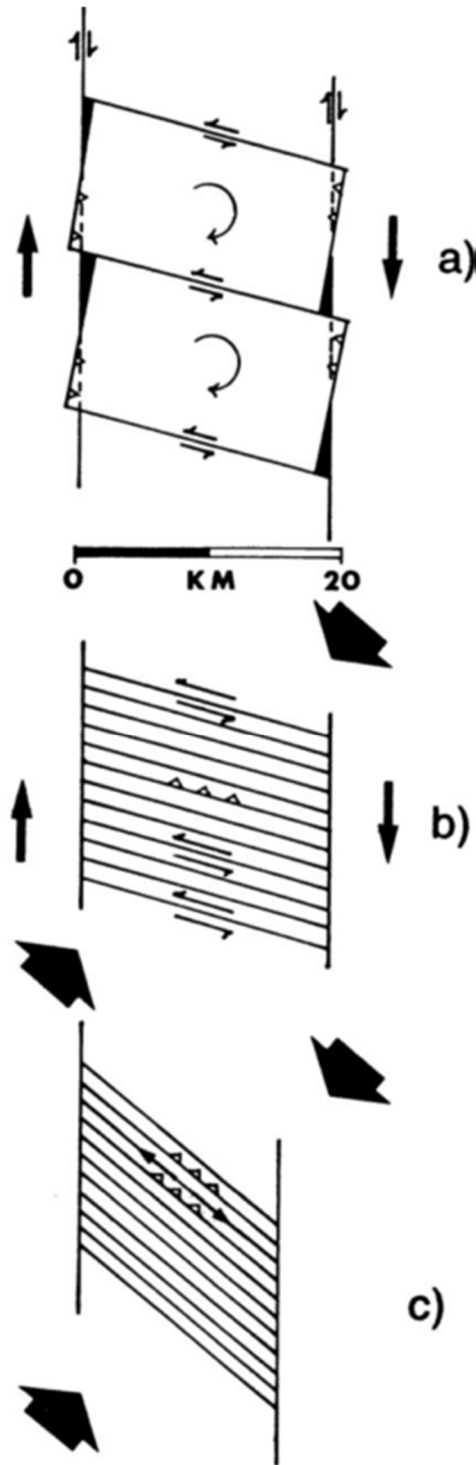


Figure 1.7. Models of block rotation during NE-SW directed compression. a) and b) show blocks of different sizes where internal sinistral shear between blocks accommodates overall dextral offset. Model (a) may produce gaps (dark) or overlaps (teeth), resulting in local extension or compression, respectively. Model (c) shows highly strained blocks, and extensional faults perpendicular to the maximum compressive stress. This mechanism was proposed to allow for observed left-lateral pseudotachylyte-bearing faults in the Nason Terrane by Magloughlin (1993). There is a possibility of local thrusting along block margins in each model.

2. Methods

2.1. Field work

Field work was performed July 30 to August 14, 2014 on the Foam Creek Stock (FCS) within the Mt. Baker-Snoqualmie National Forest, Washington. The Foam Creek Stock is in the Nason Terrane, 6 kilometers south of the Glacier Peak stratovolcano (Figs. 1.6, 2.1). The North Fork Sauk Trail 649 was taken to the White Pass camping area, which served as a base camp.

A total of 56 samples were gathered from the accessible northwest portion of the FCS, 22 from *ex situ* and 34 from *in situ* rock, oriented accordingly. Sample targeting was dictated by the presence of fractures, fault rock, and visible alteration (*e.g.* Fig. 2.2). The samples were gathered from the accessible northwest portion of the FCS (Fig. 2.3). Of the samples collected, 25 were of discrete faults, 8 were of faults that displayed obvious alteration halos, and 5 were of quartz veins. No samples were taken from the same fault. Two samples of undeformed and unaltered FCS host rock were collected. The sample naming convention is as follows: AK1## - #, where the first number indicates the day the sample was gathered, and the second space differentiates -between multiple samples gathered that day. For example, sample AK104-5 was the fifth sample gathered during the fourth day of field work. Sample GPS coordinates are shown in Appendix A.

Strike and dip measurements of planar features observed in the field, including faults and foliations, were recorded using the “right-hand-rule” method, and subsequently input into the Stereonet 8 program to generate stereonet (Allmendinger et al., 2012; Cardozo and Allmendinger, 2013). Each measurement records the orientation of an individual feature.

Field observations are presented in section 3.1.



Figure 2.1. Photo of the Foam Creek Stock (upper right), adjacent to the White Chuck Glacier, looking north toward Glacier Peak (center).



Figure 2.2. Photo from an exposed surface of an FCS outcrop. The glacially smoothed, felsic tonalite is cut by multiple faults, including a P1 fault showing a bleached zone approximately 15 cm wide. View toward the south.

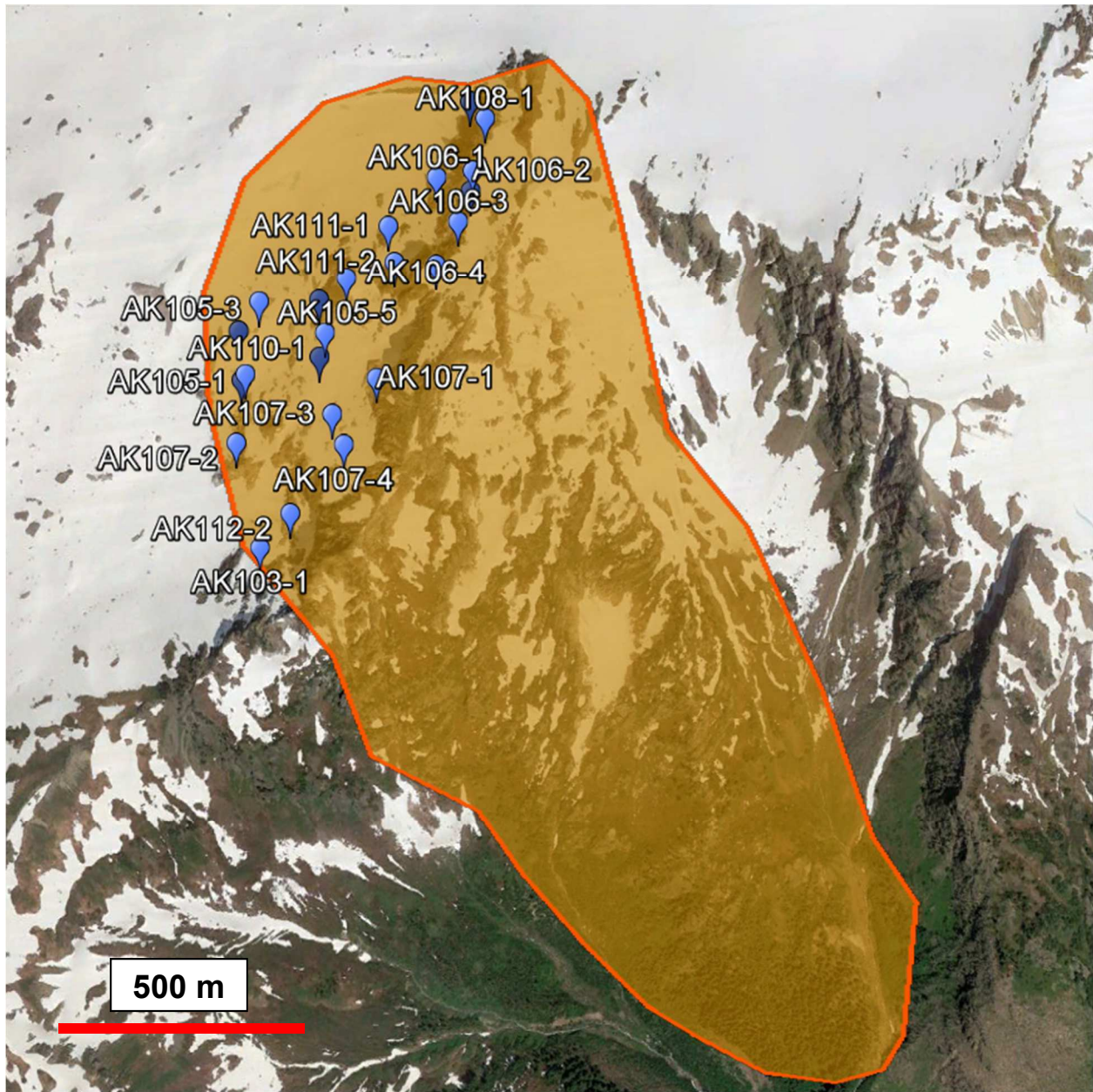


Figure 2.3. Satellite image of the Foam Creek Stock (outlined in orange), enlarged from Figure 1.6. *In situ* sample locations are labelled in the image. Sample gathering was concentrated in the more accessible northwest portion of the FCS. Sample GPS coordinates are shown in Appendix A.

2.2. Petrography

Sixty regular 30 μm thick polished thin sections were prepared by Wagner Petrographic. Of those regular thin sections, 41 were oriented. During preparation, saw cuts were made orthogonal to the fault planes, parallel to the strike direction, to emphasize any possible microstructural kinematic indicators. Where possible, secondary cuts were also made perpendicular to the initial cut face, still orthogonal to the fault plane, along the dip direction. This was done to provide a qualitative sense of three-dimensional kinematics associated with faulting, and to mitigate any apparent offset versus true displacement. These thin sections were named according to host sample number, followed by "A" or "B", indicating the along-strike or along-dip thin section, respectively. For example, thin section 103-4A contains the fault core in sample 103-4, and shows the along-strike section of that fault, orthogonal to the dip-direction.

Microscopic observations were performed on a Leica DM2500 microscope. Photomicrographs were taken using Clemex Captiva software and a Camex petrographic camera. These observations are presented in section 3.2.

2.3. SEM

Polished thin sections were carbon coated in preparation for high resolution microscopic analysis using the Colorado State University Central Instrument Facility's JEOL JSM-6500F field emission scanning electron microscope (SEM) equipped with an In-Lens thermal field emission electro gun and a Thermo Electron energy dispersive X-ray spectrometer (EDS). Geochemical data from the EDS was processed using the EDAX TEAM software package. Visual backscatter electron (BSE) observations accompany petrographic observations in section 3.2. Selected EDS results are presented in Appendix E.

2.4. Geochemical Methods

2.4.1. Bulk Rock Geochemistry

Two samples of fresh, undeformed FCS (sample numbers AK113-4 and AK113-5) were powdered and sent to ALS Geochemical for bulk rock analysis. This analysis consisted of whole

rock characterization performed using five methods: lithium borate fusion and ICP-AES, lithium borate fusion and ICP-MS, four acid digestion and ICP-AES, aqua regia digestion and ICP-MS, and a Leco furnace for loss on ignition (LOI).

2.4.2. PXRF

Geochemical data were collected using a handheld Olympus Delta Premium XRF spectrometer (PXRF). The data are output in weight percent or PPM with 1σ errors. Values returned below the instrument's limit of detection (Appendix B) were reported and not included in the analysis. The PXRF includes an adjustable beam collimator, allowing for analyses to be performed on an ellipse having a major axis of either 3 mm or 8 mm.

To calibrate the PXRF analyses, whole rock analyses from 12 broadly tonalite-composition powders were compared to PXRF analyses from the same powders, including two from the FCS, and 10 from other tonalitic plutons in the Nason Terrane from previous studies by Jerry Magloughlin and Richard Zaggle (Zaggle, 2015). Linear regressions were calculated for each element to determine correction factors, using the following formula:

$$Y_{\text{Bulk}} = M_{\text{User Factor}} * X_{\text{PXRF}} + B_{\text{Offset}}$$

Where Y_{Bulk} is the whole rock analysis, $M_{\text{User Factor}}$ is the slope of the calibration line, X_{PXRF} is the elemental data gathered with the PXRF, and B_{Offset} is the intercept (Appendix B).

Linear regressions were assigned 95% confidence intervals, which were used to calculate the error on the corrected concentrations. This process was applied to 12 elements (Si, Al, Ti, Fe, Mn, Mg, Ca, K, Sr, Rb, Pb, and Zn) that had sufficient data in common between the PXRF and whole rock analyses. Vanadium fit these criteria, but was not fit well enough to calculate a calibration and thus was excluded.

For comparative geochemistry, analyses were performed on smooth-ground thin section billets containing fault rock, allowing a thin section to be used to compare geochemical results to petrographic observations. Analyses attempted to target visibly fine-grained, matrix-dominated portions of fault cores, avoiding clasts. Depending on sample geometry, 2 to 11 spot analyses

were obtained from each sample and averaged. Intrasample variability is primarily a product of the spot analysis technique; results vary with heterogeneities in the fault core, and thus many analyses were gathered and averaged to include all variations and heterogeneities for evaluation of the general chemical composition. All data were kept, but verified to ensure no large minerals were interfering with the spot analysis. For example, if an analysis showed 90% SiO₂, it is likely the spot was on a quartz grain rather than fault matrix.

Geochemical data gathered with the PXRF are presented in section 3.4. Box and whisker plots were generated using median values of the averaged samples within each population and used for quantitative comparative geochemistry. Upper and lower bounds of the boxes indicate the first and third quartiles. The whiskers are the minimum and maximum values. The line through the center of the box is the median (second quartile).

2.5. Fluid Inclusion Analysis

Standard thin sections were first examined to identify samples that hosted significant quantities of secondary fluid inclusion planes within fault wall rock quartz crystals, and contained inclusions large enough to be considered for microthermometry. Six samples, 2 from P1 and 4 from the P2 fault population, were sent to Leek Petrographics and prepared as double polished, 120 µm thick sections.

Photo-mosaics of thin sections were mapped using a Leica DM2500 microscope, under 20x magnification, to identify locations of fluid inclusion assemblages. The criteria for fluid inclusion microthermometry analysis includes adequate size (>5 µm), distinct phases (i.e. visible liquid-vapor meniscus), and no evidence of post-entrapment deformation of the inclusions (e.g. necking or fracturing around inclusions) (Fig. 2.4). Strike orientations of fluid inclusion planes were recorded in oriented sections, while dips were measured using simple trigonometry involving the lateral distance between the top and bottom of a fluid inclusions plane, and the thickness of the doubly polished thin sections, assumed to be 120 µm, but slight variation may contribute to error.

After identification of suitable microthermometry candidates, sections were prepared for analysis by submerging them in acetone to remove the rock from the glass, and any remaining epoxy adhesive was dissolved using ethyl alcohol. The section was then broken into individual chips to accommodate the fluid inclusion microscope's smaller stage.

Thermometry is performed assuming the contents of a fluid inclusion within the quartz have remained volumetrically and compositionally constant. Temperature was manipulated using Linksys software with a Linkam 600 heating-cooling stage on an Olympus BX51 microscope. Results were observed using at least 20x magnification.

Upon identification of a suitable fluid inclusion, the volume percent of liquid was first estimated at 25°C using Figure 3 from Roedder (1972), reproduced in Appendix C. Samples were cooled to -120°C to measure the liquid freezing temperature. Attempts were made to cool samples to -190°C in an unsuccessful effort to observe vapor freezing temperatures.

Samples were then heated to 0°C to observe melting temperatures (T_m). In some cases, an initial melting temperature (T_i) was recorded where a transition from slush to individual ice crystals occurred in the ambient liquid phase. This observation was difficult, manifesting as a small "jump" of the vapor phase within the inclusion, and was only possible with relatively large (>10 μm) inclusions. T_m was readily observable as the ice completely melted, demonstrated by sudden motion of the high relief vapor phase, moving freely about the inclusion. Finally, the stage was heated until homogenization temperature (T_h) was reached, indicated by gradual size reduction and eventual disappearance of the vapor phase. In vapor-dominated inclusions, homogenization resulted in loss of the liquid phase.

To perform geothermobarometry, T_h , T_m , estimated % volume, and phase change behavior were input into the FLUIDS BULK thermometry software package by Bakker (2003).

In BULK, the following procedure was followed:

- 1) Component definition: (1) predefined systems or (2) manually defined system
- 2) Choose the fluid inclusion system.

- 3) Partial density of non-aqueous phase is obtained from: (3) Homogenisation Temperature
- 4) Enter homogenization temperature in degrees Celsius
- 5) Choose mode of homogenization (vapor, liquid, or critical)
- 6) Choose the ion interaction model: (8) Archer (1992) NaCl (*See section 4.4*)
- 7) Salinity of dissolved salts: (1) ice melting temperature
- 8) Enter final melting temperature of ice in degrees Celsius
- 9) Enter percentage of aqueous liquid phase at 20°C
- 10) Enter the desired file name for output

Data output by BULK includes molar volume (cc/mol), density (g/cc), homogenization temperature, homogenization pressure, and salinity (Fig. 2.5)

Fluid inclusion observations and microthermometry results are presented in section 3.5, and all fluid inclusion data are presented in Appendix C.



Figure 2.4. A typical fluid inclusion assemblage adjacent to the faults in the FCS, consisting of three liquid-vapor fluid inclusions (red arrows) aligned along one fluid inclusion plane. Thermometry measurements for all three inclusions were within 2°C of one another, suggesting they are temporally related and formed during the same “fluid event” (Bodnar, 2003).

Sample 111-1A, Chip 3, Assemblage 2, denoted as 111-1A_3_2. From P1 fault population.

Corresponding BULK software output is shown in Fig. 2.5.

```

111-1A_3_2.txt - Notepad
File Edit Format View Help
FLUIDS, package of computer programs for fluid inclusion studies
Program 1: BULK, version 01/03
Product development Ronald J. Bakker
Filename : 111-1A_3_2

BULK FLUID INCLUSION
Volume fraction estimates are used for bulk fluid calculations
Vm (cc/mol) 17.972570
D (g/cc) 1.057373
amount-of-substance fractions
H2O 0.908543
CH4 0.002832
Na+ 0.044312
Cl- 0.044312

Fluid inclusion at room temperature (20 °C)
Internal pressure : 36.863745 MPa
Fluid phases present :
1. liquid rim aqueous solution 95.000000 vol.%
2. liquid-like gas mixture 0.000000 vol.%
3. vapour-like gas mixture 5.000000 vol.%

LIQUID-LIKE GAS MIXTURE (at 20 °C)
Equation of state: Setzmann & Wagner (1991)
Vm (cc/mol) 0.000000
D (g/cc) 0.000000
amount-of-substance fractions
CH4 1.000000

VAPOUR-LIKE GAS MIXTURE (at 20 °C)
Equation of state: Setzmann & Wagner (1991)
Vm (cc/mol) 0.000000
D (g/cc) 0.000000
amount-of-substance fractions
CH4 1.000000

HOMOGENISATION CONDITIONS OF NON-AQUEOUS PHASES
Equation of state: Setzmann & Wagner (1991)
Th (K) 534.150000 (261.000000 °C)
Ph (MPa) 211.061274 (2110.612742 bar)
Vh (cc/mol) 0.000000
Dh (g/cc) 0.000000
amount-of-substance fractions
H2O 0.001203
CH4 0.998797

AQUEOUS SOLUTION (at 20 °C)
Equation of state for volumetric properties: Combination of Duan et al. (1992) and Krumgalz et al. (1996)
Henry constant CH4: Rettich et al. (1981)
Vm (cc/mol) 17.073941
D (g/cc) 1.113024
amount-of-substance fractions
H2O 0.908543
CH4 0.002832
Na+ 0.044312
Cl- 0.044312

ICE MELTING CONDITIONS
Ion interaction model for salinity calculation (Osmotic coefficients): Archer (1992)
Tm (K) 263.550000 (-9.600000 °C)
Pm (MPa) 0.000011 (0.000114 bar)
Salinity Aqueous Phase (associated salt molecules)
Molality Mass%
NaCl 2.707310 13.664793

```

Figure 2.5. Example BULK output window displaying results from the process described in section 1.5.1. Corresponding fluid inclusion assemblage is displayed in Fig. 2.4.

3. Data and Observations

This chapter covers the observations that relate to the structural history of the Foam Creek Stock (FCS). Data gathered during field work, by nature, holds inferences on mineralogy, petrology, and deformation style, and thus should be coupled with further observations made in the lab and under the microscope. The analytical methodology is, in turn, dictated by observations made in the field. Field results serve as the introductory section in this chapter and provide a basis for further analysis. Subsequent sections discuss lab work and results, including microstructures in both transmitted light and SEM, comparative geochemistry, and fluid inclusion data.

3.1. Field Observations

The FCS hosts two populations of faults, referred to as Populations 1 and 2 (P1 and P2). These populations are identified and characterized in the field by their different physical characteristics (*e.g.* thickness, color, *etc.*), orientations, and cross-cutting relationships.

The faults also share some commonalities: neither fault population is associated with ductile deformation of the host rock, but are instead discrete brittle features cutting through the FCS. Both fault populations have fault cores composed of cohesive fault rock with variable clast/matrix ratios, thus placing them within the *sensu lato* “cataclasite” definition of Sibson's (1977) fault rock classification scheme. No mylonite was observed in the FCS. One pseudotachylyte-bearing cataclasite vein was seen, the pseudotachylyte appearing as a thin, planar, dark seam cutting across the fault core and matrix.

3.1.1. Foam Creek Stock

The FCS is a medium to light-gray tonalite, composed predominantly of plagioclase, quartz, and biotite. Minor minerals include muscovite, microcline, epidote, clinozoisite, and titanite, all of which are more readily observed on the micro-scale. It is a coarse grained, compositionally homogeneous body of rock, not noticeably metamorphosed in contrast with the surrounding Chiwaukum Schist. Composition is similar to that of other nearby plutons in the

Glacier Peak Wilderness, with the notable absence of hornblende (Ford et al., 1988a; Tabor et al., 2002a).

A weak foliation is exhibited by preferentially aligned platy minerals, mainly biotite. The foliation is pervasive in the FCS and displays a consistent orientation, striking NE-SW and dipping SE (mean 042-44) (Fig. 3.1).

A small number of aplitic dikes and quartz veins were observed in the FCS. The dikes are white, and of variable thickness (~2-5 cm), composed primarily of quartz and plagioclase. Quartz veins are ~1 cm thick. These features serve as indicators of offset for both fault populations discussed later in the section.

3.1.2. Population 1

A total of 36 P1 faults were identified and measured in the field. P1 faults fell into two subpopulations, having average orientations of approximately 012-32 and 053-68 (Fig. 3.2).

P1 faults have a notable white to light gray “bleached zone” surrounding a thin, dark brown to dark green fault core (Figs. 3.3, 3.4). The bleached zone extends consistently ~7 cm into the wallrock on either side of the fault core. P1 faults are quite planar and laterally continuous, and were not observed to branch off or splay into multiple fractures. The bleached zone is the result of a change in mineralogy from that of host FCS. There is visible heterogeneity within this alteration halo. Rock immediately adjacent to the faults displays light gray-pale green chlorite, having entirely replaced otherwise ubiquitous biotite, and altered plagioclase exhibits a color change from white to cloudy gray. The outer portion of the alteration halo, not adjacent to the fault, also has altered plagioclase, but the biotite is its normal black color, indicating little or no chloritization.

Two of the 36 P1 faults displayed minor (<2 cm) apparent reverse and left lateral offset of an aplite dike and a quartz vein. Offsets were indeterminable in the field for the remaining 34 P1 faults, owing to the lack of crosscut features. Fault core thickness averaged ~1 mm (n=10). The sublayers in the alteration halo have relatively consistent thicknesses: the chlorite + altered

plagioclase zone makes up the 3 cm closest to the fault core, while relatively unaltered biotite + altered plagioclase is in the outer 4 cm. The fault cores were too thin for outcrop scale identification of the mineralogic makeup of clasts. No fault terminations were observed, thus fault lengths could not be measured. Fault density was not quantified, as P1 faults did not display regular spacing.

3.1.3. Population 2

The more common population observed in the FCS is the P2 population, with 191 faults identified and measured in the field. The P2 population displays three dominant mean fault plane orientations: 263-54, 069-68, and 004-40 (Fig. 3.5). These distinct orientation groups may be indicative of further division within the P2 fault population. However, for the purposes of this section, they are classified as being part of the same fault population based on their uniform physical characteristics.

P2 fault cores are cohesive, and pale to dark green in outcrop (Fig. 3.7). The faults are discrete, exhibiting a sharp contact with the surrounding rock. There is no visible halo or alteration of adjacent host rock related to the presence of P2 faults. Some fault cores contain internal structures defined by layers that can be mesoscopically identified by color banding of fault matrix material. On flat-lying portions of FCS outcrop, some P2 faults have a noticeable effect on the weathering profile of the pluton, indicating the fault cores are more resistant to weathering than ordinary FCS tonalite (Fig. 3.6).

Where evident on vertical rock faces, apparent offset by the P2 faults was exclusively normal (n=12). On horizontal surfaces, 4 displayed right lateral apparent offset, and 12 were left lateral. Offset magnitudes ranged from 1.5 to 37 cm, averaging 14.1 cm (n=24). Measured fault core thicknesses ranged from 1 to 10 mm, averaging ~3.3 mm (n=53; Figs. 3.7, 3.8). Fault geometry is generally planar. In a few instances, the P2 faults anastomose and branch off into multiple slip planes. Quartz and plagioclase are present as clasts in the fault core. P2 fault terminations were not seen in the FCS, thus fault lengths were not measured. Though more

prevalent than P1 faults and thus relatively more dense, P2 faults were not regularly spaced, nor did they display any trends or patterns in fault density.

3.1.4. Structural Relationships between P1 and P2

There were a handful of systematic cross-cutting relationships within the FCS:

- All aplite dikes and quartz veins cut the biotite foliation without any apparent deflection.
- Both fault populations displaced aplite dikes and quartz veins (Figs. 3.6, 3.9).
- P2 faults displaced P1 fault in every observed interaction (Figs. 3.8, 3.10).

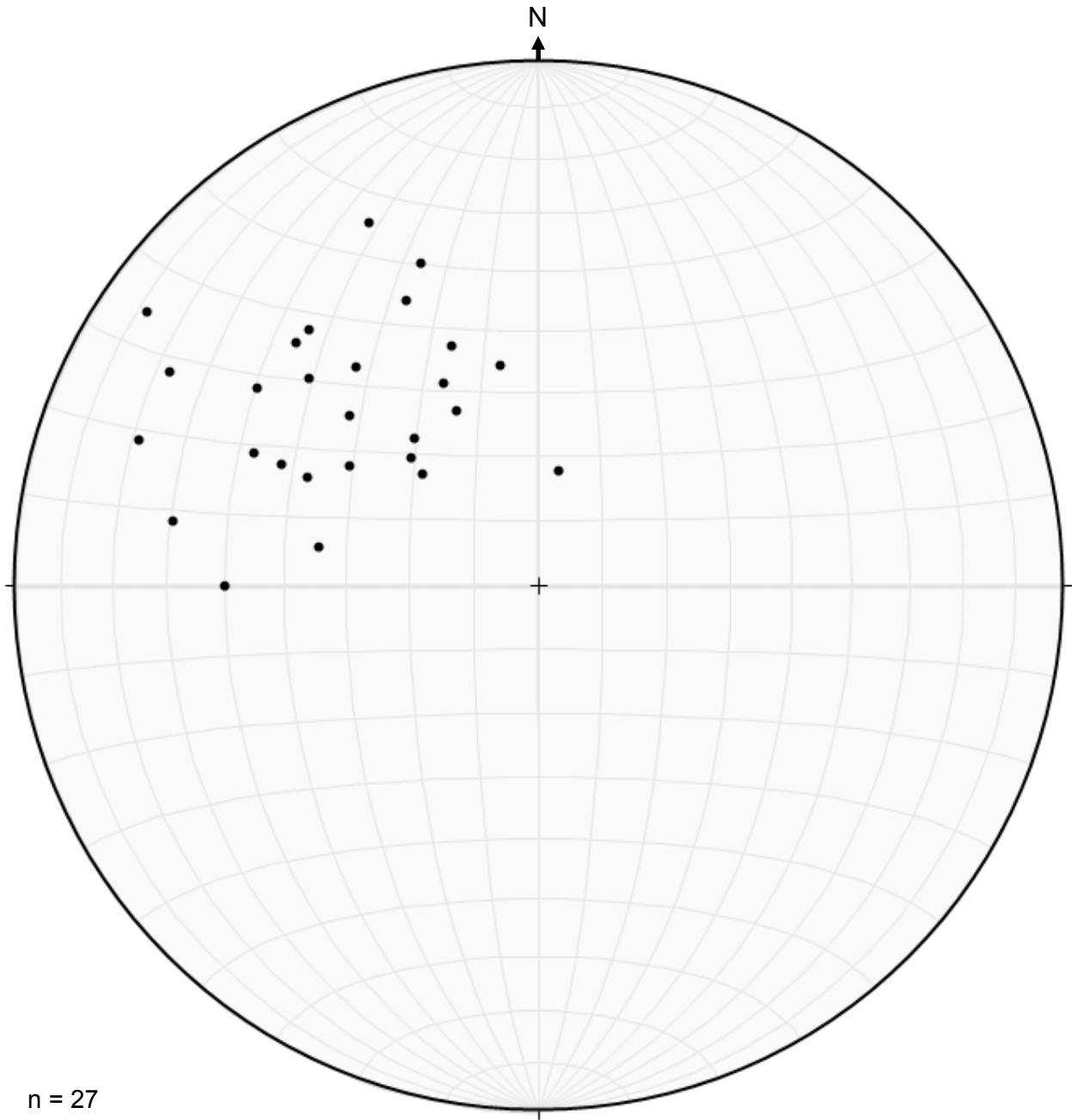


Figure 3.1. Lower hemisphere equal area stereonet displaying poles to planes of biotite-alignment foliations within the Foam Creek Stock. The mean orientation is 042-44.

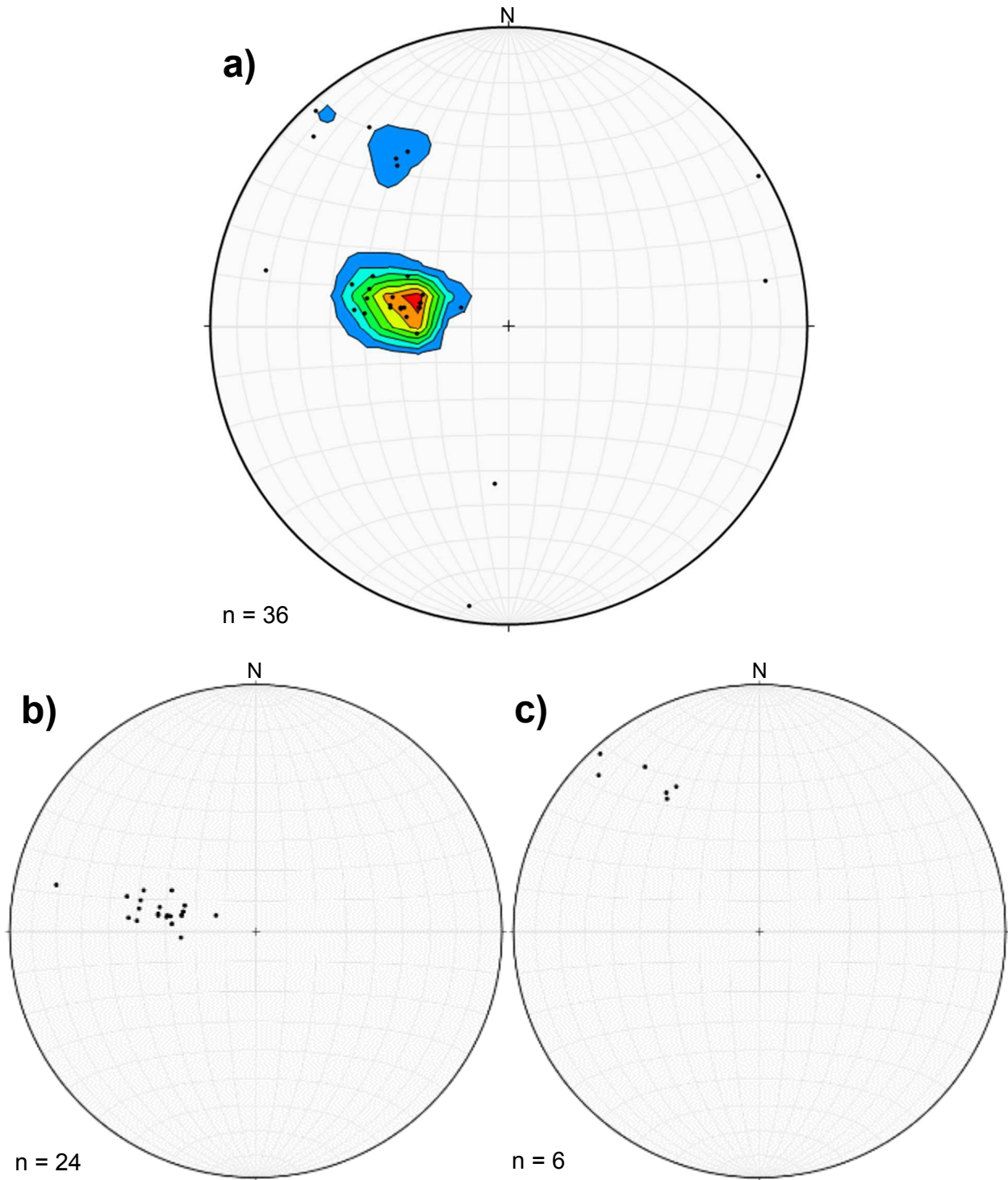


Figure 3.2. Lower hemisphere, equal area stereonet displaying orientations of poles to planes for a) the entire P1 fault population (1% Area Contour Interval = 5), b) the first subgroup, oriented approximately N-S and, shallowly dipping E, c) the second subgroup, striking NE-SW, dipping steeply SE.

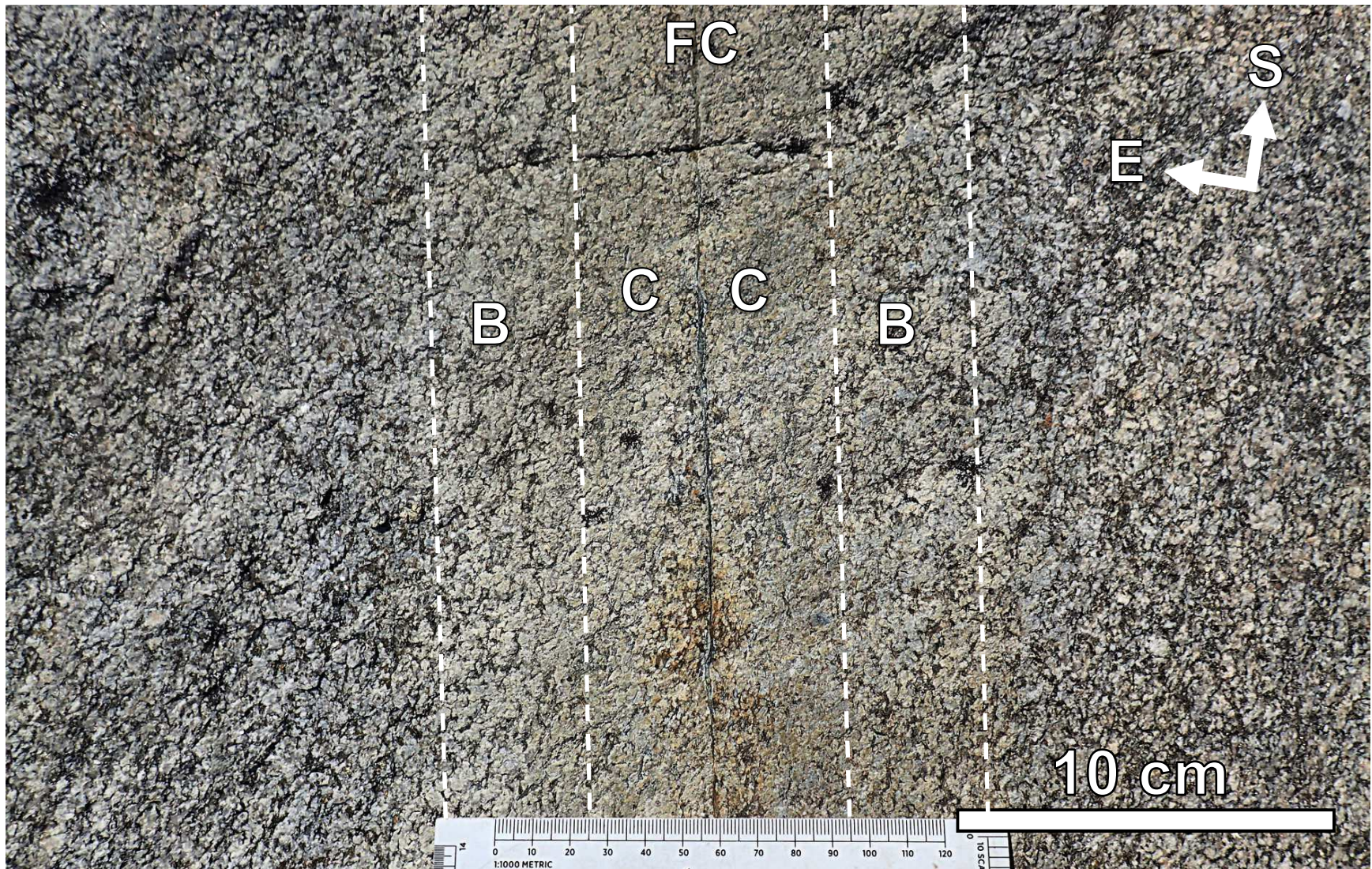


Figure 3.3. A typical P1 fault with characteristic distinct alteration halo. Note the exceptionally thin nature of the dark colored fault core, and the consistent thickness of the alteration halo on either side. The inner set of dashed lines show the adjacent zone of chloritized biotite + altered plagioclase (C), while the outer set contains the unaltered biotite and altered plagioclase (B). Looking straight down, top of photo facing 171°.

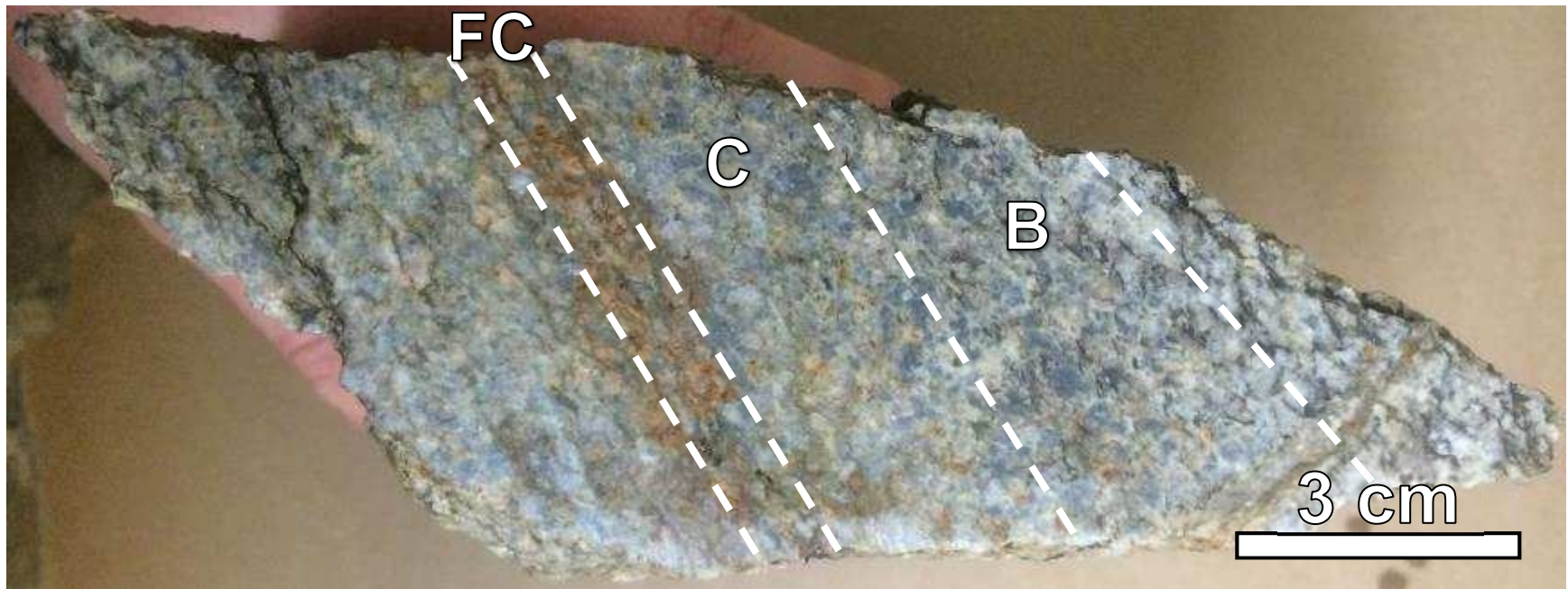


Figure 3.4. Cross section of a typical P1 fault, displaying the internal heterogeneity of the alteration halo. White dashed lines separate the fault core (reddish brown zone, labelled FC), ~2.5 cm thick adjacent chlorite + altered plagioclase zone (C) on either sound of the fault core, and ~3 cm thick outer biotite + altered plagioclase zone (B). Sample AK107-3L.

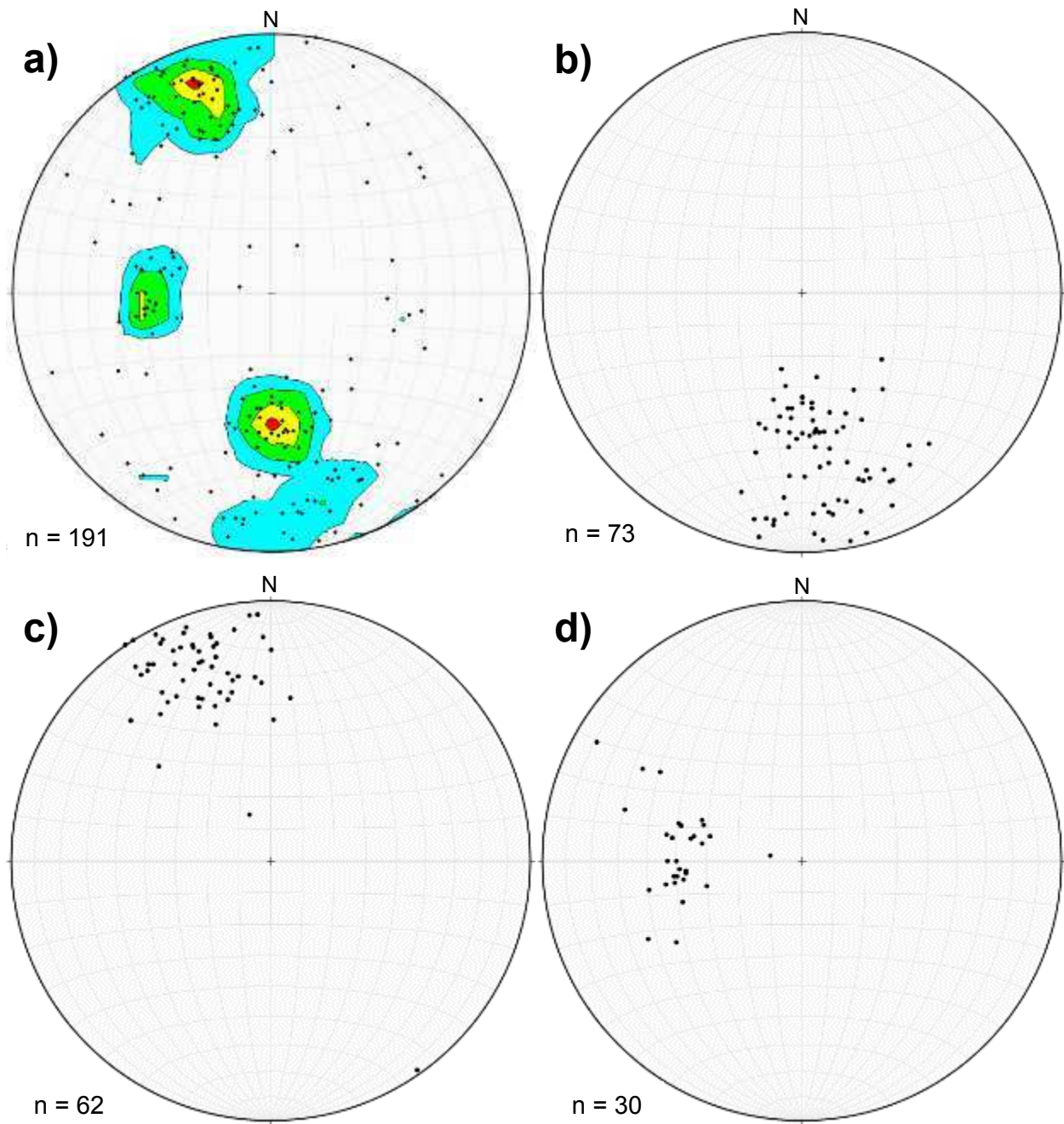


Figure 3.5. Lower hemisphere, equal area stereonet displaying orientations of poles to planes for a) the entire P2 fault population, contours displaying the three subgroups (CI = 2), b) the first subgroup of faults, oriented ~E-W and dipping an average of 55° N, c) the second subgroup of faults, striking ENE-WSW, steeply dipping SSE, and d) the third subgroup, striking N-S, dipping ~40° E.

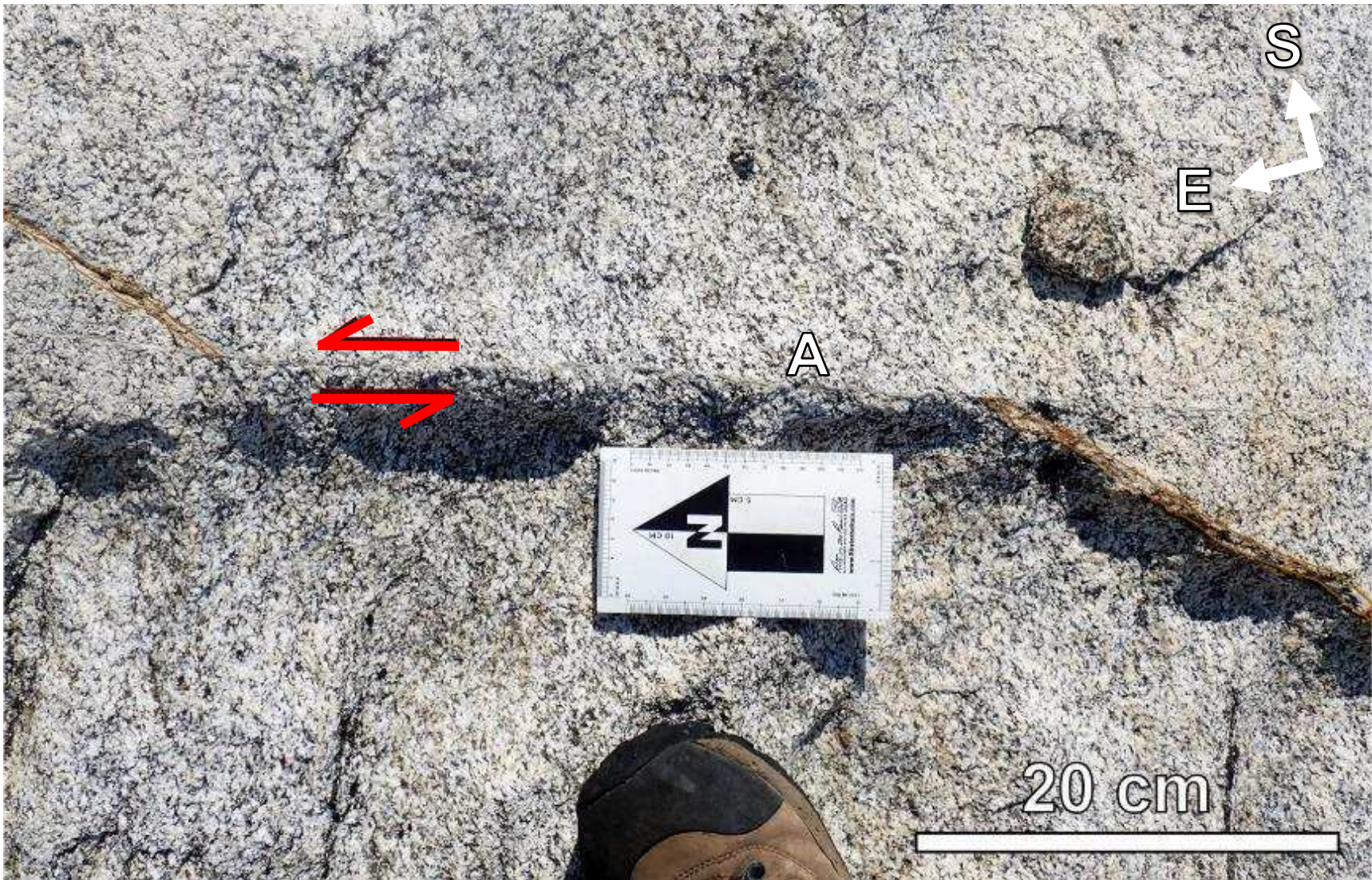


Figure 3.6. A P2 fault (A) offsetting a quartz vein (above the fault at left and below the fault at right, outlined in orange). Apparent offset is left lateral. Note the fault forms a more weathering-resistant band. Looking straight down, top of photograph facing 200°.

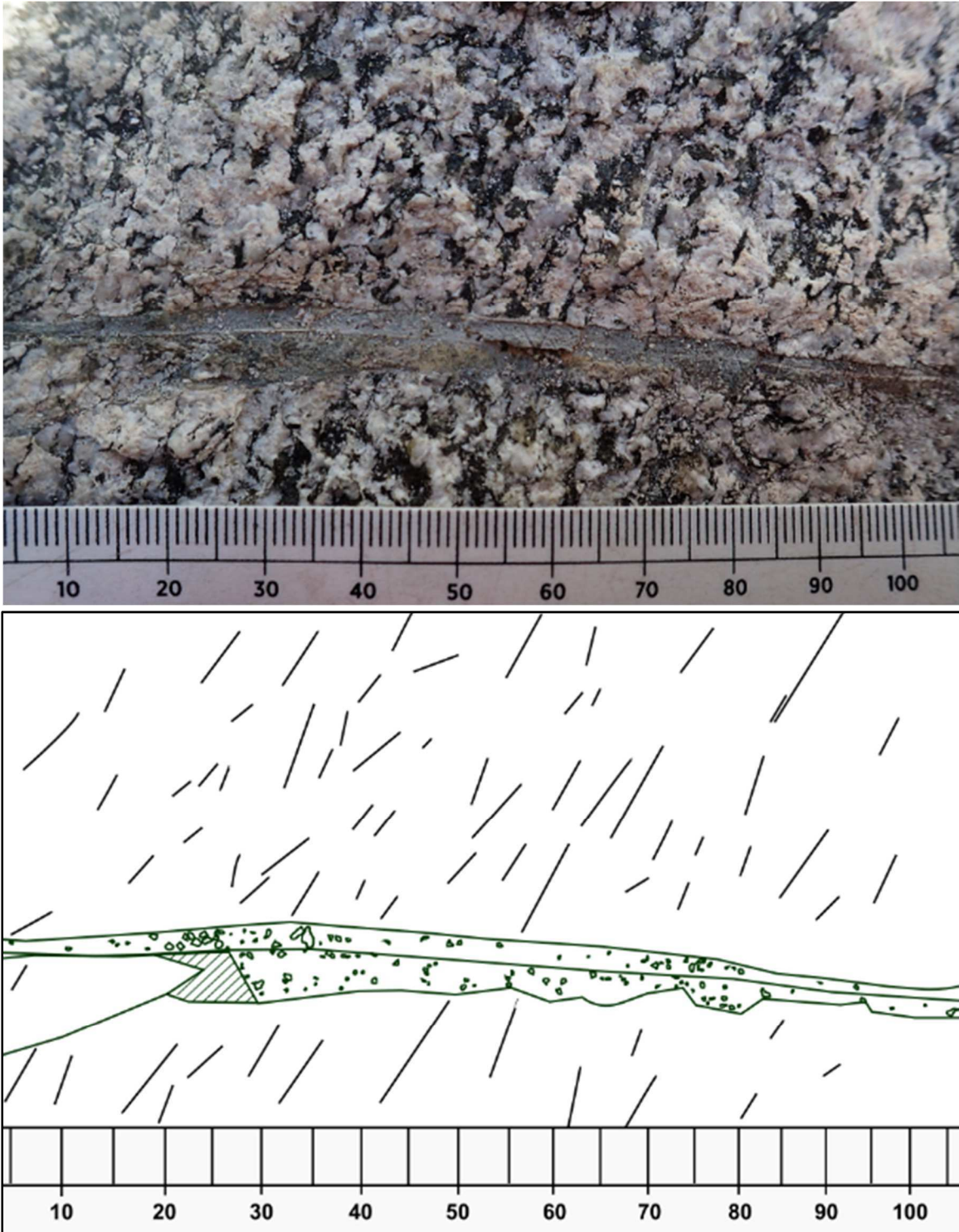


Figure 3.7. (*Top*): Photo showing the discrete nature typical of P2 faults, with sharp, well defined boundaries between fault core and host FCS. Visible clasts are present within the light green fault matrix. (*Bottom*): Schematic diagram of the photo. Generalized biotite foliation in the FCS is shown in by black lines. In green is the outline of fault containing outlined clasts. Scale bar is in mm. Field of view horizontal, facing 132° (SE).

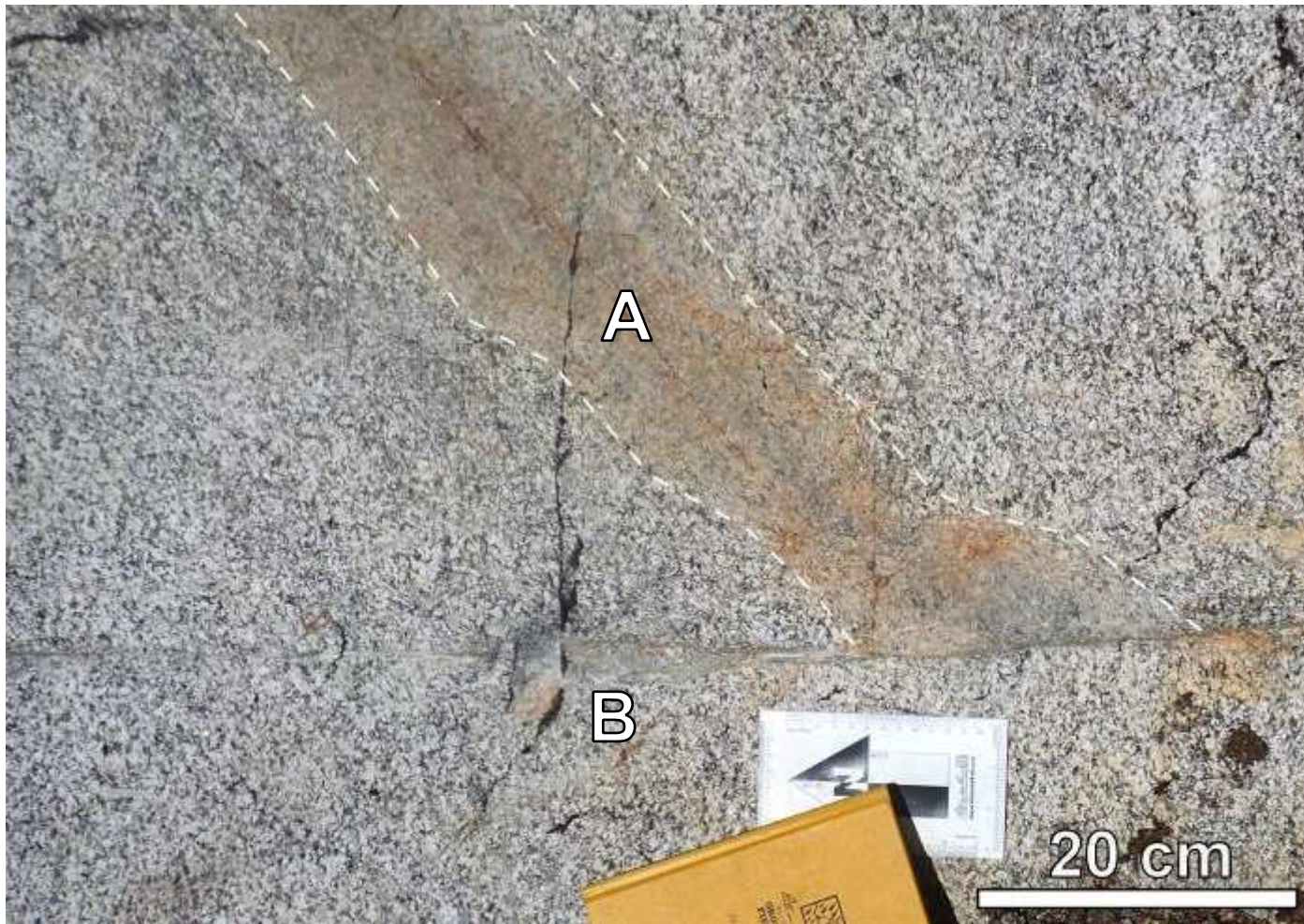


Figure 3.8. P1 fault (A) being truncated and cut by a P2 fault (B). White dashed lines denote the edges of an obvious color change on either side of the P1 fault core, indicative of its characteristic alteration halo. Note the thin, dark seam of P1 fault core within the halo. Also on display is the heterogeneity of thickness along P2. The displaced P1 fault was not found on the other side of the P2 fault; minimum displacement was 30 cm. P1 faults are commonly cut by P2 faults, never the other way around. Field of view horizontal, facing north.

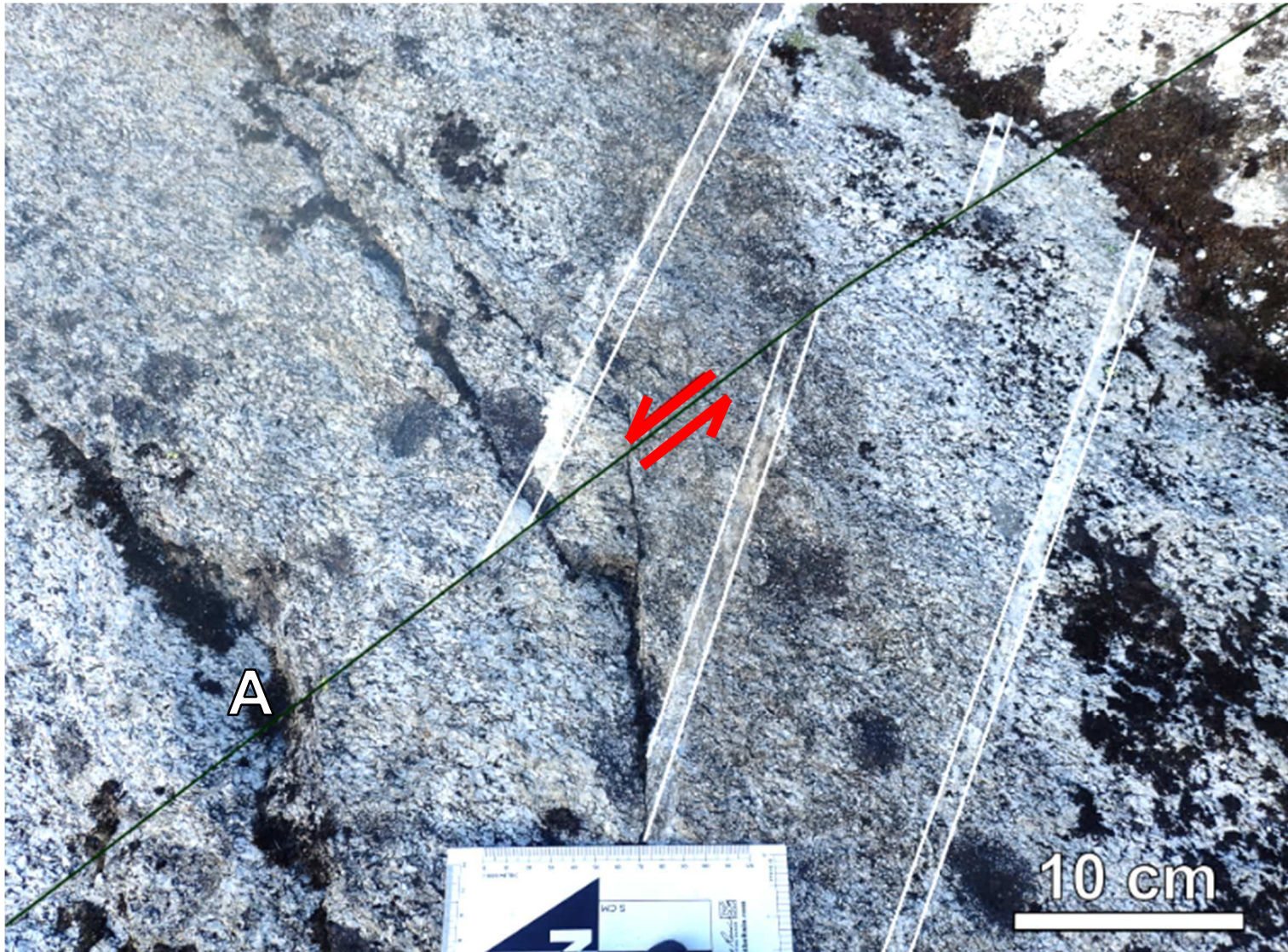


Figure 3.9. Two subparallel aplite dikes (outlined in white) crosscut by a P2 fault (A, traced in dark green), displaying apparent normal offset. Field of view horizontal, facing 46° (NE).

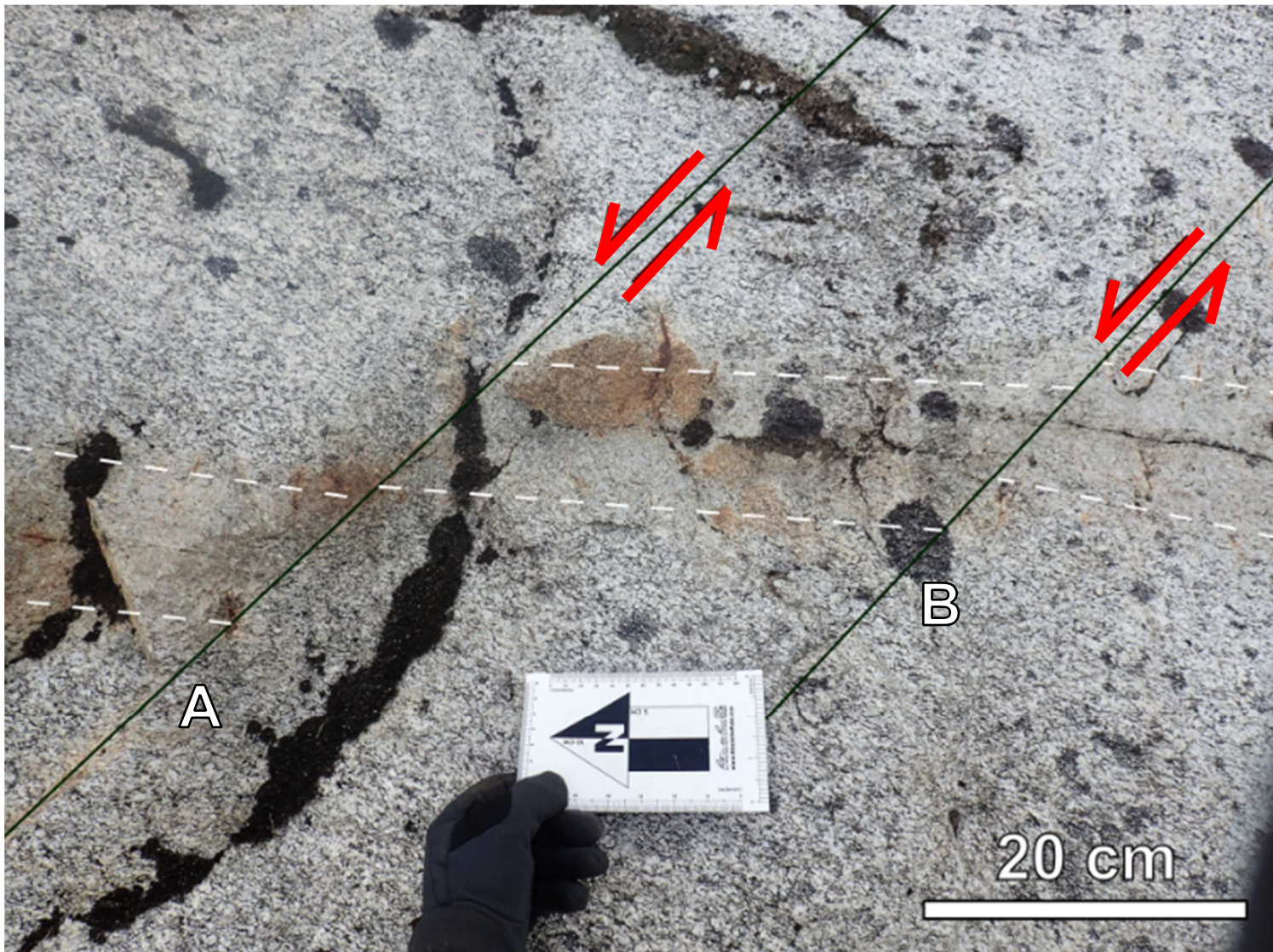


Figure 3.10. P1 fault cut by two parallel P2 faults, both displaying apparent normal offset (A, B, traced in dark green). The alteration halo associated with P1, outlined by white dashed lines, is offset as well. Field of view horizontal, facing 56° (NE).

3.2. Petrographic Observations

This section focuses on petrographic observations, including mineralogy and microstructural indicators of deformation, of the Foam Creek Stock and the faults cutting it. SEM and EDS were used for additional investigation of textural relationships and mineral identification.

3.2.1. Foam Creek Stock

Two fresh and undeformed samples, AK113-4 and AK113-5 were collected, and most of the following observations pertain to these two representative samples.

According to point counting results (Table 3.1.), the FCS is primarily composed of plagioclase (~48%), quartz (~30%), and biotite (~13%) (Fig. 3.11).

Table 3.1. Point counting results, shown as modal abundances from observations across two thin sections (Samples AK113-4 and AK113-5, 595 points each) of unaltered host rock, and their average:

Mineral	AK 113-4	AK 113-5	Average
Quartz	30.42	28.86	29.64
Plagioclase	46.39	50.50	48.45
Alkali Feldspar	2.02	2.35	2.18
Biotite	14.79	10.40	12.59
Muscovite	3.87	4.36	4.11
Chlorite	0.50	1.85	1.18
Epidote Group	1.68	1.68	1.68
Titanite	0.34	0.00	0.17

Plagioclase grains are typically 0.5-1 mm long, locally up to 3 mm, and are euhedral to subhedral. They commonly display polysynthetic albite twinning. Minor saussuritization and sericitization of plagioclase is common, occurring as small muscovite (sericite) grains and clinozoisite + epidote (saussurite), giving the minerals a dusty appearance. Some alteration minerals are larger, reaching up to 200 μm . The degree of alteration of plagioclase is variable, ranging from zero to approximately 50%, consistent with field observations. The plagioclase is generally andesine composition, $\sim\text{An}_{35}$, based on EDS analysis (see Appendix E).

Quartz is subhedral to anhedral and grains are 0.3-1.5 mm across. Fluid inclusions are present in every grain, both isolated and within scattered, discontinuous planes spaced ~150-200 μm apart.

Biotite is tabular, 0.5-5 mm across, and its preferred orientation defines the foliation discussed in section 3.1.1 (Fig. 3.11). All biotite grains display strong reddish-brown pleochroism. Slight kinking is common. Minor chloritization is present along the edges of <10% of biotite grains, displaying anomalous blue interference colors.

Muscovite, chlorite, titanite, microcline, clinozoisite, and epidote are present in small amounts. Muscovite is associated with biotite, tends to be aligned in a similar fashion, and is commonly slightly kinked. Titanite is subhedral, and exclusively found near biotite or as part of the biotite + epidote assemblage. Subhedral microcline, <0.5 mm in diameter, make up ~2% of the FCS based on point counting results (Table 3.1).

Epidote and clinozoisite range from anhedral to euhedral. Epidote displays higher order interference colors (purple and orange) than clinozoisite (pale blue and yellow). Most grains are 50-200 μm across, some up to ~0.5 mm. Both minerals are commonly associated with biotite and biotite + muscovite assemblages. Clinozoisite and epidote commonly display a graphic intergrowth texture with adjacent plagioclase (Fig. 3.12, 3.13). They also contain dark yellow to brown cores which may display oscillatory zoning (Fig. 3.12). SEM analysis of the cores reveal they are enriched in REEs, indicating allanite (Fig. 3.13; Appendix E). The textural relationship with plagioclase, consistent close proximity to biotite, large grain sizes, and allanite cores are commonly indicative of primary, magmatic formation of epidote and clinozoisite (Zen and Hammarstrom, 1984).

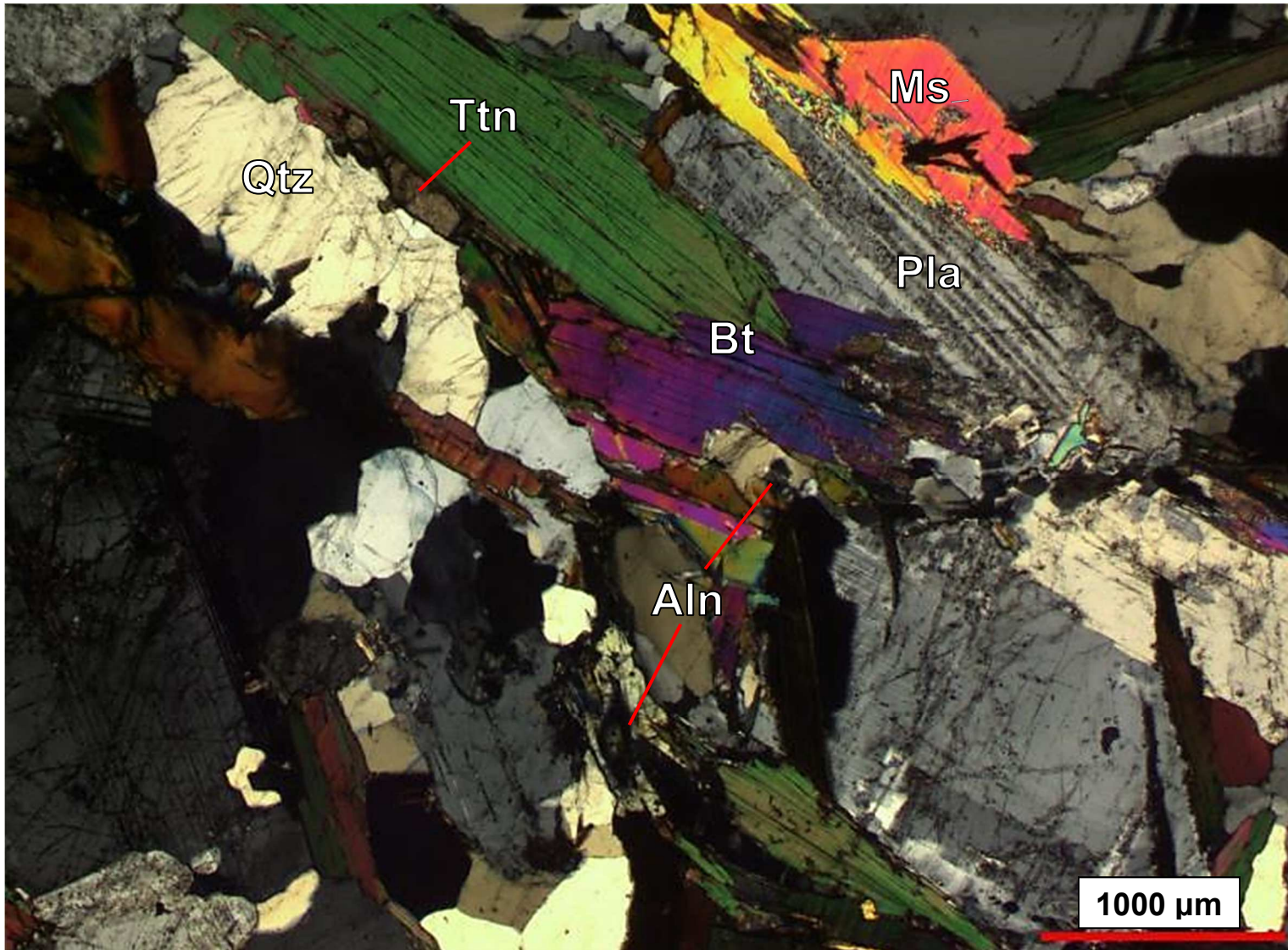


Figure 3.11. Representative photomicrograph (XPL) of Foam Creek Stock tonalite, showing primarily quartz (Qtz), plagioclase (Pla), foliation-defining biotite (Bt), and muscovite (Ms). Titanite (Ttn) is present exclusively associated with biotite. Clinzoisite and epidote are also commonly associated with biotite, commonly with cores of allanite (Aln). Sample AK113-1A.

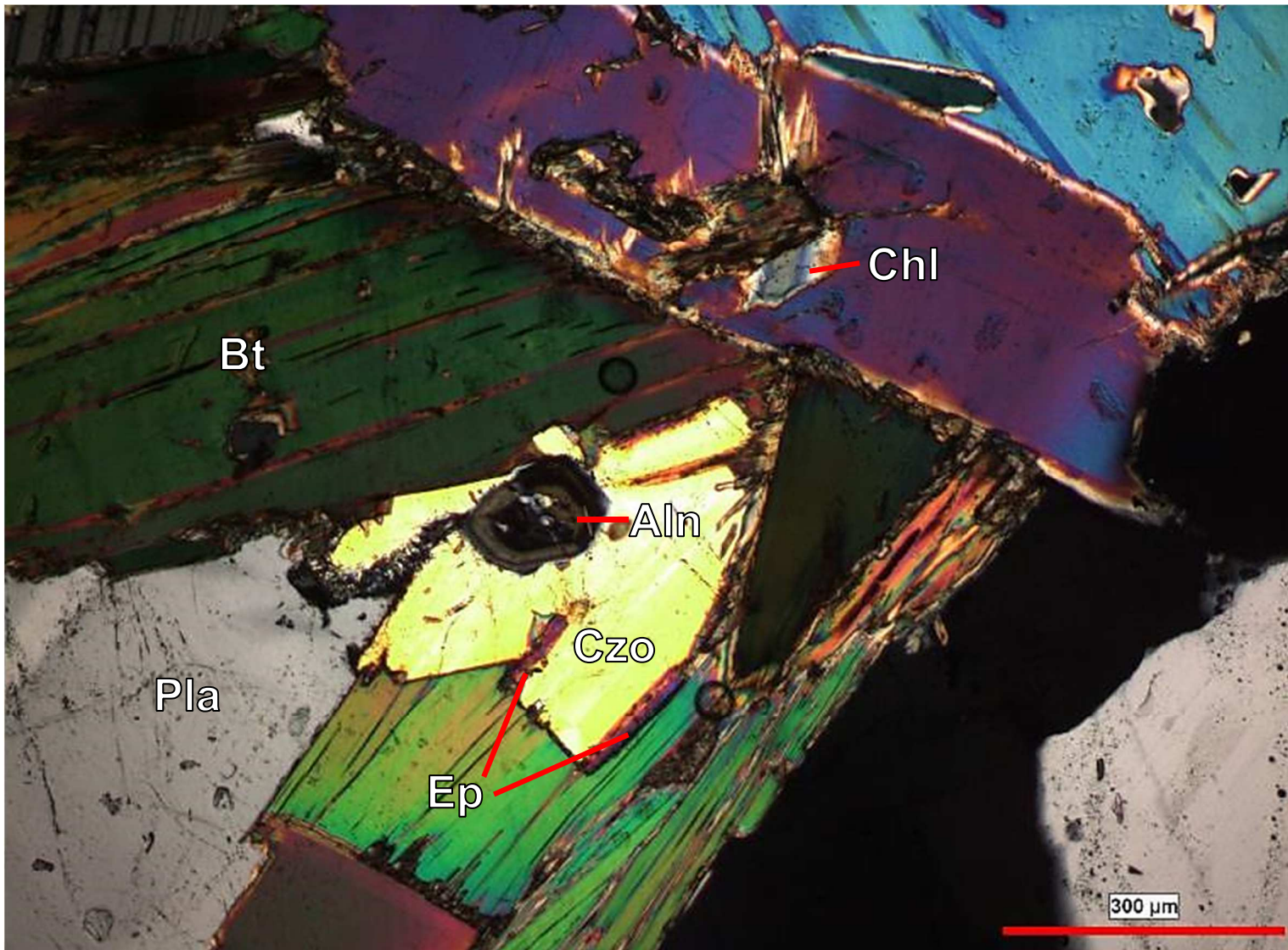


Figure 3.12. Biotite (Bt), displaying minor partial alteration to chlorite (Chl), and clinzoisite (Czt) with epidote rims (Ep). Note the euhedral epidote, and the graphic texture along the boundary between plagioclase (Pla) and epidote. A higher magnification example of this texture is in Fig. 3.13. The allanite core (Aln) displays oscillatory zoning. Sample AK113-1A.

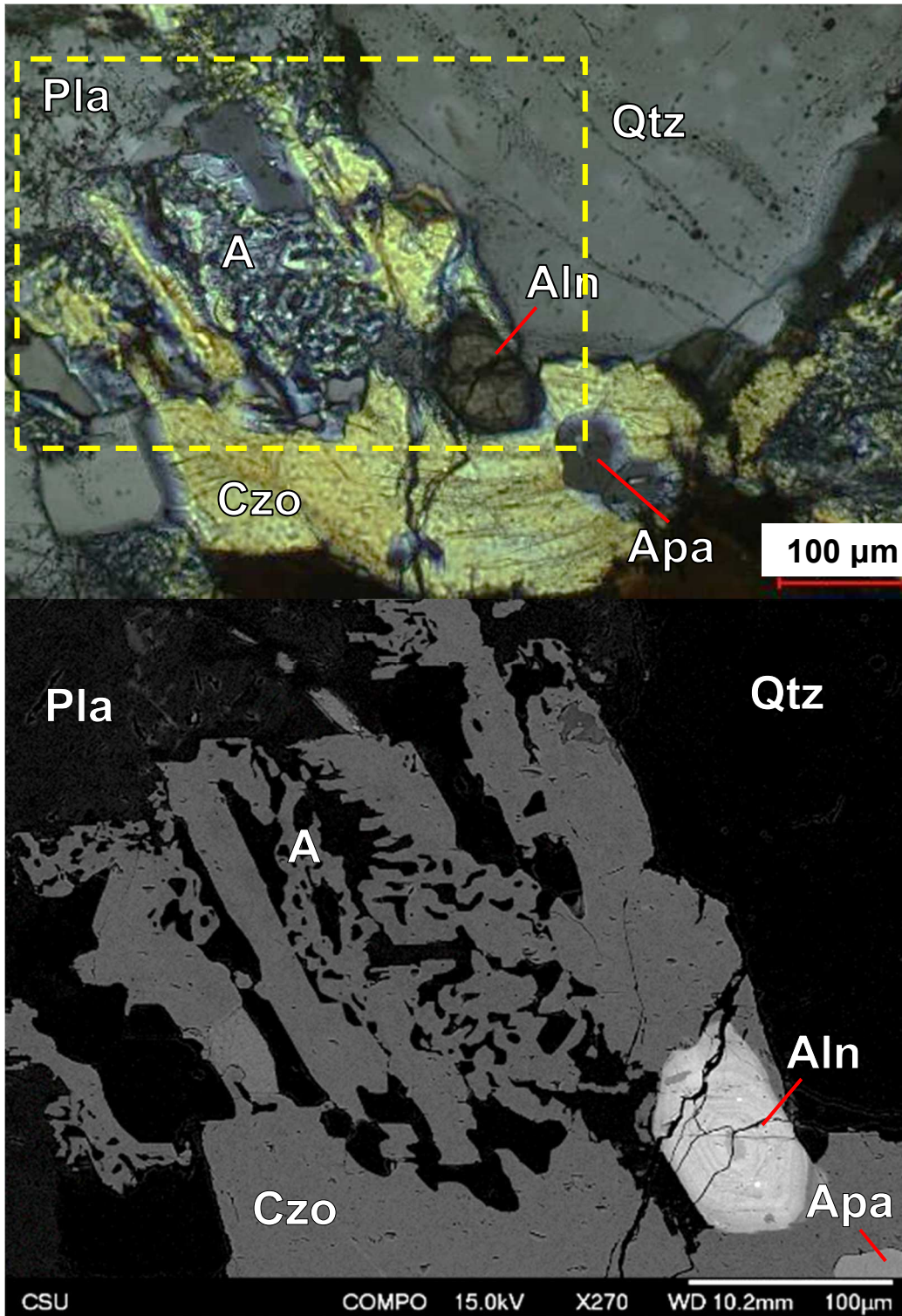


Figure 3.13. XPL photomicrograph (top) and BSE image (bottom, area outlined in yellow) of a magmatic clinzoisite grain showing (A) characteristic graphic intergrowth texture between quartz, plagioclase, and epidote and the oscillatory zoned allanite (Aln) core. Plagioclase (Pla), clinzoisite (Czo), apatite (Apa), and quartz (Qtz) are labelled. For EDS results, see Appendix E. Sample AK113-1A.

3.2.2. Population 1

Microscale observations of mineralogy, deformation, and alteration related to the P1 faults were made using thirteen thin sections cut from seven samples. The P1 fault cores are unusual in that they do not have distinct clast and matrix components. Rather, they are defined by a narrow fault core that hosts extensive secondary mineralization.

As introduced in section 3.1.2, P1 faults have extensive alteration of the wall rock on either side of the fault core (Fig. 3.3). Primary mineralogy within the alteration halo is the host FCS plagioclase, quartz, and biotite. Alteration within the halo is consistent throughout the P1 fault population, and can be divided into two zones based on secondary mineralogy. The zone adjacent to the fault core is defined by extensive saussuritization of plagioclase and chloritization of biotite, and the outer zone also contains altered plagioclase but non-chloritized (fresh) biotite. Secondary mineralization, dominantly saussuritization and chloritization, is also hosted in fractures in the wallrock, with decreasing abundance away from the fault core. Similarly, fluid inclusion planes in quartz decrease in abundance away from the fault core. Using fault zone architecture descriptions from Caine *et al.* (1996), the alteration halo can be considered the fault damage zone.

Quartz within the alteration halo displays some deformation indicators not present within the undeformed host FCS. Minor grain boundary migration (GBM) in the form of bulging is present (Fig. 3.14). Quartz commonly contains healed fractures in the form of systematic fluid inclusion trails (Fig. 3.14). More commonly, quartz grains show evidence of brittle deformation by fracturing, particularly adjacent to the fault core.

Plagioclase is highly altered across the entire alteration halo, with characteristic twinning variably overprinted by secondary mineralization. This mineralization is composed primarily of small (~100 μm), acicular to tabular sericite grains, oriented preferentially along crystallographic planes (Fig. 3.15). Minor saussurite is also present in altered plagioclase. Deformation of plagioclase is exclusively through brittle fracturing. EDS analysis reveals the composition of the plagioclase that was not replaced by sericite or saussurite is albite (~An₀₋₁₀; see Appendix E).

Biotite is commonly deformed and altered in the adjacent section (inner zone) of the alteration halo. In this inner zone, kinking is common, and biotite is typically completely chloritized, showing pale green pleochroism and anomalous blue birefringence.

As mentioned previously, matrix and clasts are not associated with P1 faults (Figs. 3.16, 3.17). Instead, a very thin, sub-mm band of fractured rock hosts intense alteration and secondary mineralization. The fracture surfaces are not truly planar, but instead anastomose around grains of quartz and plagioclase in the wallrock. Commonly, portions of the fault core consist of optically dark to opaque seams (Fig. 3.17, 3.18). Secondary minerals within the fault core are present as fine-grained (<50 μm) masses (Figs. 3.16-3.18). BSE and EDS analysis revealed the mineralogy of the mass to be primarily adularia (modally ~50%), with chlorite (~30%), and actinolite plus an unusual chlorine-bearing amphibole (described below) comprising the remaining ~20% (Fig. 3.18; see Appendix E). Note that K-feldspar will be referred to as adularia for the remainder of the text, where applicable, as the K-feldspar observed in these faults is generally associated with the low temperature, hydrothermal conditions requisite for adularia formation. These minerals generally appear to have been precipitated in the fault core. In some cases, adularia replaced albite directly adjacent to the fault core (Fig. 3.19). Secondary, opaque iron oxide minerals with reddish rims are present as well, as hematite or magnetite with hematite or goethite rims. Some samples host rare calcite along the P1 fault core.

Despite the probable low temperature at the time of P1 faulting (discussed further in section 4.1), the previously mentioned unusual mineral optically resembles an amphibole. EDS analysis indicates the mineral is primarily composed of Si, Al, Fe, Mg, K, and Cl (see Appendix E), indicating it has an approximate composition of a K- and Cl-bearing hastingsite. Grains are present in clusters or aggregates, euhedral to subhedral, and are less than 100 μm in length. Grains show moderate relief, green pleochroism, and up to low second order interference colors (Fig. 3.18). In BSE imaging, the mineral is brighter than surrounding feldspar, quartz, and chlorite (Fig. 3.19). Grains are commonly zoned, with Mg and Al showing an inverse relationship.

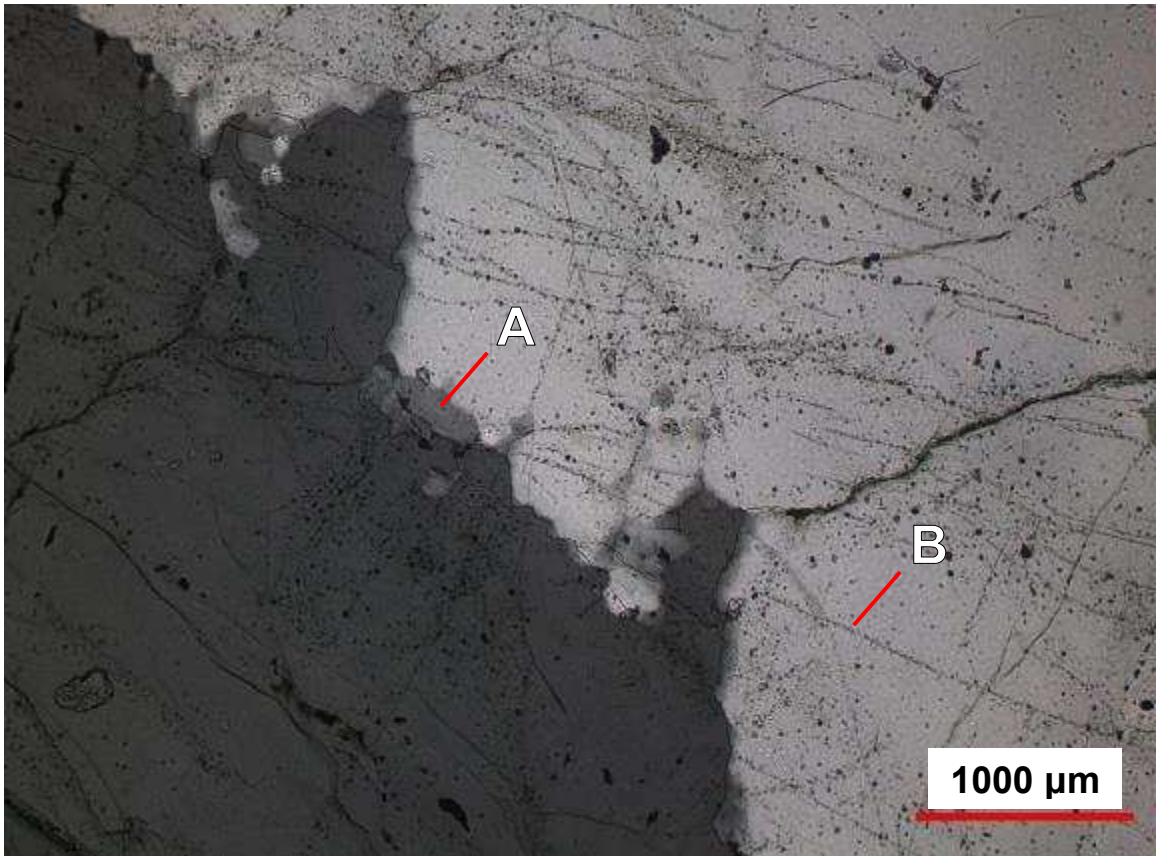


Figure 3.14. Minor grain boundary migration in the form of bulging along quartz grain boundaries (A). Note systematic trails of fluid inclusions trending roughly left-to right across the field of view (B). Sample AK107-3Au.

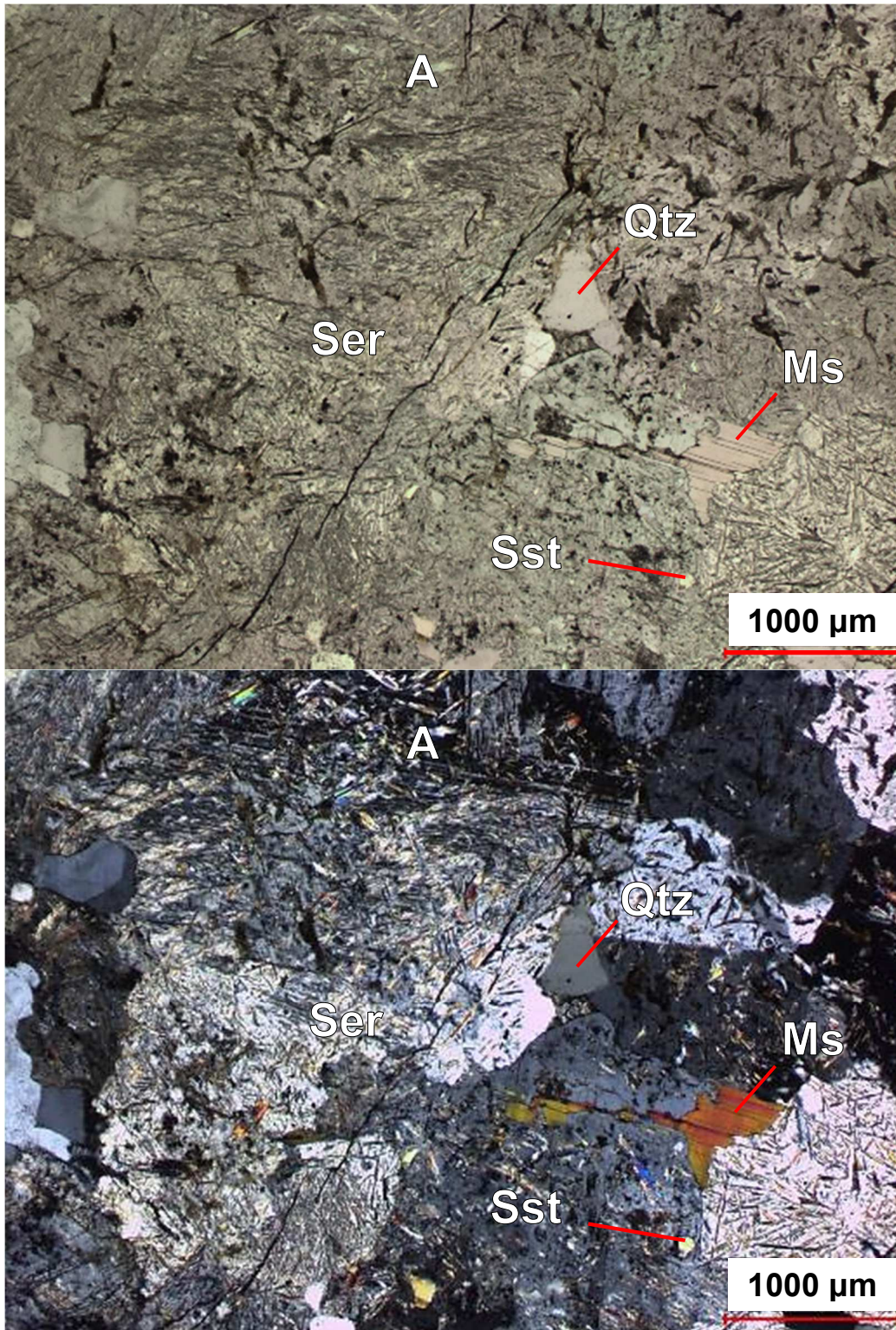


Figure 3.15. Plagioclase within the P1 alteration halo, displaying extensive alteration in the form of fine-grained sericite (Ser) and minor saussurite (Sst), partly obscuring albite twinning (A). Top image PPL, bottom image XPL. Sample AK 107-4BB.

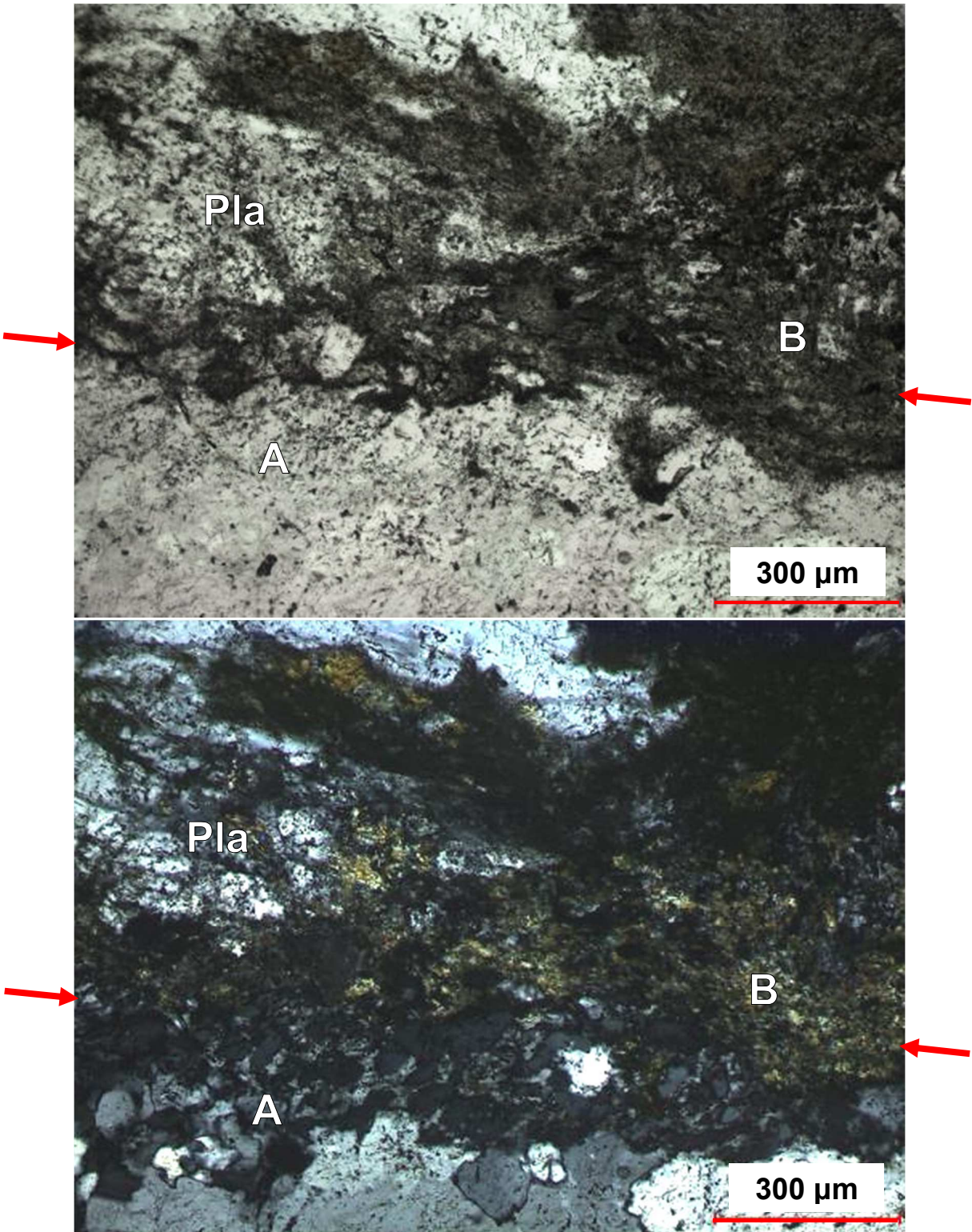


Figure 3.16. P1 fault core (red arrows) grain size reduction, directly adjacent wallrock plagioclase along the lower section of the image showing adularia infill in fractured quartz (A), aggregate of very fine minerals, primarily adularia, chlorite, iron oxides, and amphibole (B), and highly altered plagioclase (Pl). Top image PPL, bottom image XPL. Sample AK111-1B.

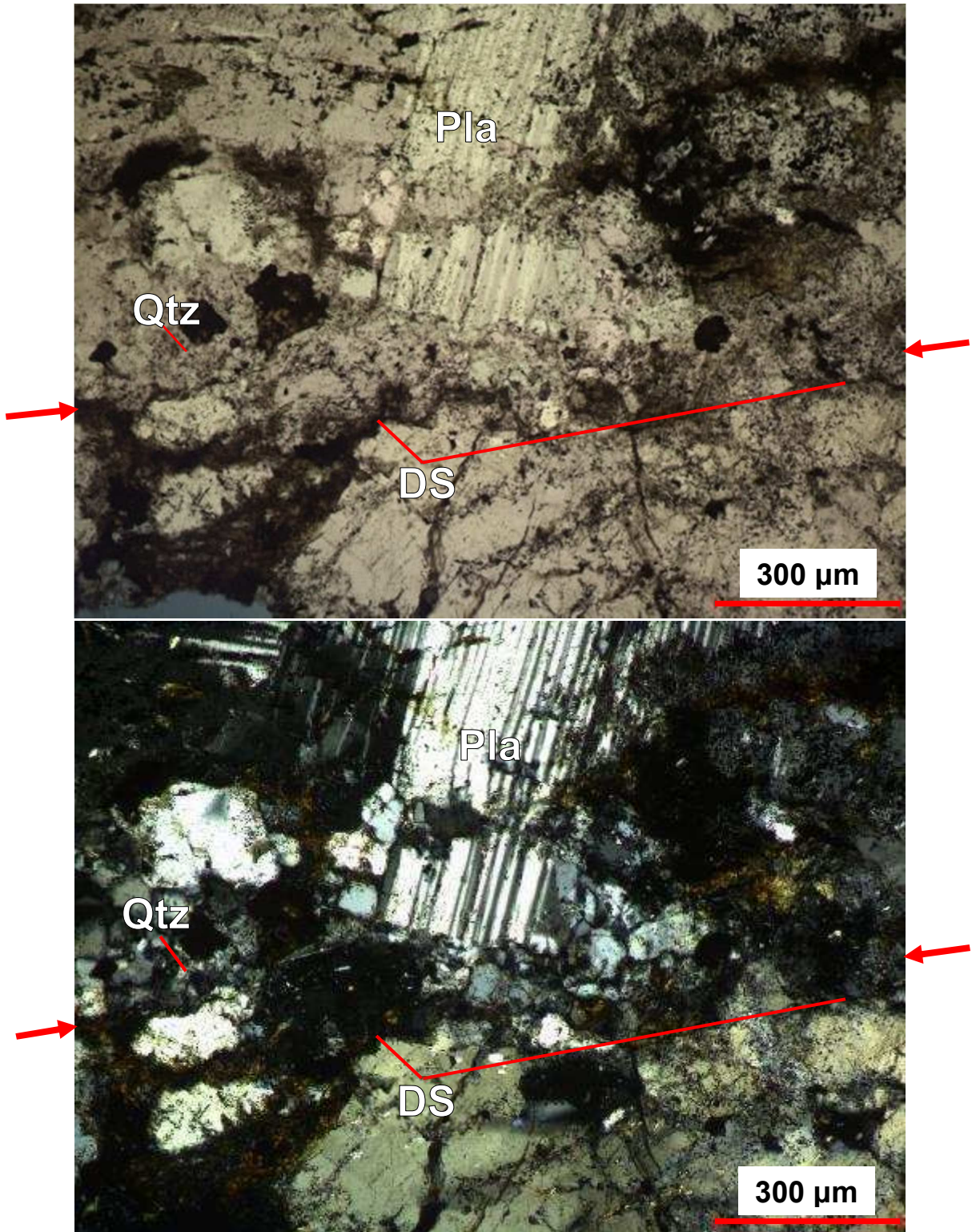


Figure 3.17. Photomicrograph showing P1 fault core (between red arrows) with fractured plagioclase (Pla), cataclastically deformed quartz (Qtz), and (DS) dark seams. Top image PPL, bottom image XPL. Sample AK107-4BB.

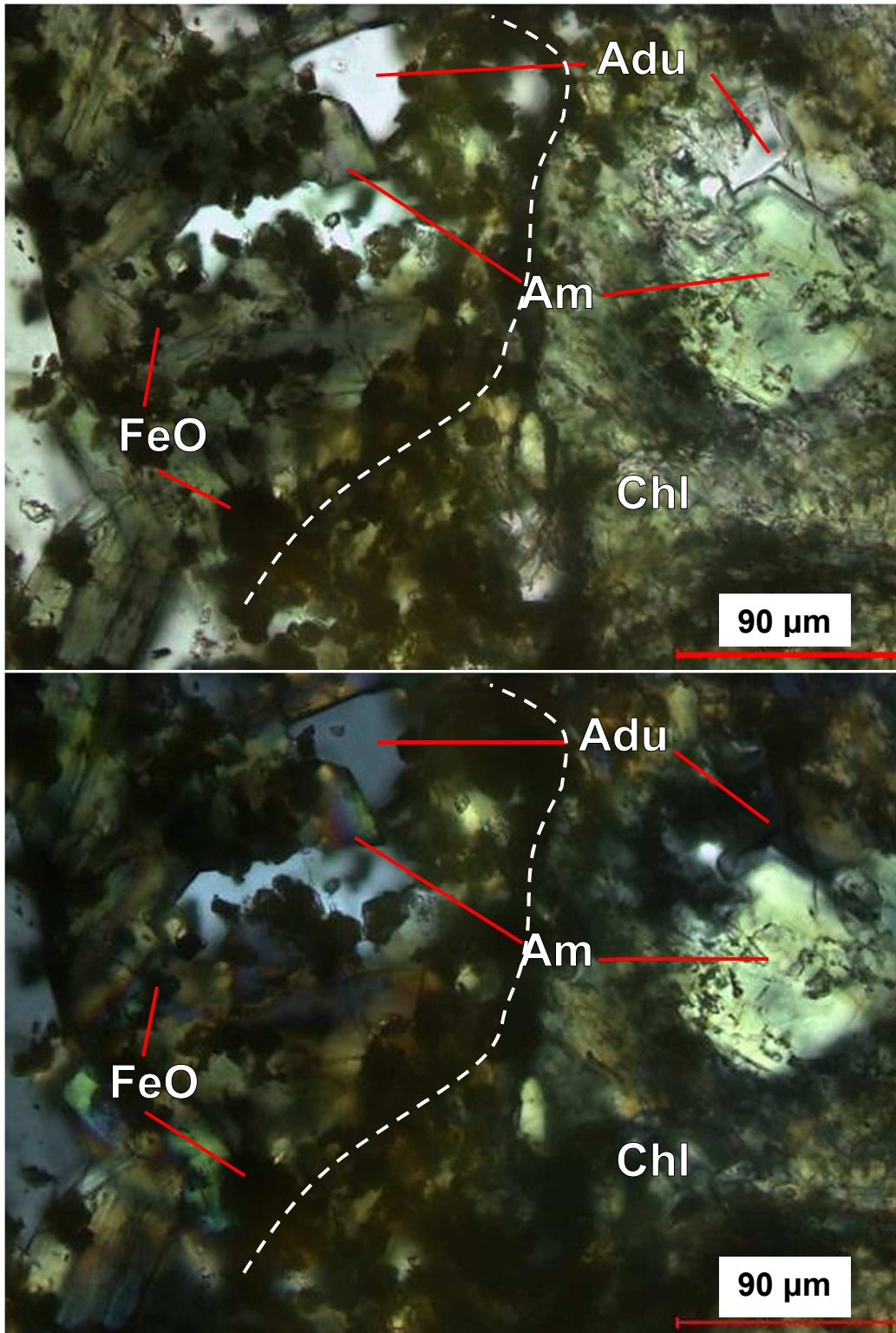


Figure 3.18. Photomicrograph showing typical mineralogy of P1 fault core constituents described in the text as “fine-grained mass”, composed of chlorite (Chl), adularia (Adu), iron oxide minerals (FeO), and amphibole (Am). The fault runs top-to-bottom across this image as an anastomosing fracture, marked by the seam of dark material (white dashed line). Top image PPL, bottom image XPL. Sample AK111-1A.

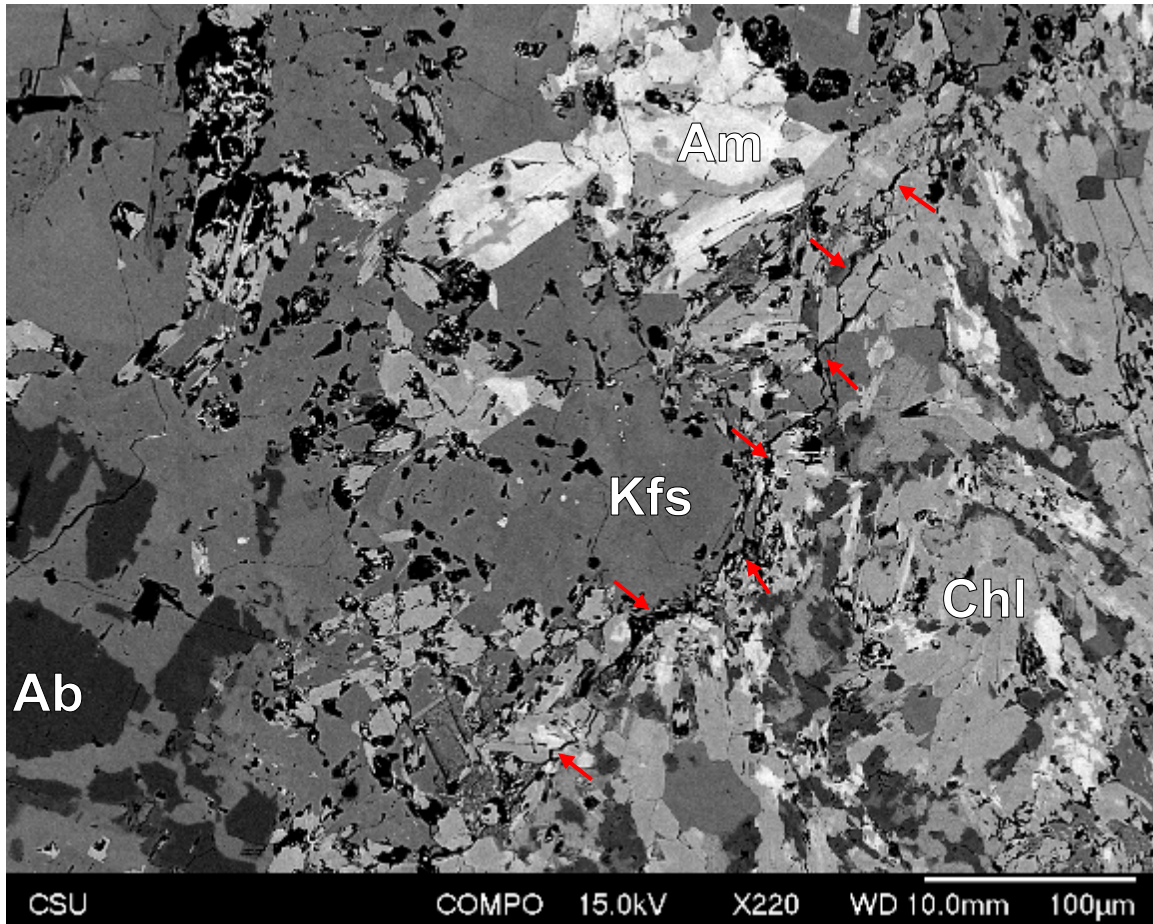


Figure 3.19. BSE image of a slightly enlarged field of view from Fig. 3.18, representative of the common minerals occurring along the P1 fault core (denoted by red arrows): Ab=Albite, Kfs=Adularia, Chl=Chlorite, Am=Amphibole. Internal chemical heterogeneity of the amphibole is evident. This figure is also representative of the relative modal abundances of the minerals within the fault core as well, roughly 20% amphibole, 50% adularia, 30% chlorite. Note the albite in the bottom left appears to be overgrown by adularia, suggesting a replacement reaction, while the adularia in the center of the image is more euhedral, suggesting secondary precipitation. Sample AK111-1A.

3.2.3. Population 2

Petrographic observations of P2 faults were made using 32 thin sections from 22 samples.

P2 faults display variability in associated fault rock composition (both clast and matrix), thickness, internal structure, style of contact between fault core and wall rock, and degree of alteration of adjacent wall rock.

In the P2 damage zone, that is, in the wallrock adjacent to the fault cores, quartz grains are more fractured than those associated with P1 faults. Grains commonly contain dense, strongly aligned fluid inclusion planes, with consistent orientations across samples regardless of fault orientation (further explored in section 3.5). Brittle fracturing is the most common mechanism of quartz deformation in the damage zone.

Plagioclase is typically slightly altered in the damage zone adjacent to the fault core. Many grains host very small sericite and saussurite grains, lending a dusty appearance to plagioclase, rather than hosting large sericite grains as seen in P1. As in P1 samples, EDS analysis reveals altered plagioclase is albitic in composition (see Appendix E). Some minor kinking is present (Fig. 3.20). Brittle fracture is common, either displaying offset, or manifesting as dilatant bands filled with secondary adularia. Fractures tend to be transgranular, cutting multiple adjacent grains, and aligned with fluid inclusion planes in quartz (Fig. 3.21). Adjacent to the fault core, strong albitization of plagioclase is common, typically in association with potassium feldspar. Albitized plagioclase grains are cut by the dilatant adularia filled fractures as well.

Biotite may be unaltered or chloritized, though not as thoroughly as in P1. Strong kinking and folding is common (Fig. 3.22). Alteration of biotite, where present, is correlated to proximity to the fault, occurring within ~15 mm of the fault core. EDS results consistently show minor chlorine content (~1 wt %) in damage zone biotite (see Appendix E), unique to P2 faults.

Minor or accessory minerals in the damage zone are the same as host FCS. Muscovite is uncommon. Like biotite, it is commonly kinked and folded. In some cases, biotite and muscovite are partly or fully altered to fine-grained masses of secondary phyllosilicates, yellow-brown under

plane polarized light. Titanite is usually associated with epidote and altered phyllosilicate minerals. Primary clinozoisite and epidote are commonly fractured in the damage zone. Adularia is present in secondary veins and replacing host plagioclase (Fig. 3.23, 3.24). Adularia veins crosscut the fault core and wall rock (Fig. 3.24, 3.25). Minor secondary actinolite is present in highly altered sections of the damage zone, associated with the fine-grained masses of altered phyllosilicates.

Unlike thin, difficult to discern P1 fault cores, P2 fault cores and their clasts and matrix are well defined. Within P2 fault cores, clasts are mostly quartz and plagioclase, present as both individual grains and polymineralic aggregates. Clasts are angular and fractured and range in size from sub- μm to thousands of μm , typical of cataclastic comminution. Larger plagioclase clasts display the same slight alteration as in the damage zone, and are generally albitized. Quartz clasts commonly contain fluid inclusion planes with no preferred orientation among clasts, indicating grain rotation during cataclasis, and fluid inclusion formation prior to fault core development. The clasts are embedded in a fine-grained, colorless to reddish-yellow matrix composed predominantly of adularia with variable amounts of biotite and chlorite.

Minor clast mineralogy includes biotite, epidote, clinozoisite, and opaque minerals. Biotite is highly comminuted within the matrix, contributing to its dark color, and larger, rare intact clasts may be partially to fully chloritized. BSE and EDS analysis reveals uncommon $<5 \mu\text{m}$ grains of chlorine-bearing amphibole in association with altered biotite and chlorite, like those observed in P1 (see Section 3.2.2). Chlorite and adularia are uncommonly present as secondary mineralization in $<100 \mu\text{m}$ cavities within the fault core matrix. Opaque minerals vary in shape and size, commonly $<10 \mu\text{m}$ and anhedral, but rarely up to $\sim 100 \mu\text{m}$ with distinct crystal faces, and are associated with altered biotite.

Also within some P2 fault cores are optically dark to opaque seams (Fig. 3.26), like those observed among P1 fault cores (Fig. 3.17). They typically accompany biotite and chlorite. In plane polarized light, the seams are opaque dark reddish-brown to black and trend subparallel to the

trend of the fault core. They are rarely planar, but instead anastomose through the fault matrix and around clasts (Fig. 3.27).

A degree of variability exists within the P2 fault cores. Six P2 samples contain “random fabric” cataclasites, composed of clasts within relatively homogeneous matrix (Fig. 3.28). Sixteen P2 samples are foliated cataclasites. Foliation-defining features in P2 faults are elongated parallel to the faults and have distinct optical properties that produce an optical heterogeneity in the fault core (Fig. 3.24). These include internal sublayers of varying clast size and clast/matrix ratio, changes in matrix composition, and rare elongated networks of phyllosilicate minerals within the fault core. These phyllosilicate networks are sometimes replaced by the dark seams. Internally, some of the sublayers have a random fabric texture. Uncommonly, P2 fault cores host exceptionally well-developed foliations including S-fabrics and throughgoing phyllosilicate networks wrapped around more resistant quartz and plagioclase clasts (Fig. 3.27).

Most of the cataclasites are weakly foliated because phyllosilicate networks are absent to poorly developed. Instead, the major contributor to the foliated appearance is heterogeneous matrix color, easily evident in plane polarized light (e.g. Fig. 3.24, 3.27, 3.30). Biotite appears to contribute to this heterogeneity. Less biotite correlates with a relatively colorless matrix in plane polarized light, which is then relatively richer in comminuted quartz and plagioclase. More biotite correlates with a darker, reddish brown to black matrix when observed in plane polarized light. Clear evidence of altered and comminuted biotite is present in these sublayers, as well as more opaque iron oxide minerals and more seams produced by DMT. As mentioned previously, EDS analysis revealed the colorless fault matrix to be very rich in adularia, (Fig. 3.24, 3.25; see Appendix E). The darker matrix is still composed mainly of adularia but with significant contribution from biotite (Fig. 3.29).

One P2 sample contains two through-going, sharply defined pseudotachylyte (PST) veins in a relatively well-developed foliated cataclasite (Fig. 3.30). The fault core displays the same style of internal heterogeneity that defines the foliations in other samples, containing juxtaposing

bands of fault rock of mainly K-feldspathic composition, and hosting varying matrix phyllosilicate content and clast sizes.

The first PST vein displays a completely different texture than previously observed fault rocks. It is composed of dark, reddish-brown aphanitic matrix in both plane- and cross-polarized light, hosting clasts of quartz, feldspar, and opaque minerals. According to EDS analysis, the PST matrix has a primarily biotite-like composition, with minor (<3%) chlorine content. It contains randomly oriented microlites of K-feldspar and chlorine-bearing biotite (Figs. 3.31, 3.32). K-feldspar needles rarely display slight alteration to illite. Clasts of quartz are commonly rimmed by K-feldspar, and are highly rounded in BSE imagery (Fig. 3.32). Note that the K-feldspar is not referred to as adularia in the pseudotachylyte, as temperatures associated with frictional melt are considered too high for adularia formation (e.g. Reyes 1990; Dong & Morrison 1995; Ennis et al. 2000). This high temperature K-feldspar could be sanidine.

The second PST vein is similarly fine-grained, but is a uniform K-feldspar composition with no microlites. The rim of this vein is mainly composed of intermediate Ca-Na bearing plagioclase composition. Clasts are invariably small (<10 μm) and composed of quartz or biotite. This PST hosts a high-angle injection vein that cuts 1 cm into the wallrock, and is in turn cut by the first PST vein (Figs. 3.30, 3.31).

The veins are highly planar and cut parallel to the cataclastic fault core. There are clear indicators of overprinting and mutual cross-cutting: pseudotachylyte veins contain clasts of quartzofeldspathic cataclasite, and pseudotachylyte is brittlely offset within the fault core (Fig. 3.30). The PST-bearing faults also contain evidence of having hosted DMT, particularly along boundaries between sublayers.

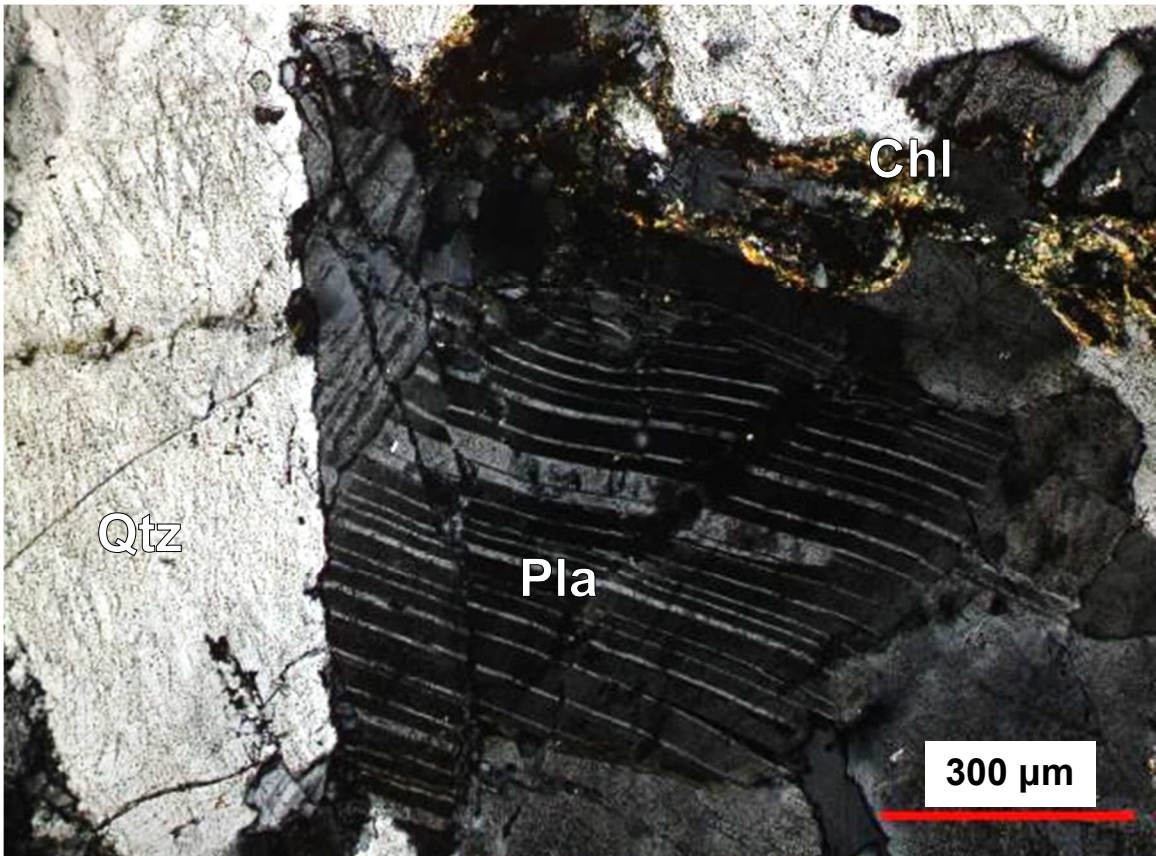


Figure 3.20. Plagioclase grain displaying minor kinking and internal fractures in the P2 damage zone. Sample AK104-2.

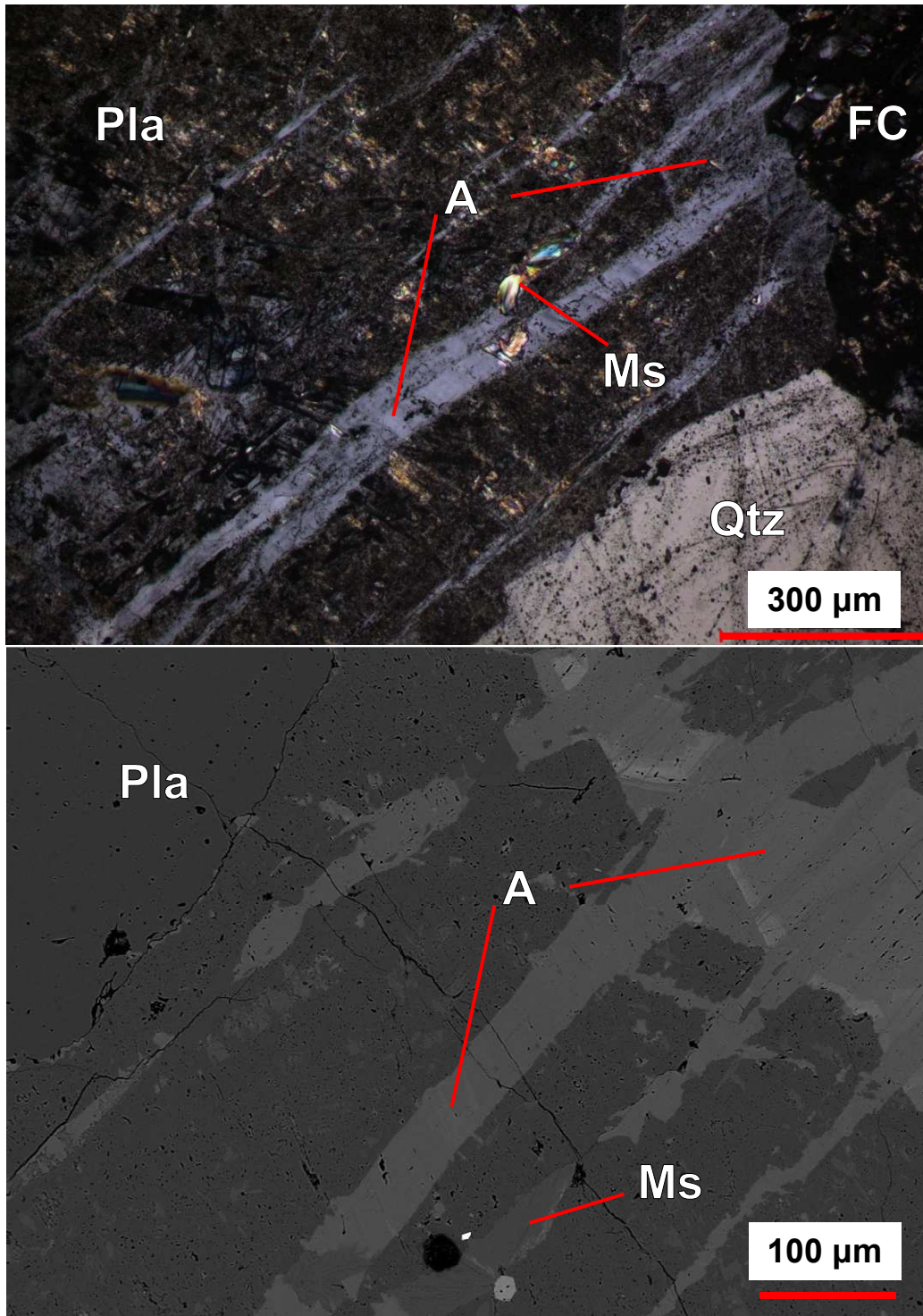


Figure 3.21. (a) XPL A highly sericitized and albitized plagioclase grain in the damage zone of a P2 fault, displaying (A) bands of K-feldspar composition. The bands trend roughly parallel to the fluid inclusion planes in surrounding quartz grains. Sericitization includes the “dusty” texture of plagioclase, and variably sized muscovite grains. The fault core is labelled FC. (b) BSE image from the same area but slightly enlarged, showing the contrast between the altered plagioclase (albite) and the bands of adularia. Sample AK108-1B.

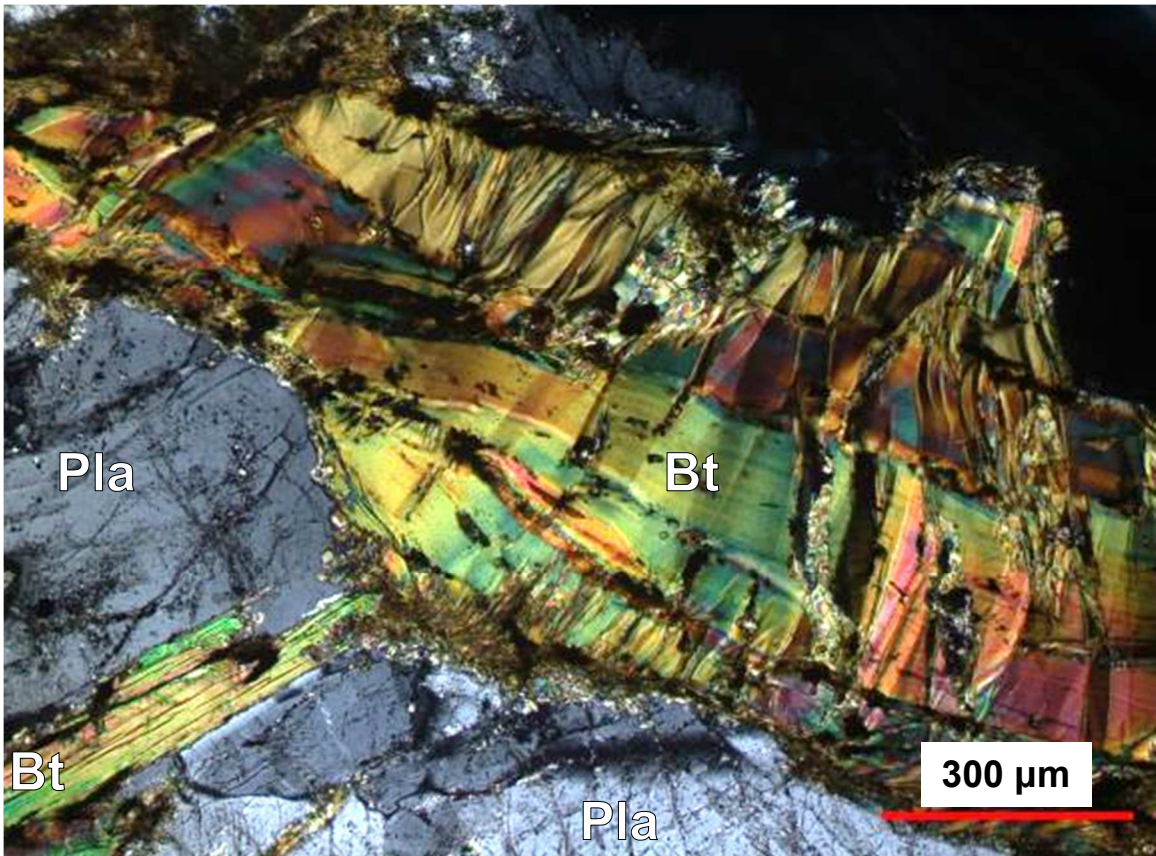


Figure 3.22. Strongly kinked biotite in P2 damage zone. Sample AK108-2A.

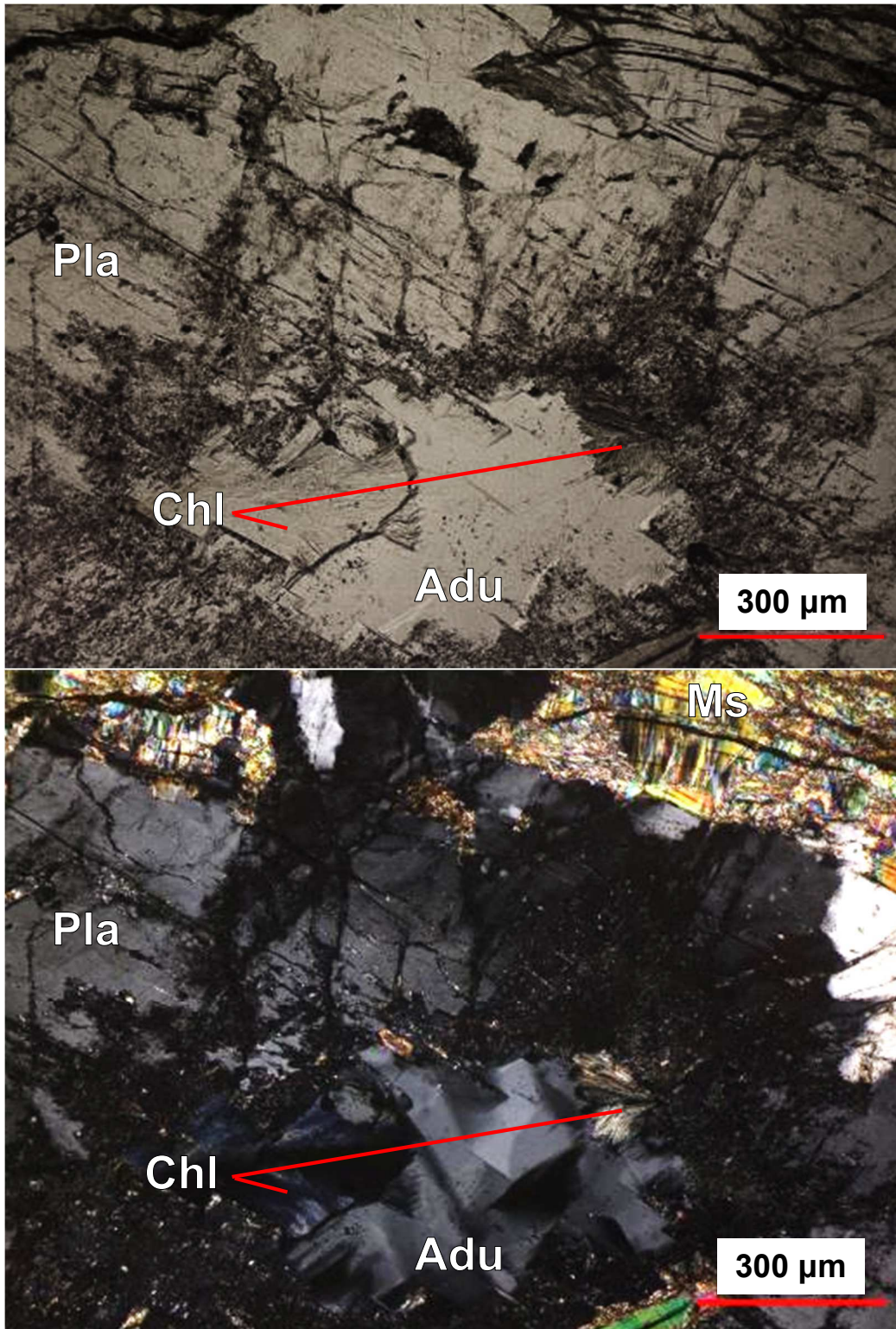


Figure 3.23. Patch of adularia (Adu) and chlorite (Chl) within altered plagioclase (Pla), in the P2 damage zone. Adularia shows hints of diamond-shaped crystals. Altered plagioclase appears as a fine-grained mass of muscovite. Kinked muscovite grains are present along the top of the image. Top image PPL, bottom image XPL. Sample AK103-1A.

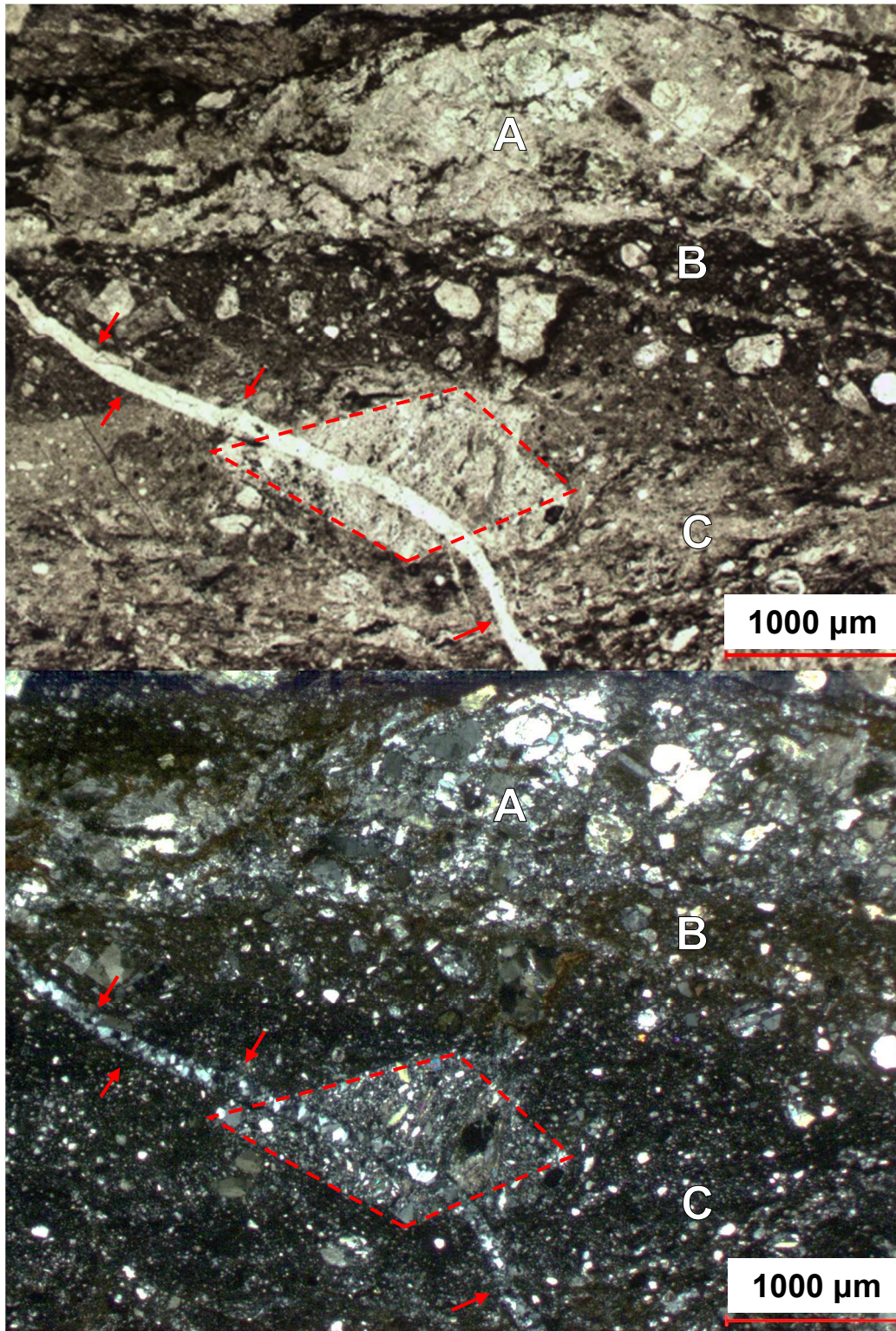


Figure 3.24. Foliated P2 fault core, displaying internal heterogeneity: (A) clast-dominated fault rock, (B) dark, phyllosilicate-rich cataclasite, and (C) lighter, quartzofeldspathic fault rock. An angular cataclasite clast, outlined in red, is present, visibly distinguishable from adjacent fault rock. An adularia vein (red arrows) cuts across all sublayers. The sublayers are nearly indistinguishable in XPL (bottom), but show clear contrast in PPL (top). Sample AK106-3A.

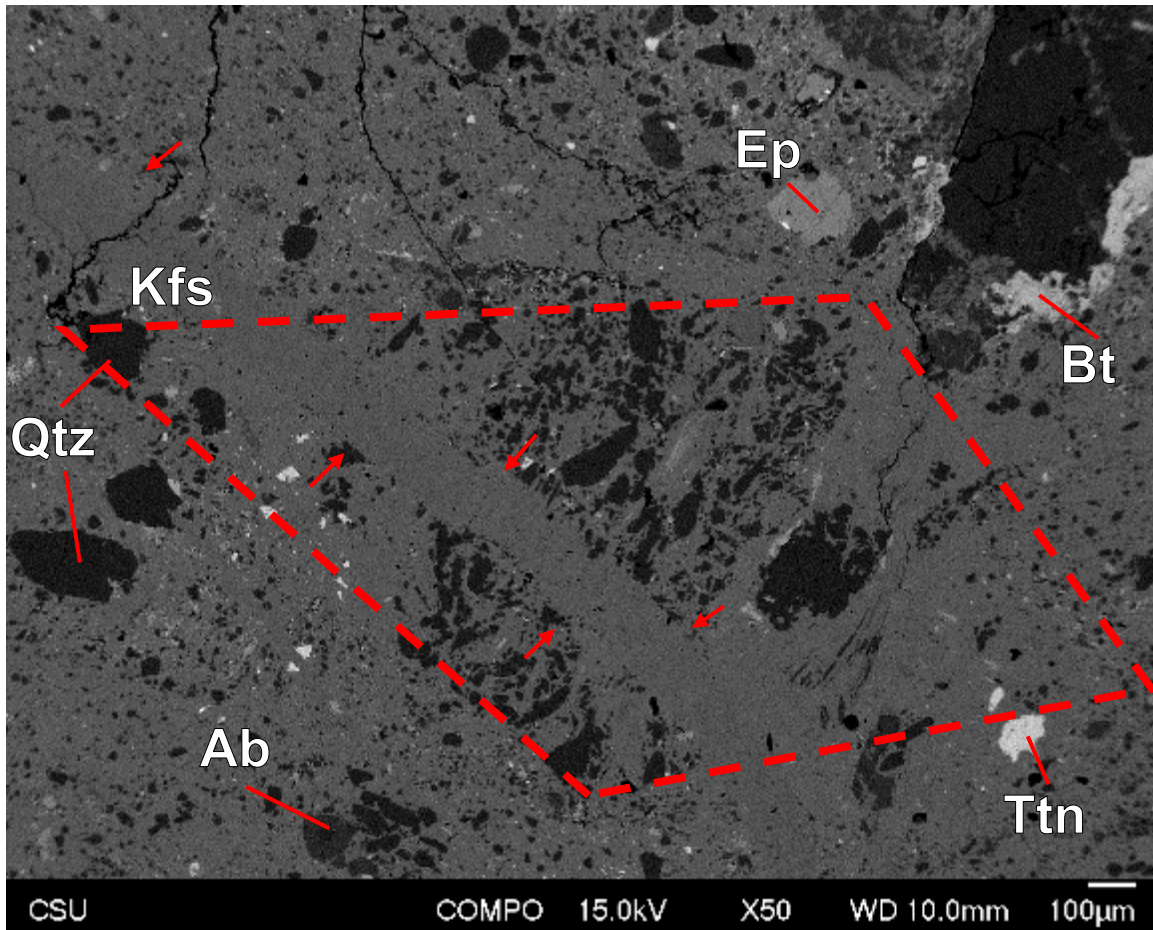


Figure 3.25. BSE image of the adularia vein from previous figure 3.24, centered on the clast of cataclasite (outlined in red). The adularia vein is indistinguishable from the fault matrix, showing both the light-colored fault matrix and the cataclasite clast are adularia-rich (K-feldspar composition). Quartz, biotite, epidote, and titanite clasts are primary, representative of host FCS composition. Albite was not observed in the host rock, and is likely altered primary plagioclase. Adularia clasts and matrix are also secondary. Sample AK106-3A.

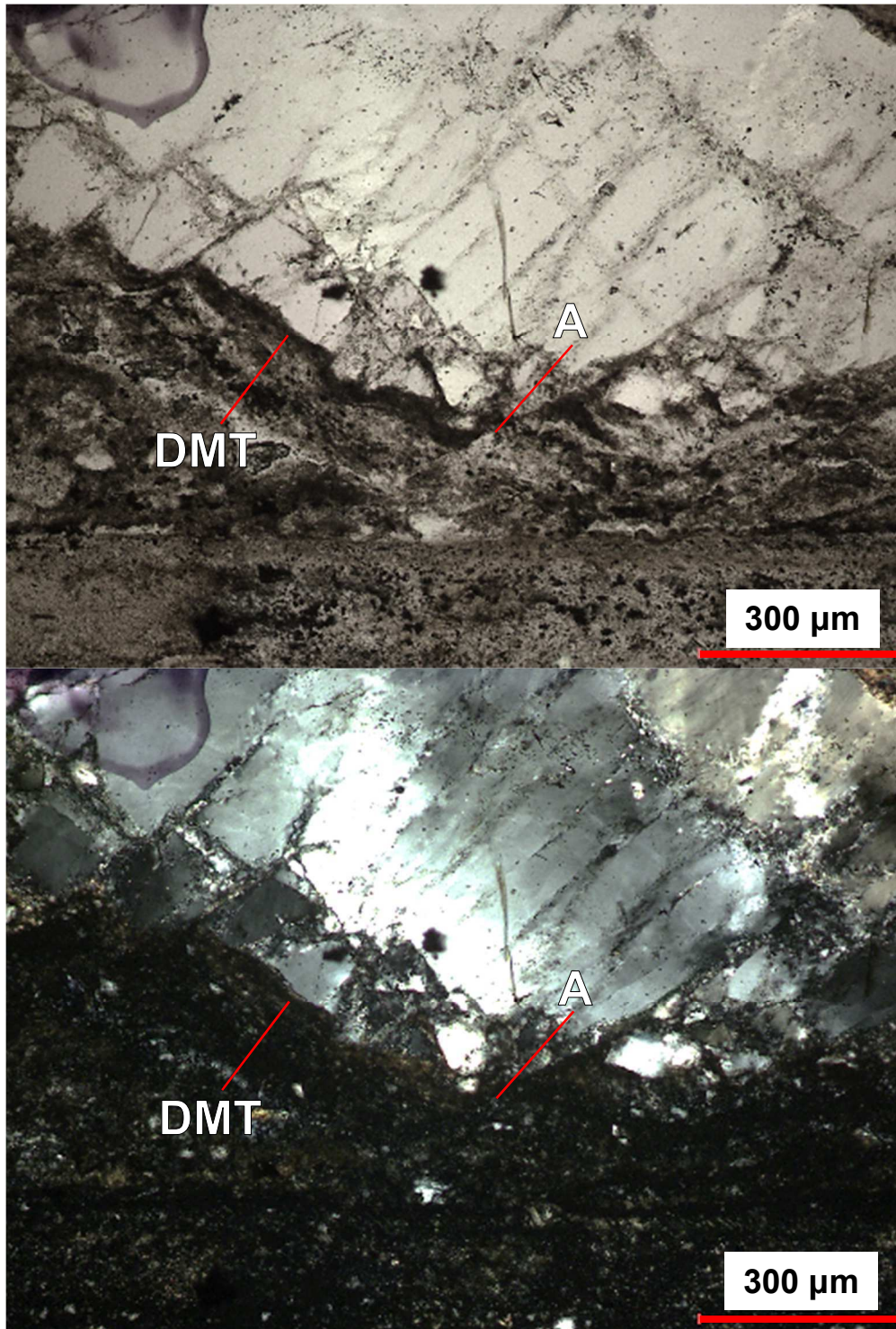


Figure 3.26. Foliated P2 cataclasite showing a dark, relatively iron-rich phyllosilicate bearing matrix. Quartz in the wallrock is highly fractured. Note the dark seam that produced by DMT along the interface between the fault core and wallrock. A fracture (A) offsets the fault matrix, dark seam, and wallrock quartz. Top image PPL, bottom image XPL. Sample AK103-1A.

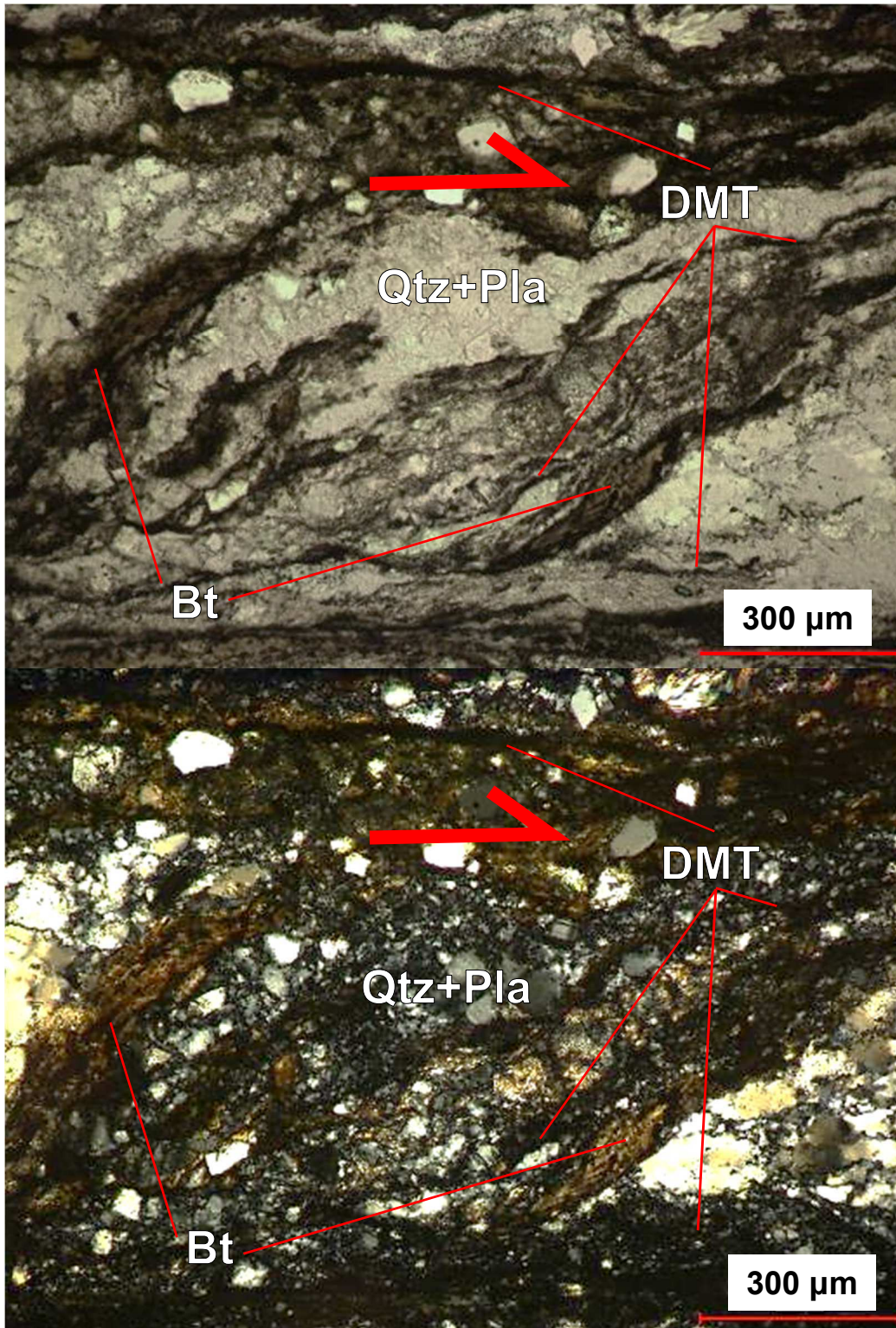


Figure 3.27. Foliated P2 cataclasite, extending horizontally along the field of view, with S-fabrics of quartzofeldspathic clasts and subhorizontal biotite grains show top-to-right displacement. Heterogeneity within the fault core is evident as quartzofeldspathic fault rocks (Qtz+Pla) in contact with phyllosilicates (Bt). Note the thin black anastomosing seams produced by diffusive mass transfer (DMT). Top image PPL, bottom image XPL. Sample AK106-2Bu.

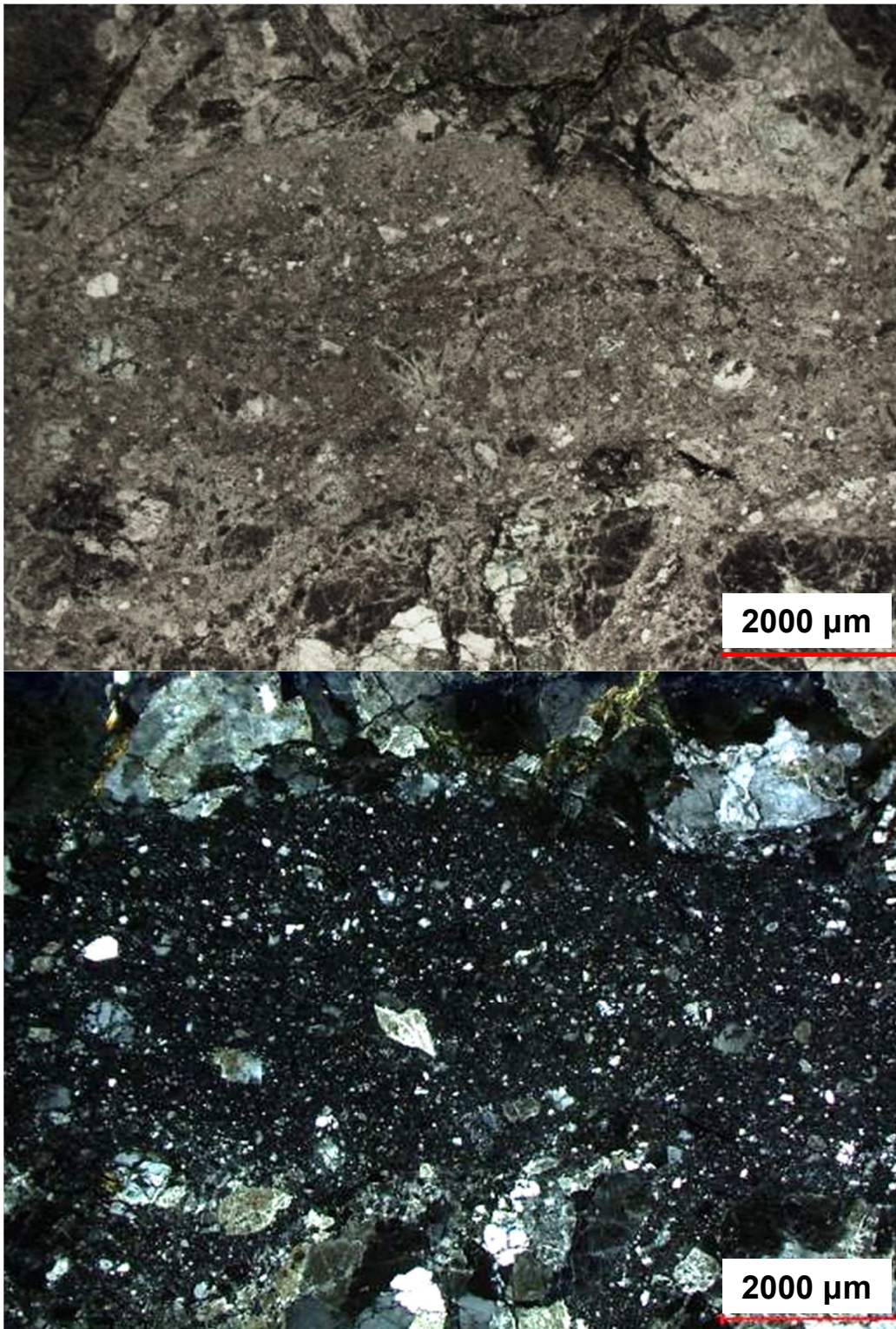


Figure 3.28. Overview of a P2 random fabric fault core, (L to R across the field of view). Notice the lack of internal heterogeneity (c.f. Fig. 3.24), especially apparent when comparing plane-polarized light images. Top image PPL, bottom image XPL. Sample AK100-3B.

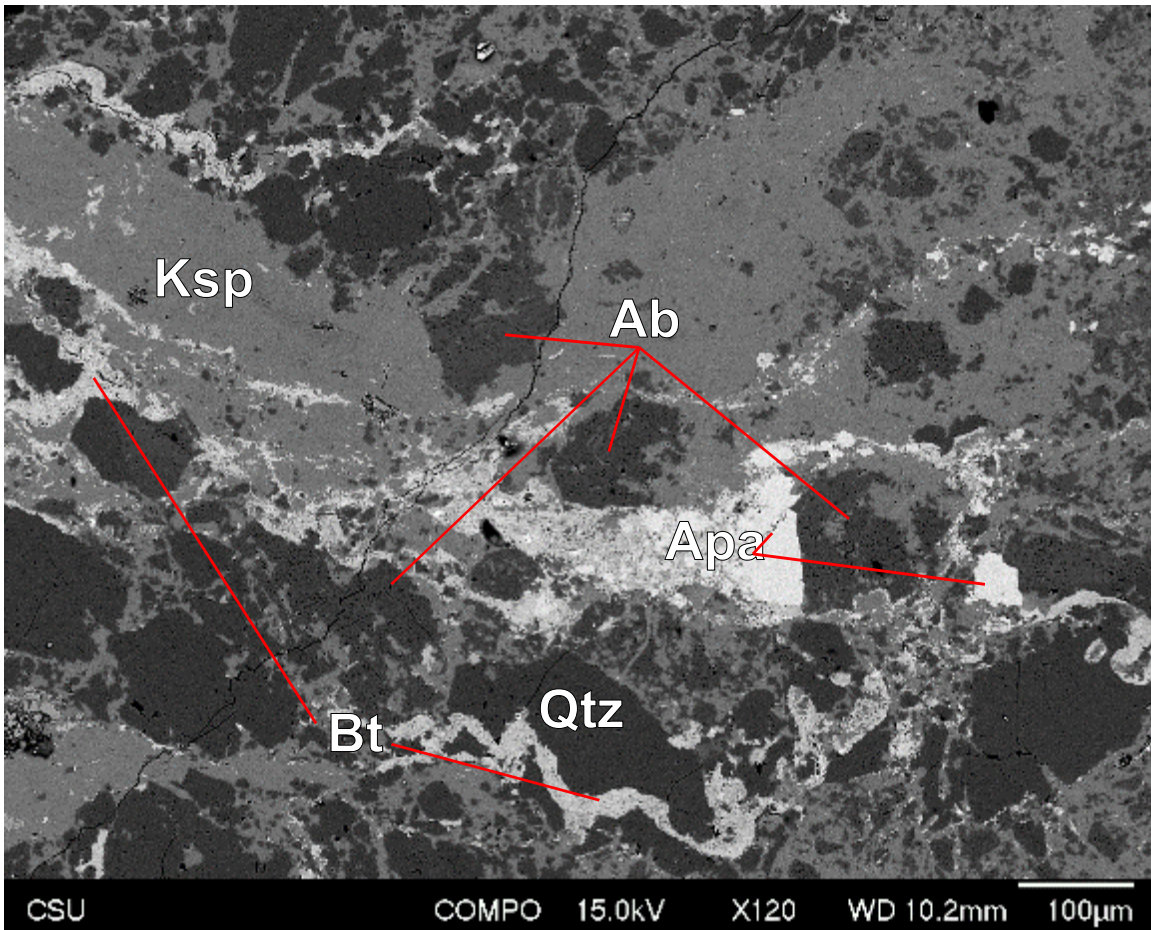


Figure 3.29. BSE image of a darker sublayer in a foliated P2 fault core, within the area labelled “B” in Fig. 3.24. The matrix is primarily adularia. Unlike the colorless sublayers, biotite weaves around clasts and displays a smeared texture in the matrix, confirming it as a contributor to the reddish-brown matrix color, and thus to the optical heterogeneity within the foliated cataclasite. A partially comminuted clast of apatite is present in the field of view. Apa=Apatite. Sample AK106-3A.

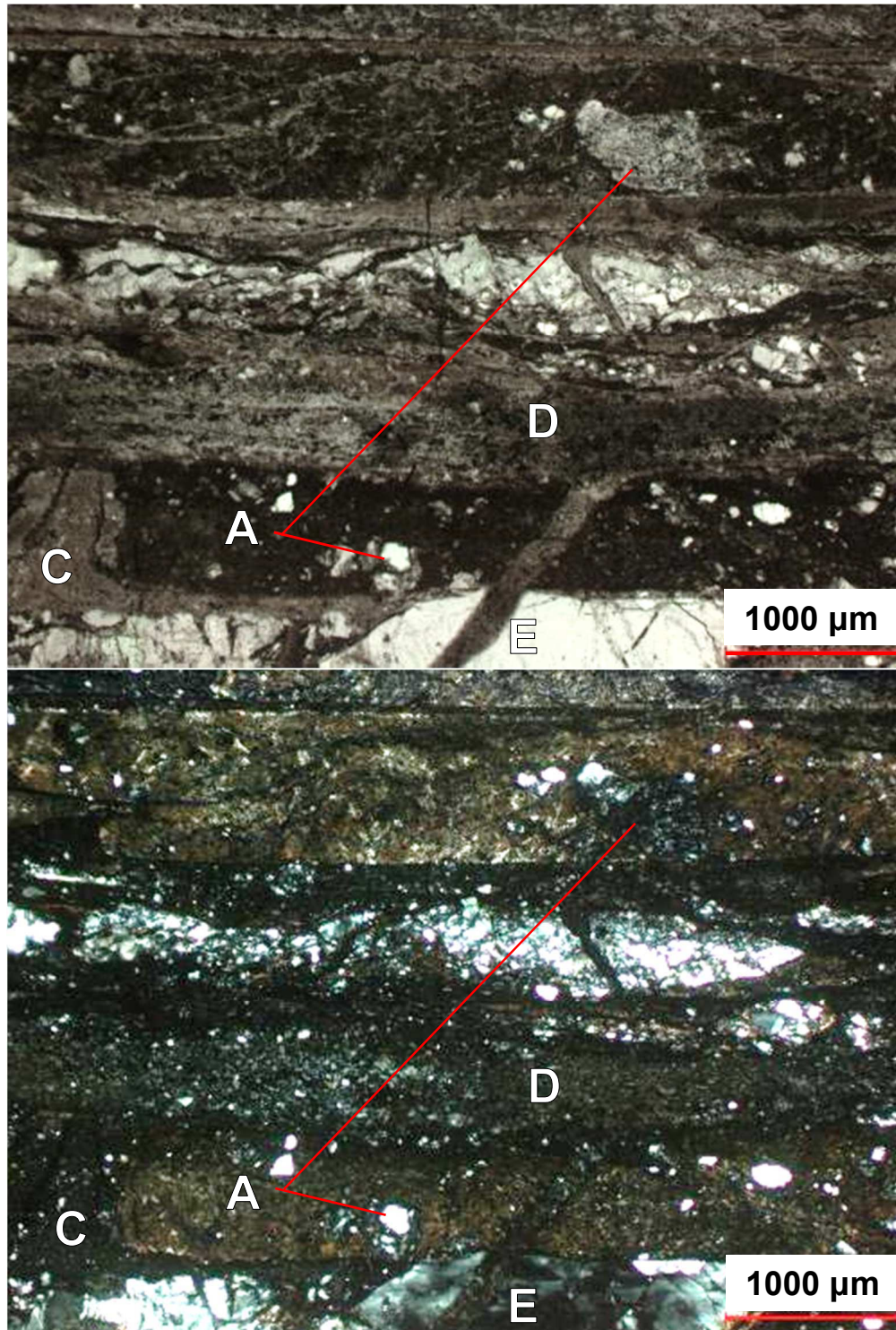


Figure 3.30. XPL photomicrograph showing a highly-foliated P2 fault core, containing sublayers of cataclasite and two styles of pseudotachylyte veins. Evidence for multiple deformation events is present, as brown pseudotachylyte veins of biotite composition contains clasts of quartzofeldspathic cataclasite (A) cut by two separate layers of a second K-feldspar composition PST (C, D). The second PST hosts injection veins that cut across both the first PST type (C) and the wallrock (E). Sample AK103-1A.

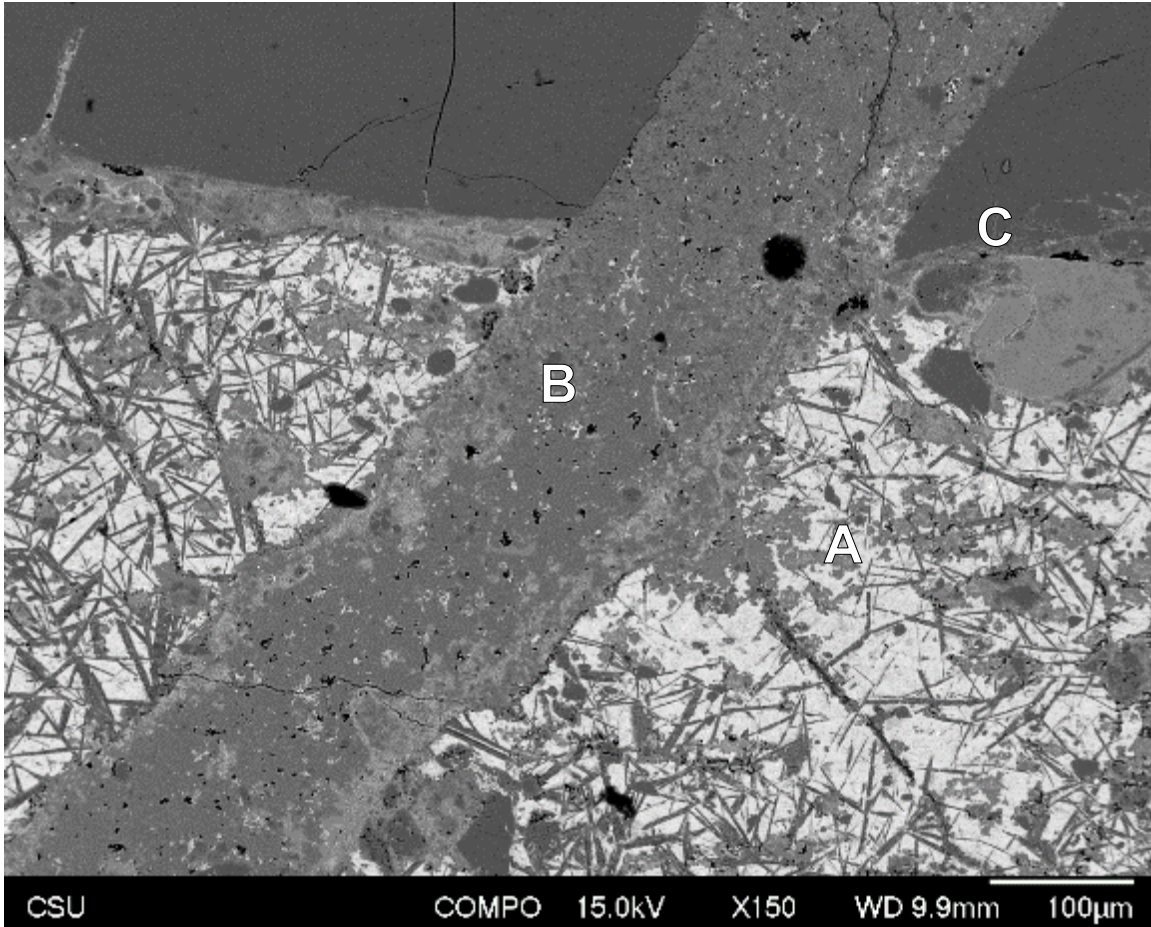


Figure 3.31. BSE image of the PST injection vein “E” at the bottom of Fig. 3.30. This figure is rotated 180° from Fig. 3.30, showing gray wallrock quartz across the top of the image, and the fault rock below. The biotite-composition PST (A) hosts numerous randomly oriented microlites of K-feldspar composition (possible sanidine), whereas the K-feldspar composition PST (B) is relatively homogeneous, containing only very small clasts, typically quartz. The darker grey wallrock along the top of the image is wallrock quartz. Note the highly planar contacts along the boundaries of both PST veins (C). Sample AK103-1A.

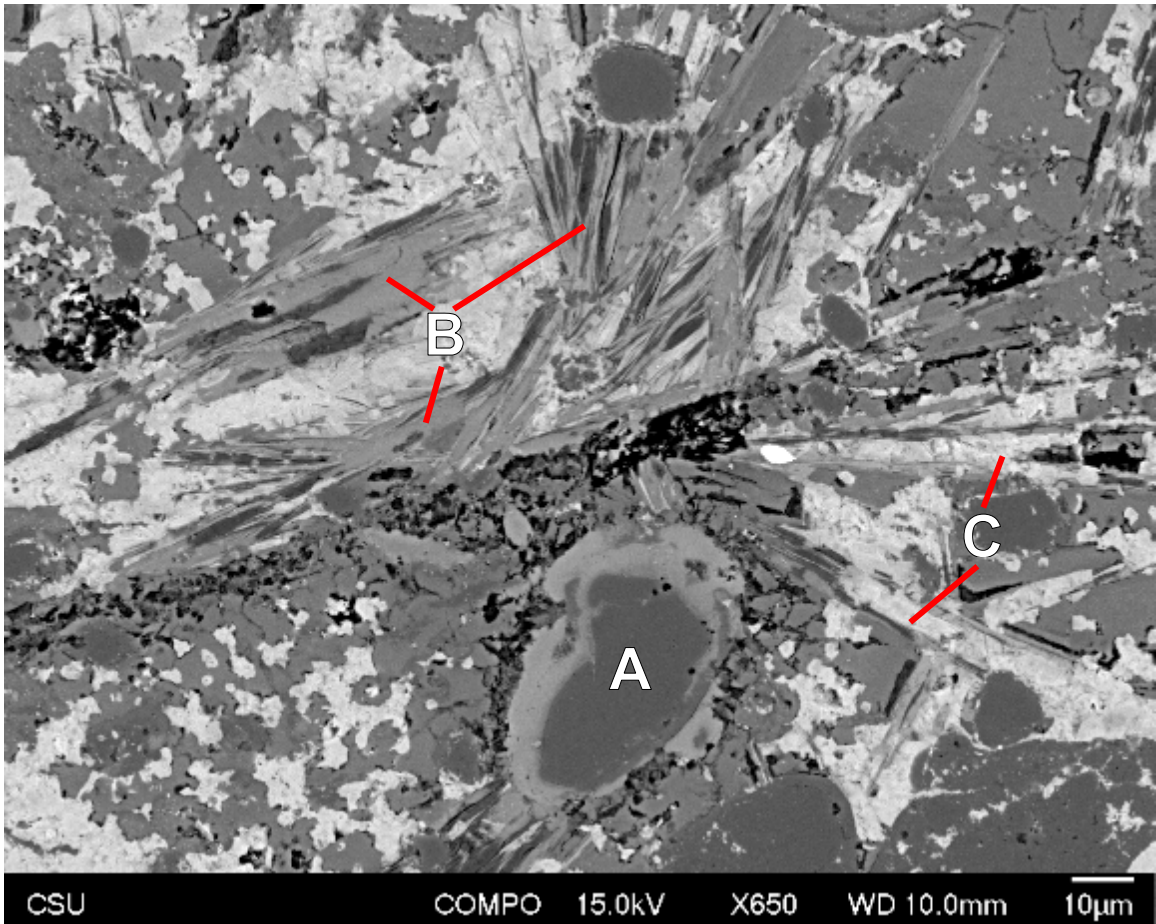


Figure 3.32. BSE imagery showing internal composition of the biotite-composition pseudotachylyte. Dark gray quartz clasts (A) with rounded edges and K-feldspar rims. Lighter gray K-feldspar microlites (B) and bright chlorine-bearing biotite-composition microlites (C). Sample AK103-1A.

3.3. Fault Kinematics

This section describes kinematic indicators present in outcrop and on the microscale.

Sense of shear was observed along 5 P1 and 36 P2 faults. In the field, apparent offsets were measured where white aplite dikes and quartz veins were offset (*e.g.* Fig. 3.33). Though they were searched for, slickensides were not observed along any of the FCS faults.

Sense of displacement was also determined in thin section using brittle fault kinematic indicators (*e.g.*, Passchier and Trouw (2005); see Appendix A). Orthogonal thin sections, one cut along strike and orthogonal to the fault plane, and one cut along dip and orthogonal to the fault plane, allowed identification of strike-slip and dip-slip components of shear. Kinematic indicators within the P1 fault population were difficult to discern owing to exceptionally thin fault cores and lack of significant structures in the wallrock (*e.g.* Fig. 3.34). The significantly thicker P2 fault cores allowed for easier identification of shear sense (*e.g.* Fig. 3.35).

The frequencies of all observed shear senses are given in Table 3.2. Due to lack of data density among P1 fault offsets, conclusive kinematics can only be tentatively assigned. However, P2 faults display dominantly normal and sinistral offset (*e.g.* Figs. 3.5, 3.8, 3.9, 3.33).

A table with fault orientations, measured offsets, and features being offset is included in Appendix A.

Table 3.2. Frequency of shear sense from field and microscopic observations of kinematic indicators, divided by population.

Offset	Outcrop		Microscope		Total	
	P1	P2	P1	P2	P1	P2
Normal	-	12	-	8	-	20
Reverse	1	-	1	-	2	-
Sinistral	1	12	1	8	2	20
Dextral	-	3	1	-	1	3

For better insight into the true kinematics of the faults, these data are plotted on stereonet showing the orientations of faults separated by components of strike- and dip-slip (Figs. 3.36, 3.37). Even with limited data, the low-angle orientations of N-S striking, E-dipping P1 faults

combined with observed slip senses identify them as east-dipping reverse faults with inconclusive strike-slip sense. In contrast, P2 faults are both north-dipping extensional (normal) faults with a significant sinistral component, and steep, generally N-dipping sinistral strike-slip faults.

In cases where microscopic and mesoscopic measurements were made on the same fault, the microscope observation took precedent, as both slip and dip senses were observable.



Figure 3.33. Photograph of a horizontal surface of the FCS, showing a thin quartz vein offset left-laterally 32.5 cm by a P2 fault (red arrows). This observation allows for identification of the strike-slip component, but not the dip-slip. Fault orientation is 020, 33° SE. Quartz vein has a strike of 160°.

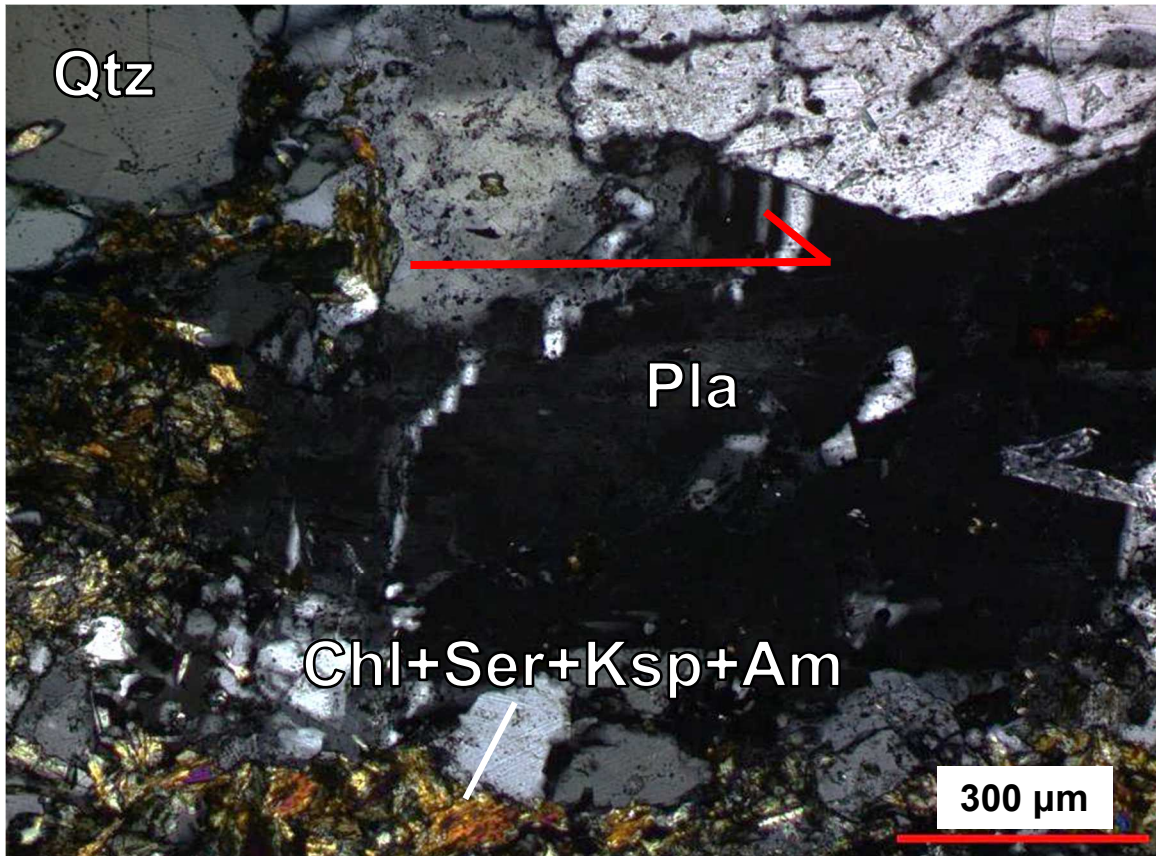


Fig. 3.34. XPL photomicrograph showing offset twins in a plagioclase grain adjacent to a P1 fault core (horizontal, below the field of view), displaying top-to-right displacement, indicating this is a left-lateral fault. The fine-grained mass at bottom is the chlorite + sericite/muscovite + adularia + chlorine-bearing amphibole (see section 4.2) present along many P1 population fault cores. Sample AK107-3AL.

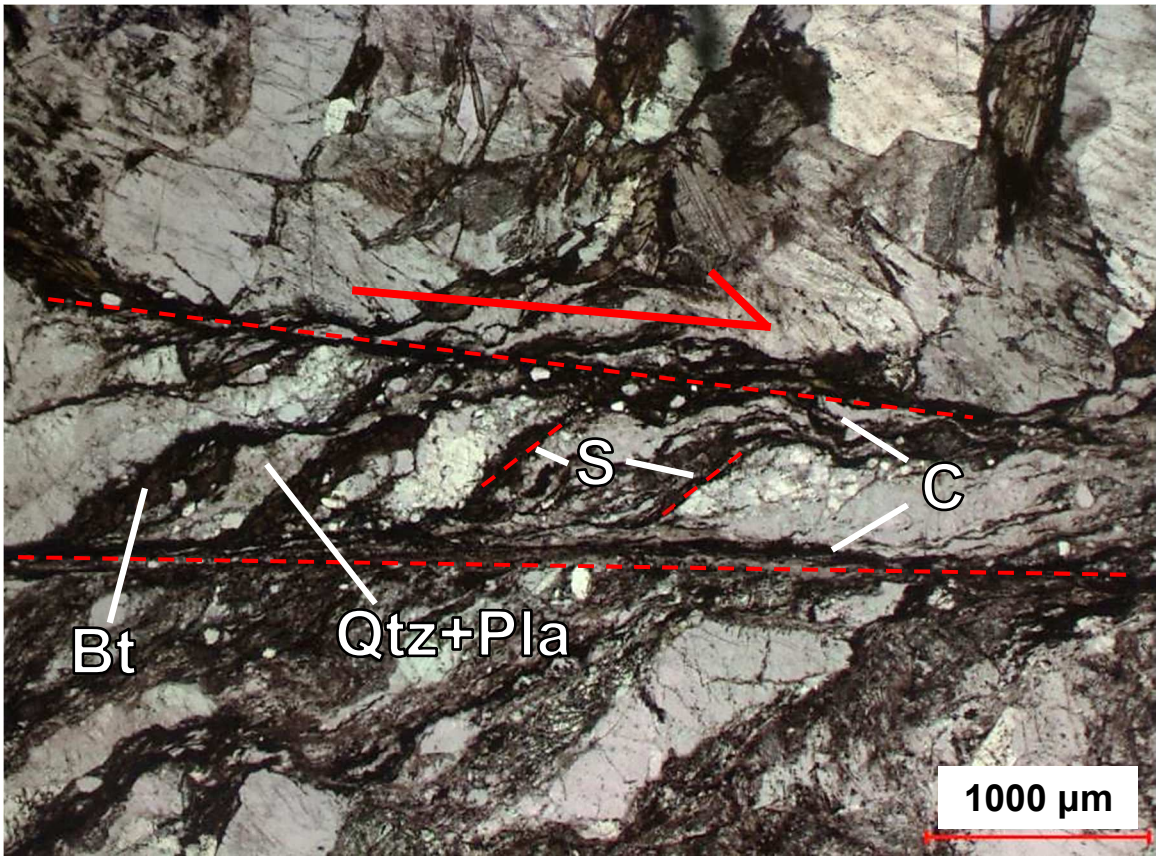


Figure 3.35. PPL photomicrograph, taken from same sample in Fig. 3.27, of a well-foliated P2 fault, showing masses of cataclastically deformed quartz and plagioclase, and biotite having formed S-C fabrics (dashed red lines) displaying top to right shear, indicating this is a normal fault. The corresponding orthogonal thin section has been determined to show left lateral motion. These combined observations indicate that this fault is normal-sinistral. Sample AK106-2Bu.

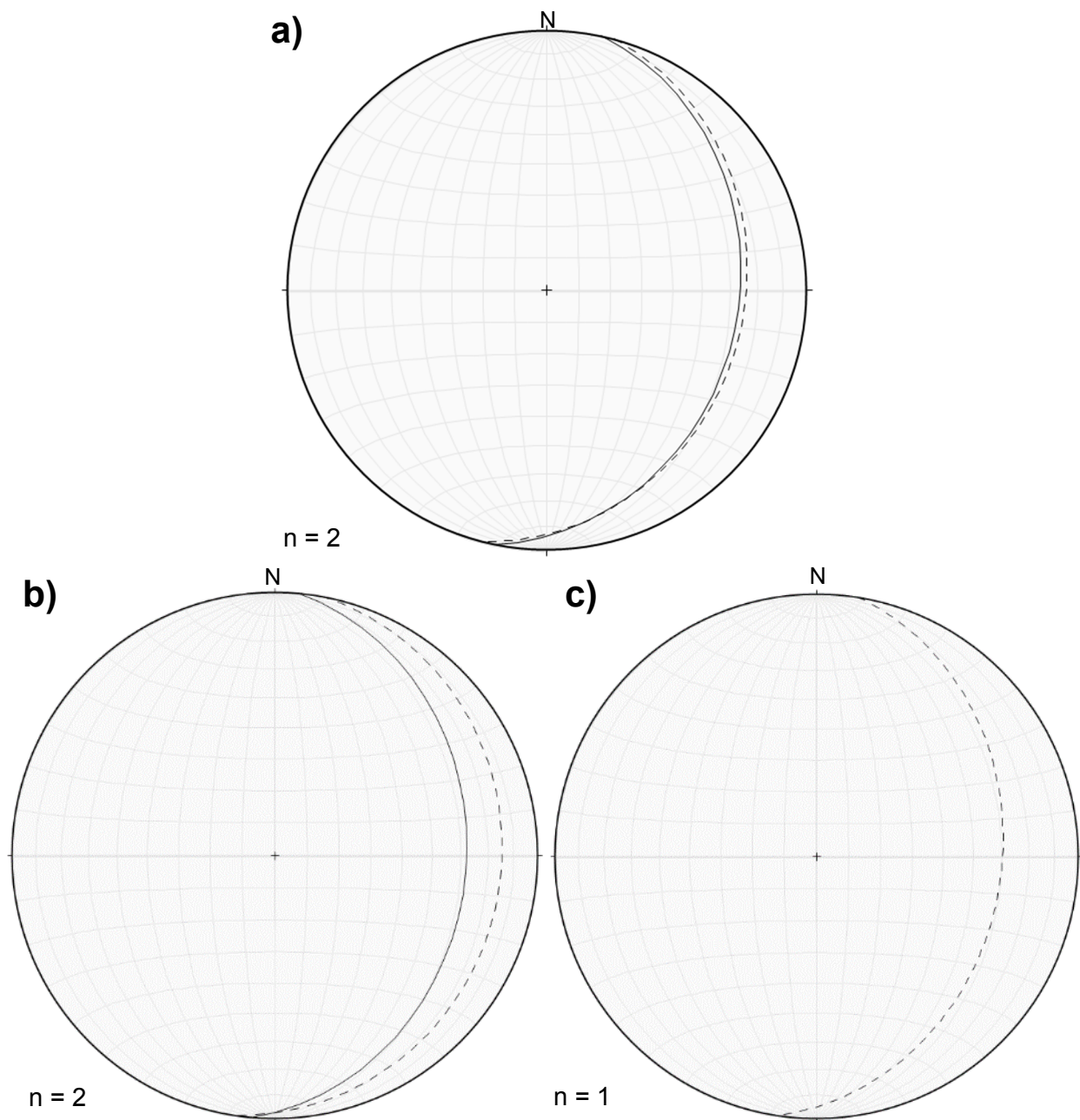


Figure 3.36. Lower hemisphere, equal area stereonets displaying orientations of P1 fault planes with observed sense of shear data from field and thin section observations. “Unknown” offsets indicate observations made in thin section, where only the sense of shear, not the total displacement, was observable.

Unknown offset=Dashed; 0-5 cm offset=Solid

- a) Reverse
- b) Left lateral
- c) Right lateral

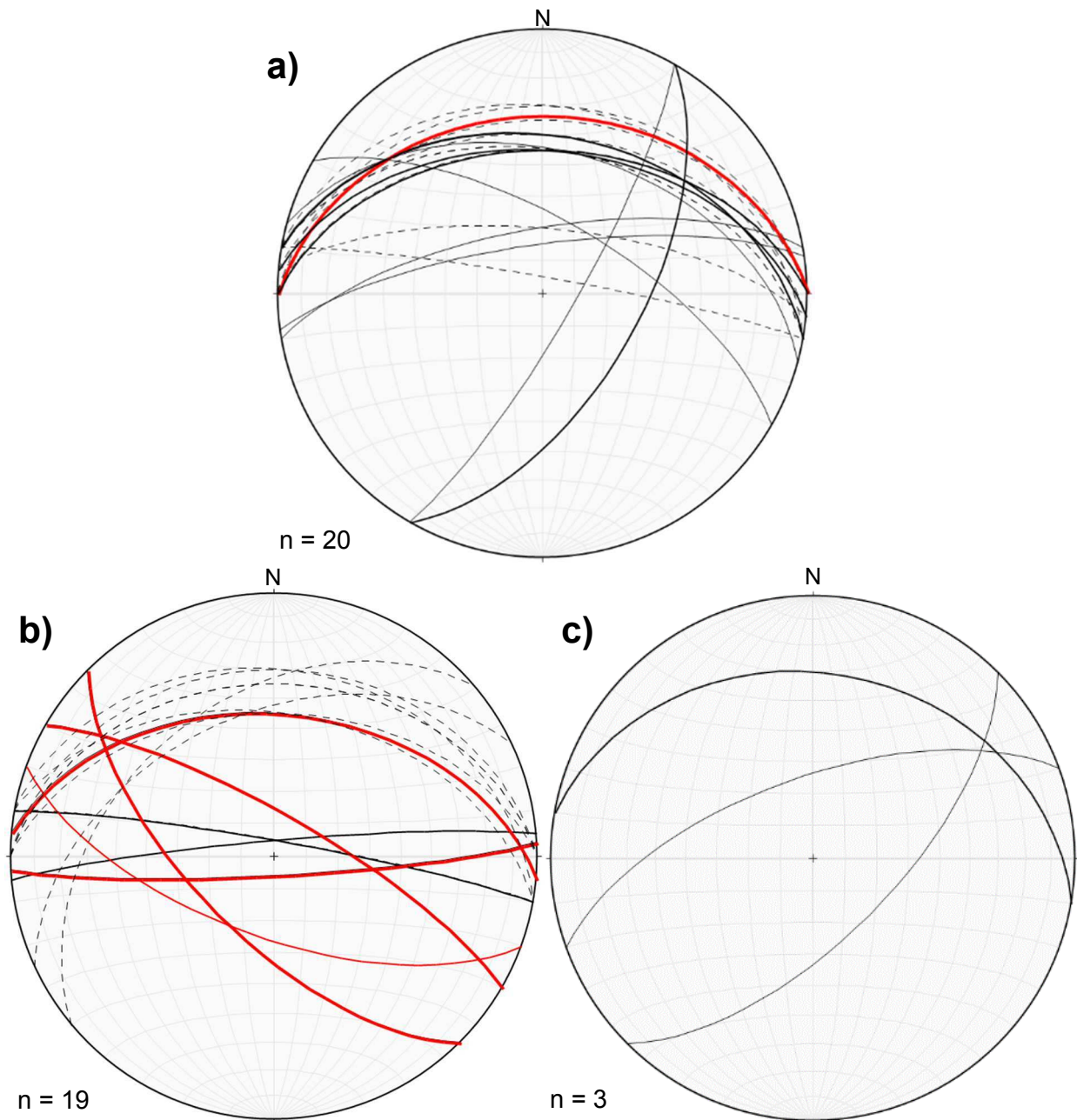


Figure 3.37. Lower hemisphere, equal area stereonets displaying orientations of P2 fault planes with observed sense of shear data from field and thin section observations. “Unknown” offsets indicate observations made in thin section, where only the sense of shear, not the total displacement, was observable.

Unknown offset=Black (Dashed); 0-10 cm offset=Black (Solid); 11-20 cm offset=Black (Bold); 20-30 cm offset=Red (thin lines); 30+ cm offset=Red (thick lines)

- a) Normal
- b) Left Lateral
- c) Right Lateral

3.4. Geochemical Data

This section contains spot chemical analyses gathered using the PXRF from P1 and P2 fault cores, and the host tonalite, comparing them to gain a better understanding of geochemical changes accompanying faulting. In addition, data from the separated alteration zone adjacent to one representative P1 fault (AK107-3L) are presented. This sample was cut into three sections: the fault core, the adjacent chlorite + saussurite zone, and the outer biotite + saussurite zone (see sections 3.1, 3.2.2), which form visibly distinct zones within the alteration halo (Fig. 3.4).

All chemical data shown in this section were gathered using the Olympus PXRF (see methods section). Major and select minor or trace element concentrations were compared between fault populations and the unaltered FCS host rock. Comparative geochemistry is displayed three ways:

- 1) Averages of each fault population compared to host rock, displayed as tables to quantify enrichment and depletion (Tables 3.3, 3.4, 3.5, 3.6).
- 2) Two sets of box and whisker plots:
 - a) averages of unaltered FCS tonalite, P1 and P2 (Figs. 3.38, 3.39)
 - b) averages of FCS host rock, and the three previously mentioned zones of internal heterogeneity within the P1 alteration halo (Figs. 3.40, 3.41).

Corrected PXRF data for individual analyses of specific samples are shown in Appendix B. The whole rock analyses of two samples of the FCS (AK113-4, AK113-5) and tonalites from previous studies in the Nason Terrane, all of which were used for calibration and correction of PXRF data, are shown in Appendix C.

Some analyses reported “zero” Ca values. Experimenting with the instrument indicated a “BDL” indication occurred when Ca was significantly less than 1 weight percent despite a claimed 20 PPM detection limit (Appendix B). A rough inverse relationship between K and Ca may point to possible interference of the Ca- α peak by the K- β peak. Complete absence of calcium is highly unlikely, and thus these values were left as null, rather than treated as zeros.

3.4.1. Population 1

Forty analyses were obtained from 5 samples containing P1 faults. Results are shown in the following table.

Table 3.3 Average PXRF values of individual P1 samples. Samples 107-4A and 107-4B are not from the same fault.

Sample #	AK107-2		AK107-3L		AK107-4A		AK107-4B		AK111-1	
	Average	1 σ	Average	1 σ	Average	1 σ	Average	1 σ	Average	1 σ
SiO ₂	71.21	3.23	73.98	2.90	74.25	5.21	71.98	3.11	71.71	2.78
TiO ₂	0.14	0.07	0.20	0.08	0.35	0.23	0.25	0.11	0.30	0.30
Al ₂ O ₃	16.03	3.53	18.09	2.36	15.27	4.43	16.11	2.73	17.28	1.92
Fe ₂ O ₃	3.10	1.93	2.56	0.92	2.97	1.65	3.14	0.97	3.15	1.47
MnO	0.02	0.00	0.02	0.01	0.06	0.04	0.05	0.01	0.04	0.02
MgO	0.73	0.49	1.10	0.68	0.61	0.35	0.53	0.37	1.01	0.79
CaO	1.91	-	1.71	0.55	1.24	0.77	1.60	0.10	1.90	0.88
K ₂ O	3.26	1.23	2.58	0.50	1.48	0.46	1.68	0.57	1.89	0.59
SrO	0.04	0.01	0.06	0.01	0.04	0.01	0.04	0.01	0.05	0.01
ppm										
Rb	95	52	73	15	49	12	45	13	46	13
Zr	45	28	90	62	73	28	68	41	82	76
Pb	-	-	-	-	149	84	90	66	17	7
Zn	22	5	17	-	141	50	214	115	35	14
# of Analyses	5		5		15		5		10	

Relative depletions and enrichments are listed in Table 3.5, and shown by box and whisker plots in Figs. 3.38 and 3.39. Compared to host rock data, P1 fault cores show minor relative change (less than $\pm 10\%$) in SiO₂, Al₂O₃, Fe₂O₃, K₂O, Zr, and Zn. The faults are generally depleted in TiO₂ (-27%), MgO (-27%), CaO (-46%), and SrO (-38%). P1 is also enriched in MnO (+24%) and Rb (+20%). Pb is significantly enriched (+802%), though this is the result of two samples out of 5 displaying consistently large enrichments. Two other samples contained negligible Pb, below the detection limit of 4 ppm, and another showed minor enrichment.

Depletion of Ti is unexpected, and unlikely, due to the general immobility of the element. It may be the result of low levels of Ti-bearing minerals in the host FCS, and thus based on a statistical lack of host information the result is skewed. Similarly, the significant enrichment in Pb in some samples may simply be the result of the spot analyses containing Pb-rich minerals such as galena, which were uncommon in the host FCS.

3.4.2. Population 2

The P2 data consists of 85 analyses of fault core matrix from 14 samples. Results are shown in Table 3.4.

Relative depletions and enrichments are summarized in Table 3.5, and shown as box and whisker plots in Figs. 3.38 and 3.39. When compared to host rock data, P2 fault cores display less than 10% deviations in SiO_2 , TiO_2 , and Zr. Fe_2O_3 (-22%), MnO (-15%), MgO (-29%), SrO (-32%), and Zn (-40%) are depleted. CaO is generally depleted as well, though the average is being pulled up by a small group of highly enriched samples (-4% mean, -32% median). K_2O (+70%), Rb (+122%), Pb (+35%), and Al_2O_3 (+11%) are all enriched.

Table 3.4. Average PXRF values of individual P2 samples.

Sample #	AK100-3		AK101-6		AK103-1		AK104-1		AK104-4		AK105-1		AK105-2	
Oxide Wt %	<i>Average</i>	<i>1σ</i>	<i>Average</i>	<i>1σ</i>	<i>Average</i>	<i>1σ</i>	<i>Average</i>	<i>1σ</i>	<i>Average</i>	<i>1σ</i>	<i>Average</i>	<i>1σ</i>	<i>Average</i>	<i>1σ</i>
SiO2	74.16	0.92	68.97	2.80	71.98	4.83	72.69	4.36	67.42	2.77	71.23	3.38	72.16	2.32
TiO2	0.37	0.05	0.42	0.09	0.57	0.24	0.25	0.00	0.37	0.18	0.24	0.12	0.33	0.03
Al2O3	18.51	1.06	17.13	0.91	16.41	3.35	14.95	2.95	16.37	1.57	19.00	1.63	18.66	1.21
Fe2O3	1.07	0.32	2.09	0.67	3.63	0.85	3.28	1.41	1.89	0.58	1.19	0.52	1.44	0.22
MnO	0.02	0.00	0.02	0.01	0.04	0.01	0.07	0.04	0.02	0.00	0.02	0.00	0.02	0.01
MgO	0.62	0.26	0.76	0.38	0.98	0.47	1.02	0.61	0.88	0.37	1.04	0.62	0.56	0.52
CaO	-	-	2.74	1.15	1.81	1.09	2.97	1.60	2.00	0.24	2.30	0.76	2.02	0.64
K2O	5.05	0.67	2.61	0.70	2.71	0.51	2.82	0.09	3.37	1.28	3.31	0.99	5.55	0.80
SrO	0.04	0.00	0.05	0.01	0.05	0.02	0.06	0.00	0.06	0.01	0.04	0.01	0.04	0.00
ppm														
Rb	158	25	60	11	96	25	123	6	85	30	110	34	144	12
Zr	32	5	45	14	63	12	56	25	162	81	53	11	40	7
Pb	6	2	8	-	-	-	-	-	-	-	-	-	4	-
Zn	17	4	28	10	58	27	81	49	29	16	24	5	29	3
# of Analyses	10		7		6		3		6		6		6	
Sample #	AK106-1		AK106-3		AK107-1		AK108-1		AK110-1		AK111-4		AK112-2	
Oxide Wt %	<i>Average</i>	<i>1σ</i>	<i>Average</i>	<i>1σ</i>	<i>Average</i>	<i>1σ</i>	<i>Average</i>	<i>1σ</i>	<i>Average</i>	<i>1σ</i>	<i>Average</i>	<i>1σ</i>	<i>Average</i>	<i>1σ</i>
SiO2	73.44	3.25	74.99	1.59	73.16	1.21	74.98	3.83	69.91	2.82	67.09	0.38	72.64	2.02
TiO2	0.37	0.12	0.40	0.16	0.44	0.11	0.37	0.13	0.41	0.13	0.27	0.04	0.37	0.11
Al2O3	17.60	1.87	16.28	1.14	18.00	1.83	15.55	3.83	18.68	2.13	26.08	1.13	16.16	1.27
Fe2O3	2.04	0.65	1.96	0.41	2.73	1.27	2.63	1.20	2.98	1.04	1.87	0.41	2.87	0.41
MnO	0.02	0.00	0.02	0.00	0.04	0.02	0.02	0.01	0.03	0.01	0.03	0.01	0.05	0.01
MgO	0.74	0.37	0.39	0.27	0.82	0.58	0.71	0.83	1.23	0.57	0.81	0.19	0.69	0.37
CaO	1.55	0.61	1.21	0.15	0.88	0.05	1.48	0.47	3.15	1.71	8.83	1.10	6.77	1.71
K2O	4.51	1.37	5.14	0.39	5.47	1.72	3.76	0.80	2.06	0.66	0.85	0.41	1.55	0.56
SrO	0.04	0.01	0.04	0.01	0.03	0.01	0.05	0.02	0.04	0.00	0.06	0.00	0.09	0.01
ppm														
Rb	121	35	126	5	194	44	125	47	76	21	27	11	46	14
Zr	67	12	67	14	64	16	83	41	95	32	65	7	85	21
Pb	5	1	-	-	16	3	-	-	13	-	5	2	58	68
Zn	23	6	23	8	146	164	37	11	39	18	51	22	225	150
# of Analyses	10		3		9		4		7		4		7	

3.4.3. Population 1 Alteration Halo

Sample AK107-3L was cut into three slices, each powdered. The powders were again compared to host rock FCS. The slices were based on the previously described “internal heterogeneities” present within the P1 alteration halo that denote the adjacent saussurite + chlorite and outer saussurite + biotite zones. Fig. 3.4 shows a photo of sample AK107-3L with the sections labelled. Sample P1-1 contains the fault core, <1 cm thick with no visible clasts. Due to the nonplanar, exceptionally thin nature of the P1 fault core, it was not possible to fully isolate the fault core material from the adjacent alteration halo (damage zone). Sample P1-2, the adjacent saussurite + chlorite damage zone, contains 2-3 cm of wallrock adjacent to the fault core along each side of the fault core, displaying near complete chloritization of all biotite and thorough saussuritization of plagioclase, and extensive dark brown staining. P1-3, the outer damage zone, contains the outer section of the alteration halo extending ~3-4 cm from P1-2 and is distinct through the presence of biotite rather than chlorite, though still containing significant altered gray plagioclase. P1-3 also contains less visible reddish-brown staining than P1-1 and P1-2 in hand sample. Geochemically, sample AK107-3L is representative of the P1 fault population based on the P1 fault core PXRF results, except for enrichment of Fe_2O_3 , and lack of change in Pb concentration.

Relative depletions and enrichments are given in Table 3.6, and displayed in box and whisker plots in Figs. 3.40 and 3.41. Compared to the unaltered FCS host rock, SiO_2 is mostly unchanged throughout the fault zone (<10% change). TiO_2 is slightly depleted in the fault core (-14%), shows little change in the inner damage zone (+5%), and minor enrichment in the outer damage zone (+16%). Al_2O_3 is slightly depleted in the fault core (-15%), and unchanged in the damage zone. Fe_2O_3 is enriched in the fault core (+43%), slightly depleted in the inner damage zone (-14%), and negligibly changed in the outer damage zone. MgO is slightly depleted in the fault core (-6%), and depleted in the inner (-35%) and outer (-24%) damage zones. CaO is depleted in the fault core (-21%) and across the damage zone (-51% and -42%). K_2O is enriched

in the fault core (+19%) and in the inner (+24%) and outer (+8%) zones. Rb and Zr are both enriched throughout the fault core and damage zone. Pb and Zn are both depleted in the entire fault zone.

Table 3.5. Average concentrations and relative enrichments and depletions of P1 and P2 versus whole rock analysis of the FCS. Significant results, based on major differences in enrichment or depletion, and sufficiently high concentrations, have been bolded.

Element	Host	P1	% Change	P2	% Change
SiO2	69.50	72.739	+5%	72.374	+4%
TiO2	0.36	0.262	-27%	0.357	-1%
Al2O3	15.85	16.481	+4%	17.597	+11%
Fe2O3	2.83	3.050	+8%	2.176	-22%
MnO	0.04	0.043	+24%	0.030	-15%
MgO	1.09	0.790	-27%	0.768	-29%
CaO	2.93	1.595	-46%	2.721	-7%
K2O	2.10	2.059	-2%	3.552	+70%
SrO	0.08	0.046	-38%	0.050	-32%
Rb (ppm)	49	58	+20%	108	+122%
Zr (ppm)	76	73	-3%	68	-9%
Pb (ppm)	10	86	+802%	13	+35%
Zn (ppm)	94	88	-6%	56	-40%

Table 3.6. Average concentrations and relative enrichments and depletions of the P1 fault core (P1-1), the adjacent saussurite + chlorite portion of the alteration halo (P1-2), and the outer saussurite + biotite portion of the alteration halo (P1-3). Each powder was analyzed three times. Sample AK107-3L

Element	Host	P1-1	% Change	P1-2	% Change	P1-3	% Change
SiO2	69.50	66.392	-4%	69.168	0%	69.797	0%
TiO2	0.36	0.310	-14%	0.378	+5%	0.417	+16%
Al2O3	15.85	13.473	-15%	16.030	+1%	15.686	-1%
Fe2O3	2.83	4.040	+43%	2.419	-14%	2.859	+1%
MnO	0.04	0.033	-6%	0.024	-30%	0.026	-27%
MgO	1.09	1.143	+5%	0.704	-35%	0.830	-24%
CaO	2.93	2.313	-21%	1.450	-51%	1.703	-42%
K2O	2.10	2.500	+19%	2.601	+24%	2.269	+8%
SrO	0.08	0.052	-31%	0.066	-12%	0.065	-14%
Rb (ppm)	49	87	+79%	87	+79%	72	+49%
Zr (ppm)	76	95	+26%	110	+45%	111	+47%
Pb (ppm)	10	7	-28%	6	-40%	6	-34%
Zn (ppm)	94	19	-79%	24	-74%	32	-66%

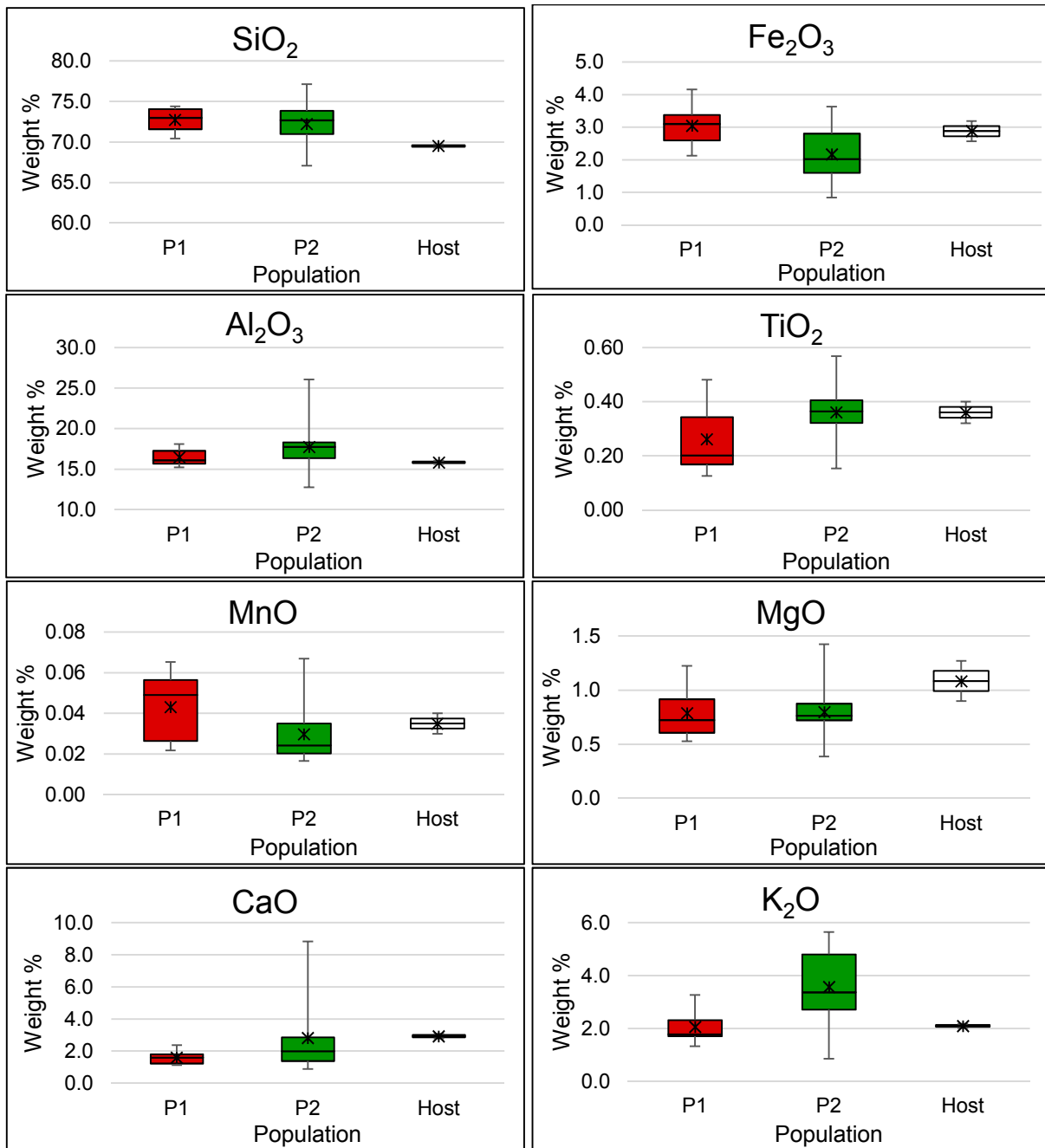


Figure 3.38. Box and whisker plots showing relative changes in major element concentration between P1 fault cores, P2 fault cores, and unaltered host FCS. Mean values are denoted by “x”. Whiskers represent the minimum and maximum values.

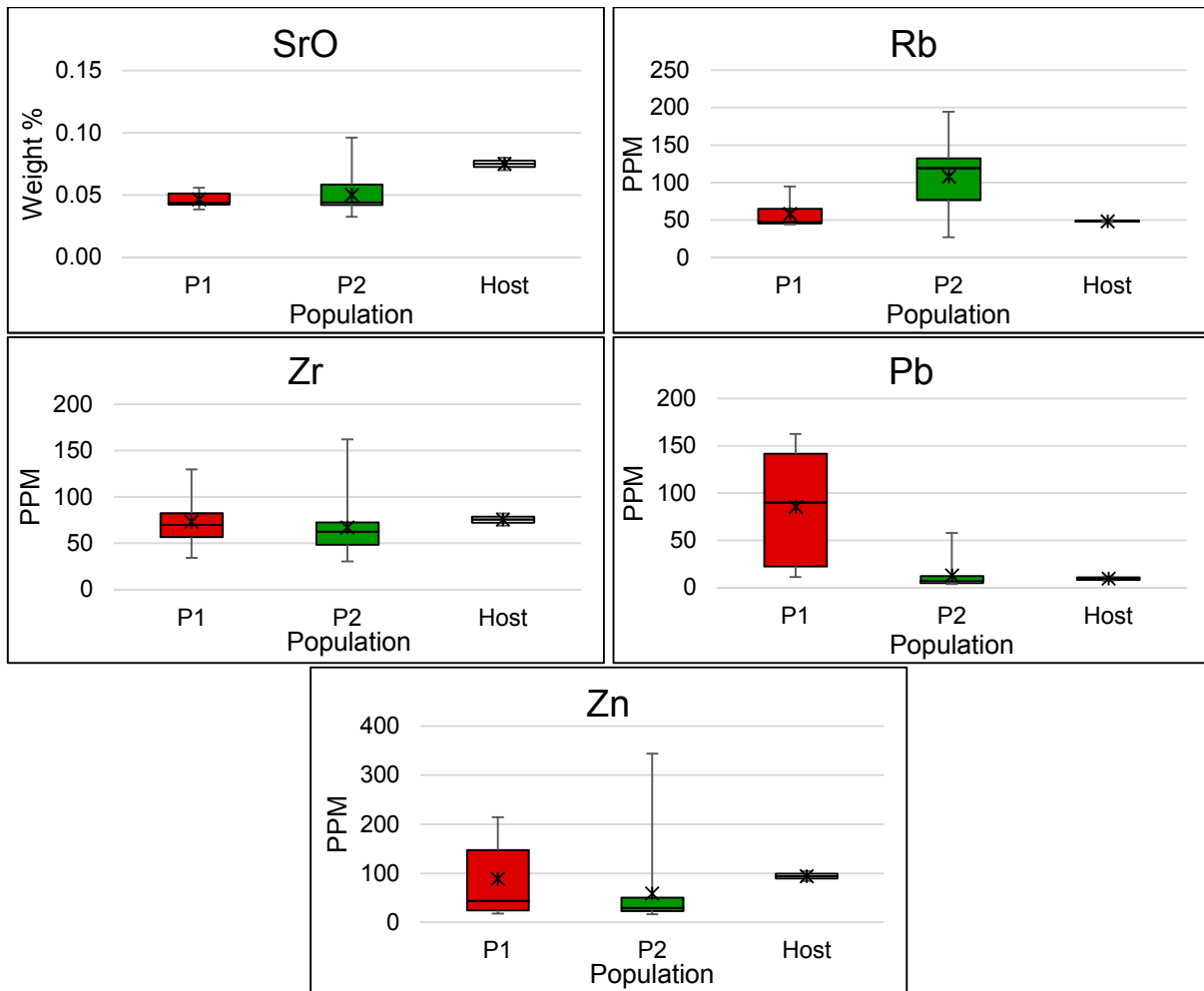


Figure. 3.39. Box and whisker plots showing relative changes in minor element concentration between P1 fault cores, P2 fault cores, and unaltered host FCS. Mean values are denoted by “x”. Whiskers represent the minimum and maximum values.

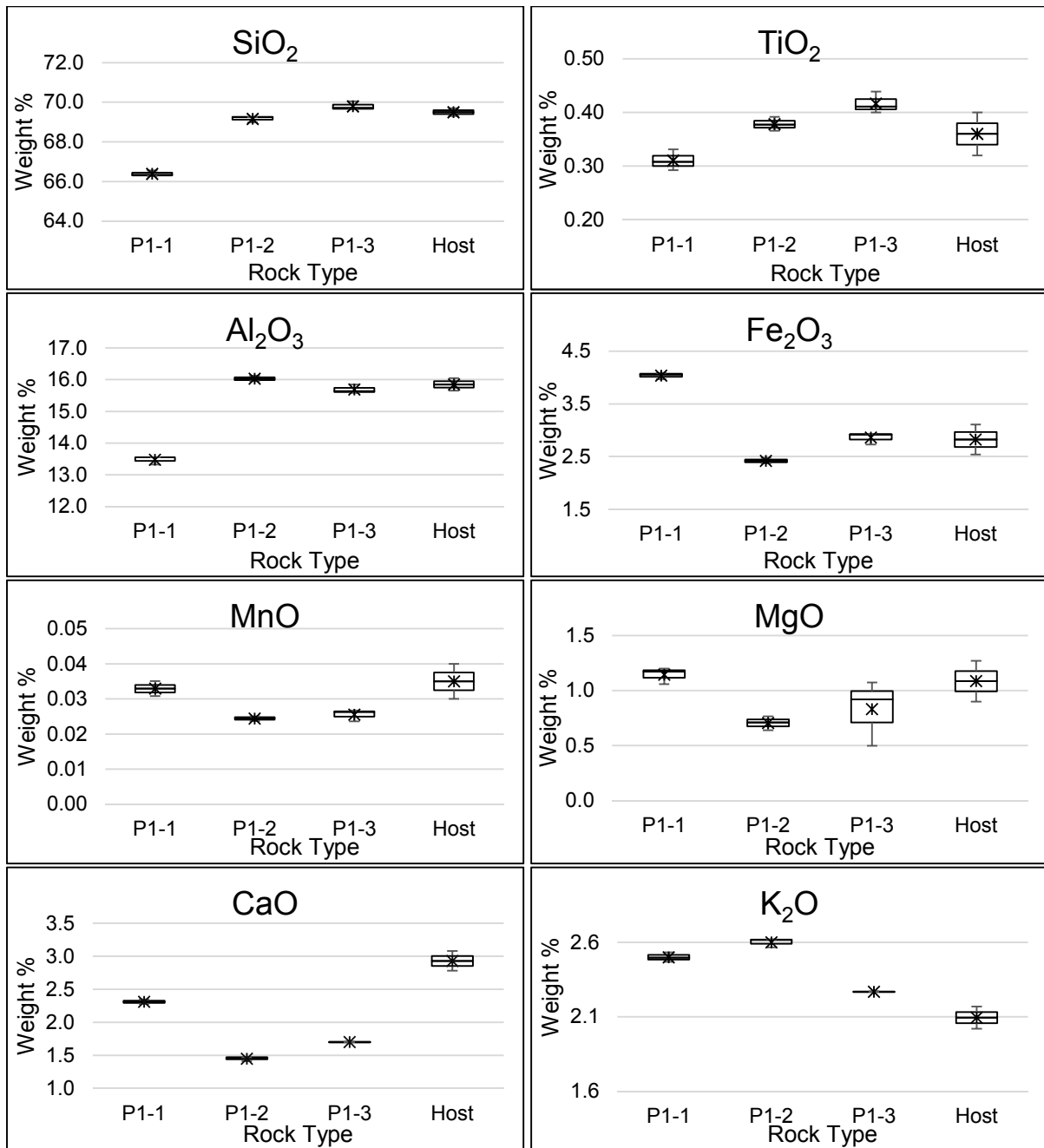


Figure 3.40. Box and whisker plots showing relative changes in major element concentrations between P1-1, P1-2, P1-3 (descriptions in text), and unaltered host FCS. Mean values are denoted by “x”. Whiskers represent the minimum and maximum values.

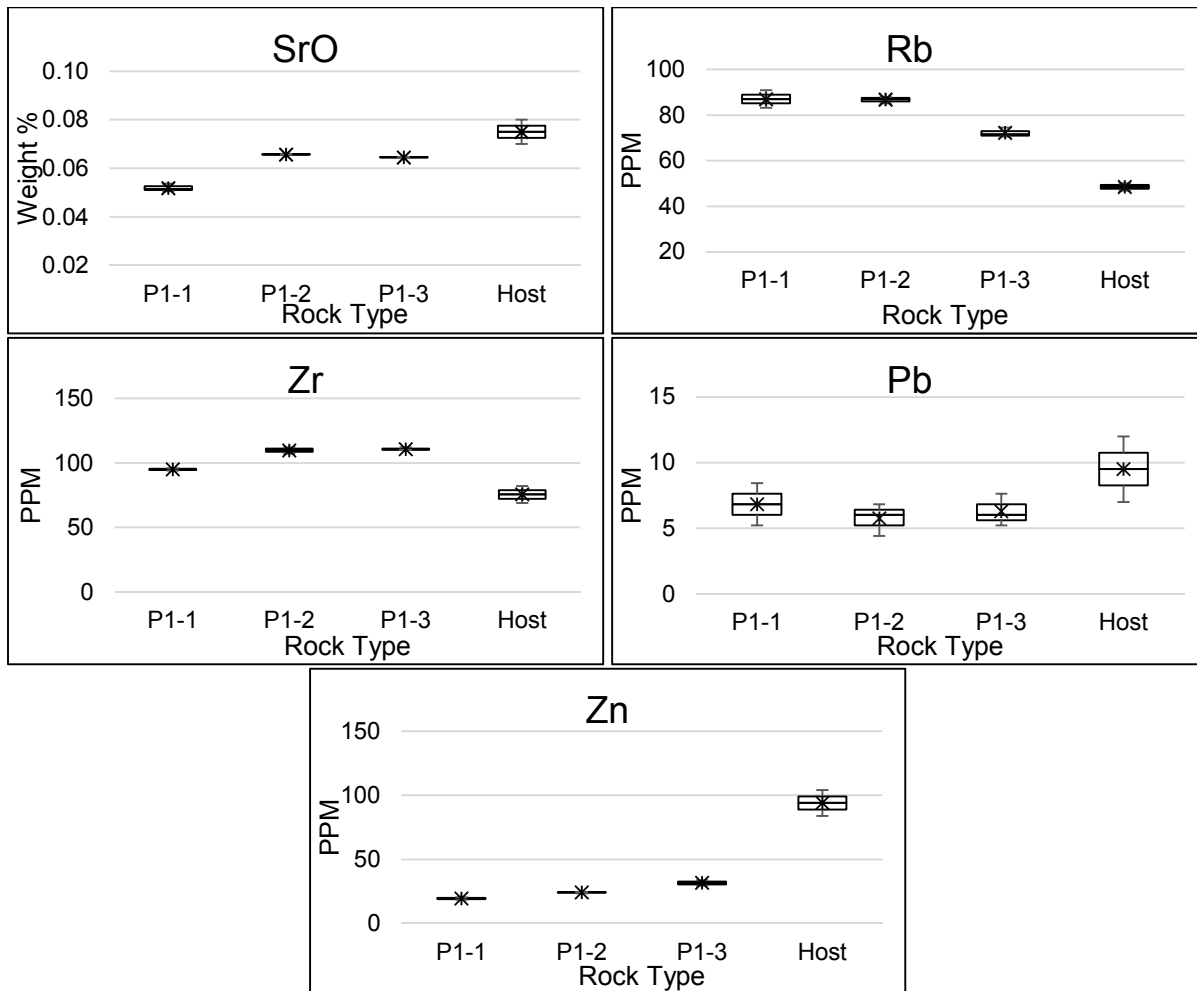


Figure 3.41. Box and whisker plots showing relative changes in minor element concentrations between P1-1, P1-2, P1-3 (descriptions in text), and unaltered host FCS. Mean values are denoted by “x”. Whiskers represent the minimum and maximum values.

3.5. Fluid Inclusions

Thin sections were analyzed for fluid inclusion assemblages (FIAs), with a focus on secondary, planar, structurally controlled FIAs. Throughout all samples in both populations, physical characteristics of the secondary fluid inclusions were similar. Fluid inclusions along healed cracks adjacent to both P1 and P2 fault cores displayed two phase liquid-vapor (L-V) compositions at room temperature. The aqueous phase is colorless and the vapor phase is a single high relief dark bubble (Fig. 3.42). Inclusions are commonly negative crystal shapes or elongated along the fluid inclusion planes (FIPs), ranging from sub-micron to more than 25 μm across (Figs. 3.43, 3.44). No solid phases were observed in secondary inclusions.

The vast majority of observed fluid inclusions were vapor rich (>70% total volume = vapor). However, most were too small (<5 μm) for microthermometry analysis. Across all samples, 69 assemblages were of sufficient size for microthermometry analysis. L-V ratios of the analyzed assemblages were bimodally distributed: 7 were vapor-rich, while the remaining 62 were liquid-rich (Fig. 3.45).

There is no evidence that secondary fluid inclusions in the FCS have reequilibrated since initial entrapment. Many inclusions used for microthermometry analysis were too small, agreeing with a study by Bodnar *et al.*, (1989) found that fluid inclusions with volumes less than 1200 μm^3 (approximately 13 μm diameter) in quartz are less likely to reequilibrate. Reequilibration commonly occurs during heating post-entrapment. However, the FCS was in the process of being exhumed at the time of P1 and P2 faulting, and thus the rocks likely progressively cooled after faulting and fluid inclusion entrapment. Though reequilibration is possible during uplift through fluid diffusion from the fluid inclusions into host quartz, (Bakker, 2009), no evidence for this process, such as “implosion halo” textures (Sterner and Bodnar, 1989), was observed.

3.5.1. Fluid Inclusion Plane Orientations

Studies of secondary fluid inclusion planes (FIPs) in quartz have established them as paleostress indicators (Boullier, 1999; Lespinasse, 1999), and thus their orientations are aligned

with the σ_1 - σ_2 plane of maximum compressive stress (e.g. Fig. C.3). FIPs were measured in five oriented thin sections, two from P1 and three from P2 samples. A minimum of 15 orientations were gathered from each section. Measurements are shown in Appendix C. For both fault populations, the planes are oriented nearly vertical (dip $\sim 90^\circ$), and strike E-W to WNW-ESE (Fig. 3.46). A 10° discrepancy between mean P1 (104-90) and P2 (094-89) orientations may be within the margin of error or the product of changing regional stress.

3.5.2. Microthermometry

Microthermometry measurements were made on six samples, two from P1 wallrock, and four from P2 wallrock. Each sample contained multiple FIAs suitable for analysis. A total of 30 FIAs associated with P1 and 39 from P2 were measured. The inclusions targeted for microthermometry were exclusively those found in systematically oriented secondary planes in quartz. Microthermometry data from fluid inclusions associated with both fault populations can be found in tables 3.7 and 3.8. Behavior was consistent independent of L-V ratio. Vapor-rich and liquid-rich inclusions homogenized to vapor and liquid, respectively. A table with individual microthermometry results, including L-V ratios can be found in Appendix C.

3.5.2.1. Population 1

Total homogenization temperatures (T_h) of P1 fluid inclusions ranged from 239 to 338°C, with a median of 289°C (Q1=274, Q3=301, n=30) (Figs. 3.47, 3.48). Initial melting temperatures (T_i) of the liquid phase were between -30 and -25°C, median -26°C (Q1=-27.5, Q3=-26, n=6) (Fig. 3.49). Final ice melting temperatures (T_m) ranged from -18.1 to -2°C with a median value of -9.8°C (Q1=-12.2, Q3=-7.4, n=30) (Fig. 3.50). The three sets of P1 microthermometry data were unimodally distributed.

3.5.2.2. Population 2

T_h of P2 fluid inclusions were between 234 and 337°C, median of 262°C (Q1=258, Q3=273, n=39) (Figs. 3.47, 3.48). T_i ranged from -50 to -22°C with a median of -27°C (Q1=30,

Q3=-25, n=16) (Fig. 3.49). T_m ranged from -32.8 to -0.2°C, with a median of -10.3°C (Q1=-24.5, Q3=-5.4, n=39) (Fig. 3.50). T_h displays a generally unimodal distribution, although two weak subsets, 225-240°C and 300-315°C, can be recognized. See table 3.7.

T_i and T_m data were bimodally distributed: one P2 sample, AK108-1B, exclusively contained inclusions with significantly more depressed temperatures than the rest of the population. Upon removal of the data from this sample, median T_h was generally unchanged at 264°C (Q1=258, Q3=271, n=24), and median T_i and T_m were -26.5°C (Q1=-29.8, Q3=-25, range -32 to -22, n=14) and -6.2°C (Q1=-8.5, Q3=-4.3, range -11.6 to -0.2, n=24), respectively. See table 3.8.

Note that there were no correlations between microthermometry results and L-V ratio (Fig. 3.51).

Table 3.7. Fluid inclusion microthermometry data from fault-hosting samples of FCS, showing the median values, ranges of minimum to maximum in parentheses. There is overlap among all data sets.

	P1	P2
T_h (°C)	289 (Q1=274, Q3=301, min=239, max=339)	262 (Q1=258, Q3=273, min=234, max=337)
T_i (°C)	-26 (Q1=-27.5, Q3=-26, min=-30, max=-25)	-27 (Q1=-30, Q3=-25, min=-50, max=-22)
T_m (°C)	-9.8 (Q1=-12.2, Q3=-7.4, min=-18, max=-2)	-10.3 (Q1=-24.5, Q3=, min=-5.4, max=-0.2)

Table 3.8. Fluid inclusion microthermometry data with the sample AK108-1B containing outlier depressed melting temperatures removed. Note T_h remained roughly the same. The minimum values of T_i and T_m increased, as did median T_i and T_m values.

	P1	P2
T_h (°C)	289 (Q1=274, Q3=301, min=239, max=339)	264 (Q1=258, Q3=271, min=234, max=337)
T_i (°C)	-26 (Q1=-27.5, Q3=-26, min=-30, max=-25)	-26.5 (Q1=-29.8, Q3=-25, min=-32, max=-22)
T_m (°C)	-9.8 (Q1=-12.2, Q3=-7.4, min=-18, max=-2)	-6.2 (Q1=-8.5, Q3=-4.3, min=-11, max=-0.2)

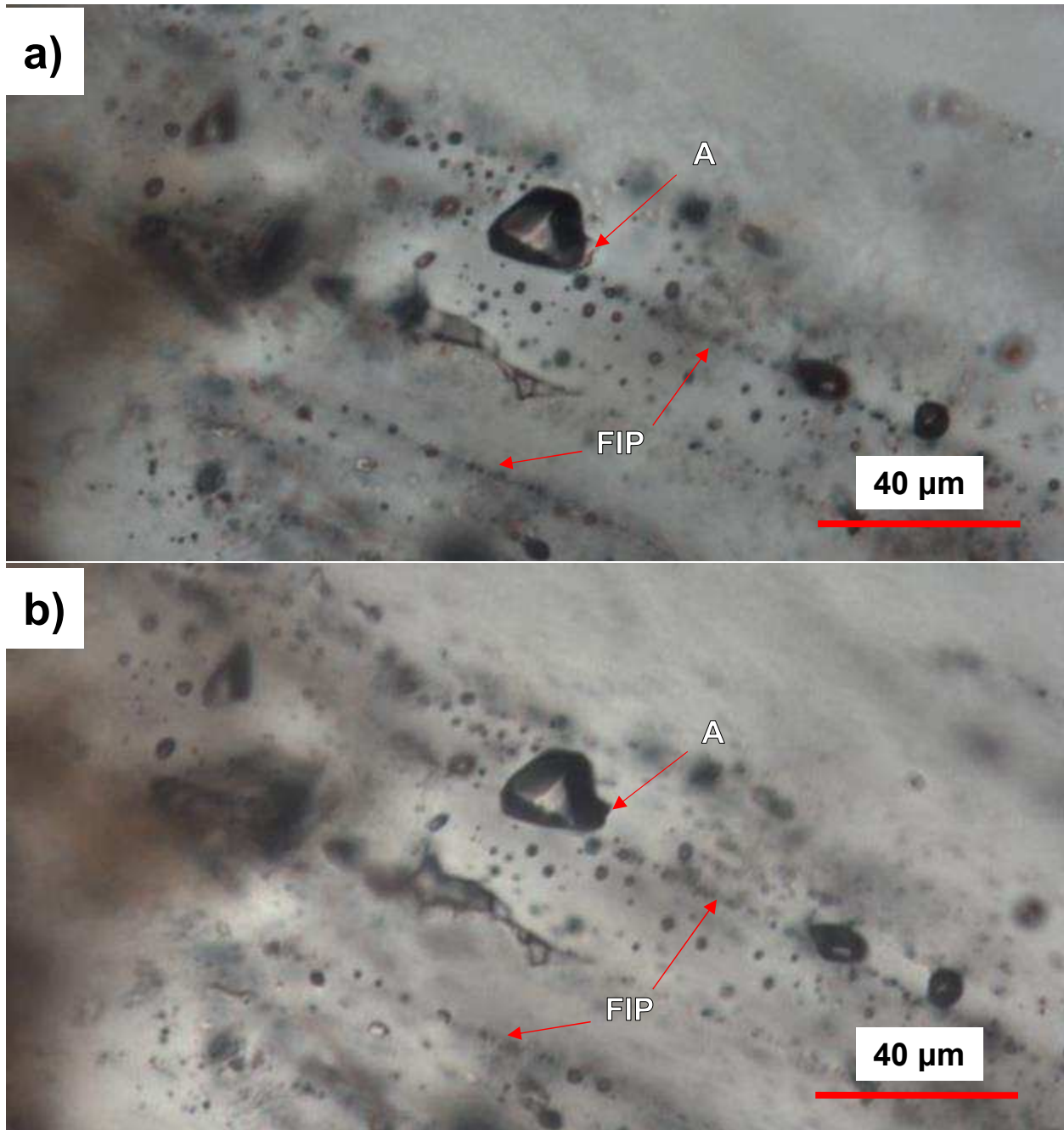


Figure 3.42. (a) Trail of mostly vapor-rich fluid inclusions at ambient temperature ($\sim 25^{\circ}\text{C}$), including a particularly large inclusion that was targeted for microthermometry analysis. (b) The same assemblage at 289°C , the temperature at which the large inclusion reached total homogenization to the vapor phase. Homogenization was recognized as the expansion of the dark gas bubble to fully occupy the originally liquid-filled gap in the lower right corner of the inclusion, marked (A). Sample AK107-4BA.

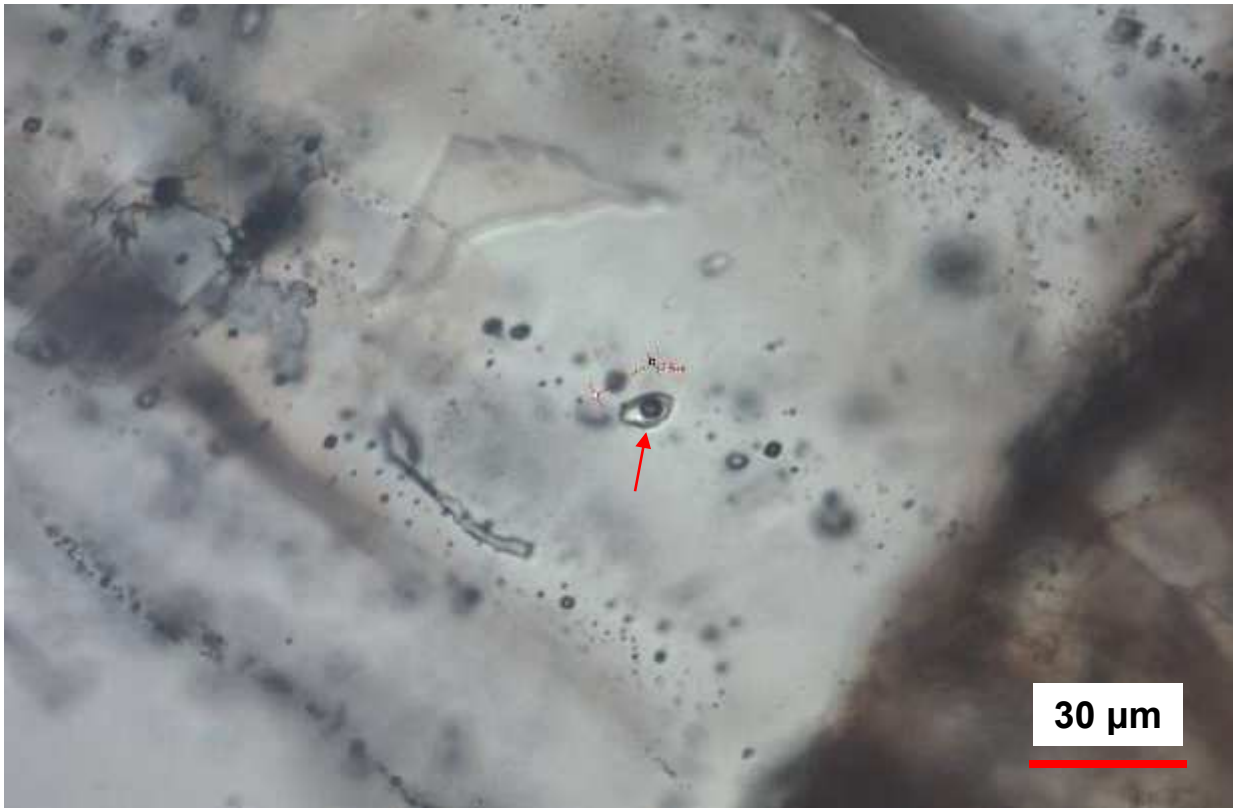


Figure 3.43. Figure showing several aligned FIPs. One two phase L-V fluid inclusion (red arrow) along an FIP in quartz, displaying a negative crystal shape. Note the systematically oriented FIPs, trending from top-left to bottom-right of the photo. Sample AK107-4BA.



Figure 3.44. Figure showing three two-phase L-V fluid inclusions within an FIA, along an FIP. The inclusion in the center (red arrow) is elongated along the FIP. Sample AK111-1A.

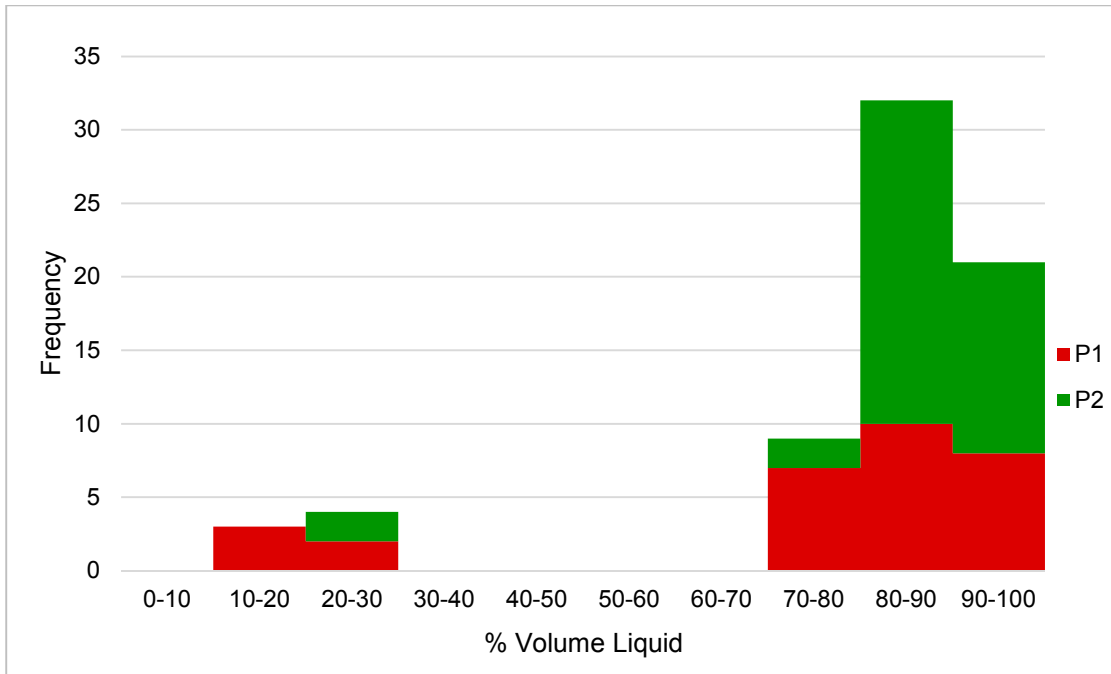


Figure 3.45. Histogram displaying the bimodal frequency distribution of vapor-rich and liquid-rich secondary FIAs used in thermometry analysis. Both populations contain both liquid- and vapor-dominated inclusions. P1: n=30, P2: n=39.

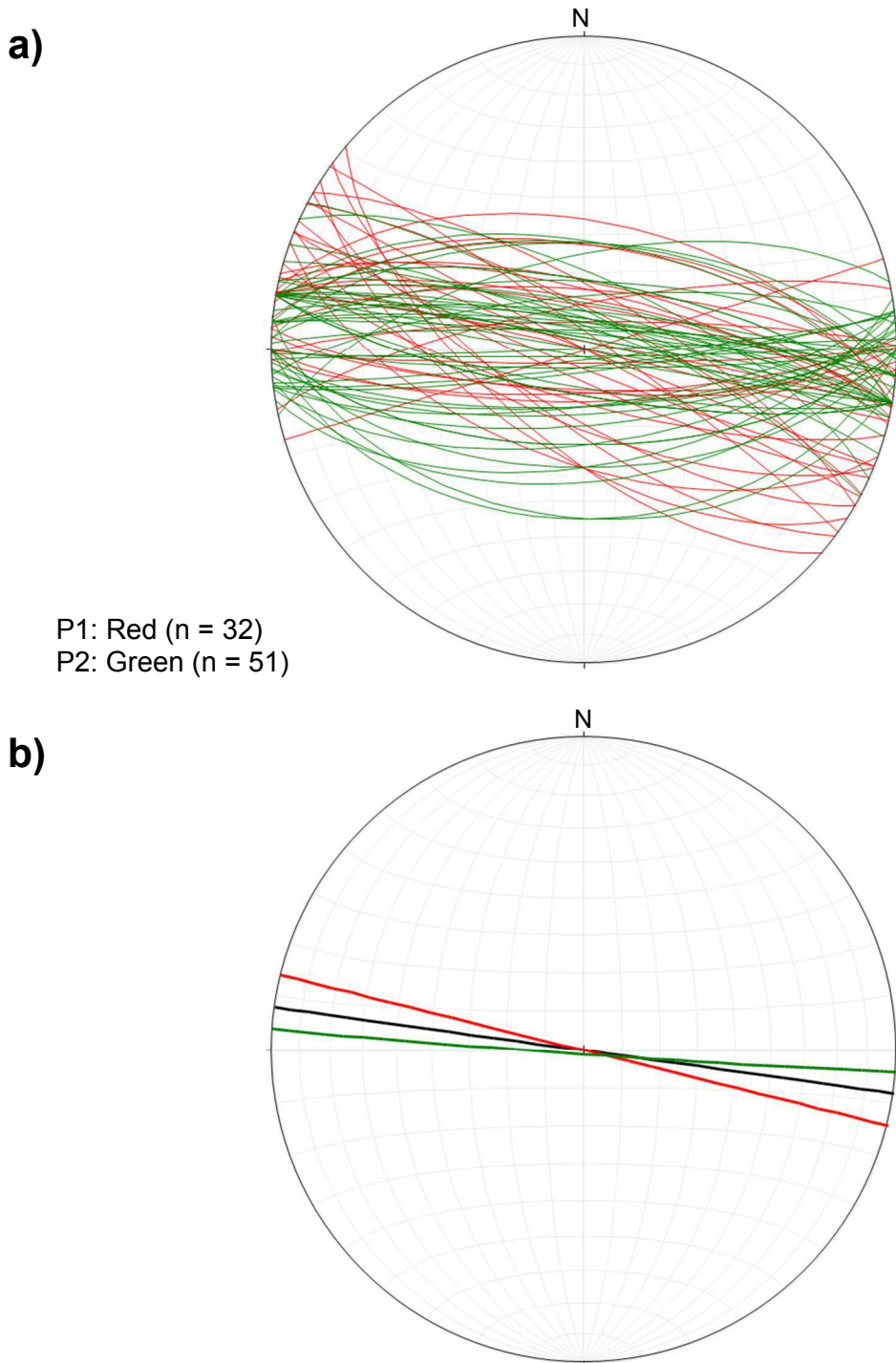


Figure 3.46. (a) Stereonet displaying fluid inclusion plane orientations, showing steeply dipping, roughly E-W striking planes (P1=red, P2=green). (b) Mean plane orientations from P1 (red), P2 (green), and combined (black) FIPs. The FIPs are interpreted to have grown parallel to the maximum compressive stress direction, and thus represent the σ_1 - σ_2 plane. The mean P1 FIP orientation is 104-90 (n=32), mean P2 FIP orientation is 94-89 (n=51), and mean combined FIP orientation is 98-90 (n=83).

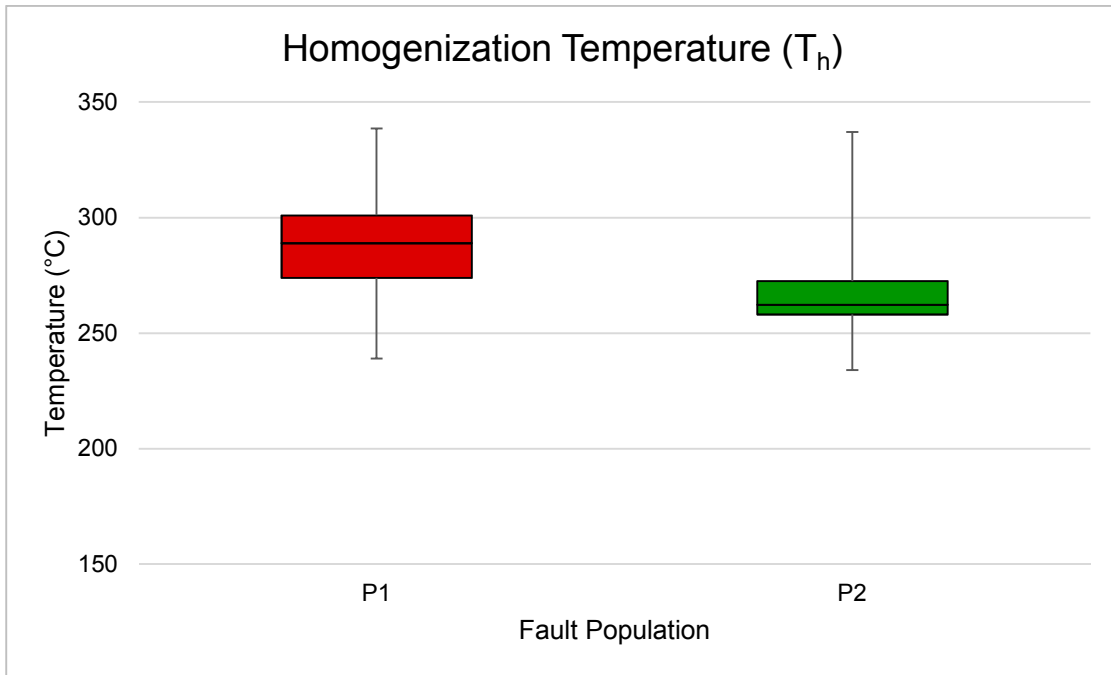


Figure 3.47. Box and whisker plot displaying T_h of all FIAs divided by fault population. Whiskers denote minimum and maximum values; boxes represent the upper and lower quartiles. The box is intersected by a line indicating the median value. Note the two populations are skewed in opposite directions; P1 to the low T side and P2 to the high T side. P1: $n=30$, P2: $n=39$.

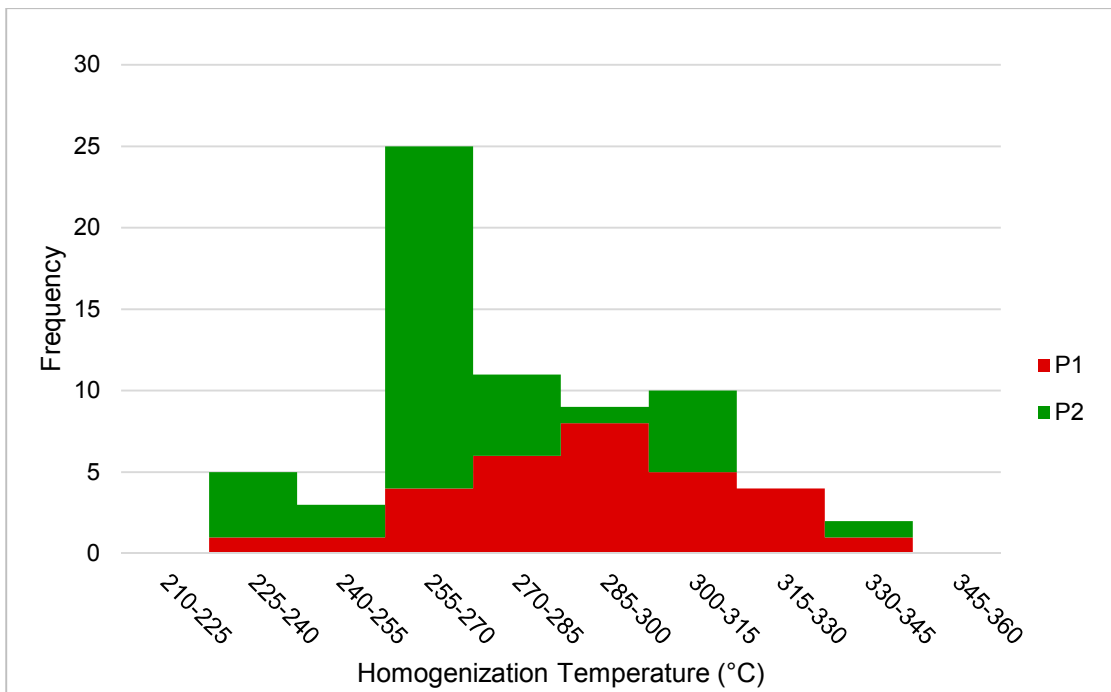


Figure 3.48. Histogram displaying the frequency distribution of T_h . Both populations are unimodal, and contain both liquid- and vapor-dominated inclusions. P1: $n=30$, P2: $n=39$.

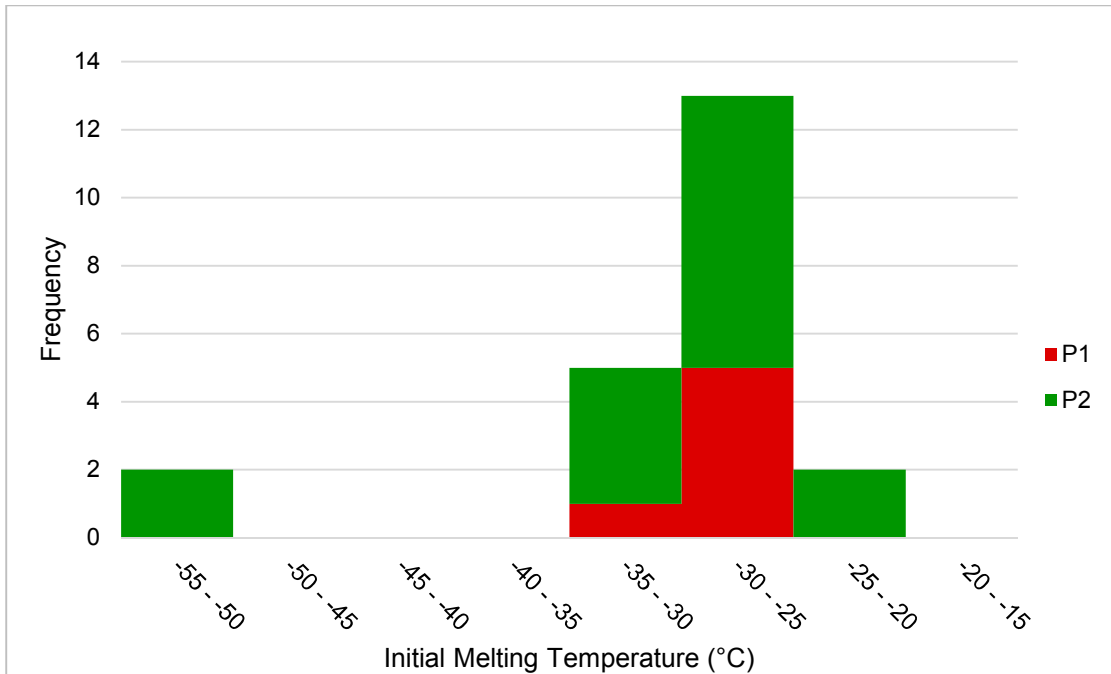


Figure 3.49. Histogram displaying the frequency distribution of T_i of the liquid phases in the fluid inclusions. Distribution of P2 data is bimodal; one sample hosting FIAs with significantly lower T_i between -55 and -50°C. P1: n=6, P2: n=16.

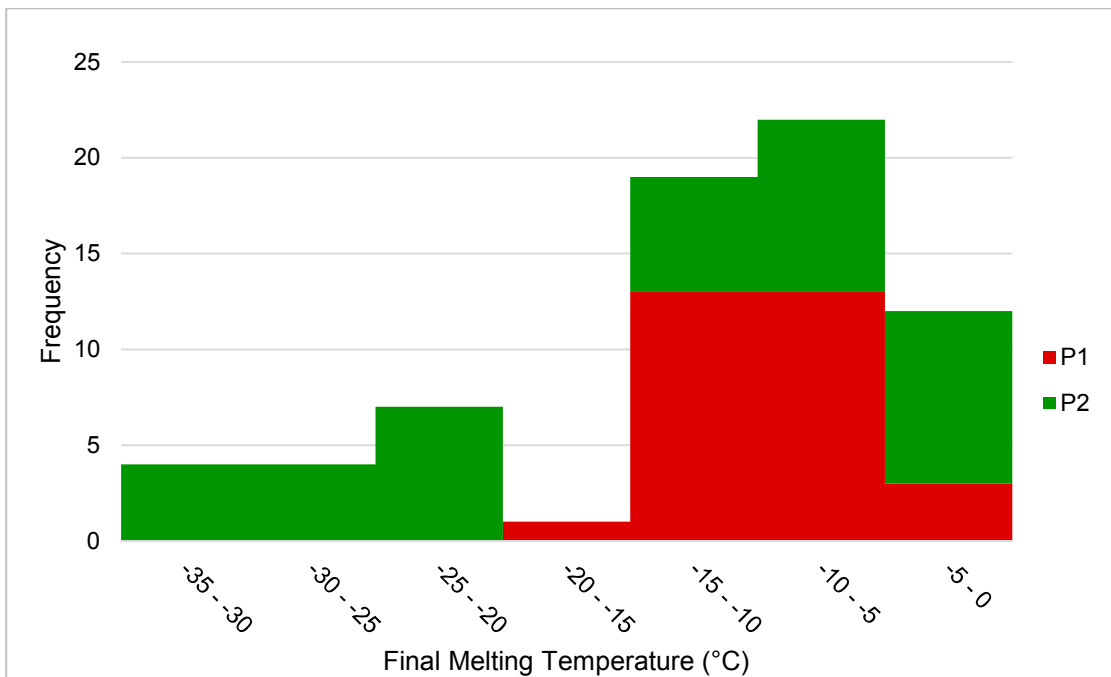


Figure 3.50. Histogram displaying the frequency distribution of T_m of the liquid phases in the fluid inclusions. Distribution of P2 data is bimodal; one sample hosting FIAs with significantly lower T_m between -35 and -20°C, corresponding with the sample showing anomalous T_i shown on Fig. 3.48. P1: n=30, P2: n=39.

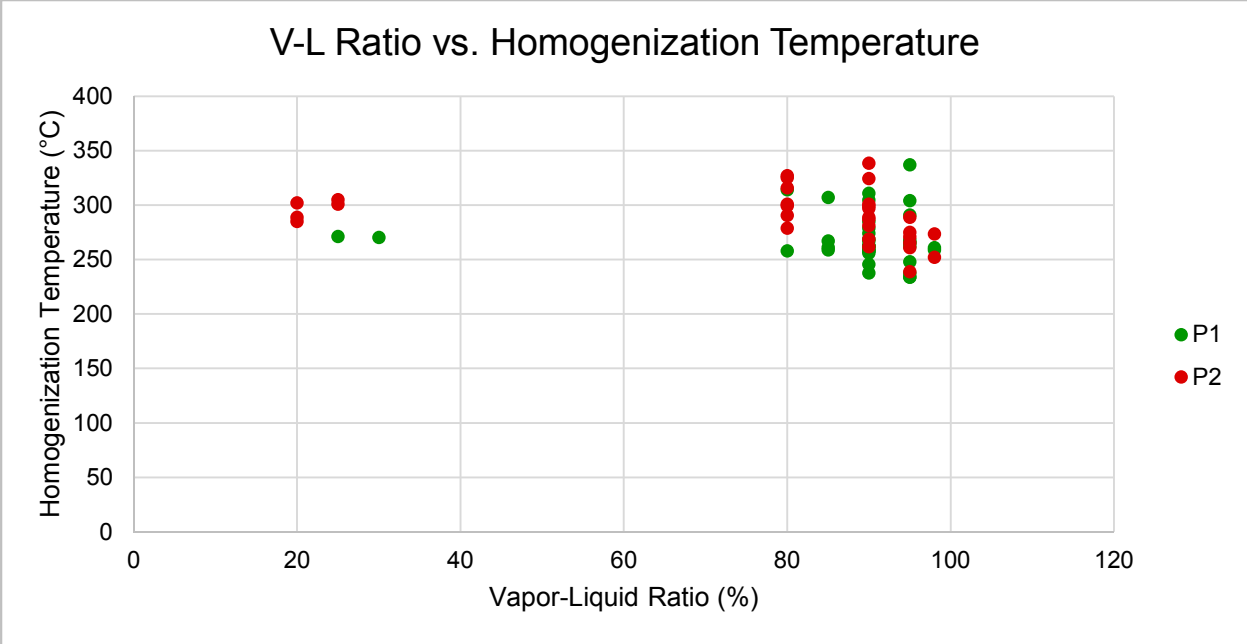


Figure 3.51. Graph of fluid inclusion vapor-liquid ratio versus homogenization temperature, showing lack of correlation between the two measurements.

4. Interpretation and Discussion

The presence of the two separate fault populations observed in this study implies the Foam Creek Stock underwent two distinct episodes of brittle deformation. Though both populations are marked by cataclastic fault rocks, there are clear distinctions in their physical, chemical, and mineralogical characteristics. Alteration assemblages in both populations suggest fluids played a significant role during deformation. This chapter investigates the implications of observations made in this study in an effort to establish likely deformation mechanisms, significance of fluids during faulting, and the conditions during formation of both fault populations. Finally, connections between the small-scale deformation present in the FCS and regional tectonics are explored.

4.1. Host Rock Features

4.1.1. Foliation

The NE-SW striking foliation present (section 3.1.1) within the FCS is discordant with regional foliation fabrics. The predominant foliation both in nearby plutons and the host Chiwaukum Schist is tectonic, striking NW-SE, consistent with NE-SW shortening (Magloughlin, 1993; Tabor *et al.*, 2002a; Tabor *et al.*, 2002b). To explain this discordance, it is likely the FCS hosts magmatic foliation, formed during emplacement. Magmatic foliations typically align parallel to pluton margins (Paterson *et al.*, 1989), consistent with orientations measured in this study (NE-SW alignment along the NW margin of the FCS; see Fig. 2.3). Magmatic foliations are also defined by alignment of primary igneous minerals, such as the biotite in the FCS. Finally, magmatically foliated rocks lack evidence for solid-state deformation. The lack of deformation indicators in the unfaulted FCS, particularly undeformed quartz grains (no undulose extinction, bulging, etc.), suggests a magmatic foliation.

4.1.2. Magmatic Epidote and Clinozoisite

As mentioned in section 3.2.1, magmatic epidote and clinozoisite is present in the FCS, suggesting high pressure crystallization, potentially corresponding to emplacement depths of 25

km or greater (Zen and Hammarstrom, 1984; Zen, 1985). Retrograde, subsolidus alteration assemblages of chloritized biotite and saussuritized plagioclase in the host rock FCS introduce the possibility that alteration processes and introduction of fluids may have resulted in formation of secondary epidote group minerals. However, the observed lack of complete alteration of biotite or plagioclase indicates that alteration processes were not sufficient to form the large grains of epidote and clinozoisite observed in the FCS. Although late alteration processes formed minor amounts of saussurite with extremely fine-grained clinozoisite and epidote, the magmatic clinozoisite and epidote have distinct textures.

Schmidt & Poli (2004) list several indicators of magmatic epidote:

- 1) Occurrence in tonalite plutons,
- 2) Inclusion in biotite grains, consistent with the epidote forming pre- or syn-biotite crystallization (Tulloch, 1986),
- 3) The magmatic epidote may have allanite cores,
- 4) Magmatic epidote displays a unique, graphic intergrowth texture where in contact with plagioclase (Fig. 3.13.).

All of these are observed for the epidote group minerals within the FCS, suggesting it was emplaced at or below 25 km, similar to nearby Late Cretaceous tonalitic plutons, such as the Tenpeak and Sulphur Mountain, which also host magmatic epidote and clinozoisite (Zen and Hammarstrom, 1984; Zen, 1985).

4.2. Deformation Mechanisms in the FCS

The following section discusses the four deformation mechanisms associated with the FCS faults, as observed mesoscopically and microscopically. Also included is an interpretation of these mechanisms and their implications on the deformation of the FCS.

4.2.1. Cataclasis

Observations indicate that deformation in the FCS was accommodated through generally brittle processes. The primary deformation mechanism within both P1 and P2 was cataclasis.

Development of cataclasite is an indicator of faulting within the brittle regime (Sibson, 1977; Woodcock and Mort, 2008). Classification of cataclasite by Sibson (1977) described it as a cohesive fault rock composed of angular, fractured, rotated clasts within a matrix of crushed rock. Strain rate conditions for cataclasites are poorly understood. It is believed that cataclasis typically occurs at intermediate strain rates, between creep ($<10^{-8}$ m/s) and coseismic slip ($>10^{-4}$ m/s), though some cataclasites developed under seismic conditions (Rowe et al., 2005; Rowe and Griffith, 2015). However, the conditions under which such brittle faulting occurs are dependent on lithology, temperature, strain rate, and fluids, which facilitate cataclasis, as increased pore fluid pressure effectively reduces the confining pressures working to keep the rock intact (Sibson, 1992a). Importantly, brittle fault zones may act as conduits for fluid flow (e.g. Magloughlin 1992; Sibson 1996; Caine & Forster 1999; Micklethwaite & Cox 2006).

Cohesive cataclasites like those in the FCS are indicative of deeper deformation than incohesive breccia and gouge, and thus closer to the $\sim 300^{\circ}\text{C}$ transition from brittle to plastic behavior of fault rocks (Sibson, 1977; Passchier and Trouw, 2005). Further distinction within cohesive cataclasite is made between the higher strain rate, purely brittle random fabric and the lower strain rate, semi-brittle foliated cataclasites (Sibson, 1977; Wise et al., 1984; White, 2001), and each is discussed in further detail here.

Some P2 fault cores contain random fabric cataclasite. Random fabric cataclasites are poorly sorted, fractured fault rocks that form during relatively high strain rate (Sibson, 1977; Wise et al., 1984). In addition to being associated with higher strain rates, random fabric cataclasites suggest shallower, cooler conditions during deformation (White, 2001; Rowe et al., 2011). In the FCS, these cataclasites share orientations and crosscutting relations with foliated cataclasites of the P2 population, suggesting they formed through higher slip rates rather than different P-T conditions.

Many of the faults in the P2 fault population are foliated cataclasites (Fig. 3.27; Section 3.3.). Foliation during cataclasis was first described by Chester *et al.* (1985), as brittlely deformed

individual grains that give a macroscopic appearance of ductile flow. It has been established that the host rocks of foliated cataclasites are typically phyllosilicate-rich (Evans and Chester, 1995; Lin, 1999). This is consistent with observed phyllosilicates in sublayers within the foliated P2 cataclasites (Figs. 3.24, 3.27), in contrast to the phyllosilicate poor random fabric cataclasites (e.g. Fig. 3.26). The development of foliation depends on low-strain rate or relatively high temperature “semi-brittle” deformation of phyllosilicates within polymineralic fault cores (White, 2001). Foliation strength is defined by the development of aligned phyllosilicate networks, and the formation of a dominant fault-parallel fabric within the fault core (Lin, 1999, 2001; Jefferies et al., 2006; Lloyd et al., 2009). Therefore, the scarcity of strong throughgoing networks and associated textures in most P2 faults classifies them as weakly foliated. Though P1 faults do contain phyllosilicates in the form of secondary chlorite precipitation, no internal layering or alignment of minerals was observed.

4.2.2. Diffusive Mass Transfer

Fluid assisted diffusive mass transfer (DMT), sometimes referred to as pressure solution (e.g. Magloughlin 1989; Gratier 1999; Rowe 2011), was active in P1 and P2 fault cores (Figs. 3.17, 3.18, 3.27). The process occurs during low strain rates as fluids are expelled from hydrous minerals during compression against more resistive minerals (Passchier and Trouw, 2005) or as fluids migrate through rocks and react with mineral surfaces. Strain rates associated with DMT have been experimentally determined to be $\sim 10^{-7}$ to 10^{-11} m s⁻¹ between 250 and 350°C, consistent with aseismic creep (Shimizu 1995). Cataclastic fault cores containing comminuted minerals are conducive to DMT, as there are more channels for fluid infiltration, and more surface area for the process to occur (Gratier *et al.*, 1999). In the FCS, this is consistent with the lack of DMT observed in the fault damage zone. Rather, all mass transfer processes were confined to the fault cores. Previous studies have found evidence for DMT within brittle fault zones, typically as seams of immobile iron- and titanium-rich opaque minerals, left behind after the solution process dissolved precursor biotites and muscovites (Groshong, 1988; White, 2001; Jefferies et

al., 2006). Figs. 3.17, 3.26, and 3.27 show evidence for these dark seams within both fault populations of the FCS, typically at the contact between phyllosilicates (biotite or chlorite) and more resistant clasts of plagioclase or quartz.

4.2.3. Pseudotachylyte

One sample of P2 fault rock (Sample AK103-1) contains pseudotachylyte veins (Fig. 3.30). Pseudotachylyte is a product of frictional melt during coseismic slip (Sibson, 1975; Magloughlin, 1989). The temperature of such melts can reach 1200°C or higher (Magloughlin, 2005; Sibson and Toy, 2006), at slip rates greater than 10 cm s⁻¹. Pseudotachylyte fault veins are highly planar, and are commonly associated with dilational injection veins of frictional-melt material (Sibson, 1975; Magloughlin, 1989). Pseudotachylyte is considered the only direct evidence of seismicity in the rock record (Swanson, 1988; Cowan, 1999; Rowe and Griffith, 2015), therefore it is implied that a portion of the deformation accommodated by the P2 fault population was coseismic. Strain-softened cataclastic faults provide zones of weakness within which pseudotachylyte can preferentially form during seismic slip (Magloughlin, 1989). Alternatively, precipitation of adularia cement within cataclasite, commonly observed in P2 faults, is a strain hardening process, and K-feldspar mineralization within fault cores has been proposed as a precursor for pseudotachylyte generation (Di Toro and Pennacchioni, 2005).

The process of frictional melting may also be accompanied by significant fluids and associated elemental depletions and/or enrichments (Magloughlin, 1992). Additionally, presence of fluid serves to reduce melting temperatures for host rocks, further facilitating frictional melt and pseudotachylyte generation (Magloughlin, 1992). Reduction of host rock melting point is also partly aided by release of water from biotite (Allen, 1979), a common mineral within the FCS.

The pseudotachylyte in the FCS has incorporated components of host rock: rounded quartz and plagioclase clasts are common while biotite is absent (Fig. 3.32). This is likely due to partial melting of the quartzofeldspathic components of the FCS, while ferromagnesian biotite melted completely and produced an amorphous, aphanitic, Fe- and Mg-enriched material similar

to processes described by Magloughlin & Spray (1992). This is consistent with enrichment in Fe (+20%) content of this pseudotachylyte-bearing fault core, unique among the P2 samples, (see sample AK103-1 in Appendix B), and likely the result of incorporation of melted FCS biotite in the pseudotachylyte veins.

Additionally, the melt contained microlites of biotite and K-feldspar composition, providing possible clues for temperature of pseudotachylyte (e.g. Magloughlin, 2005). The melting point of sanidine (high temperature K-feldspar) in the presence of hydrothermal fluids is pressure dependent, ranging from ~950°C at 200 MPa to ~700°C at 2800 MPa (Goldsmith and Petersen, 1990). Minimum pressures were established through fluid inclusion analysis, discussed later, as 210 to 230 MPa during P2 faulting. Using 220 MPa, this indicates the melt was considerably over 950°C initially, and cooled to allow sanidine crystallization at around 950°C. This temperature is in agreement with the dehydration melting point of biotite experimentally determined by Gardien *et al.* (2000) in quartzofeldspathic gneisses.

4.2.4. Bulging in Quartz

Bulging recrystallization, or simply bulging, is rare within quartz grains in P1 wallrock, and absent along P2 faults (Fig. 3.14). As a deformation mechanism, bulging is the lowest temperature form of grain boundary migration (GBM), an early precursor to the ductile deformation of quartz (Hirth and Tullis, 1992; Stipp *et al.*, 2002). It correlates with relatively low-strain rate, and the low-temperature “regime 1” of Hirth & Tullis (1992). As low strain rates are applied to the rock, point defects form within the crystal structure of quartz grains, causing strain weakening (Hirth and Tullis, 1992). Subsequently, the defects migrate through the crystal lattice. Bulging, and the onset of quartz plasticity, begins to occur at ~300°C (Tullis and Yund, 1977; Stipp *et al.*, 2002). Hydrolytic weakening of quartz may also occur: the presence of water in the system may lower the required temperature of the transition from brittle deformation to GBM through bulging by up

to ~100°C (Hirth and Tullis, 1992). Section 4.4 further explores the temperature conditions during deformation.

4.2.5. Implications of Deformation Mechanisms in the FCS

In summary, P1 and P2 faults deformed primarily through brittle cataclasis. Development of weak foliations in P2 faults was contingent on phyllosilicate presence in the fault core, and deformation at relatively low strain rates. Though P1 fault cores also hosted phyllosilicates, these were poorly developed compared to P2 fault cores, and did not form appreciable amounts of cataclastic fault rock or foliations. P1 faults hosted bulging in wallrock quartz, and DMT within the fault core, suggesting a component of aseismic deformation accommodated some of the strain. In contrast, P2 faults hosted aseismic DMT and coseismic pseudotachylyte, indicating strain was accommodated across a wide range of strain rates. The presence of DMT within both fault populations suggests fluid accompanied deformation and that both sets of faults served as conduits for fluid flow at some point in their development.

In other parts of the Nason Terrane, cataclasites hosting fluid-assisted DMT and pseudotachylyte are present (Magloughlin 1989, 2011). Also, tonalitic plutons in the Italian Alps, similar in composition to the FCS, host brittle faults, DMT, bulging, and pseudotachylyte (Di Toro and Pennacchioni, 2005; Pennacchioni et al., 2006; Mittempergher et al., 2014). Thus, the deformations mechanisms observed in the FCS and their implications are not unique and are consistent with other brittle fault rock studies.

4.3. Fluid-Rock Reactions

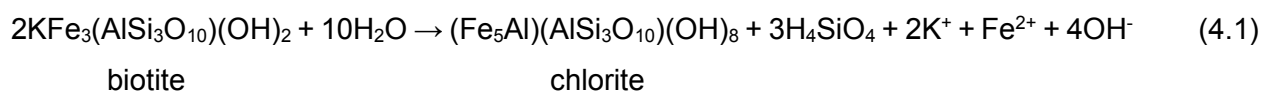
Brittle faults commonly act as conduits for fluid transport (Caine et al., 1996). Thus, they can be associated with metasomatism, mineral alteration, and new mineral growth, which are observed in both P1 and P2 faults. Alteration assemblages can be used to estimate temperature of mineral formation and, by deduction, conditions during fluid-assisted faulting, as discussed in section 4.5. Alteration of existing minerals and growth of new minerals may also have significant effects on the mechanical deformation along faults, explored further in section 4.7.

This section explores the likely reactions involved with alteration observed in this study. It draws upon previous studies of analogous rocks under similar conditions. Upon establishing possible mechanisms for alteration, the reactions are connected to mineralogical changes observed in outcrop and microscope scale, and geochemical data gathered by EDS and PXRF. These data are synthesized to propose a fluid history model (section 4.3.7).

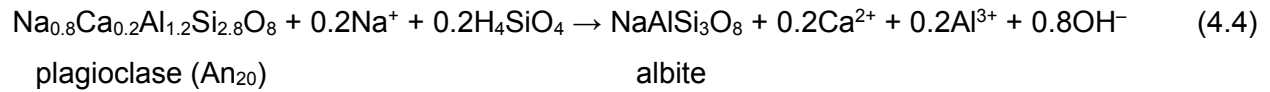
Note that the reactions proposed here are idealized, and involve end-member compositions for minerals (e.g. iron-bearing biotite end member annite). Additionally, these reactions are based on the assumption that Al remained immobile and thus the products and reactants are balanced around aluminum. The true chemical reactions are more complex but cannot be quantified without more precise geochemical tools.

4.3.1. Chlorite

Chlorite is present in both P1 and P2 faults. It is ubiquitous along P1 faults, both replacing *in situ* biotite in the wallrock and as growth of new chlorite within the fault cores. In contrast, chlorite in P2 faults is not ubiquitous, but is sometimes present as minor alteration of biotite within the wallrock or fault cores. A possible hydration reaction, after a study by Veblen & Ferry (1983) of biotite breaking down to chlorite in hydrothermally altered quartz monzonite at ~425°C, simplified using the Fe end-members, is:



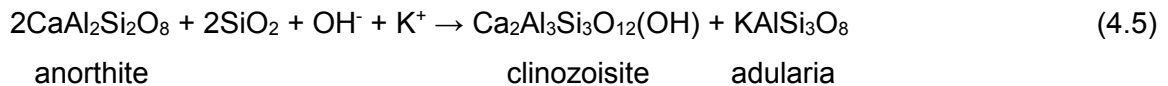
The replacement of biotite by chlorite, as proposed in this reaction, is particularly apparent in P1 faults. The breakdown of biotite would have required a large volume of fluid. This reaction released potassium and iron, likely consumed in the alteration of plagioclase through sericitization and saussuritization, and the production of adularia, all discussed later in this section. This is consistent with a correlation observed between chlorite and altered plagioclase: P1 faults display both extensively, while P2 faults do not. Iron-rich opaque minerals are more common in P1 than P2, the result of liberated iron introduced to the system (Figs. 3.17, 3.18, 3.27).



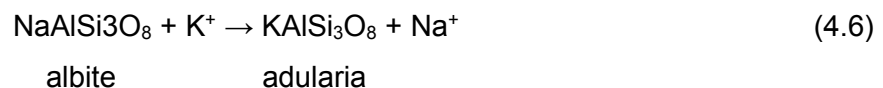
This reaction is proposed as both dissolution-precipitation and replacement (Harlov and Austrheim, 2013). As in reactions 4.2 and 4.3, sodium is likely sourced from an external fluid. Released aluminum is proposed to be involved in sericitization of plagioclase (Engvik et al., 2008). This is consistent with reaction 4.2 and my observations of albite hosting sericite.

4.3.3. Adularia

Adularia is common among both P1 and P2 faults. In both fault populations, secondary adularia occupies significant volumes of the fault core. It is modally more abundant in P2 faults than in P1 faults. Sandström *et al.* (2010) proposed a reaction involving hydrothermal alteration of plagioclase to clinozoisite and adularia in granitic rocks at intermediate temperatures (150-350°C) generalized here:



In this case, anorthite is the calcium end member of plagioclase, and K is made available after chloritization of biotite. Potassium may have also been introduced as a free ion in the fluid, or from chloritization (Reaction 4.1) However, the clinozoisite + adularia assemblage was uncommon, while albite and adularia were abundant in both fault populations. Therefore, a more likely source of adularia involving a simple ion exchange reaction of Na⁺ and K⁺ between albite and a K⁺-bearing fluid, derived experimentally from Orville (1963) at temperatures between 200-700°C, is as follows:

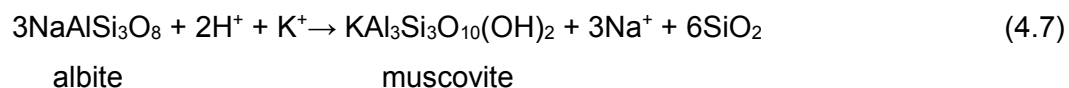


However, according to Wintsch (1975) and Carten (1986), a K⁺-Na⁺ exchange as in reaction 4.6 is a surface reaction that only produces limited volumes of adularia in a closed system. The introduction of K⁺ in an open system allows for more significant volumes of adularia

formation, suggesting both P1 and P2 faults hosted a K⁺-bearing fluid, rather than K being solely sourced from local chloritization (Reaction 4.1). Additionally, albite and adularia may exist in equilibrium, and thus reaction 4.6 is reversible depending on the saturation of Na⁺ or K⁺ in the system, and the availability of feldspar mineral surfaces upon which the reaction occurs (Orville, 1963; Wintsch, 1975).

4.3.4. Sericite

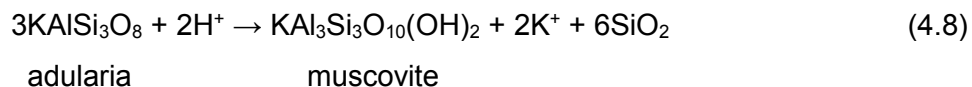
Plagioclase grains contain sericite (hydrothermal muscovite) along both P1 and P2 faults. P1 wallrock plagioclase displays pervasive, well developed sericitization. In contrast, it is less common and less developed along P2 faults. Altered plagioclase is commonly albitized and sericitized, consistent with reaction 4.2. Alternatively, sericitization may have followed albitization of plagioclase, rather than accompanied it, through a reaction proposed by Hemley & Jones (1964):



According to Wintsch et al. 1995, Reaction 4.7 occurs when the system is “fluid-dominated”, meaning the fluid/rock ratio is high and the rock is relatively permeable. Sericitization also requires a slightly acidic fluid, providing a source of free H⁺ ions, and thus the associated the alkali/H⁺ ratio (Na⁺/H⁺) is low. Reaction 4.7 is reversible upon establishment of a higher alkali/H⁺ ratio, through either deformation through fracture providing more available surface area of albite, thus more potential reactant Na⁺, restriction of fluid flow and reduction in available H⁺, or introduction of a less acidic fluid (Wintsch, 1975; Que and Allen, 1996).

To initiate reaction 4.7, potassium may have been released by chloritization of biotite (Reaction 4.1), or introduced as a free ion in the fluid. Release of sodium may have been consumed during albite production (Reactions 4.2, 4.3, 4.4), which in turn may have provided more reactants for sericitization to continue through reaction 4.7, dependent on the Na⁺/H⁺ ratio mentioned earlier.

Similar to reaction 4.7, The following dissolution-precipitation reaction from Wintsch (1975) occurs in fluid-rich systems, and allows for precipitation of secondary muscovite from K-feldspar (adularia):



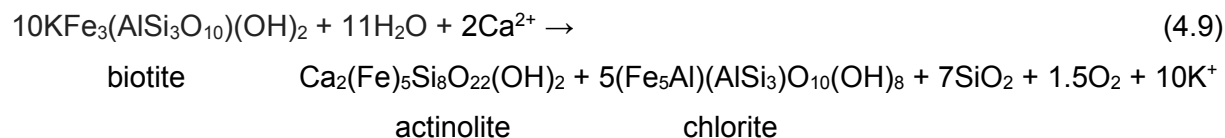
Reaction 4.8 is analogous to reaction 4.7 in that it is reversible and controlled by the alkali/H⁺ and fluid/rock ratios, where the alkali is K⁺ rather than Na⁺ (Wintsch, 1975; Wintsch et al., 1995). These reactions, along with reaction 4.6, are closely related: a high Na⁺/K⁺ ratio in the system results in reaction 4.7 occurring, while a low Na⁺/K⁺ ratio results in reaction 4.8 (Wintsch, 1975). The adularia-muscovite-albite system are stable in equilibrium depending on Na⁺/H⁺ and K⁺/H⁺ ratios (Hemley and Jones, 1964; Wintsch, 1975), where fluids with high ratios, enriched in Na⁺ or K⁺, produce albite or adularia, respectively.

Reaction 4.8 requires K-feldspar to proceed. However, K-feldspar was not a modally abundant mineral in the unaltered tonalite. Additionally, no evidence for sericitization of secondary adularia was observed in either fault population. Therefore, this reaction likely did not occur within the faults. However, it is believed that the reversal of this reaction may have been significant, as there is textural evidence for overprinting of sericitized and albitized plagioclase by adularia. The relationship between these minerals and reactions in the FCS is further explored in section 4.3.7.

4.3.5. Amphibole

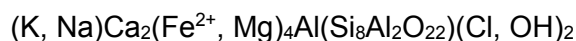
Actinolite is present in both P1 and P2 fault cores. Actinolite is commonly associated with hydrothermal alteration in lower greenschist facies around ~300-350°C (Reyes, 1990; Hawke et al., 1996). Actinolite mineralization associated with albite, chlorite, and sericite is common in low grade rocks, *e.g.* within hydrothermally altered granites, and involves the breakdown of biotite to form actinolite and chlorite (Carten, 1986; Battles and Barton, 1995). This is consistent with the assemblages and conditions observed across both fault populations in the FCS. A reaction

involving actinolite production is proposed here, using the iron end members for biotite (annite), actinolite (ferroactinolite), and chlorite (chamosite) for simplicity:



This reaction involves release of potassium, likely consumed during adularia growth. This is consistent with the close spatial relationship between actinolite and adularia (Fig. 3.19). Replacement of biotite by amphibole was possible in the fluid-rich systems of both P1 and P2, as both minerals are ferromagnesian, and Ca was available through reactions 4.3, 4.5, 4.6, and possibly introduced into the system via the fluid. Additionally, reaction 4.9 may provide an explanation for the lack of biotite in both fault populations. The presence of hydrothermal amphibole may correlate to higher degrees of chloritization: they were both more modally abundant in P1 faults than in P2 faults.

The chlorine-bearing mineral observed within both populations, previously mentioned in sections 3.2.2 and 3.2.3, is tentatively identified as a low-temperature hydrothermal amphibole: Cl-rich and K-bearing hastingsite, or potassic chlorohastingsite, as outlined in previous research (Vanko, 1986; Suwa *et al.*, 1987; Enami *et al.*, 1992; McCormick and McDonald, 1999), with a general formula as follows:



The chlorine ion is located in the site usually occupied by OH (Suwa *et al.*, 1987; Oberti *et al.*, 1993). EDS analysis suggests this amphibole is also present in the high salinity P2 sample AK108-1B (See figs. 4.4, 4.5 in section 4.4).

Similar to actinolite, the conditions of formation for Cl-amphiboles can be lower greenschist facies (Vanko, 1986; Enami *et al.*, 1992). The Cl-bearing amphiboles are unique in that high-salinity fluid is required for their formation (Vanko, 1986; McCormick and McDonald, 1999). This is consistent with fluid inclusion salinity observations made later in this study,

discussed further in section 4.4. It is possible that this saline fluid, containing a volumetrically significant amount of chlorine anions, also hosted enough salt-forming cations (Na^+ , K^+ , Ca^{2+}) to initiate several of the reactions discussed earlier in this section.

4.3.6. Interpretation of Geochemical Data

Using the fluid-rock reactions established in the previous section, this section draws connections between observed microscopic evidence for alteration and precipitation of secondary minerals, and chemical changes of major elements described in section 3.5.

4.3.6.1. Population 1

The inner part of the damage zone around P1 faults contains chlorite and no biotite, whereas the outer damage zone retains unaltered biotite. This is consistent with iron depletion in the inner damage zone, and no change in iron content in the outer damage zone, per reaction 4.1. Iron liberated in the inner damage zone through chloritization of biotite likely migrated into the fault core, consistent with the presence of chlorite and iron-rich opaque minerals concentrated in the fault core (Fig. 3.18), and PXRF results showing iron enrichment. Relative concentration of magnesium mirrors that of iron, likely the result of the same process, as magnesium is also a constituent of host rock biotite.

Calcium is depleted within the fault core (-21%), and more so throughout the damage zone (-51% and -42%). Reactions 4.2, 4.3, and 4.4 liberate calcium from plagioclase through albite and muscovite production. This is consistent with albite and muscovite being the dominant alteration products in the extremely sericitized damage zone plagioclase (Fig. 3.15). The lesser degree of calcium depletion observed in the fault core can be explained through reaction 4.9, which consumed some of the calcium liberated from the damage zone to precipitate secondary actinolite. Remaining freed calcium was then likely removed from the system by the fluid.

Potassium shows either no change or is enriched throughout the fault core (+19%) and damage zone (+24%). Therefore, any depletion due to chloritization (reaction 4.1) was likely offset by adularia production in the fault core through reactions 4.5, 4.6, and reversal of 4.8, and

ubiquitous secondary muscovite production throughout the fault zone, through reactions 4.2 and 4.7. Both of these relationships were observed petrographically, though muscovite was restricted to the damage zone, while adularia was only present in the fault core.

4.3.6.2. Population 2

Iron and magnesium are both depleted (-22% and -29%) in the P2 fault core. Unlike P1, where relative change in abundance of Fe and Mg is likely the result of chloritization, chlorite was not observed along P2 faults. Biotite is uncommon within the fault cores as well. Therefore, depletion in these elements is likely the result of dissolution and removal of biotite from P2 fault cores during fluid flux.

Ca is slightly depleted in P2 faults. This is consistent with less observed albitization of plagioclase within P2 faults as compared to P1 faults. Though significant amounts of albite and adularia were observed, there were also appreciable amounts of unaltered plagioclase clasts with only slightly altered rims in the fault core.

The major elemental change within the P2 fault cores is an extreme enrichment in potassium (+70%), apparent across all samples. This is clearly the result of abundant adularia formation, the major constituent of the fault matrix in these fault cores (Fig. 3.25). adularia producing reactions 4.5, 4.6, and the reversal of reaction 4.8 are thus considered the most significant in P2 faults. The potential impact of adularia precipitation on fault evolution is discussed in section 4.7.

4.3.7. Fluid History Model

A general model explaining the alteration assemblages observed in both the P1 and P2 faults is proposed here. The basis for this model involves the textural relations present within the faults, the reactions discussed earlier in this section, the net geochemical changes within the fault zones, and previous research on the formation conditions of these secondary minerals, under similar temperature, hydrothermal conditions.

In P1 faults, abundant chlorite replaces biotite, and the albite + muscovite assemblage replaces host rock plagioclase. No direct interaction between these two assemblages was observed, therefore the order of alteration is unclear. Referring to reactions 4.2 and 4.7, albite was either coeval with or preceded muscovite. Adularia overprints albite along the P1 fault core (Fig. 4.1), thus likely representing the last stage of alteration. The fine-grained mass of chlorite, adularia, and actinolite is restricted to the P1 fault core and it was observed that they are generally undeformed, thus it appears that these minerals formed together.

The modal abundance of albite along P1 faults indicates the hydrothermal fluid was enriched in Na^+ compared to the host rock (Berndt and Seyfried Jr., 1993; Engvik et al., 2008). As albitization and chloritization proceeded, sodium was consumed while K^+ and Ca^{2+} were released. Continued albitization and chloritization, or introduction of another K^+ -rich fluid, may have led to an increase in the K^+/Na^+ ratio and a lower Na^+/H^+ ratio (Wintsch et al., 1995). Regardless of the process, the resultant system would have been more acidic and favored sericite production (Wintsch, 1975), supported by the observation of albite hosting sericite in thin section. This process has also been seen in previous work under similar conditions, and the intensity of sericitization of plagioclase has been linked to a high fluid/rock ratio (Que and Allen, 1996; Wibberley, 1999).

The shift from sericite to adularia production, supported by the observation of sericitized albite replaced by adularia, may have been caused by a decrease in fluid acidity, perhaps associated with introduction of a new, K^+ -bearing fluid, and thus less H^+ ions to drive reactions 4.7 and 4.8. A second explanation for the precipitation of adularia in the sericite-albite-adularia system has also been proposed to reflect a decrease in the fluid/rock ratio (Wintsch et al., 1995). This shift may have been achieved through precipitation of secondary minerals within the P1 fault cores, including actinolite and chlorite, which in turn restricted fluid permeability pathways. As mentioned previously, chlorite, actinolite, and adularia appear coeval. However, this is considered unlikely, as the reaction that produces chlorite and actinolite requires significant fluid volumes

(reaction 4.9; Que & Allen 1996), while the production of adularia can be a relatively fluid-poor process (Wintsch et al., 1995). Therefore, it is more likely that adularia represents the last stage of alteration, where the precipitation of chlorite and actinolite within the fault core served to reduce permeability, consumed fluids and H⁺ ions, and released K⁺, per reaction 4.9. These conditions may have contributed to a high K⁺/H⁺ ratio and an associated low fluid/rock ratio, both needed for adularia to precipitate (Wintsch, 1975). Further, low permeability caused restriction of fluid flow, preventing supply of H⁺ ions that would have buffered the system for sericite production (Wintsch et al., 1995). Additional evidence supporting a late adularia forming event lies in the small crystals and undeformed nature of the adularia, suggesting it formed at the end of deformation. It is possible that the initial fluid contained higher concentrations of K⁺ and Ca²⁺, but further microanalytical geochemistry must be performed on fluid inclusions to determine exact fluid composition.

The P2 system is comparatively less complicated, in that there are only two major alteration minerals: albite and adularia. There are only minor amounts of chlorite, muscovite, and actinolite. Albite hosts minor sericite, and is clearly crosscut by adularia (Fig. 3.21), providing a paragenetic sequence of alteration minerals.

Albite formation as an initial stage of alteration implies, similar to P1, that the fluid introduced appreciable Na⁺ into the fault zone (Berndt & Seyfried 1993; Engvik *et al.* 2008). The crosscutting adularia is indicative of a shift in fluid composition from Na⁺- to K-rich (Carten, 1986; Morad et al., 2010), and was likely produced through the ionic exchange outlined in reaction 4.6. However, unlike in P1 faults where chloritization of biotite may have produced free K⁺, chlorite is uncommon within P2 faults. Therefore, it is likely that the fluid was highly enriched in K⁺ compared to the fluid associated with P1, as adularia is extremely abundant within all P2 fault cores, and PXRF results show strong enrichment in K⁺.

However, this does not explain why sericite production did not follow albitization, as it did along P1 faults. A possible explanation for the shift from albite to adularia production in P2 faults

may involve a lower fluid/rock ratio in the system (Wintsch, 1975), supported in part by the relative lack of chloritization and sericitization, which are two fluid-dependent processes (Que and Allen, 1996). Although mechanical deformation within the fault may have initially promoted permeability and influx of an albite-producing fluid, cataclasis in the P2 fault cores resulted in inherently more surface exposure of feldspar through fracturing. Surface exposure of feldspar is an important factor in maintaining a relatively low fluid/rock ratio in the albite-sericite-adularia assemblage, as surface exchange reactions (i.e. Reaction 4.6) occur preferentially over muscovite production in short timescales (Orville, 1963; Wintsch, 1975). In contrast, cataclasis was less pronounced in P1 fault cores, consistent with thinner fault cores and less displacement (e.g. Torabi & Berg 2011), and thus fluid/rock ratios remained sufficiently high for sericitization. Alternatively, it is possible that the fluids associated with P2 faults were simply less acidic. A higher alkali/H⁺ ratio would keep the system in the adularia-albite field rather than produce sericite (Orville, 1963; Hemley and Jones, 1964).

Possible scenario involving fluids hosted in each fault population are summarized here. The fluid hosted in P1 faults was likely sodic, with a possible component of potassium, resulting in initial production of albite and chlorite through alteration reaction with the host FCS. Sericitization of albite followed, caused by a change in fluid chemistry that involved degrees of increased acidity and a reduced Na⁺/K⁺ ratio either through K⁺ introduced by a new generation of fluid, or evolution of the fluid during continued chloritization and albitization. Further change in the fluid system led to less available H⁺, caused by either lower permeability or introduction of a less acidic fluid. This reduced alkali/H⁺ ratio provided an environment for adularia precipitation during the last stage of alteration.

P2 faults also hosted initial albitization and thus likely an associated sodic fluid. However, the lack of chloritized biotite suggests the fluid was potassic as well, as adularia was modally abundant within the P2 fault cores. Further, the lack of sericite, muscovite, and chlorite in P2 suggests either the fluid/rock ratio was relatively low initially and throughout alteration, or the fluid

was less acidic than in P1 faults. This inherent difference between P1 and P2 fluid systems is reflected in a direct shift from albitization to adularia precipitation in P2 fault cores. Additionally, the simple presence of an alteration halo in P1 faults suggests fluids were available for longer timescales, during which they permeated the rock through diffusion (Guilbert and Park, Jr., 1986).

The paths of the fluids in the framework of Na^+/H^+ and K^+/H^+ activity for both faults are illustrated in fig. 4.2, and an idealized paragenetic sequence is shown in fig. 4.3.

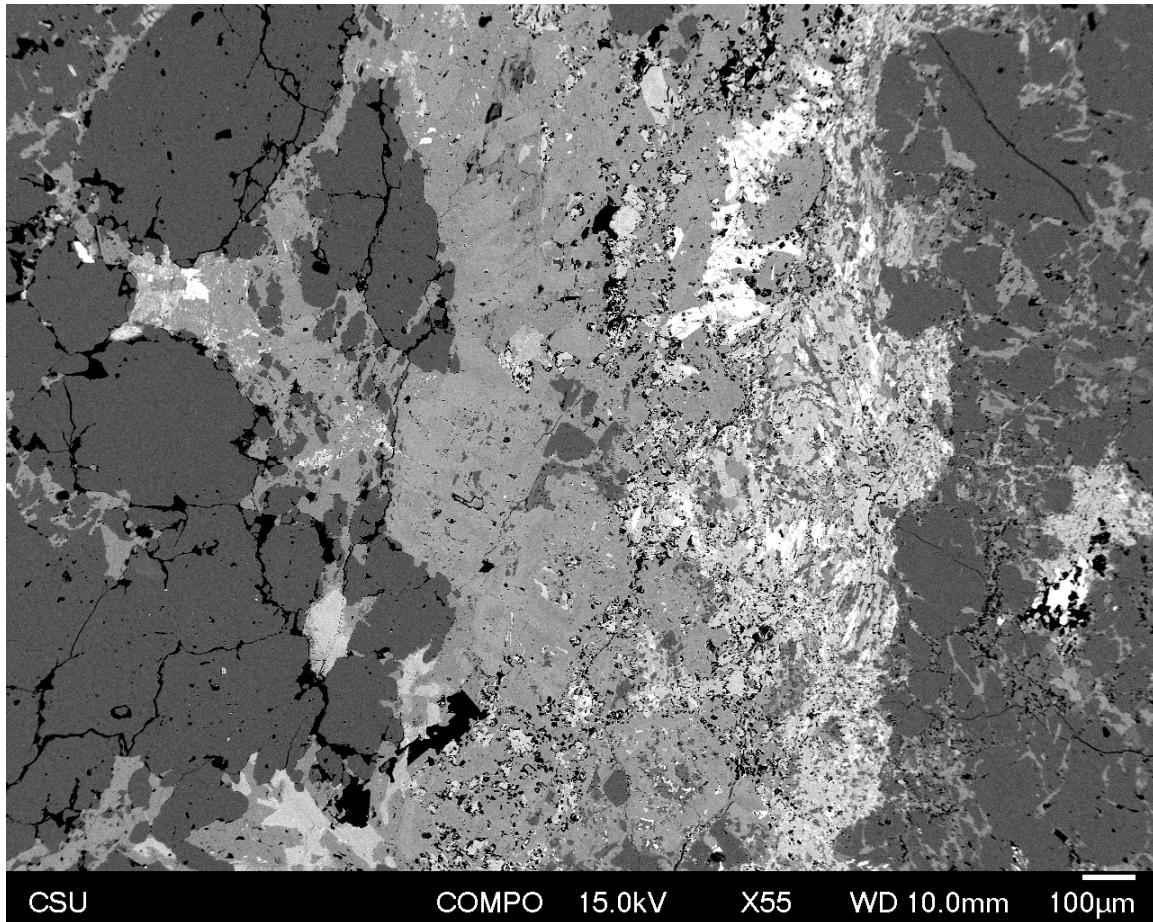


Figure 4.1. BSE image of a P1 fault core, which extends from top to bottom across the image. The dark gray mineral on either side is albite. The lighter gray along the left side of the fault core is adularia. The mass of lighter gray and white material on the right side of the fault core is actinolite and chlorite. In this figure, adularia appears to be overprinting albite. The fluid that resulted in albite to adularia (reaction 4.6) replacement travelled preferentially along cracks in the albitized wallrock on both sides of the figure, as indicated by reactions along grain boundaries. Further, the albite shows brittle fracturing while the adularia does not, indicating relative timing. Sample AK111-1A.

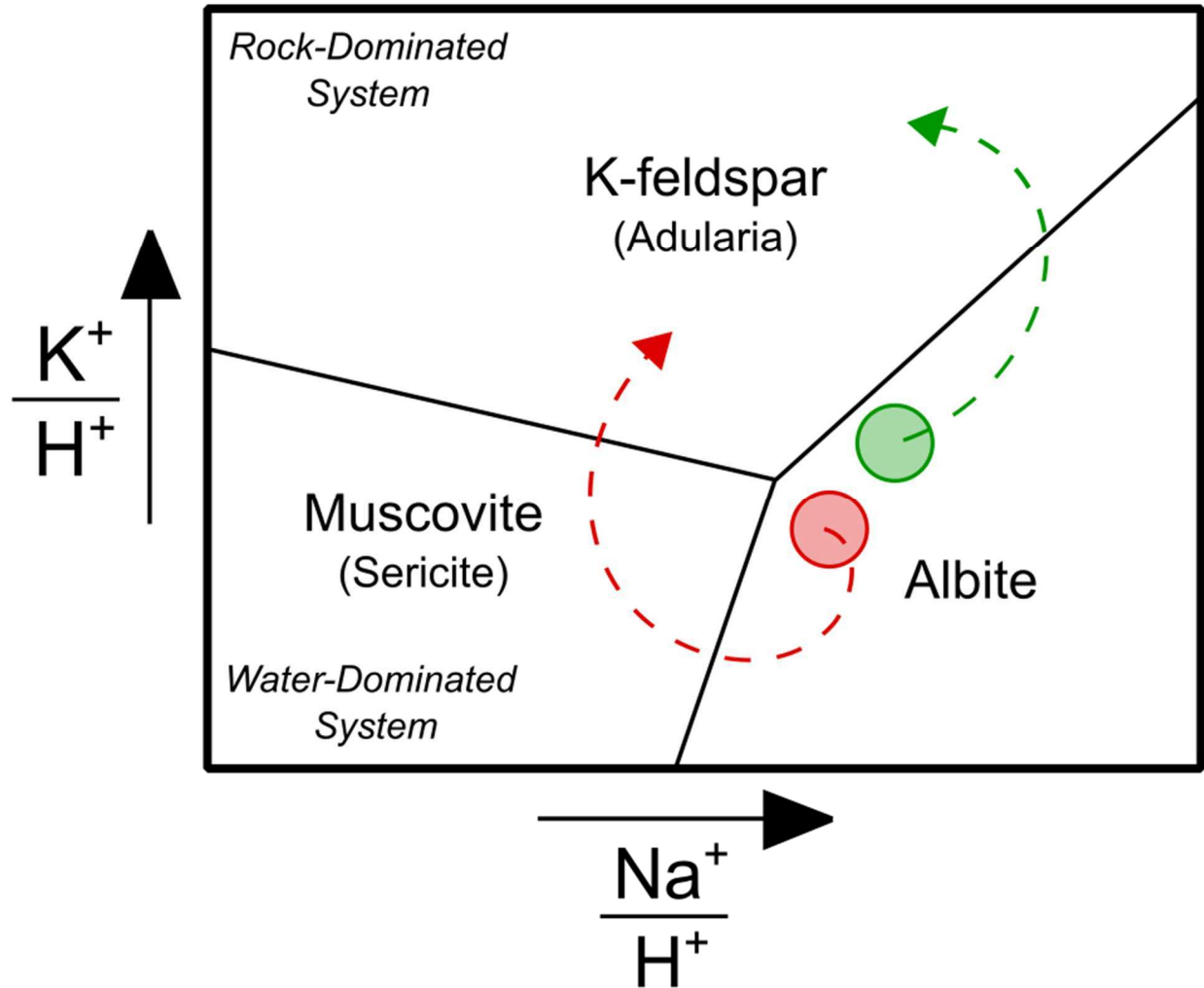


Figure 4.2. Schematic diagram, modified from Wintsch (1975), showing stability fields of three major alteration products observed in hydrothermal systems within granitic rocks. The general paths of the fluids associated with the P1 and P2 fault populations are red and green dashed lines, respectively. The stability of the adularia and albite is dependent on the Na/K ratio in the system (Reaction 4.6). The production of muscovite depends on the availability of H^+ ions in the system, which is controlled by two factors: acidity of the fluid, and fluid/rock ratio. The fluid/rock ratio is the fluid volume relative to the surface of a reactive rock. In this model, a high fluid/rock ratio is termed “water-dominated” by the authors, a low fluid/rock ratio is “rock-dominated”, referring to the surface reactions occurring through surface exposure in feldspars (Wintsch, 1975). The initial alteration assemblages of both fault populations in the FCS hosted albite, denoted by the circles. P1 faults show clear alteration of albite by sericite, followed by replacement by adularia. P2 faults do not contain appreciable sericite, but also show replacement of albite by adularia. It is unclear if the fluid was initially K^+ and Na^+ bearing, and through continuous albite-production and associated Na^+ consumption evolved to be K^+ -rich, or if two separate fluids were introduced to the system sequentially: an initial Na^+ -bearing fluid, and a subsequent K^+ -bearing fluid.






P1 Fluid-Rock System				
<i>Mineral</i>	Stage 1: Introduction of Na-bearing fluid to fault	Stage 2: Shift to K-rich fluid	Stage 3: Initial precipitation in fault core	Stage 4: Restricted permeability
Albite				
Chlorite				
Sericite				
Actinolite				
Adularia				
	Relatively High Na ⁺ /H ⁺ Unknown Fluid/Rock	Low K ⁺ /H ⁺ High Fluid/Rock	Low K ⁺ /H ⁺ Low Fluid/Rock	High K ⁺ /H ⁺ Low Fluid/Rock
Relative Alkali/H⁺ Ratio & Relative Fluid/Rock Ratio				

Figure 4.3a. Idealized paragenetic sequence showing the P1 fluid-rock system (section 4.3.7). The stages are defined by major changes in the system that result in a shift in the alkali/H⁺ or fluid/rock ratios, but may also be related to fluid pH. Note that chlorite includes both replacement of biotite and precipitation in the fault core, though the latter is confined to stage 3. For further discussion, see text.



P2 Fluid-Rock System		
<i>Mineral</i>	Stage 1: Introduction of Na-bearing Fluid to Fault	Stage 2: Shift to K-rich fluid
Albite		
Adularia		
	High Na ⁺ /H ⁺ Low Fluid/Rock	High K ⁺ /H ⁺ Low Fluid/Rock
Relative Alkali/H⁺ Ratio - Relative Fluid/Rock Ratio		

Figure 4.3b. Idealized paragenetic sequence showing the albite to adularia succession in the P2 fluid-rock system (section 4.3.7). The stages are defined by a shift in the Na⁺/K⁺ ratio in the fluid composition. It is recognized that the fluid/rock ratio may not be low, rather, the fluid may simply lack sufficient H⁺ ions to drive sericitization. However, the scarcity of chlorite and sericite suggests that the system hosted relatively lower fluid volumes than P1. For further discussion see text.

4.4. Nature and Composition of Fluid Inclusions in the FCS

Microthermometry of two-phase liquid- and vapor-bearing (L-V) fluid inclusions in the FCS provides insight into fluid compositions, fluid entrapment temperatures, and pressure conditions. Temperatures of phase changes of the liquid and vapor phases are helpful in estimating concentrations of individual components. Microthermometry also provides insight into conditions of faulting, as the secondary fluid inclusion planes measured in this study are believed to be synkinematic, as will be explained in section 4.6.

Unimodal distributions of homogenization (T_h), final melting (T_m), and initial melting (T_i) temperatures within each fault population suggest one dominant phase of fluids infiltrated the system per faulting episode (Figs. 3.48, 3.49, 3.50).

T_m and T_i are bimodal within the P2 population, but all variability stems from data gathered from one sample, AK108-1B, and will be treated as an outlier to be discussed later in this section.

4.4.1. Composition of the Aqueous Component

Composition of the aqueous component of fluid inclusions can be estimated through analysis of T_m and T_i data. Depression of T_m indicates a degree of salinity, and bulk salinity can be calculated with T_m data from the equation (Bodnar, 1993):

$$\text{Salinity (wt. \% NaCl eq.)} = 1.78\theta - 0.0442\theta^2 + 0.000557\theta^3$$

where θ is the depressed T_m in degrees Celsius.

Resulting median salinities for P1 and P2 are 13.7 (min=3.4, max=21) and 14.2 (min=0.4, max=30.5) wt.% NaCl equivalent, respectively (Fig. 4.4). However, one P2 sample displays high salinity (>22 wt. %) and depressed melting points (<-20°C) well below the rest of the population (all of which were <11 wt. %, and >-20°C) (Figs. 4.4, 4.5). Disregarding this sample as an outlier, median P2 salinity is 9.4 wt.% NaCl eq. (min=0.4, max=15.6) (Fig. 4.4b). This suggests that fluids flowing through P1 faults were generally more saline than those associated with P2, though there

was strong overlap. The composition of the liquid phase in fluid inclusions is assumed to be H₂O-NaCl where $T_m > -21.2^\circ\text{C}$ (Hall et al., 1988).

Where measurement of T_m provides insight into bulk salinity of fluids, T_i allows for interpretation of the composition of the salt component in the aqueous phase when combined with compositional data from further microanalytical techniques (Steele-MacInnis et al., 2016). Chloride is the most common anion associated with crustal fluids (Yardley and Bodnar, 2014), and thus is assumed to be present in the fluid systems that affected the FCS during deformation. High chlorine content in biotite and amphibole within both faults (Sections 3.2, 3.3, 4.2) is consistent with chlorine-rich fluids accompanying faulting.

P2 sample 108-1B is anomalously saline, and displays a depressed T_m . An aqueous phase was observed at temperatures below $T_{m\text{H}_2\text{O-NaCl}}$; this typically indicates a mixture more complex than simple H₂O-NaCl (Steele-MacInnis et al., 2016). Significantly depressed T_m is possible through presence of one or more divalent cation-bearing salts such as CaCl₂ or MgCl₂ in solution along with NaCl (e.g., Sisson & Hollister 1990), which could lower the melting temperature to as low as -55°C (Table 1, from Steele-MacInnis et al., 2016).

Petrographic observations of alteration, supported by XRF data, provide evidence for elemental mobility. The presence of a syntectonic brine provides a mechanism for transport of cations into and away from the faults, thus providing an opportunity for metasomatism. In order to maintain a charge-balanced system, as cations dissolved out of the fluid, newly freed anions (Cl⁻) either remained bonded in solution during direct cation exchange with surrounding rock (Yardley and Bodnar 2014; e.g. Reactions 4.3 or 4.6), or were incorporated into the chlorine-bearing amphibole, biotite, and possibly other minerals in the fault cores.

4.4.2. Composition of the Vapor Component

Estimates of vapor composition can be made by measuring low-temperature phase changes of the vapor phase. CO₂ is assumed to be a significant component within crustal fluids, with a T_{m,CO_2} of -56.6°C when $X_{\text{CO}_2} = 1$. Fluid inclusions within the FCS did not show signs of vapor

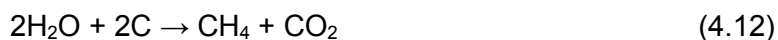
freezing when cooled to -190°C (the minimum temperature of the liquid nitrogen-cooled freezing stage). The presence of stable, unfrozen gas at temperatures below T_{m,CO_2} suggest another volatile component must be contributing to the vapor (Van den Kerkhof and Thiery, 2001). The two most common gases within the earth's crust after carbon dioxide are methane and nitrogen ($T_{m,\text{CH}_4} = -182.5^{\circ}\text{C}$, $T_{m,\text{N}_2} = -210^{\circ}\text{C}$; Table 5-1 from Diamond, 2003). The presence of a vapor phase at these extreme low temperatures suggests a combination of one or more low boiling point gases, and likely negligible CO_2 in the mixture due to the significant degree of depression below T_{m,CO_2} . It is also possible that the vapor component is composed of H_2O vapor, and the H_2O in the inclusion is of sufficiently low density that it remains in the vapor phase even during cooling. This explanation is considered unlikely, however, due to a few factors: 1) Initial petrographic observations point to gas-rich vapors rather than H_2O vapors due to the dark appearance of the bubbles (e.g. Fig. 7.20 in Goldstein and Reynolds, 1994), and 2) $\text{H}_2\text{O(L-V)-NaCl}$ systems are typically restricted to lower entrapment pressures (Bodnar and Vityk, 1994), and thus depths, than the interpretations of microstructures and secondary mineralogy along faults in the FCS would suggest (See Section 4.5).

Two end-member vapor compositions, based on the depressed $T_{m,\text{vapor}}$, are $X_{\text{CH}_4} = 1$ and $X_{\text{N}_2} = 1$. Of course, this does not preclude the possibility or even likelihood of a mixture of these two gases.

The first end member consists of a pure methane vapor phase. Samples were cooled 10°C below T_{m,CH_4} , but no freezing occurred. It is possible the activation energy of homogeneous nucleation required to initiate freezing of the vapor was never exceeded, i.e., the vapor was supercooled. This phenomenon has been observed by previous studies attempting to freeze methane vapor in fluid inclusions (Van den Kerkhof and Thiery, 2001).

If the vapor is indeed methane, and considering the host rock for the faults are intrusive igneous rocks and therefore unlikely to have contained any methane, where might it have originated? A possible source is the Chiwaukum Schist, which appears to surround the FCS and

contains significant graphite (Magloughlin, 1993). Previous work has shown fluids commonly react with graphite in pelitic schists at deep crustal levels to form CH₄ (Morikiyo, 1986; Sisson and Hollister, 1990; Huff and Nabelek, 2007). A mechanism for methane production in reducing conditions through the following reactions, outlined by Morikiyo (1986), is



Reaction 4.11 requires free H₂ to drive the reactions. Reaction 4.12 produces both carbon dioxide and methane. No evidence for CO₂ was found in the fluid inclusions studied, so if this is the correct reaction CO₂ produced may have been consumed in the presence of the remaining fluids in the system through the following reaction:



CO₂ may also have reacted with free calcium to form carbonate (CaCO₃).

Though the Chiwaukum Schist experienced temperatures of ~650°C in mid-amphibolite facies, methane can withstand temperatures of >1000°C before decomposing (Abbas & Wan Daud 2010; Amin *et al.*, 2011).

A second end-member explaining a low freezing point vapor is that of pure nitrogen, which has T_{m,N₂} = -210°C. Organic-rich protoliths may contain nitrogen, present as NH₄⁺ (ammonium) and substituted for K⁺ in micas (Duit *et al.*, 1986; Bottrell *et al.*, 1988). The occurrence of nitrogen-rich fluids has been observed in a number of metamorphic rocks, including pelitic schists (Duit *et al.*, 1986; Sisson & Hollister 1990; Pascal *et al.*, 2016), slates (Bottrell *et al.*, 1988) and eclogites (Andersen *et al.*, 1990). The mechanism for nitrogen production can be expressed through following the reactions proposed by Pascal *et al.* (2016):



As with methane, the hypothesized nitrogen-bearing fluids would be sourced from the country rock. Unlike methane production, nitrogen is released from ammonia under oxidizing conditions. High graphite content in the Chiwaukum Schist is indicative of significant organic matter in the protolith, implying the micas in the Chiwaukum could contain at least some NH_4^+ for nitrogen production.

Methane is considered a more likely gas in these fluid inclusions, based on a few lines of indirect evidence. First, as there is likely more carbon (~1%) than ammonia (a fraction of the 10% of the rock that is composed of biotite) in the Chiwaukum Schist (J. Magloughlin, pers. comm. 2017). Furthermore, methane is simply more common than nitrogen in geologic fluids associated with rocks that have undergone retrograde conditions (Van den Kerkhof and Thiery, 2001). However, more quantitative analyses, such as RAMAN spectroscopy of the fluid inclusions, must be performed to draw a conclusion.

4.4.3. Possible Sources of the Fluids

In both end member models discussed above, the reactions producing either methane or nitrogen from the Chiwaukum Schist likely required the influx of water-rich fluids, as by the time of faulting, the region had cooled some 300°C below the peak metamorphic temperature (Valley et al., 2003) and the schist was a relatively dry rock with little more than biotite as the hydrous mineral. Thus, where did these fluids originate? Derivation of the fluids as a result of prograde metamorphism and resultant dehydration reactions, particularly within K-micas (Morikiyo 1986; Pascal *et al.*, 2016), seems unlikely as it would require fluid immobility over the course of metamorphism and subsequent cooling. Another possibility is retrograde production of water, as has been proposed through alteration of epidote to plagioclase in experiments on exhumed greywacke (Vry *et al.*, 2010). These conditions may have been met in the deeper crustal section underlying the FCS, although epidote is minor in the Chiwaukum itself. A third possibility is that the fluids were released during contact metamorphism of the Chiwaukum. However, there are no known nearby plutonic bodies emplaced around the same time as the deformation in the FCS

(Miller et al., 2009). Finally, the fluids may have been externally derived; meteoric fluids at this crustal depth are possible (Menzies et al., 2014; Lawther et al., 2016). This is considered the most likely source for the fluids, as it does not involve crustal fluids remaining stationary over significant periods of time.

The vapor phase observed could be a mixture of the two gases. Magloughlin (1993) observed chloritization of biotite in the Chiwaukum Schist, accompanying cataclasite and pseudotachylyte-bearing fault zones. The same hydrothermal fluid may have caused both chloritization of biotite (releasing NH_4^+) and reaction with graphite (producing CH_4). As brittle faults propagated across the boundary between the Chiwaukum Schist and the FCS, they served as conduits for the flow of methane and/or nitrogen bearing fluids from the country rock into the FCS.

4.4.4. Implications of Homogenization Temperatures

The conditions of fluid entrapment are believed to be representative of ambient conditions during faulting, based on the following assumptions:

- T_h values are indicative of minimum fluid entrapment temperatures.
- Fluids that flowed through secondary FIPs, microcracks that were directly related to the stresses and deformation that induced faulting, as mentioned in section 3.5.1.
- Fluid inclusions did not undergo re-equilibration, remaining volumetrically and compositionally static between time of trapping and time of observation in the lab setting.

T_h data suggest P1 faults (med. $T_h=289^\circ\text{C}$) hosted hotter fluids than P2 faults (med. $T_h=262^\circ\text{C}$). This is consistent with cross-cutting relationships (P2 faults cut P1 faults), as the development of the two generations of faults occurred during uplifting and cooling of the crust in the late Cretaceous and early Paleogene.

4.4.5. Estimation of Pressure from Fluid Inclusions

Geothermobarometry was performed using the FLUIDS BULK computer program by Bakker (2003) to calculate pressure of fluid entrapment (Table 4.1; Fig. 4.6). The two previously proposed end-members for vapor composition were each input separately into the BULK

software. Resulting pressure calculations are based on equations of state for nitrogen (Jacobson *et al.*, 1986) and methane (Setzmann and Wagner, 1991). There is a positive correlation between T_h and estimated pressure at time of entrapment. Salt composition does not significantly affect pressure calculations (e.g. $H_2O-CaCl_2-NaCl$ vs. $H_2O-NaCl$). All pressure calculations were performed using T_h , or minimum temperature of entrapment, therefore resulting pressures (P_h) are minimum trapping pressures. It is important to note that the pressure calculations are dependent on some assumed variables discussed earlier in this section (liquid and vapor phase composition) that do not similarly impact the thermometry calculations. Therefore, these pressures are to be used more as a guide for conditions during faulting.

P1 fluid pressures output by BULK using the $X_{CH_4} = 1$ model had a median P_h of 235 MPa (Q1=222, Q3=245, min=193, max=276) at 289°C. Median P2 pressure estimates were 212 MPa (Q1=209, Q3=221, min=239, max=275) at 262°C.

Pressure calculations for the $X_{N_2} = 1$ model resulted in median P1 P_h of 251 MPa (Q1=243, Q3=258, min=223, max=278) at 289°C. P2 pressures were 236 MPa (Q1=234, Q3=242, min=220, max=277) at 262°C.

Note that a vapor composition of water vapor (two phase L-V, with composition $H_2O-NaCl$) was also considered, but upon running some samples through the BULK software, low homogenization pressures (<10 MPa) were recorded, suggesting shallow depths inconsistent with the interpretations of the microstructural and secondary mineralogical observations discussed in Section 4.5.

Table 4.1. Showing the measured homogenization temperatures (T_h), and calculated pressures during homogenization (P_h), for pure methane and pure nitrogen vapor compositions.

Fault Population:	P1		P2	
	T_h (°C)	P_h (MPa)	T_h (°C)	P_h (MPa)
CH ₄	289	235	262	212
N ₂	289	251	262	236

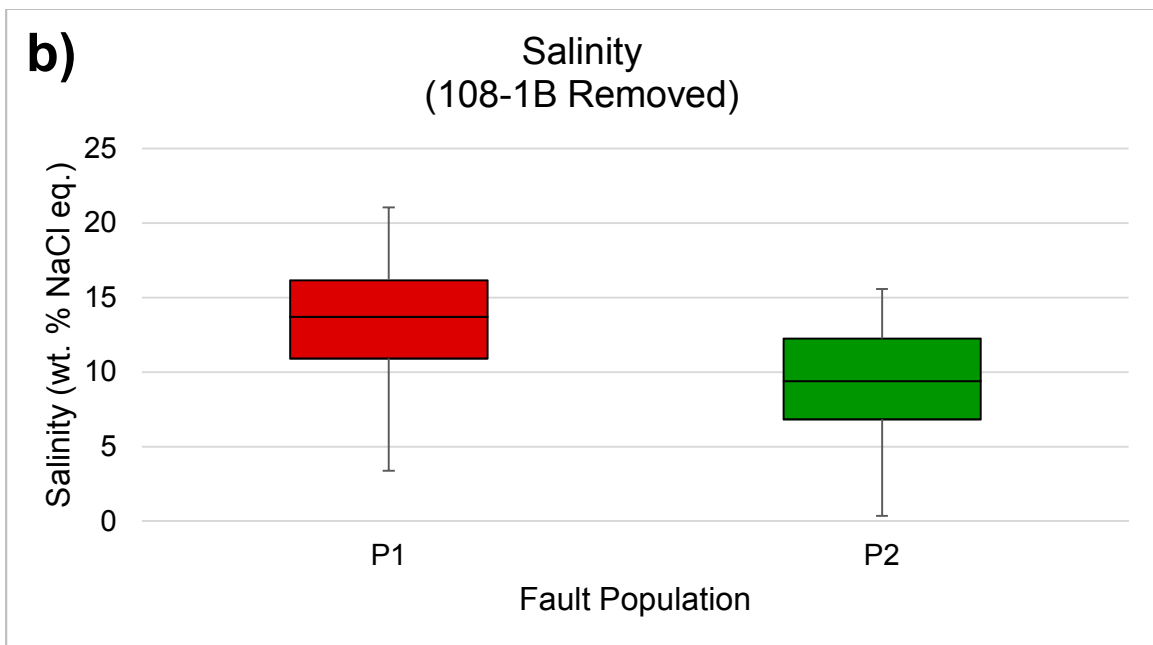
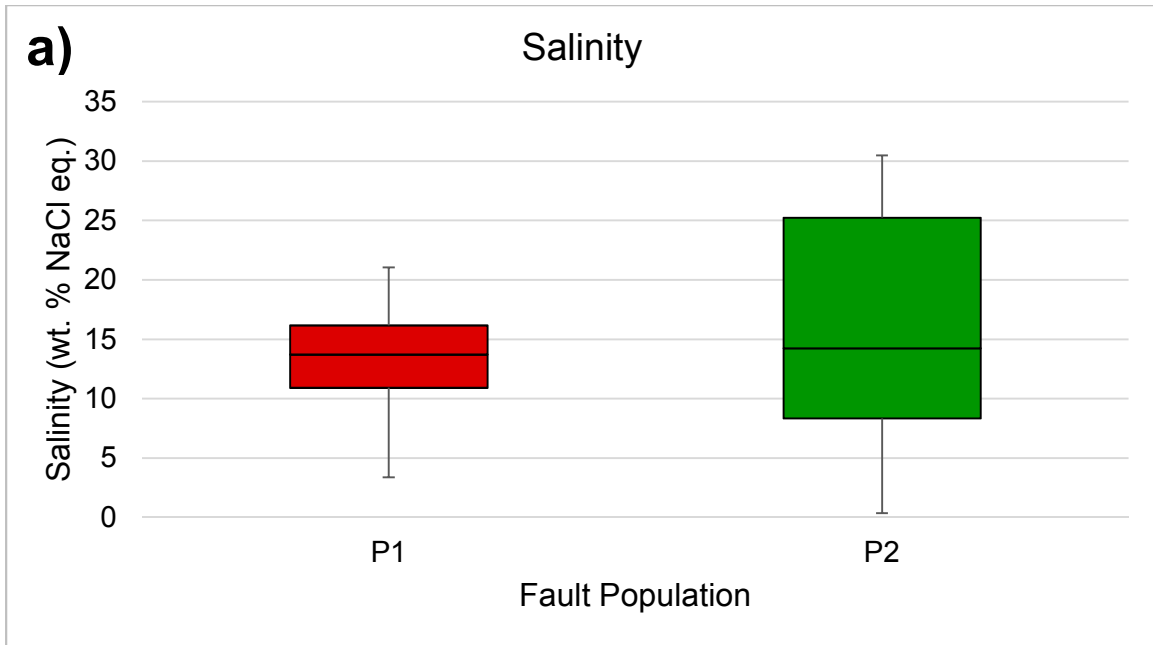


Figure 4.4. (a) Box and whisker plots showing salinity data from all fluid inclusions in the FCS. P1: n=30, P2: n=39. (b) Salinity data from fluid inclusions with the anomalous high salinity sample 108-1b removed. P1: n=30, P2: n=24.

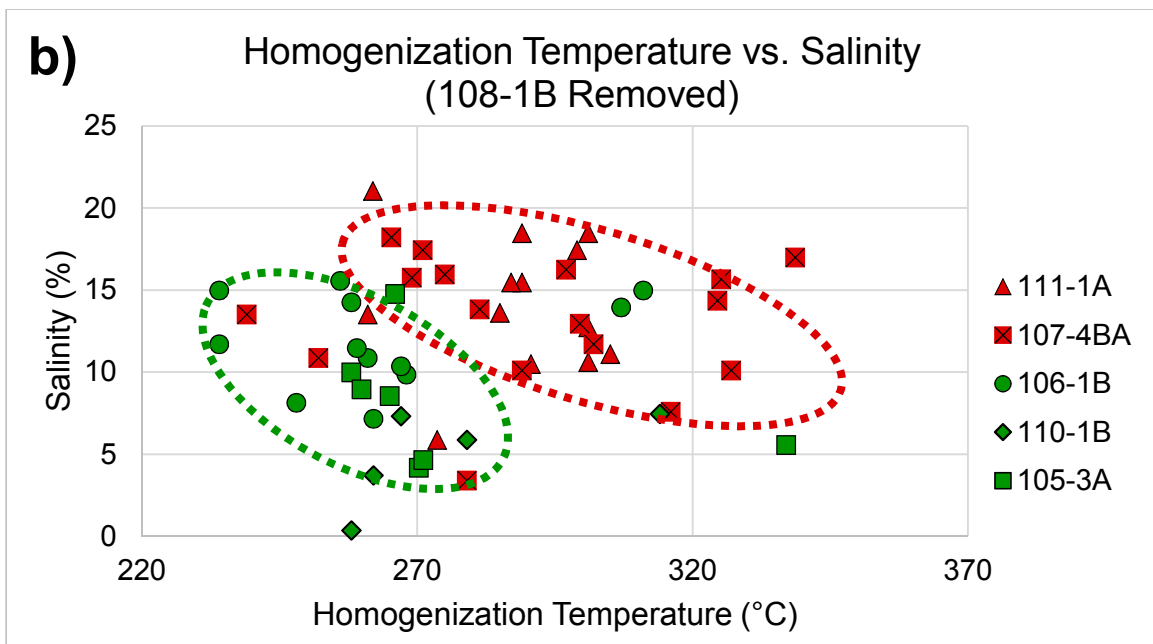
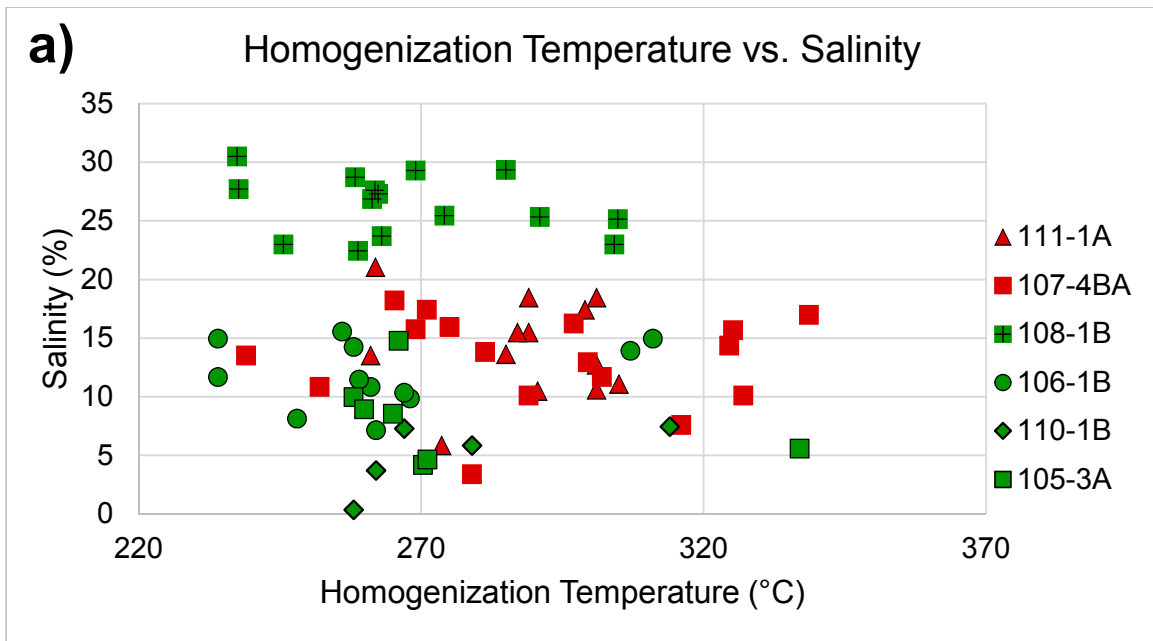


Figure 4.5. Graphs showing the relationship between T_h and salinity across (a) all samples and (b) with the anomalous sample 108-1B removed, illustrating the higher T_h and salinity among P1 faults (red) versus the P2 faults (green).

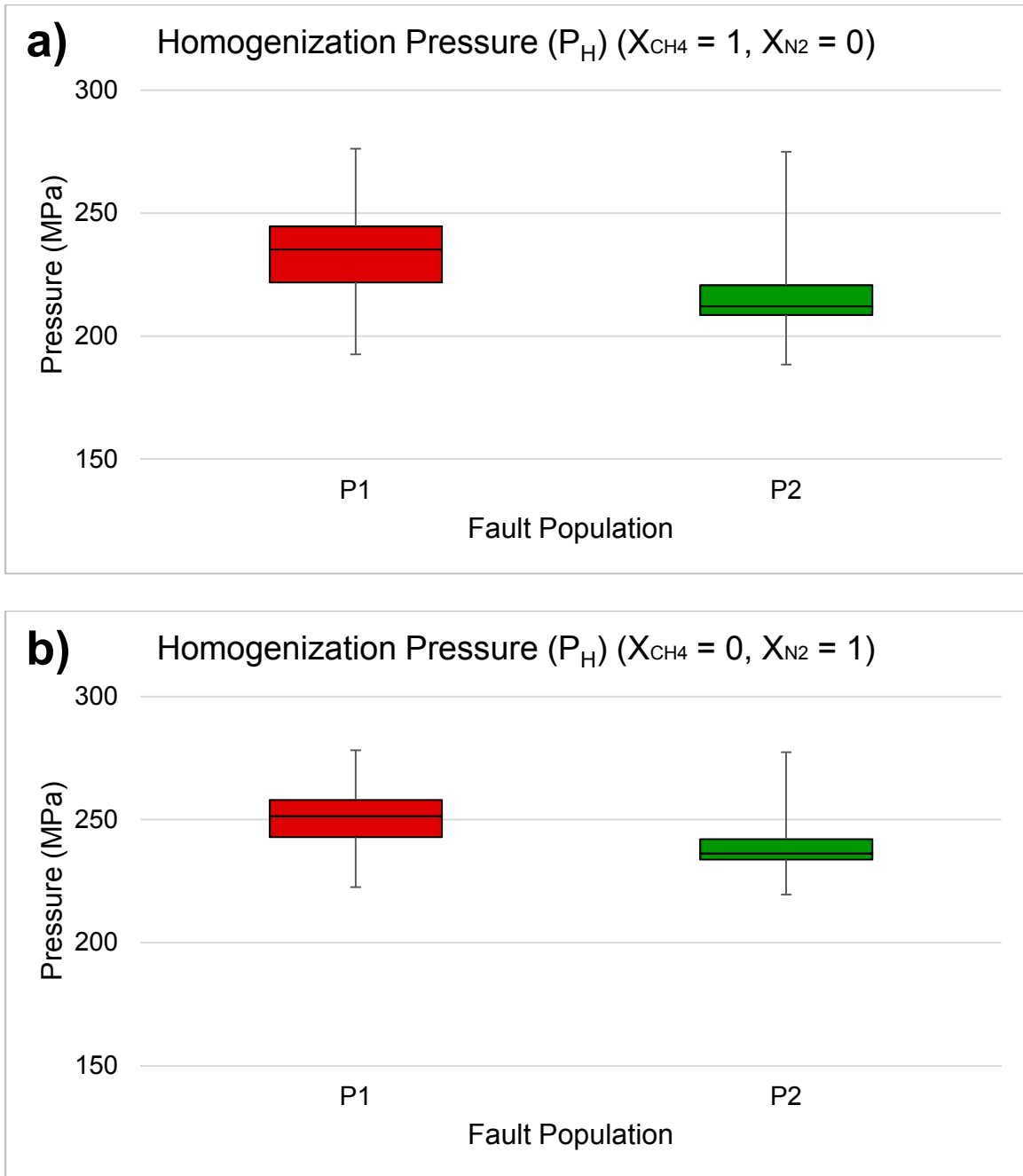


Figure 4.6. Box and whisker plots of pressure during homogenization for the two end-member vapor models discussed in the text. (a) Pressure estimates based on microthermometry data from the H_2O - $NaCl$ - CH_4 model system. (b) Pressure estimates based on microthermometry data from the H_2O - $NaCl$ - N_2 model system. Note the pressure is slightly higher when a pure nitrogen vapor component is assumed ($X_{N_2} = 1$).

4.5. Conditions during Faulting

P-T conditions can be estimated through interpretation of deformation mechanisms, mineral assemblages, and fluid inclusion thermometry. This section synthesizes results from the previous sections to better constrain the conditions during deformation.

Based on the observed brittle nature of the fault rocks in the FCS, deformation occurred at temperatures below the brittle-ductile transition zone (~300-350°C, Scholz, 1988). The well-cemented nature of the cataclasites in P1 and P2, suggests temperatures closer to the 300-350°C onset of crystal plasticity, as opposed to unconsolidated gouges and breccias that form below ~150°C (Sibson, 1977). Pseudotachylyte and diffusive mass transfer (pressure solution) also favor these temperatures (Fig. 4.7), though they have a much wider range of formation conditions, dependent largely on strain rate (Passchier and Trouw, 2005; Prante and Evans, 2015).

Bulging recrystallization occurs between ~280 and ~400°C (Stipp et al., 2002). Therefore, the presence of minor bulging of quartz within P1 samples suggests temperatures of deformation could not have exceeded 400°C. In fact, poorly developed bulging is likely indicative of deformation closer to the lower threshold of 280°C. Lower deformation temperatures due to hydrolytic weakening (Hirth and Tullis, 1992) are not likely significant in P1 faults, due to the other supporting evidence for temperature conditions discussed further in this section. Quartz associated with P2 faults hosted no grain boundary migration, suggesting deformation occurred below 280°C. Given the estimated uplift rates in the area (J. Magloughlin pers. comm. 2017), P1 and P2 episodes must have been separated by a short amount of time, and thus a small amount of cooling, which additionally indicates P1 faulting must have been only slightly above 280°C.

These temperatures around 280°C correspond to lowest greenschist facies to upper “subgreenschist” facies (Fig. 4.8; e.g. Stipp et al., 2002; Bucher and Grapes, 2011; Fagereng and Toy, 2011), and the alteration minerals present (albite + adularia + chlorite + quartz + biotite + actinolite + epidote) are consistent with this range (Bucher and Grapes, 2011). Reyes (1990) established mineral assemblage formation conditions from various alteration assemblages for

metasomatic systems hosted in faulted quartzofeldspathic rocks. The results of the Reyes study are applicable here due to similarities in lithology and hydrothermal conditions, and independently indicate P1 and P2 assemblages formed between 280 and $320 \pm \sim 20^\circ\text{C}$ (Fig. 4.9).

Adularia provides the lower temperature limit for the assemblage. Previous work has described adularia as a low temperature authigenic or hydrothermal K-feldspar, with temperature of formation ranging from 220-340°C (e.g. Steiner 1970; Dong & Morrison 1995; Dreher *et al.* 1998; Ennis *et al.* 2000); thus, 220°C is a likely extreme lower temperature limit, but more importantly, this range is entirely consistent with all other indications of temperature.

Amphibole serves as an upper temperature limit of the assemblage. As mentioned in section 4.3.5, actinolite can be associated with hydrothermal alteration in lower greenschist facies ($\sim 300^\circ\text{C}$; Hawke *et al.*, 1996; Reyes, 1990). Similar to actinolite, conditions of formation for Cl-amphiboles are lower greenschist facies, $\sim 300\text{-}350^\circ\text{C}$ (Vanko, 1986; Enami *et al.*, 1992).

Though the hydrothermal minerals overlap across the two populations, a slightly hotter fluid accompanying P1 faulting is consistent with relatively more abundant amphibole; similarly, a lower temperature accompanying P2 faulting is consistent with more abundant adularia.

Fluid inclusion microthermometry reveals temperatures during faulting, assuming the fluids were entrapped under ambient conditions (Section 4.4). The possibility of hotter fluids accompanying deformation appears unlikely, as there are no nearby plutons emplaced synchronously with faulting (see Section 4.6; Miller *et al.*, 2009) to supply hot fluids. According to fluid inclusion data, fluids were $\sim 289^\circ\text{C}$ along P1 faults, and 262°C along P2 faults (Table 3.7). Assuming a typical geothermal gradient of $25^\circ\text{C}/\text{km}$, P1 faults formed at $\sim 11.5 \pm 1$ km depth, while P2 faults were slightly shallower, forming at $\sim 10.5 \pm 1$ km. Combined with corroborative microstructural and mineralogical evidence, these values are accepted to represent approximate temperatures in the FCS during faulting. The temperature constraints from the previously discussed observations are summarized in Fig. 4.10.

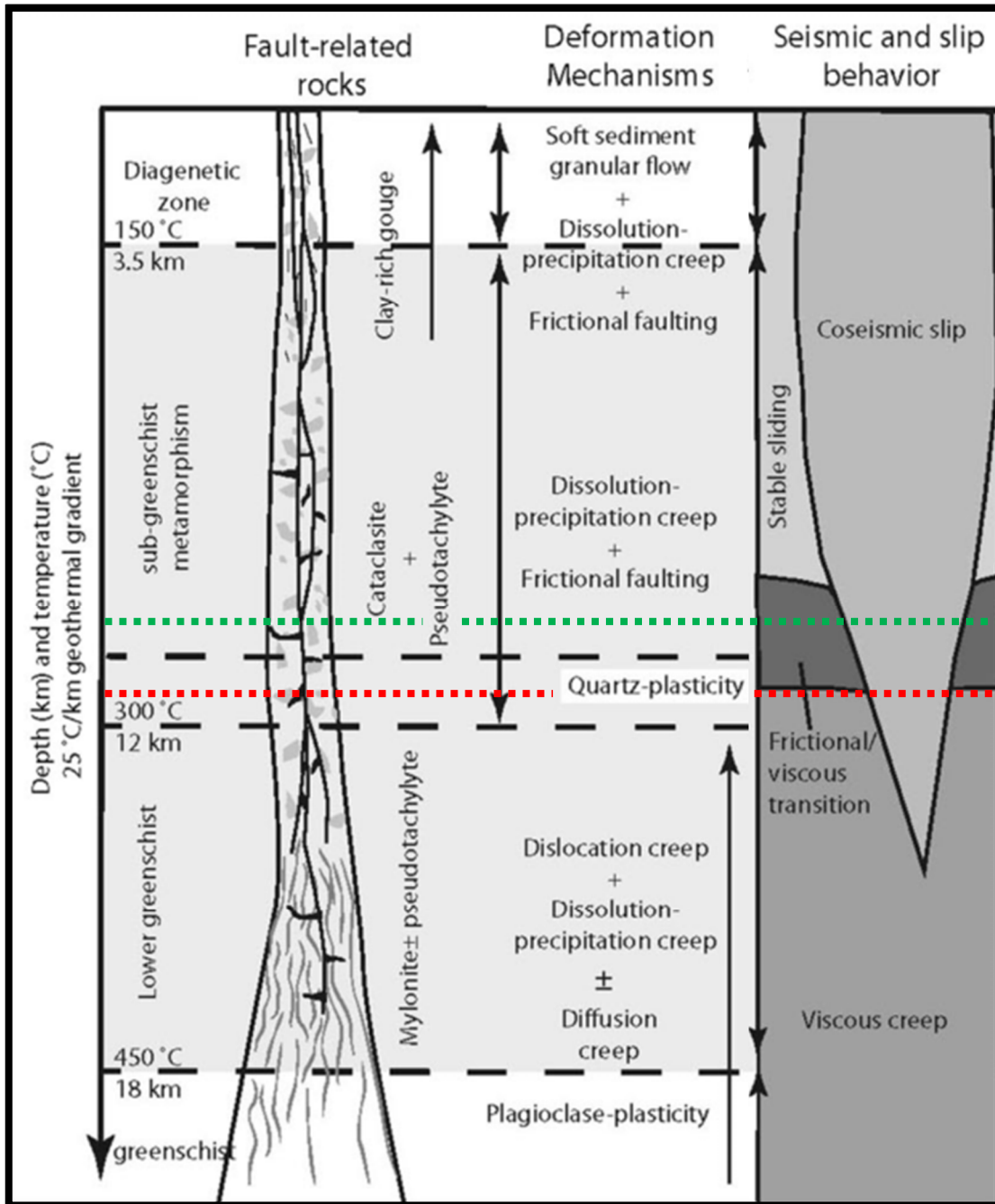


Figure 4.7. This figure, modified from Prante and Evans (2015) shows the general temperature and depth conditions of crustal deformation accompanying faulting. The observed fault rocks and deformation mechanisms (cataclasite, minor bulging, diffusive mass transfer (dissolution-precipitation creep), pseudotachylyte) and mineralogy (lowest greenschist facies to subgreenschist facies) all point to temperatures of ~250-300°C and therefore to depths of ~10 km, in agreement with fluid inclusion results and mineral geothermometry. The red and green lines represent mean fluid inclusion homogenization temperatures of P1 and P2, respectively.

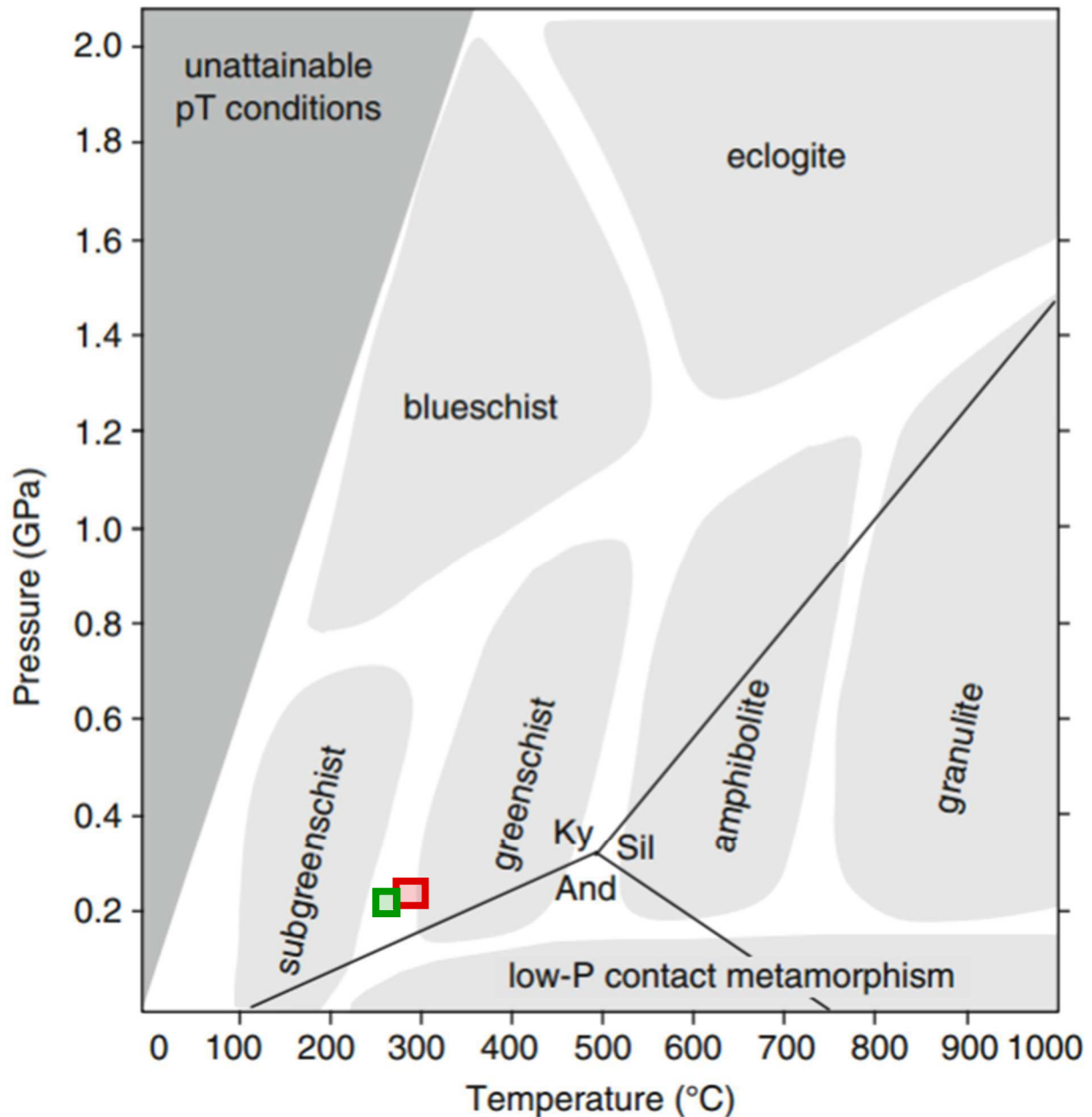


Figure 4.8. Figure from Bucher and Grapes (2011), showing P-T conditions for metamorphic facies. Note the P1 (red box) and P2 (green box) represent temperatures and pressures (table 4.1., discussed in sections 3.5 and 4.4) of ~250-300°C fall along the subgreenschist-greenschist boundary. Diagnostic greenschist assemblage is albite + adularia + chlorite + quartz + biotite + actinolite + epidote (Bucher and Grapes, 2011), all minerals observed in association with P1 and P2 faults. Subgreenschist facies includes “clay minerals”, interpreted to include sericite.

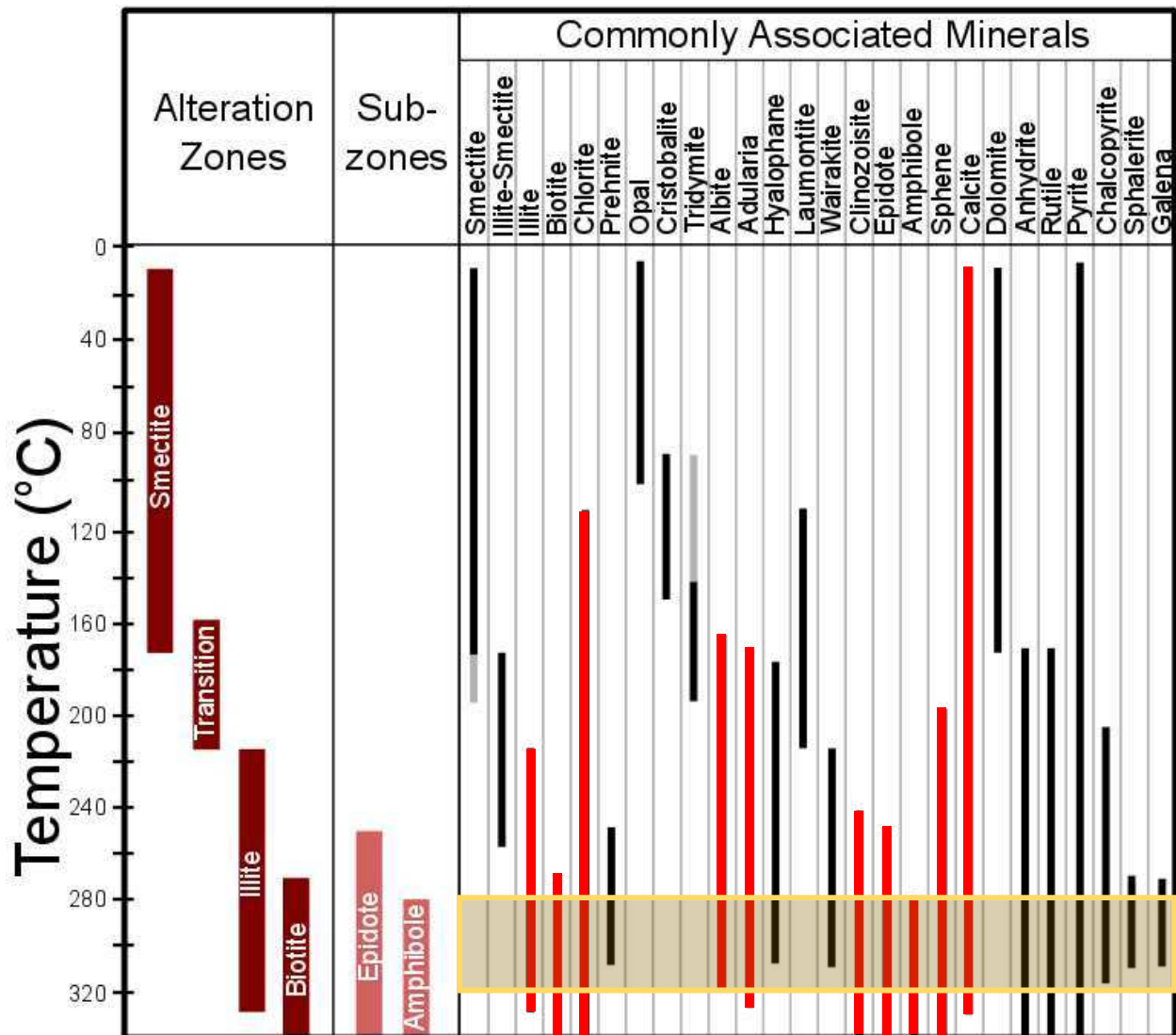


Figure 4.9. Modified from Reyes (1990), showing temperatures of formation for alteration mineral assemblages in metasomatically altered diorite to quartz monzodiorite plutons and andesite volcanic rocks, $\pm 20^\circ\text{C}$. The dark yellow box denotes the range of alteration minerals observed in P1 and P2. Minerals present along P1 and P2 faults are marked with red lines. The upper temperature bound is set by albite ($\sim 320^\circ\text{C}$), the lower bound by amphibole ($\sim 280^\circ\text{C}$).

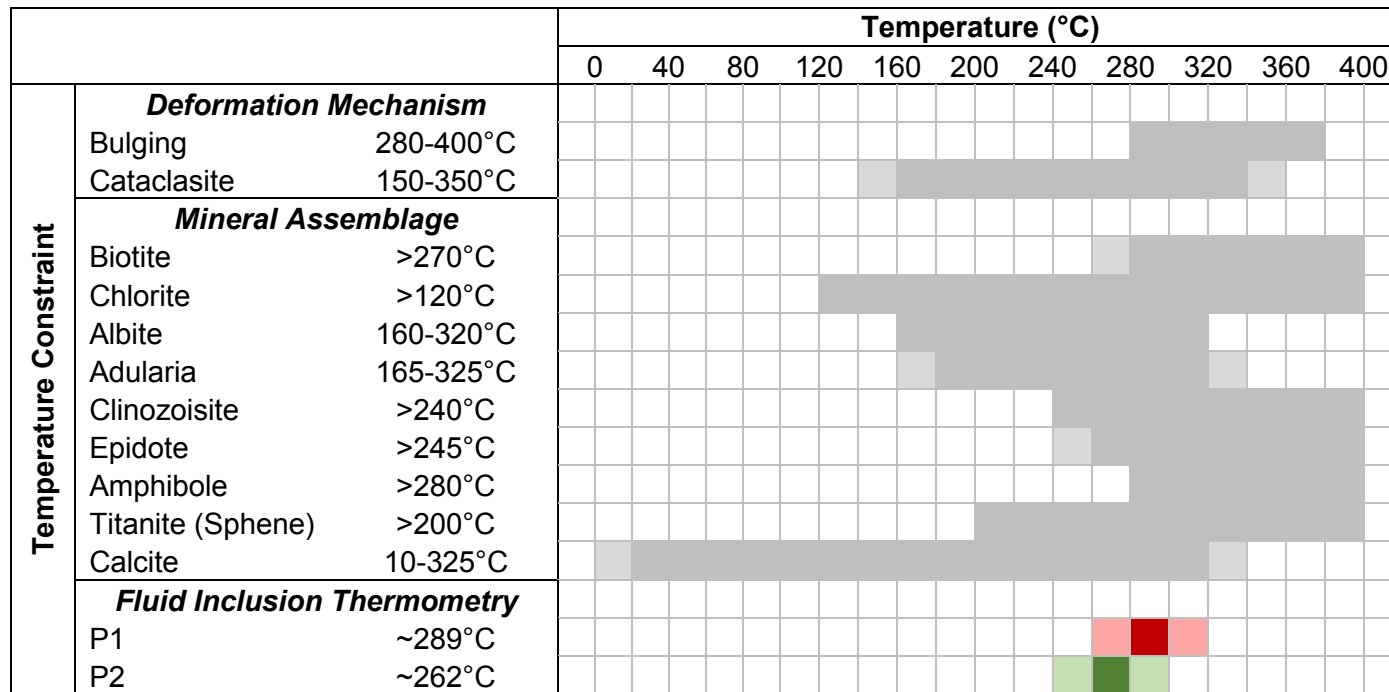


Figure 4.10. Chart summarizing the lines of evidence for temperature estimates of P1 and P2 faulting. The lower end of the “Cataclasite” temperature constraint (~150°C) is marked by a transition to incohesive breccia and gouge, while the upper bound (~350°C) marks a transition to ductile deformation through mylonite formation. The middle section includes the temperatures from the Reyes (1990) study, as mentioned in the text. The bottom of the chart shows the fluid inclusion thermometry data of either fault population. There is considerable overlap among the lines of deformation mechanism and mineral assemblage evidence that support the accuracy of the fluid inclusion data.

4.6. Regional Significance of Faults in the Foam Creek Stock

This section ties observations and interpretations made in this study to the regional geology and geologic history (see section 1.2). Estimates of temperature during faulting, discussed in section 4.5, are combined with previous local and regional thermochronology work to establish timing of deformation. Fault ages are then compared to the established regional structural history, through which orientations of faults (section 3.1) and FIPs (section 3.5), and fault kinematics (section 3.3), can be explained.

4.6.1. Estimated Timing of Faults

Previous studies produced K-Ar dates of the FCS and nearby plutons which are believed to be, at least broadly, part of the same emplacement event (Engels et al. 1976; Ford et al. 1988). Experimental work has shown K-Ar closure temperatures of hornblende, muscovite, and biotite to be 530 ± 40 , 350 ± 40 , and $280 \pm 40^\circ\text{C}$, respectively (Harrison 1981; Harrison *et al.*, 1985; McDougall & Harrison 1990). In the FCS, one muscovite and one biotite K-Ar cooling date from a study by Engels *et al.* (1976) are 77.58 ± 2.1 Ma and 71.11 ± 2.1 Ma, respectively (see Appendix D). Though these are only two data points, regional K-Ar dates from the same study, and more recent Ar-Ar thermochronology performed on nearby plutons support these results (Matzel 2004; Appendix D). These data can be used to generate a time-temperature cooling curve for the FCS (Fig. 4.11). When combined with fluid inclusion T_h of P1 and P2, determined to be robust in section 4.5, fault ages can be estimated using this curve.

Applying this process, P1 and P2 ages can be estimated to be 71.9 ± 3.5 Ma and 69.2 ± 3.5 Ma, respectively. Errors are based on the $\pm 40^\circ\text{C}$ for K-Ar closure temperatures, which encompass both the ± 2.1 Ma error from the Engels study, and the temperature ranges of the fluid inclusion T_h results presented in section 3.5 and substantiated in section 4.5. The relative ages of the fault populations are supported by the observation of P2 faults crosscutting P1 faults. Moreover, this timing coincides with a time of transition in the tectonic regime from E-W shortening to dextral transpression across the Pacific Northwest, as the convergence vector of the Farallon

plate began to rotate counterclockwise (Coney and Harms, 1984; Engebretson et al., 1985; Brown and Talbot, 1989; Gordon et al., 2010). Therefore, the orientations and kinematics of P1 and P2 faults can be used to place deformation in a regional context.

4.6.2. Population 1

Fault and fluid inclusion plane (FIP) orientations provide insight into the tectonic regimes and paleostresses at the time of faulting. FIPs form parallel to the maximum compressive stress (σ_1), and normal to the minimum (σ_3) (Lespinasse & Cathelineau 1995; Boullier 1999; Lespinasse 1999; Appendix C). Therefore, the E-W striking, vertical FIPs associated with both fault populations provide a plane within which σ_1 was oriented during FCS deformation (Fig. 3.46). Given this constraint, it is proposed that the orientation of σ_1 during P1 faulting was horizontal, striking E-W, and resulted in reverse faults dipping shallowly E. The average dip of the major P1 subpopulation is $\sim 32^\circ$ (Fig. 3.36). This is consistent with ideal Andersonian conditions for reverse faults, where σ_1 is horizontal and faults dip $\sim 30^\circ$ (Anderson, 1905). This is supported by abundant regional evidence for E-W shortening in the Cretaceous, a product of the convergent Farallon-North American plate margin (Miller et al., 1993, 2009; Whitney et al., 1999; Valley et al., 2003).

4.6.3. Population 2

In comparison, the younger P2 faults display clear N-, S-, and E-dipping normal and sinistral slip (Fig. 3.37). Much of the normal slip was accommodated along north dipping faults, suggesting northward extension. The sinistral slip sense was generally accommodated along northward dipping, \sim E-W striking faults, though some steeply S-dipping P2 faults also displayed sinistral offset. These orientations and kinematics agree with Andersonian conditions for normal faults, where σ_1 is vertical and faults dip $\sim 60^\circ$ (Anderson, 1905). However, FIP orientations, and thus paleostresses, remained aligned with those associated with P1 faults, that is, E-W striking and vertical. This is not problematic, as the paleostress regime can still accommodate these faults: E-W compression can produce N-S extension and conjugate strike slip faulting.

The question of *why* a new generation of normal faults formed rather than reverse faults under similar stress orientations must be addressed. The transition in the regional tectonic regime from E-W compression to dextral transpression can provide an explanation. Many rocks along the entire Coast Plutonic Complex record variable rates of post-compressional uplift and associated extension (Coney and Harms, 1984; Brown and Talbot, 1989; Valley et al., 2003; Matzel, 2004). In fact, in the neighboring Chelan Block to the east of the Nason Terrane, northward-verging, brittle extensional faults, developed during Tertiary exhumation (Paterson et al., 2004; Miller et al., 2006). Though these brittle faults postdate those in the FCS, they were recorded in rocks significantly deeper than the FCS and surrounding Chiwaukum Schist (Miller et al., 2009).

Additionally, previous work has shown exhumation occurred in the entire North Cascades beginning ~90 Ma (Matzel, 2004). This may have included the unroofing of the Nason Terrane by the previously overthrust rocks, evidence for which includes generally north-south directed normal faulting observed in the Mount Stuart Batholith (J. Magloughlin, pers. comm. 2016). Further regional evidence for synchronous extension has been observed in Late Cretaceous plutons in the Canadian Coast Plutonic Complex (Crawford *et al.* 1999).

Sinistral faulting was observed by Magloughlin (1993) in brittle faults elsewhere within the Nason Terrane. As mentioned in section 1.2, left lateral faulting likely occurred through internal block rotation (Fig. 1.6; *e.g.* Magloughlin 1993). Multiple small sinistral faults, such as those observed in the FCS, allow for larger-scale overall dextral shear, consistent with the regional dextral shear zones (*e.g.* Straight Creek Fault, Ross Lake Shear Zone, *etc.*) (Cowan et al., 1997; Wyld et al., 2006). These shear zones are the product of the rotating Farallon Plate (Engebretson et al., 1985). This provides a mechanism for the extensive left lateral sense of shear observed in many P2 faults.

Therefore, it is proposed that the two generations of faults in the FCS, occurring only a few million years apart, may have captured the rotation of the converging Farallon plate, and the

resultant shift from E-W compression to dextral transpression was locally expressed as reverse P1 faults followed by northward P2 extension with a sinistral component during uplift and regional dextral shear.

4.6.4. Baja BC

Finally, the potential effects of Baja BC-affiliated rotation on deformation of the FCS are briefly discussed here. Deformation of the FCS coincides with the hypothesized Baja BC system, active between about 100 and 50 Ma (Wyld et al., 2006) Even if the FCS underwent 20° of clockwise vertical axis rotation, as Housen *et al.* (2003) proposed for the southern end of the Nason Terrane, the paleo-orientations of the FIPs would still be striking E-W, oriented ~080, and thus the previously discussed regional implications of the P1 and P2 faults would remain unchanged. If any rotation occurred, it is likely that the faults and FIPs would only host partial evidence for rotation, as deformation occurred >25 million years after initiation of the hypothesized Baja BC system. Further, without paleomagnetic data, the influence of potential tilt (Butler et al., 2001) in the FCS cannot be measured. Further work must be performed to fully address the link between deformation of the FCS and the Baja BC hypothesis.

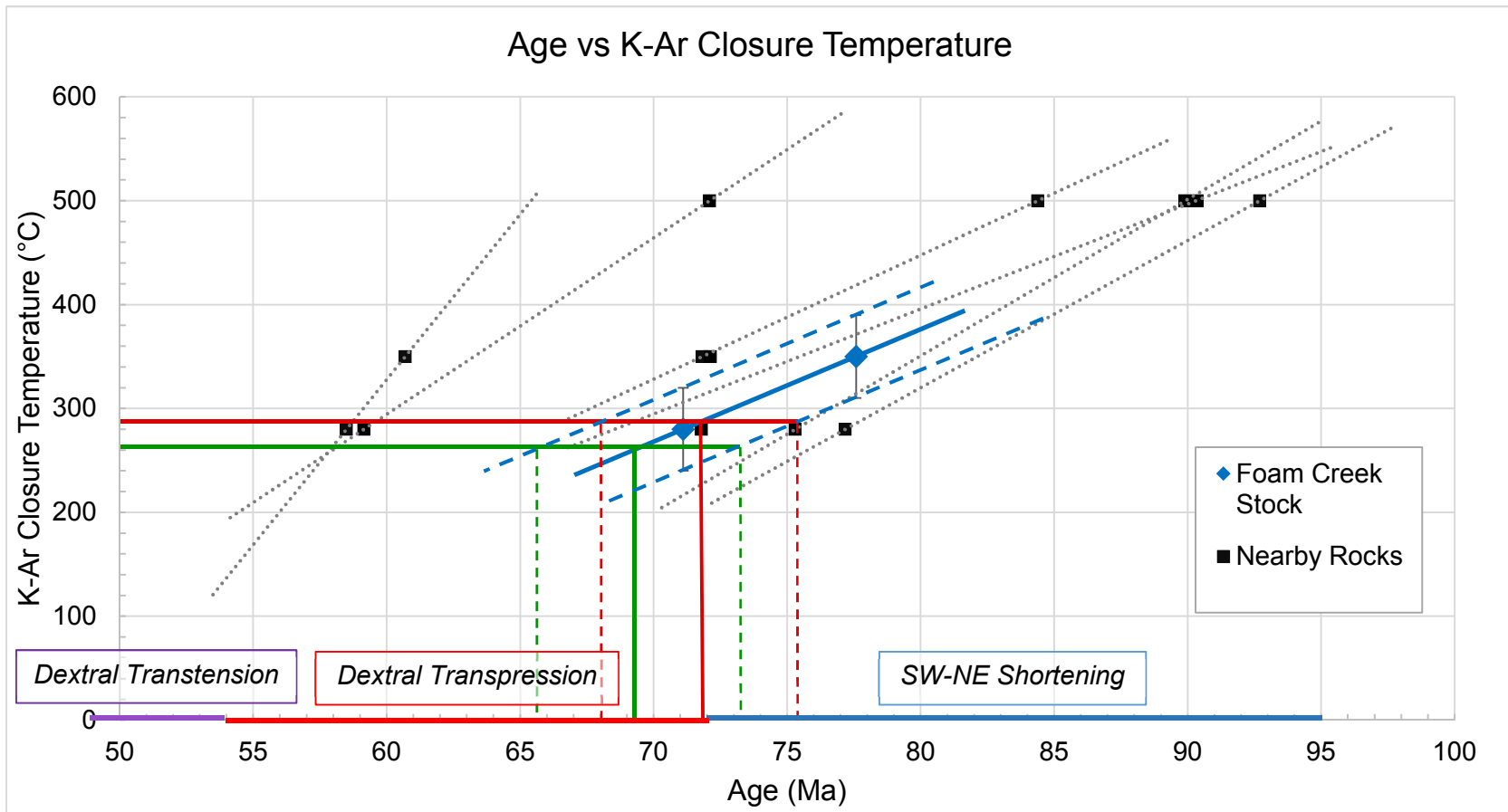


Figure 4.11. K-Ar dates from minerals in the Foam Creek Stock and nearby plutons (Engels *et al.*, 1976). Cooling data from nearby rocks suggests the FCS cooled/exhumed at a similar rate, supporting the validity of the thermochronology. Data can be found in Appendix D. Points are based on closure temperatures of biotite (280°C), muscovite (350°C), and hornblende (530°C), as described in the text. Horizontal red and green lines denote median fluid inclusion T_h for P1 and P2, 289°C and 262°C, respectively. Vertical orange and green lines mark age of the FCS at the time of faulting per the extrapolated age-temperature curve (blue line): P1 occurred 72.1 ± 3.5 Ma, P2 occurred 69.2 ± 3.5 Ma. Errors are represented by blue dashed lines, and based on the $\pm 40^\circ\text{C}$ for K-Ar closure temperatures, which encompass both the ± 2.1 Ma error from the Engels study, and the temperature ranges of the fluid inclusion T_h results presented in section 3.5 and substantiated in section 4.5. Ages of regional tectonic regimes as summarized by Paterson *et al.* (2004) are displayed at the bottom of the graph.

4.7. Evolution of Faults in the FCS

This section aims to answer two separate but related questions regarding the deformation history of faults in the FCS, raised from previous discussions in this paper:

1) Section 4.3 explored the fluids present during faulting of the FCS, and proposed a fluid model based on the relationships of secondary minerals associated with the faults. How did this change in the fluids affect the structural history of the faults?

2) Section 4.6 established that P2 faults are younger than P1 faults. Why did P1 fault planes not reactivate during later P2 faulting?

To answer the first question, effects of fluids on fault strength are reviewed, and then compared to observations of P1 and P2, to provide a structural summary of the evolution of both fault populations. To answer the second question, the relationships between the inferred paleostress orientations and observed fault plane orientations are explored.

4.7.1. Effects of Fluids on Fault Strength

Fluid-rock interaction, and associated chemical and mineralogical changes, are closely tied to the mechanical strength of rocks (Ikari et al., 2011). First, it is well established that pore fluid pressure exhibits a primary control on the frictional strength of faults, counteracting normal stress and facilitating slip (Raleigh et al., 1976; Sibson, 1985, 1992b). Evidence for high pore fluid pressures includes veining associated with faults (Pollard and Aydin, 1988; Cox, 1995). No dilatant veins, quartz or otherwise, were observed along either fault population in the FCS, suggesting pore fluid pressures did not have a significant effect on deformation. Second, as hydrothermal fluids flowed through faults in crystalline rock, fluid-dependent processes formed secondary minerals that affected the internal friction and strength of the fault core. In the FCS, the two major groups of secondary minerals are phyllosilicates (muscovite, chlorite), and feldspars (albite, adularia), and their effects on the bulk strength of rock are reviewed here.

The strain-weakening properties of phyllosilicates may facilitate fault reactivation and reshear, a well-documented process affecting cataclasites (Wintsch et al., 1995; Bos and Spiers,

2001; Jefferies et al., 2006; Collettini et al., 2009). Phyllosilicates have been shown to display shear strengths up to an order of magnitude lower than quartz and feldspar-rich rocks (Kronenberg et al., 1990; Mares and Kronenberg, 1993). Deformation of mica is dependent on crystal orientation, as frictional sliding tends to occur along the {001} direction of the cleavage planes, thus aligned micas oriented near parallel to the maximum compressive stress contribute to mechanical weakening (Shea and Kronenberg, 1993). As slip occurs, interconnected and through-going networks of phyllosilicates may develop, producing planes along which continued slip tends to localize (Shea and Kronenberg, 1993; Jefferies et al., 2006; Ikari et al., 2011).

The other common secondary mineral group associated with fluid alteration in the FCS are feldspars. They are comparatively strong, and their precipitation in fault cores causes strain hardening (Wintsch et al., 1995; Scruggs and Tullis, 1998). Experimental studies have shown that phyllosilicate-poor rocks, including quartzofeldspathic granitoids, display higher internal friction and strain hardening behavior, compared to phyllosilicate-rich rocks containing chlorite, biotite, and muscovite (Ikari et al., 2011). Further, previous studies of brittle faults in crystalline rocks have recognized feldspar cement as a strain hardening agent, inhibiting further slip by cataclasis (Wibberley, 1999; Di Toro and Pennacchioni, 2005; Lawther et al., 2016).

4.7.2. Fault Evolution Model

The previous review of the effects of secondary minerals on fault strength provides a basis for a fault evolution model for both P1 and P2 faults proposed here, illustrated in Fig. 4.13.

Upon nucleation, faults of both populations served as conduits for fluid flow and hosted abundant hydrothermal alteration. This initiated the fluid model described in section 3.3.7. Both faults contain adularia, but P1 faults also contain appreciable chlorite and actinolite (section 3.3). Adularia was undeformed in both fault populations. This suggests that fluid penetrated the faults after they formed and, subsequently, after possible repeated slip events and associated alteration (forming albite, sericite, chlorite, etc.), sufficient adularia precipitated within the fault cores to strengthen them to a point approaching or greater than that of host tonalite. Foliated P2 faults

also host adularia, but the foliations are typically weak and failed to produce throughgoing planar surfaces upon which significant slip could have localized. Therefore, the inherent weakening associated with phyllosilicate foliation development, described in section 4.7.1, does not appear to have affected the overall strength of P2 faults.

The phyllosilicate-bearing P1 fault cores and foliations in P2 fault cores display evidence of having hosted diffusive mass transfer (DMT). The effect of DMT on the mechanical strength of rocks is unclear, other than the fluid-dependency of this process (Weyl, 1959) being further indicative of infiltration of alteration-inducing fluids during slip along phyllosilicate-bearing faults.

The presence of abundant P1 and P2 faults may be a function of the mechanical strengths of the faults. A cycle of fault nucleation, followed by strain hardening through adularia precipitation, likely resulted in strengthening of individual faults and the “shutting down” of the fault plane (Fig. 4.13). As stress continued to act on the rock, strain was accommodated through nucleation of new faults, as the preexisting faults were mechanically hardened and thus no longer planes of weakness. This is a process known as “slip delocalization”, and has been observed in other fault systems in tonalites under hydrothermal conditions at temperatures of 250 to 300°C (Di Toro and Pennacchioni, 2005), analogous to conditions in the FCS during faulting. It is unclear where DMT occurs in this cycle. Textural evidence shows seams of DMT material offset by brittle fracture within fault cores (Fig. 3.26), suggesting inter-faulting formation. It is likely facilitated by fluids that have infiltrated the fault core during slip.

Finally, one of the strong, adularia-bearing P2 faults hosted pseudotachylyte during deformation. Three lines of evidence suggest the generation of pseudotachylyte succeeded precipitation of adularia. 1) Sanidine-composition microlites within the pseudotachylyte suggest a potassium-rich host, consistent with the abundant adularia observed in the fault core. 2) Cataclasite with adularia-rich matrix has been crosscut by pseudotachylyte. 3) Clasts of adularia-bearing cataclasite are contained within the pseudotachylyte. It has been established that frictional melt causes the recovery of fault core strength relative to that of the host rock, a process

coined “fault welding” (Wenk et al., 2000; Sibson and Toy, 2006; Griffith, 2016; Mitchell et al., 2016; Proctor and Lockner, 2016). However, only one sample contained pseudotachylyte, and thus, within the P2 faults of the FCS, this is not considered a significant strain hardening process compared to ubiquitous adularia precipitation.

4.7.3. Lack of Reactivation of Population 1 Faults

Faults tend to nucleate upon preexisting planes of weakness or mechanical strength heterogeneities (Sibson, 1985; Pennacchioni et al., 2006; Crider, 2015). Thus, it would seem likely that P2 faulting would have reactivated the earlier P1 faults. However, there is no obvious evidence of reactivation of P1 faults. Drawing upon the kinematics and stress orientations proposed in section 4.6, a hypothesis is introduced here to explain why P1 faults were not reactivated.

A few reasons for the lack of P1 fault reactivation may lie in the geometry of the P1 faults. They were likely too thin to reactivate, as previous work has shown a correlation between fault core thickness and fault strength (Byerlee and Summers, 1976; Marone, 1995). Their nonplanar nature may also inhibit reactivation, as roughness along fault surfaces provides friction allowing the rock to remain macroscopically strong (Sagy et al., 2007; Fang and Dunham, 2013). Finally, the presence of adularia, though much less significant than in P2 faults, may still have strengthened the P1 faults sufficiently to inhibit reactivation.

Additionally, P1 faults are generally low-angle reverse faults dipping shallowly east, coinciding with an E-W compressional regime. P2 faults contain N- dipping extensional faults, suggestive of a shift from horizontal to vertical maximum compressive stress. Though the paleostress indicating fluid inclusion planes were aligned across P1 and P2, their general E-W, steeply dipping orientation allows for rotation around a north trending horizontal axis. The angle (θ_R) between the horizontal maximum principal stress (σ_1) and P1 fault planes is generally $\sim 30^\circ$, but if we accept that the stress regime rotated to produce later extension on north dipping P2 faults, σ_1 would shift to vertical, and θ_R would be closer to $\sim 60^\circ$. This is too steep of an angle, as

faults favored for reactivation in extensional regimes dip 58-60° (Sibson, 1985). According to (Sibson, 1990), these high angle “severely misoriented” faults require high pore fluid pressures to reactivate. Though there is evidence for high fluid volumes within the faults (alteration, fluid inclusions, *etc.*), it is unlikely pore fluid pressures were high, as no significant veining was observed in association with the faults (Pollard and Aydin, 1988; Cox, 1995).

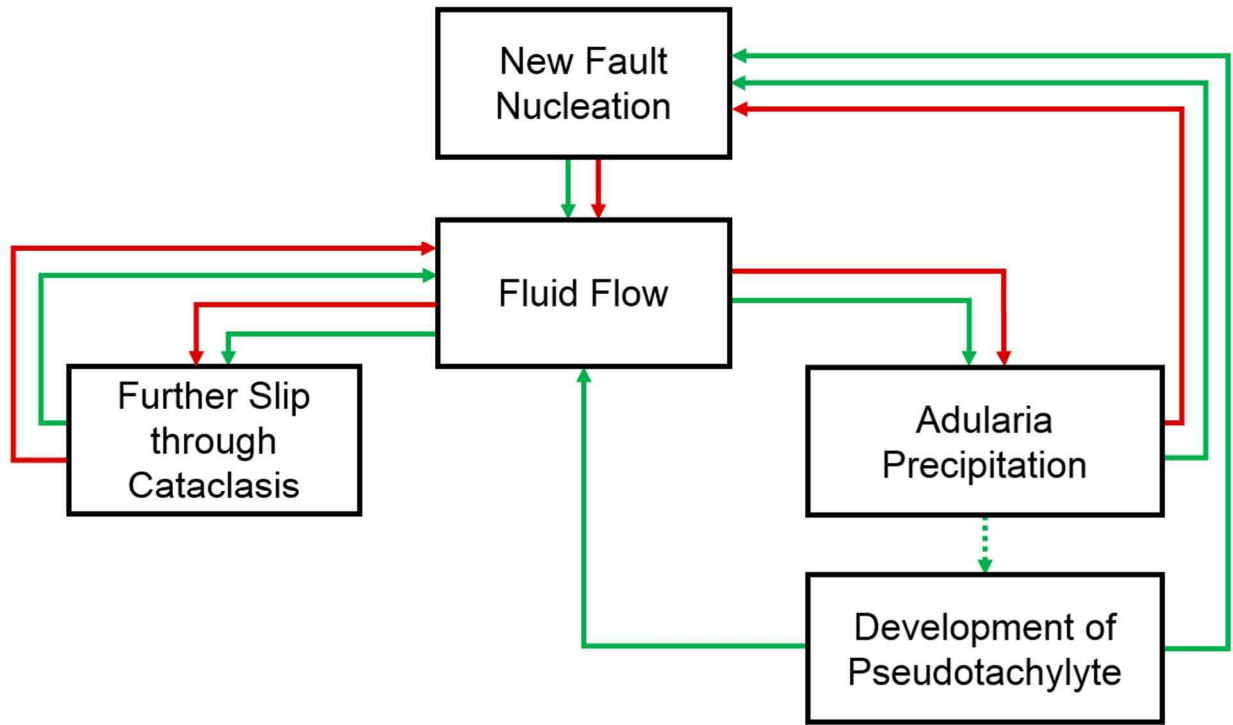


Figure 4.13. A schematic showing the proposed P1 and P2 fault evolution cycle. The path of P1 faults is red, P2 faults is green. The general path of the faults involves nucleation, followed by fluid flow and the initiation of the fluid system discussed in section 4.3.7, where eventual mineralization of the mechanically strong adularia leads to slip delocalization and the nucleation of a new fault plane. The “Fluid Flow” to “Further Slip through Cataclasis” path likely involves continued alteration and secondary mineralization. The development of pseudotachylyte is recognized as a fault hardening process that may shut down the fault plane and force slip delocalization. However, there is observed evidence of pseudotachylyte cutting pseudotachylyte, and thus the possibility of continued fluid flow and slip after pseudotachylyte generation is included. Additionally, DMT may occur along any of the lines between events.

5. Conclusion and Future Work

5.1. Conclusion

The Foam Creek Stock (FCS) is a relatively little-studied biotite tonalite pluton located in the geologically complex North Cascade Mountains. Therefore, this study contributes new observations and insights into the geologic history of the area. Based on the results of this study, the questions posed in section 1.1 are readdressed here:

How many generations of faults cut the FCS?

Two distinctive sets of faults, P1 and P2, cut the FCS. They show different chemical signatures, secondary mineral assemblages, microstructures, fluid homogenization temperatures, fluid salinities, and kinematics. P1 faults are generally E-dipping, display an obvious alteration halo, and fault cores are exceptionally thin fractures with small offsets. Microscopically, grains are fractured, and pressure solution and abundant secondary mineralization of adularia, actinolite, chlorite, albite, and sericite were observed along narrow fault cores. In contrast, P2 faults are generally N- and S-dipping, do not display an alteration halo, fault cores are thicker than P1 faults, and appear to have accommodated the majority of FCS deformation due to greater observed offsets. They are more typical cataclasites, with a fault core composed of discernable clasts embedded within an adularia-rich matrix. The presence of both pressure solution and pseudotachylyte in the dominantly cataclastic P2 fault population indicates slip occurred over a wide range of slip rates (Rowe and Griffith, 2015). In all observed interactions, P1 faults are cut by P2 faults.

What geochemical changes accompanied faulting of the FCS?

According to comparative geochemistry using PXRF results, P1 faults are generally unchanged in SiO_2 , Al_2O_3 , Fe_2O_3 , and K_2O composition, and generally depleted in TiO_2 , MgO , and CaO . Though potassium depletion may be expected in P1 faults due to abundant chloritization of biotite observed in the damage zone, the sericitization of plagioclase and production of adularia in the fault core served to consume potassium, leaving the system neutral. Similarly, chloritization

of biotite and associated removal of iron may have been balanced by chlorite precipitation in the fault core. Depletion in calcium is likely due to abundant alteration and replacement of host plagioclase by albite and sericite.

When compared to host rock data, elemental concentrations in P2 fault cores are generally unchanged in SiO₂ and TiO₂, depleted in CaO, Fe₂O₃, and MgO, enriched in Al₂O₃, and significantly enriched in K₂O. Depletion in iron and magnesium is likely the result of dissolution and removal of biotite from P2 fault cores during fluid flux. Minor change in Ca composition is consistent with the common clasts of unaltered plagioclase in P2 fault cores. The most significant elemental change observed in this study was potassium enrichment in P2 fault cores, consistent with abundant adularia precipitation.

How did fluids associated with faults play a role in FCS alteration?

Both P1 and P2 show abundant evidence for fluid flow. Petrographic observations reveal dense, systematic fluid inclusion planes hosted in wallrock directly adjacent to fault cores. Pressure solution is typically associated with fluid presence, and is observed in both faults. Chemical changes along the faults, and associated alteration assemblages, indicate elemental mobility facilitated by fluid flow.

This study proposed a model for the changing nature of the fluids that flowed through the faults (Fig. 4.2, 4.3), based on interpretation of observed crosscutting relations between secondary minerals. P1 faults display initial chloritization and albitization, followed by sericitization, chlorite and actinolite precipitation, and final adularia precipitation. P2 faults hosted albitization in the wallrock and subsequent adularia precipitation within their fault cores. Changes in the Na⁺/H⁺ and K⁺/H⁺ ratios of the fluid-rock systems over the course of deformation likely controlled the sequence of alteration events, and further differentiate the P1 and P2 systems.

Under what temperature conditions did faulting occur?

Deformation in the FCS was almost exclusively brittle, and P1 faulting likely occurred near the brittle-ductile transition zone (~300°C; Scholz 1988), while temperatures during P2 faulting

were cooler, based on interpretation of deformation mechanisms, alteration assemblages, and fluid inclusion microthermometry. Additionally, abundant alteration and secondary mineralization are evidence that faulting occurred under hydrothermal conditions. Cataclasis within both P1 and P2 fault cores is a clear indicator of brittle deformation. Microstructurally, there is minor bulging of P1 quartz grain boundaries, indicative of the onset of quartz plasticity at $\sim 300^{\circ}\text{C}$. However, there is clear brittle fracture within the damage zones across both fault populations. The cohesive nature of the fault cores is also suggestive of higher temperature brittle deformation, between 250°C and 300°C . Secondary mineral assemblages observed in the fault populations corroborate these temperatures, according to formation conditions outlined by Reyes (1990). Finally, fluid inclusion thermometry of secondary fluid inclusion planes adjacent to the faults suggest P1 faulting occurred at $289 \pm 23^{\circ}\text{C}$, slightly cooler than the ideal transition zone, and P2 faults formed at $262 \pm 24^{\circ}\text{C}$. These temperatures correspond to depths of $\sim 11.5 \pm 1$ km and $\sim 10.5 \pm 1$ km, assuming geothermal gradient of $25^{\circ}\text{C}/\text{km}$.

What is the rheological evolution of the faults?

A basic model for P1 and P2 fault evolution was introduced in this study (Fig. 4.13), based on petrographic observations, comparative geochemistry, and fault kinematics. Both fault populations hosted significant fluid flow after nucleation, that contributed to secondary mineral precipitation. These alteration mineral assemblages influenced the mechanical strength of the faults. P1 faults hosted significant K^+ and Na^+ bearing fluids, that resulted in sericitization and albitization, followed by adularia precipitation and fault strengthening. Upon the shift from reverse faulting to normal and sinistral faulting, P1 fault planes were shut down and did not reactivate. P2 faults hosted similar alteration assemblages, with adularia mineralization following albitization. This also resulted in significant fault strengthening. Except for high strain-rate pseudotachylite generating events, additional strain in the FCS was accommodated along new fault planes, as

the adularia hosting faults likely were too strong to undergo reshear, thus accounting for the large number of faults observed in the field.

What is the regional significance of the faults, their orientations, and kinematics?

Thus, fluid inclusion homogenization temperatures can be used as estimates for temperature during faulting. When combined with previous thermochronology data, the faults are estimated to have formed at $\sim 71.9 \pm 3.5$ Ma and $\sim 69.2 \pm 3.5$ Ma for P1 and P2, respectively. Additionally, the orientations of the fluid inclusion planes were observed at consistent angles from fault planes, suggesting they formed under the same stress field. Fluid inclusion plane orientations, used as estimates for paleostress orientations, align with the presumed \sim E-W oriented regional paleostress during faulting.

Putting these ages in a regional framework, it is proposed that deformation of the FCS observed in this study records rotation of the converging Farallon plate and the resultant dynamic shift in tectonic regime from E-W compression to dextral transpression during regional uplift. Kinematics determined in the field and on the microscale indicate that this regional transition was locally expressed as E-dipping reverse P1 faults followed by extensional P2 faults, with a sinistral component accommodating regional dextral shear. This change in faulting regime likely prevented the older P1 fault planes from reactivating during P2 deformation.

5.2. Suggestions for Future Work

This study of the FCS raises new questions that could be addressed by future studies, including:

Radiometric dating of faults, including possible Ar-Ar dating of adularia in P1 and P2 fault cores, and potassium-bearing pseudotachylyte vein in the P2 fault sample, to further constrain timing of deformation.

Paleomagnetic study of the pluton, or nearby plutons such as the Tenpeak or Sulphur Mountain, to determine any possible tilting or rotation history, and thus the effects of hypothesized Baja-BC motion on the orientations and kinematics of the faults in the FCS. Previous work on

paleomagnetism had involved the Mount Stuart Batholith in the southern part of the Nason Terrane (e.g. Ague & Brandon 1996; Housen et al. 2003), and may provide a basis of comparison to an analogous study.

Laser RAMAN spectroscopy or laser ablation ICP-MS analysis of fluid inclusion compositions, to determine exact cation compositions in the fluids associated with both fault populations, and constrain the proposed fluid model.

Perform low temperature thermometry with a lower freezing point substance than the liquid nitrogen used in this study, such as liquid helium (Van den Kerkhof and Thiery, 2001), in order to provide better insights into the nature of the vapor component in the fluid inclusions.

Oxygen and hydrogen stable isotope study of minerals in the unaltered FCS and P1 and P2 faults to test the hypothesis of the fluids originating from meteoric sources, and to compare the fluids against one another.

Additional geochemical analysis of the P1 and P2 fault rocks to record Na concentrations, as albitization of plagioclase is an important part of the chemical evolution of the faults. Abundant albitization within the damage zone of both fault populations suggests that Na should be enriched in those areas, and depleted in the fault cores.

Further field study to search for evidence of extension or unroofing along NE boundary of Nason terrane. This may include a similar fault rock study of nearby plutons, like the Tenpeak or Sulphur Mountain, that may have experience similar regional tectonic regimes, and similar P-T conditions. The results from this study can provide a basis of comparison to determine regional extent of fluid flow and deformation. This may be combined with field observation and lab analysis of faults cutting the FCS into the Chiwaukum, perhaps involving a fluid inclusion study in the associated damage zones to compare to the observations made here.

References

- Abbas, H.F., Wan Daud, W.M.A., 2010. Hydrogen production by methane decomposition: A review. *International Journal of Hydrogen Energy* 35, 1160–1190.
- Ague, J.J., Brandon, M.T., 1996. Regional tilt of the Mount Stuart batholith, Washington, determined using aluminum-in-hornblende barometry: Implications for northward translation of Baja British Columbia. *Bulletin of the Geological Society of America* 108, 471–488.
- Allen, A.R., 1979. Mechanism of frictional fusion in fault zones. *Journal of Structural Geology* 1, 231–243.
- Allmendinger, R.W., Cardozo, N., Fisher, D.M., 2012. *Structural geology algorithms: Vectors and tensors in structural geology*. Cambridge University Press.
- Amin, A.M., Croiset, E., Epling, W., 2011. Review of methane catalytic cracking for hydrogen production. *International Journal of Hydrogen Energy* 36, 2904–2935.
- Andersen, T., Austrheim, H., Burke, E.A.J., 1990. Fluid inclusions in granulites and eclogites from the Bergen Arcs, Caledonides of W. Norway. *Mineralogical Magazine* 54, 145–158.
- Anderson, E.M., 1905. The Dynamics of Faulting. *Transcripts of the Edinburgh Geological Society* 8, 387–402.
- Bakker, R.J., 2009. Reequilibration of fluid inclusions: Bulk-diffusion. *Lithos* 112, 277–288.
- Bakker, R.J., 2003. Package FLUIDS 1. Computer programs for analysis of fluid inclusion data and for modelling bulk fluid properties. *Chemical Geology* 194, 3–23.
- Battles, D.A., Barton, M.D., 1995. Arc-related sodic hydrothermal alteration in the western US. *Geology* 23, 913–916.
- Berndt, M.E., Seyfried Jr., W.E., 1993. Calcium and sodium exchange during hydrothermal alteration of calcic plagioclase at 400° C and 400 bars. *Geochimica et Cosmochimica Acta* 57, 4445–4451.
- Bodnar, R.J., 2003. Introduction to Fluid Inclusions. In: Samson, I., Anderson, A., Marshall, D.

- (Eds.), *Fluid Inclusions: Analysis and Interpretation*. Mineralogical Association of Canada Short Course, Quebec, 1–8.
- Bodnar, R.J., 1993. Revised equation and table for determining the freezing point depression of H₂O-NaCl solutions. *Geochimica et Cosmochimica Acta* 57, 683–684.
- Bodnar, R.J., Binns, P.R., Hall, D.L., 1989. Synthetic fluid inclusions - VI. Quantitative evaluation of the decrepitation behaviour of fluid inclusions in quartz at one atmosphere confining pressure., *Journal of Metamorphic Geology*.
- Bodnar, R.J., Vityk, M.O., 1994. Interpretation of microthermometric data for H₂O-NaCl fluid inclusions. In: De Vivo, B., Frezzotti, M.L. (Eds.), *Fluid Inclusions in Minerals, Methods and Applications*. Virginia Tech, Blacksburg, VA, 117–130.
- Bos, B., Spiers, C.J., 2001. Experimental investigation into the microstructural and mechanical evolution of phyllosilicate-bearing fault rock under conditions favouring pressure solution. *Journal of Structural Geology* 23, 1187–1202.
- Bottrell, S.H., Carr, L.P., Dubessy, J., 1988. A nitrogen-rich metamorphic fluid and coexisting minerals in slates from North Wales. *Mineralogical Magazine* 52, 451–457.
- Boullier, A.M., 1999. Fluid inclusions: Tectonic indicators. *Journal of Structural Geology* 21, 1229–1235.
- Brown, E., Talbot, J.L., McClelland, W.C., Feltman, J.A., Lapen, T.J., Bennett, J.D., Hettinga, M.A., Troost, M.L., Alvarez, K.M., Calvert, A.T., 2000. Interplay of plutonism and regional deformation in an obliquely convergent arc, southern Coast Belt, British Columbia. *Tectonics* 19, 493–511.
- Brown, E.H., 1987. Structural geology and accretionary history of the Northwest Cascades system, Washington and British Columbia. *Geological Society Of America Bulletin* 99, 201–214.
- Brown, E.H., Talbot, J.L., 1989. Orogen-Parallel Extension in the North Cascades Crystalline Core, Washington. *Tectonics* 8, 1105–1114.

- Brown, E.H., Walker, N.W., 1993. A magma-loading model for Barrovian metamorphism in the southeast Coast Plutonic Complex, British Columbia and Washington. *Geological Society of America Bulletin* 105, 479–500.
- Bucher, K., Grapes, R., 2011. *Petrogenesis of Metamorphic Rocks*, 8th ed, Journal of Chemical Information and Modeling. Springer-Verlag, Berlin.
- Butler, R.F., Gehrels, G.E., Kodama, K.P., 2001. A Moderate Translation Alternative to the Baja British Columbia Hypothesis. *GSA Today* 11, 4.
- Byerlee, J., Summers, R., 1976. A note on the effect of fault gouge thickness on fault stability. *International Journal of Rock Mechanics and Mining Sciences and Geomechanics* 13, 35–36.
- Caine, J.S., Evans, J.P., Forster, C.B., 1996. Fault zone architecture and permeability structure. *Geology* 24, 1025–1028.
- Caine, J.S., Forster, C.B., 1999. Fault zone architecture and fluid flow: Insights from field data and numerical modeling. *Faults and Subsurface Fluid Flow in the Shallow Crust Geophysica*, 101–127.
- Cardozo, N., Allmendinger, R.W., 2013. Spherical projections with OSXStereonet. *Computers and Geosciences* 51, 193–205.
- Carten, R.B., 1986. Sodium-calcium metasomatism: chemical, temporal, and spatial relationships at the Yerington, Nevada porphyry copper deposit. *Economic Geology* 81, 1495–1519.
- Chester, F.M., Friedman, M., Logan, J.M., 1985. Foliated Cataclasites. *Tectonophysics* 111, 139–146.
- Collettini, C., Niemeijer, A., Viti, C., Marone, C., 2009. Fault zone fabric and fault weakness. *Nature* 462, 907–910.
- Coney, P.J., 1989. Structural aspects of suspect terranes and accretionary tectonics in western North America. *Journal of Structural Geology* 11, 107–125.

- Coney, P.J., 1987. The regional tectonic setting and possible causes of Cenozoic extension in the North American Cordillera. Geological Society, London, Special Publications 28, 177–186.
- Coney, P.J., Harms, T.A., 1984. Cordilleran metamorphic core complexes: Cenozoic extensional relics of Mesozoic compression. *Geology* 12, 550–554.
- Coney, P.J., Jones, D.L., Monger, J.W.H., 1980. Cordilleran Suspect Terranes. *Nature* 288.
- Cowan, D., Brandon, M.T., Garver, J.I., 1997. Geologic Tests of Hypothesis for Large Coastwise Displacement - A Critique Illustrated by the Baja British Columbia Controversy. *American Journal of Science* 297, 117–173.
- Cowan, D.S., 1999. Do faults preserve a record of seismic slip? A field geologist's opinion. *Journal of Structural Geology* 21, 995–1001.
- Cox, S.F., 1995. Faulting processes at high fluid pressures: An example of fault valve behavior from the Wattle Gully Fault, Victoria, Australia. *Journal of Geophysical Research* 100, 12841–12859.
- Crawford, M.L., Klepeis, K.A., Gehrels, G., Isachsen, C., 1999. Batholith emplacement at mid-crustal levels and its exhumation within an obliquely convergent margin. *Tectonophysics* 312, 57–78.
- Crider, J.G., 2015. The initiation of brittle faults in crystalline rock. *Journal of Structural Geology* 77, 159–174.
- Davis, G.H., Reynolds, S.J., 1996. *Structural Geology of Rocks and Regions*, 2nd ed. John Wiley & Sons, Inc., New York.
- Diamond, L.W., 2003. Introduction to gas-bearing, aqueous fluid inclusions. In: Samson, I., Anderson, A., Marshall, D. (Eds.), *Fluid Inclusions: Analysis and Interpretation*. Mineralogical Association of Canada Short Course, Quebec, 101–158.
- Di Toro, G., Pennacchioni, G., 2005. Fault plane processes and mesoscopic structure of a strong-type seismogenic fault in tonalites (Adamello batholith, Southern Alps).

- Tectonophysics 402, 55–80.
- Di Toro, G., Pennacchioni, G., 2004. Superheated friction-induced melts in zoned pseudotachylytes within the Adamello tonalites (Italian Southern Alps). *Journal of Structural Geology* 26, 1783–1801.
- Dickinson, W.R., 2004. Evolution of the North American Cordillera. *Annual Review of Earth and Planetary Sciences* 32, 13–45.
- Dong, G., Morrison, G.W., 1995. Adularia in epithermal veins, Queensland: morphology, structural state and origin. *Mineralium Deposita* 30, 11–19.
- Dobrovine, P. V., Tarduno, J.A., 2008. A revised kinematic model for the relative motion between Pacific oceanic plates and North America since the Late Cretaceous. *Journal of Geophysical Research: Solid Earth* 113, 1–20.
- Dreher, A., Vlach, S., Martini, S., 1998. Adularia associated with epithermal gold veins in the Tapajós Mineral Province, Pará state, northern Brazil. *Brazilian Journal of Geology* 28, 397–404.
- Duit, W., Jansen, B.H., van Breemen, A., Bos, A., 1986. Ammonium micas in metamorphic rocks as exemplified by Dome de l'Agout (France). *American Journal of Science* 286, 702–732.
- Enami, M., Liou, J.G., Bird, D.K., 1992. Cl-bearing amphibole in the Salton Sea geothermal system, California. *Canadian Mineralogist* 30, 1077–1092.
- Engebretson, D., Cox, A., Gordon, R., 1985. Relative motions between oceanic and continental plates in the Pacific Basin. *Geological Society of America Special Papers* 206, 59.
- Engels, J.C., Tabor, R.W., Miller, F.K., Obradovich, J.D., 1976. Summary of K-Ar, Rb-Sr, U-Pb, Pb-alpha, and fission-track ages for rocks from Washington State prior to 1975 (exclusive of Columbia Plateau basalts): U.S. Geological Survey Miscellaneous Field Studies Map MF-710.
- Engvik, A.K., Putnis, A., Gerald, J.D.F., Austrheim, H., 2008. Albitization of Granitic Rocks: the

- Mechanism of Replacement of Oligoclase By Albite. *The Canadian Mineralogist* 46, 1401–1415.
- Ennis, D.J., Dunbar, N.W., Campbell, a. R., Chapin, C.E., 2000. The effects of K-metasomatism on the mineralogy and geochemistry of silicic ignimbrites near Socorro, New Mexico. *Chemical Geology* 167, 285–312.
- Evans, J.P., Chester, F.M., 1995. Fluid-rock interaction in faults of the San Andreas system: Inferences from San Gabriel fault rock geochemistry and microstructures., *Journal of Geophysical Research*.
- Fagereng, A., Toy, V.G., 2011. *Geology of the earthquake source: an introduction*. Geological Society, London, Special Publications 359, 1–16.
- Fang, Z., Dunham, E.M., 2013. Additional shear resistance from fault roughness and stress levels on geometrically complex faults. *Journal of Geophysical Research: Solid Earth* 118, 3642–3654.
- Ford, A.B., Drinkwater, J.L., Garwin, S.L., 1988a. Petrographic data for plutonic rocks and gneisses of the Glacier peak Wilderness and vicinity, northern Cascades, Washington. USGS Open File Report.
- Ford, A.B., Senterfit, R.M., Flanigan, V.J., 1988b. Magnetic susceptibility and density determinations for plutonic and metamorphic rocks of the Glacier Peak Wilderness and vicinity, northern Cascades, Washington. USGS Open File Report 86, 35.
- Fossen, H., Tikoff, B., 1998. Extended models of transpression and transtension, and application to tectonic settings. Geological Society, London, Special Publications 135, 15–33.
- Gardien, V., Thompson, A.B., Ulmer, P., 2000. Melting of Biotite + Plagioclase + Quartz Gneisses: the Role of H₂O in the Stability of Amphibole. *Journal of Petrology* 41, 651–666.
- Goldsmith, J.R., Petersen, J.W., 1990. Hydrothermal melting behavior of KAlSi₃O₈ as microcline and sanidine. *American Mineralogist* 75, 1362–1369.

- Goldstein, R.H., Reynolds, T.J., 1994. Systematics of fluid inclusions in diagenetic minerals, Society for Sedimentary Geology.
- Gordon, S.M., Bowring, S. a., Whitney, D.L., Miller, R.B., McLean, N., 2010. Time scales of metamorphism, deformation, and crustal melting in a continental arc, North Cascades USA. *Bulletin of the Geological Society of America* 122, 1308–1330.
- Gratier, J.P., Renard, F., Labaume, P., 1999. How pressure solution creep and fracturing processes interact in the upper crust to make it behave in both a brittle and viscous manner. *Journal of Structural Geology* 21, 1189–1197.
- Griffith, W.A., 2016. How Dynamic Weakening Makes Faults Stronger: The Role Of Melting In Post-Seismic Healing. *Geology* 44, 1063–1064.
- Griffith, W.A., Di Toro, G., Pennacchioni, G., Pollard, D.D., 2008. Thin pseudotachylytes in faults of the Mt. Abbot quadrangle, Sierra Nevada: Physical constraints for small seismic slip events. *Journal of Structural Geology* 30, 1086–1094.
- Groshong, R.H., 1988. Low Temperature Deformation Mechanisms and their Interpretation. *Geological Society of America Bulletin* 100, 1329–1360.
- Guilbert, J.M., Park, Jr., C.F., 1986. *The Geology of Ore Deposits*. Freeman & Company, New York.
- Hall, D.L., Sterner, S.M., Bodnar, R.J., 1988. Freezing point depression of NaCl-KCl-H₂O solutions. *Economic Geology* 83, 197–202.
- Harlov, D., Austrheim, H., 2013. *Metasomatism and the Chemical Transformation of Rock*. Springer.
- Harrison, T., 1981. Diffusion of ⁴⁰Ar in hornblende. *Contributions to Mineralogy and Petrology* 78, 324–331.
- Harrison, T.M., Duncan, I., McDougall, I., 1985. Diffusion of ⁴⁰Ar in biotite: Temperature, pressure and compositional effects. *Geochimica et Cosmochimica Acta* 49, 2461–2468.
- Haugerud, R., Van Der Heyden, P., Tabor, R.W., Stacey, J.S., Zartman, R.E., 1991. Late

- Cretaceous and early Tertiary plutonism and deformation in the Skagit Gneiss Complex, north Cascade Range, Washington and British Columbia. *Geological Society of America Bulletin* 103, 1297–1307.
- Hawke, M.M., Leach, T., Thompson, J.F.H., 1996. Actinolite. In: Thompson, A.J.B., Thompson, J.F.H. (Eds.), *Atlas of Alteration: A Field and Petrographic Guide to Hydrothermal Alteration Minerals*. Geological Association of Canada, Mineral Deposits Division, 14–15.
- Hemley, J.J., Jones, W.R., 1964. Chemical aspects of hydrothermal alteration with emphasis on hydrogen metasomatism. *Economic Geology* 59, 538–569.
- Hirth, G., Tullis, J., 1992. Dislocation creep regimes in quartz aggregates. *Journal of Structural Geology* 14, 145–159.
- Housen, B.A., Beck, J.E., Burmester, R.F., Fawcett, T., Petro, G., Sargent, R., Addis, K., Curtis, K., Ladd, J., Liner, N., Molitor, B., Montgomery, T., Mynatt, I., Palmer, B., Tucker, D., White, I., 2003. Paleomagnetism of the Mount Stuart batholith revisited again: What has been learned since 1972? *American Journal of Science* 303, 263–299.
- Huff, T.A., Nabelek, P.I., 2007. Production of carbonic fluids during metamorphism of graphitic pelites in a collisional orogen—An assessment from fluid inclusions. *Geochimica et Cosmochimica Acta* 71, 4997–5015.
- Ikari, M.J., Niemeijer, A.R., Marone, C., 2011. The role of fault zone fabric and lithification state on frictional strength, constitutive behavior, and deformation microstructure. *Journal of Geophysical Research: Solid Earth* 116, 1–25.
- Jacobson, R.T., Stewart, R.B., Jahangiri, M., 1986. Thermodynamic Properties of Nitrogen from the Freezing Line to 2000 K at Pressures to 1000 MPa. *Journal of Physical and Chemical Reference Data* 15.
- Jefferies, S.P., Holdsworth, R.E., Shimamoto, T., Takagi, H., Lloyd, G.E., Spiers, C.J., 2006. Origin and mechanical significance of foliated cataclastic rocks in the cores of crustal-scale faults: Examples from the Median Tectonic Line, Japan. *Journal of Geophysical Research:*

Solid Earth 111, 1–17.

Klepeis, K.A., Crawford, M.L., 1999. High-temperature arc-parallel normal faulting and transtension at the roots of an obliquely convergent orogen. *Geology* 27, 7–10.

Kronenberg, A.K., Kirby, S.H., Pinkston, J., 1990. Basal slip and mechanical anisotropy of biotite. *Journal of Geophysical Research* 95, 19257.

Lawther, S.E.M., Dempster, T.J., Shipton, Z.K., Boyce, A.J., 2016. Effective crustal permeability controls fault evolution: An integrated structural, mineralogical and isotopic study in granitic gneiss, Monte Rosa, northern Italy. *Tectonophysics* 690, 160–173.

Lespinasse, M., 1999. Are fluid inclusion planes useful in structural geology? *Journal of Structural Geology* 21, 1237–1243.

Lespinasse, M., Cathelineau, M., 1995. Paleostress magnitudes determination by using fault slip and fluid inclusions planes data. *Journal of Geophysical Research* 100, 3895.

Lin, A., 2001. S-C fabrics developed in cataclastic rocks from the Nojima fault zone, Japan and their implications for tectonic history. *Journal of Structural Geology* 23, 1167–1178.

Lin, A., 1999. S-C cataclasite in granitic rock. *Tectonophysics* 304, 257–273.

Liu, M., 2001. Cenozoic extension and magmatism in the North American Cordillera: The role of gravitational collapse. *Tectonophysics* 342, 407–433.

Lloyd, G.E., Butler, R.W.H., Casey, M., Mainprice, D., 2009. Mica, deformation fabrics and the seismic properties of the continental crust. *Earth and Planetary Science Letters* 288, 320–328.

Magloughlin, J.F., 2011. Bubble collapse structure: A microstructural record of fluids, bubble formation and collapse, and mineralization in pseudotachylyte. *Journal of Geology* 119, 351–371.

Magloughlin, J.F., 2005. Immiscible sulfide droplets in pseudotachylyte: Evidence for high temperature (1200 C) melts. *Tectonophysics* 402, 81–91.

Magloughlin, J.F., 1993. A Nason Terrane trilogy; I, Nature and significance of pseudotachylyte;

- II, Summary of the structural and tectonic history; III, Major and trace element geochemistry and strontium and neodymium isotope geochemistry of the Chiwaukum Schist, amphibolite, an. University of Minnesota.
- Magloughlin, J.F., 1992. Microstructural and chemical changes associated with cataclasis and frictional melting at shallow crustal levels: the cataclasite-pseudotachylyte connection. *Tectonophysics* 204, 243–260.
- Magloughlin, J.F., 1989. The nature and significance of pseudotachylyte from the Nason terrane, North Cascade Mountains, Washington. *Journal of Structural Geology* 11, 907–917.
- Magloughlin, J.F., Spray, J.G., 1992. Frictional melting processes and products in geological materials: introduction and discussion. *Tectonophysics* 204, 197–204.
- Mares, V.M., Kronenberg, A.K., 1993. Experimental deformation of muscovite. *Journal of Structural Geology* 15, 1061–1075.
- Marone, C., 1995. Fault Zone Strength and Failure Criteria. *Geophysical Research Letters* 22, 723–726.
- Matzel, J.E.P., 2004. Rates of tectonic and magmatic processes in the North Cascades continental magmatic arc. Massachusetts Institute of Technology.
- Matzel, J.E.P., Bowring, S.A., Miller, R.B., 2006. Time scales of pluton construction at differing crustal levels: Examples from the Mount Stuart and Tenpeak intrusions, North Cascades, Washington. *Bulletin of the Geological Society of America* 118, 1412–1430.
- McCormick, K.A., McDonald, A.M., 1999. Chlorine-bearing amphiboles from the Fraser mine, Sudbury, Ontario, Canada: Description and crystal chemistry. *Canadian Mineralogist* 37, 1385–1403.
- McDougall, I., Harrison, T., 1990. *Geochronology and Thermochronology by the $^{40}\text{Ar}/^{39}\text{Ar}$ method*. Oxford University Press, New York.
- Menzies, C.D., Teagle, D.A.H., Craw, D., Cox, S.C., Boyce, A.J., Barrie, C.D., Roberts, S.,

2014. Incursion of meteoric waters into the ductile regime in an active orogen. *Earth and Planetary Science Letters* 399, 1–13.
- Micklethwaite, S., Cox, S.F., 2006. Progressive fault triggering and fluid flow in aftershock domains: Examples from mineralized Archaean fault systems. *Earth and Planetary Science Letters* 250, 318–330.
- Miller, R., Paterson, S., Matzel, J., 2009. Plutonism at different crustal levels: insights from the ~5-40 km (paleodepth) North Cascades crustal section, Washington. *Geological Society of America Special Paper* 456, 125–149.
- Miller, R.B., Bowring, S.A., 1990. Structure and chronology of the Oval Peak Batholith and adjacent rocks: implications for the Ross Lake Fault Zone, North Cascades, Washington. *Geological Society of America Bulletin* 102, 1361–1377.
- Miller, R.B., Brown, E.H., McShane, D.P., Whitney, D.L., 1993. Intra-arc crustal loading and its tectonic implications, North Cascades crystalline core, Washington and British Columbia. *Geology* 21, 255.
- Miller, R.B., Paterson, S.R., 2001. Influence of lithological heterogeneity, mechanical anisotropy, and magmatism on the rheology of an arc, North Cascades, Washington. *Tectonophysics* 342, 351–370.
- Miller, R.B., Paterson, S.R., Lebit, H., Alsleben, H., Lüneburg, C., 2006. Significance of composite lineations in the mid- to deep crust: A case study from the North Cascades, Washington. *Journal of Structural Geology* 28, 302–322.
- Misch, P., 1966. Tectonic evolution of the Northern Cascades of Washington State. *Tectonic History and Mineral Deposits of the Western Cordillera* 8, 101–148.
- Mitchell, T.M., Toy, V., Di Toro, G., Renner, J., Sibson, R.H., 2016. Fault welding by pseudotachylyte formation. *Geology* G38373.1.
- Mitterpergher, S., Dallai, L., Pennacchioni, G., Renard, F., Di Toro, G., 2014. Origin of hydrous fluids at seismogenic depth: Constraints from natural and experimental fault rocks. *Earth*

- and Planetary Science Letters 385, 97–109.
- Monger, J.W.H., Price, R. a., Tempelman-Kluit, D.J., 1982. Tectonic accretion and the origin of the two major metamorphic and plutonic belts in the Canadian Cordillera. *Geology* 10, 70–75.
- Morad, S., El-Ghali, Caja, Sirat, Al-Ramadan, Mansurbeg, 2010. Hydrothermal Alteration of Plagioclase in Granitic Rocks from Proterozoic Basement of SE Sweden. *Geological Journal* 45, 105–116.
- Morikiyo, T., 1986. Hydrogen and carbon isotope studies on the graphite-bearing metapelites in the northern Kiso district of central Japan. *Contributions to Mineralogy and Petrology* 94, 165–177.
- Oberti, R., Ungaretti, L., Cannillo, E., Hawthorne, F.C., 1993. The mechanism of Cl incorporation in amphibole. *American Mineralogist* 78, 746–752.
- Orville, P.M., 1963. Alkali ion exchange between vapor and feldspar phases., *American Journal of Science*.
- Pascal, M., Boiron, M.-C., Ansdell, K., Annesley, I.R., Kotzer, T., Jiricka, D., Cuney, M., 2016. Fluids preserved in variably altered graphitic pelitic schists in the Dufferin Lake Zone, south-central Athabasca Basin, Canada: implications for graphite loss and uranium deposition. *Mineralium Deposita* 51, 619–636.
- Passchier, C.W., Trouw, R.A.J., 2005. *Microtectonics*, Second Edi. ed. Springer-Verlag, Berlin.
- Paterson, S.R., Miller, R.B., Alsleben, H., Whitney, D.L., Valley, P.M., Hurlow, H., 2004. Driving mechanisms for 40 km of exhumation during contraction and exhumation in a continental arc, Cascades core, Washington. *Tectonics* 23.
- Paterson, S.R., Tobisch, O.T., 1988. Using pluton ages to date regional deformations: Problems with commonly used criteria. *Geology* 16, 1108–1111.
- Paterson, S.R., Vernon, R.H., Tobisch, O.T., 1989. A review of criteria for the identification of magmatic and tectonic foliations in granitoids. *Journal of Structural Geology* 11, 349–363.

- Pennacchioni, G., Di Toro, G., Brack, P., Menegon, L., Villa, I.M., 2006. Brittle-ductile-brittle deformation during cooling of tonalite (Adamello, Southern Italian Alps). *Tectonophysics* 427, 171–197.
- Pollard, D.D., Aydin, A., 1988. Progress in understanding jointing over the past century. *Geological Society of America Bulletin* 100, 1181–1204.
- Prante, M.R., Evans, J.P., 2015. Pseudotachylyte and Fluid Alteration at Seismogenic Depths (Glacier Lakes and Granite Pass Faults, Central Sierra Nevada, USA). *Pure and Applied Geophysics* 172, 1203–1227.
- Proctor, B., Lockner, D.A., 2016. Pseudotachylyte increases the post-slip strength of faults. *Geology* 44, G38349.1.
- Que, M., Allen, A., 1996. Sericitization of Plagioclase in the Rosses Granite Complex, Co. Donegal, Ireland. *Mineralogical Magazine* 60, 927–936.
- Raleigh, C.B., Healy, J.H., Bredehoeft, J.D., 1976. An Experiment in Earthquake Control at Rangely, Colorado. *Science* 191, 1230–1237.
- Raszewski, D.A., 2005. Metamorphism, lithologic relations, and structural architecture of the White River Shear Zone, North Cascade Mountains, Washington. Colorado State University.
- Reyes, A.G., 1990. Petrology of Philippine geothermal systems and the application of alteration mineralogy to their assessment. *Journal of Volcanology and Geothermal Research* 43, 279–309.
- Roedder, E., 1972. Composition of Fluid Inclusions. In: Fleischer, M. (Ed.), *Geological Survey Professional Paper: Data of Geochemistry*. 1689–1699.
- Rowe, C.D., Griffith, W.A., 2015. Do faults preserve a record of seismic slip: A second opinion. *Journal of Structural Geology* 78, 1–26.
- Rowe, C.D., Meneghini, F., Moore, J.C., 2011. Textural record of the seismic cycle: strain-rate

- variation in an ancient subduction thrust. Geological Society, London, Special Publications 359, 77–95.
- Rowe, C.D., Moore, J.C., Meneghini, F., McKeirnan, A.W., 2005. Large-scale pseudotachylytes and fluidized cataclasites from an ancient subduction thrust fault. *Geology* 33, 937–940.
- Rubin, C., Saleeby, J., Cowan, D., 1990. Regionally extensive mid-Cretaceous west-vergent thrust system in the northwestern Cordillera: Implications for continent-margin tectonism., *Geology*.
- Sagy, A., Brodsky, E.E., Axen, G.J., 2007. Evolution of fault-surface roughness with slip. *Geology* 35, 283–286.
- Saleeby, J., 1983. Accretionary Tectonics of the North American Cordillera. *Annual Review of Earth and Planetary Sciences* 15, 45–73.
- Sandström, B., Annersten, H., Tullborg, E.L., 2010. Fracture-related hydrothermal alteration of metagranitic rock and associated changes in mineralogy, geochemistry and degree of oxidation: A case study at Forsmark, central Sweden. *International Journal of Earth Sciences* 99, 1–25.
- Schmidt, M.W., Poli, S., 2004. Magmatic Epidote. *Reviews in Mineralogy and Geochemistry* 56, 399–430.
- Scholz, C.H., 1988. The brittle-plastic transition and the depth of seismic faulting. *Geologische Rundschau* 77, 319–328.
- Scruggs, V.J., Tullis, T.E., 1998. Correlation between velocity dependence of friction and strain localization in large displacement experiments on feldspar, muscovite and biotite gouge. *Tectonophysics* 295, 15–40.
- Setzmann, U., Wagner, W., 1991. A New Equation of State and Tables of Thermodynamic Properties for Methane Covering the Range from the Melting Line to 625 K at Pressures up to 1000 MPa. *Journal of Physical and Chemical Reference Data* 20, 1061–1151.
- Shea, W.T., Kronenberg, A.K., 1993. Strength and anisotropy of foliated rocks with varied mica

- contents. *Journal of Structural Geology* 15, 1097–1121.
- Shimizu, I., 1995. Kinetics of pressure solution creep in quartz: theoretical considerations. *Tectonophysics* 245, 121–134.
- Sibson, R.H., 1996. Structural permeability of fluid-driven fault-fracture meshes. *Journal of Structural Geology* 18, 1031–1042.
- Sibson, R.H., 1992a. Implications of fault-valve behaviour for rupture nucleation and recurrence. *Tectonophysics* 211, 283–293.
- Sibson, R.H., 1992b. Fault-valve behavior and the hydrostatic-lithostatic fluid pressure interface. *Earth Science Reviews* 32, 141–144.
- Sibson, R.H., 1990. Rupture nucleation on unfavorably oriented faults. *Bulletin of the Seismological Society of America* 80, 1580–1604.
- Sibson, R.H., 1985. A note on fault reactivation. *Journal of Structural Geology* 7, 751–754.
- Sibson, R.H., 1977. Fault rocks and fault mechanisms. *Journal of the Geological Society* 133, 191–213.
- Sibson, R.H., 1975. Generation of Pseudotachylyte by Ancient Seismic Faulting. *Geophysical Journal of the Royal Astronomical Society* 43, 775–794.
- Sibson, R.H., Toy, V.G., 2006. The Habitat of Fault-Generated Pseudotachylyte : Presence vs . Absence of Friction-Melt. *Geophysical Monograph Series* 153–166.
- Sisson, V.B., Hollister, L.S., 1990. A fluid-inclusion study of metamorphosed pelitic and carbonate rocks, south-central Maine. *American Mineralogist* 75, 59–70.
- Steele-MacInnis, M., Ridley, J., Lecumberri-Sanchez, P., Schlegel, T.U., Heinrich, C.A., 2016. Application of low-temperature microthermometric data for interpreting multicomponent fluid inclusion compositions. *Earth-Science Reviews* 159, 14–35.
- Steiner, A., 1970. Genesis of hydrothermal K-feldspar (adularia) in an active geothermal environment at Wairakei, New Zealand. *Mineralogical Magazine* 37, 916–922.
- Sterner, S.M., Bodnar, R.J., 1989. Synthetic fluid inclusions - VII. Re-equilibration of fluid

- inclusions in quartz during laboratory-simulated metamorphic burial and uplift., *Journal of Metamorphic Geology*.
- Stipp, M., Stünitz, H., Heilbronner, R., Schmid, S.M., 2002. The eastern Tonale fault zone: A “natural laboratory” for crystal plastic deformation of quartz over a temperature range from 250 to 700 °C. *Journal of Structural Geology* 24, 1861–1884.
- Suwa, K., Enami, M., Horiuchi, T., 1987. Chlorine-rich potassium hastingsite from West Ongul Island, Luetzow-Holm Bay, East Antarctica. *Mineral. Mag.* 51, 709–714.
- Swanson, M.T., 1988. Pseudotachylyte-bearing strike-slip duplex structures in the Fort Foster Brittle Zone, S. Maine. *Journal of Structural Geology* 10, 813–828.
- Tabor, R.W., Booth, D.B., Vance, J.A., Ford, A.B., 2002a. Description to Accompany Geologic Map of the Sauk River 30- By 60-Minute Quadrangle , Washington. USGS Map.
- Tabor, R.W., Booth, D.B., Vance, J.A., Ford, A.B., 2002b. Geologic Map of the Sauk River 30- by 60- Minute Quadrangle, Washington, USGS Map.
- Tabor, R.W., Haugerud, R.H., Brown, E.H., Babcock, R.S., Miller, R.B., Range, N.C., 1989. Accreted Terranes of the North Cascades Range, Washington.
- Torabi, A., Berg, S.S., 2011. Scaling of fault attributes: A review. *Marine and Petroleum Geology* 28, 1444–1460.
- Tullis, J., Yund, R. a., 1977. Experimental deformation of dry westerly granite. *Journal of Geophysical Research* 82, 5705.
- Tulloch, A.J., 1986. Comments and Reply on Zen’s “Implications of magmatic epidote-bearing plutons on crustal evolution in the accreted terranes of northwestern North America” and “Magmatic epidote and its petrologic significance.” *Geology* 14, 186–187.
- Valley, P.M., Whitney, D.L., Paterson, S.R., Miller, R.B., Alsleben, H., 2003. Metamorphism of the deepest exposed arc rocks in the Cretaceous to Paleogene Cascades belt, Washington: Evidence for large-scale vertical motion in a continental arc. *Journal of Metamorphic Geology* 21, 203–220.

- Van den Kerkhof, A., Thiery, R., 2001. Carbonic inclusions. *Lithos* 55, 49–68.
- Vanko, D.A., 1986. High-chlorine amphiboles from oceanic rocks: product of highly-saline hydrothermal fluids? *American Mineralogist* 71, 51–59.
- Veblen, D.R., Ferry, J.M., 1983. A TEM study of the biotite-chlorite reaction and comparison with petrologic observations. *American Mineralogist* 68, 1160–1168.
- Vry, J., Powell, R., Golden, K., Petersen, K., 2010. The role of exhumation in metamorphic dehydration and fluid production. *Nature Geoscience* 3, 31–35.
- Wells, R.E., Heller, P.L., 1988. The Relative Contribution of Accretion, Shear, and Extension to Cenozoic Tectonic Rotation in the Pacific Northwest. *Geological Society Of America Bulletin* 100, 325–338.
- Wenk, H.R., Johnson, L.R., Ratschbacher, L., 2000. Pseudotachylites in the Eastern Peninsular Ranges of California. *Tectonophysics* 321, 253–277.
- Weyl, P.K., 1959. Pressure solution and the force of crystallization: a phenomenological theory. *Journal of Geophysical Research* 64, 2001–2025.
- White, L.D., Maley, C.A., Barnes, I., Ford, A.B., 1988. Oxygen isotopic data for plutonic rocks and gneisses of the Glacier Peak Wilderness and vicinity, northern Cascades, Washington. USGS Open File Report Open-File Report.
- White, S.R., 2001. Textural and microstructural evidence for evidence for semi-brittle flow in natural fault rocks with varied mica contents. *International Journal of Earth Sciences* 90, 14–27.
- Whitney, D.L., Miller, R.B., Paterson, S.R., 1999. P-T-t evidence for mechanisms of vertical tectonic motion in a contractional orogen: North-western US and Canadian Cordillera. *Journal of Metamorphic Geology* 17, 75–90.
- Wibberley, C., 1999. Are feldspar-to-mica reactions necessarily reaction-softening processes in fault zones? *Journal of Structural Geology* 21, 1219–1227.
- Wintsch, R.P., 1975. Feldspathization as a result of deformation. *Geological Society of America*

Bulletin 86, 35–38.

Wintsch, R.P., Christoffersen, R., Kronenberg, A.K., 1995. Fluid-rock reaction weakening of fault zones. *Journal of Geophysical Research* 100, 13021–13032.

Wise, D.U., Dunn, D.E., Engelder, J.T., Geiser, P.A., Hatcher, R.D., Kish, S.A., Odom, L.A., Schamel, S., 1984. Fault-related rocks: Suggestions for terminology. *Geology* 12, 391–394.

Woodcock, N.H., Mort, K., 2008. Classification of fault breccias and related fault rocks. *Geological Magazine* 145, 435–440.

Wyld, S.J., Umhoefer, P.J., Wright, J.E., 2006. Reconstructing northern Cordilleran terranes along known Cretaceous and Cenozoic strike-slip faults : Implications for the Baja British Columbia hypothesis and other models. *Paleogeography of the North American Cordillera: Evidence For and Against Large-Scale Displacements*. Geological Association of Canada, Special Paper 46 277–298.

Yardley, B.W.D., Bodnar, R.J., 2014. Fluids in the continental crust. *Geochemical Perspectives* 3, 1–127.

Zaggle, R., 2015. Petrogenetic Analysis of the Wenatchee Ridge Orthogneiss in the North Cascade Mountains, Washington State. Colorado State University.

Zen, E., 1985. Implications of magmatic epidote-bearing plutons on crystal evolution in the accreted terranes of northwestern North America. *Geology* 13, 266–269.

Zen, E., Hammarstrom, J., 1984. Magmatic epidote and its petrologic significance. *Geology* 12, 515–518.

Appendices

Appendix A. Sample and Structural Data

Table A.1. GPS coordinates of in situ sample locations.

Sample #	Latitude	Longitude
AK103-1	48.05146	-121.12332
AK105-1	48.05437	-121.12368
AK105-2	48.05509	-121.12386
AK105-3	48.05559	-121.12334
AK105-4	48.05561	-121.12184
AK105-5	48.05598	-121.12116
AK106-1	48.05767	-121.11889
AK106-2	48.05778	-121.11799
AK106-2u	48.05744	-121.11804
AK106-3	48.05693	-121.11836
AK106-4	48.05621	-121.11891
AK107-1	48.05430	-121.12039
AK107-2	48.05322	-121.12391
AK107-3	48.05370	-121.12151
AK107-4	48.05319	-121.12122
AK108-1	48.05866	-121.11768
AK108-2	48.05894	-121.11806
AK109-3	48.05427	-121.12378
AK110-1	48.05780	-121.12180
AK110-2	48.05724	-121.12232
AK111-1	48.05686	-121.12010
AK111-2	48.05625	-121.11995
AK112-2	48.05205	-121.12256

Table A.2. Orientations of biotite-defined foliations in the Foam Creek Stock. Right Hand Rule.

Measurement #	Strike	Dip
1	065	50
2	020	70
3	044	25
4	065	35
5	042	40
6	100	18
7	010	35
8	080	35
9	025	50
10	035	55
11	010	60
12	025	40
13	030	70
14	070	40
15	025	45
16	035	80
17	050	30
18	065	65
19	065	30
20	045	55
21	048	55
22	050	45
23	045	28
24	070	55
25	032	35
26	042	49

Table A.3. Orientations of faults belonging to the P1 population. Right Hand Rule. Bold sample name indicates sample was used for fluid inclusion analysis.

Measurement #	Strike	Dip	Associated Sample?
1	009	33	
2	012	25	
3	012	25	AK106-2
4	014	33	
5	010	33	
6	170	76	
7	048	86	
8	021	14	
9	055	70	
10	026	31	
11	010	29	
12	275	44	
13	056	57	
14	044	80	
15	013	72	
16	055	55	
17	149	87	
18	060	57	
19	006	43	
20	278	84	
21	012	25	AK106-2u
22	012	25	
23	175	25	
24	200	40	
25	015	25	AK111-1
26	005	40	
27	020	25	AK107-2
28	015	45	AK107-3
29	009	30	AK107-4
30	010	30	AK108-2
31	015	40	
32	015	25	
33	011	40	
34	005	28	

Table A.4. Orientations of faults belonging to the P2 population. Right Hand Rule. Bold sample name indicates sample was used for fluid inclusion analysis.

Measurement #	Strike	Dip	Sample?	Measurement #	Strike	Dip	Sample?
1	265	37		41	070	77	
2	220	33		42	285	35	
3	288	44		43	085	60	
4	264	57		44	075	70	
5	275	37		45	153	56	
6	270	33	AK106-2u	46	147	48	
7	197	41		47	001	40	
8	264	71		48	070	76	
9	274	60		49	064	84	
10	274	74		50	265	45	
11	272	47		51	242	35	
12	287	69		52	010	42	
13	305	75		53	015	30	
14	340	79		54	011	36	
15	250	41		55	285	25	
16	265	41		56	010	10	
17	140	64		57	075	70	
18	238	67		58	071	70	
19	286	54		59	080	61	
20	253	64		60	065	55	
21	320	74		61	075	79	
22	087	84		62	068	68	
23	300	77	AK109-3	63	090	70	
24	257	39		64	075	74	
25	250	41		65	045	65	
26	098	87		66	072	65	
27	280	90		67	070	62	
28	143	63		68	070	70	
29	293	84		69	060	62	
30	189	45		70	081	79	
31	258	71		71	097	53	
32	022	34		72	075	54	
33	253	45		73	069	83	
34	261	56		74	067	57	
35	187	49		75	053	60	
36	255	76		76	065	16	
37	260	27		77	057	62	
38	275	50		78	066	58	
39	200	53		79	040	47	
40	261	45	AK105-5	80	073	57	
41	070	77		81	016	60	
42	285	35		82	070	53	
43	085	60		83	057	66	
44	075	70		84	073	67	
45	153	56		85	088	75	

Measurement #	Strike	Dip	Sample?	Measurement #	Strike	Dip	Sample?
86	071	74		133	356	39	
87	059	77		134	345	31	
88	075	78		135	351	38	
89	076	75		136	091	45	
90	011	82		137	341	40	
91	063	83		138	354	37	
92	077	63		139	131	47	
93	077	56		140	355	37	
94	071	61		141	275	68	
95	001	32		142	277	79	
96	263	45	AK108-1	143	056	90	
97	068	47		144	235	88	
98	011	44		145	085	84	
99	277	37		146	282	78	
100	260	51		147	350	41	
101	013	35		148	358	43	
102	058	78		149	100	90	
103	120	64		150	058	90	
104	055	76		151	277	77	
105	259	87		152	353	40	
106	016	40	AK103-1	153	350	44	
107	073	67		154	030	60	
108	064	66		155	030	80	
109	065	78		156	265	50	
110	063	87		157	280	45	AK105-1
111	055	80		158	256	46	
112	207	80		159	264	44	
113	087	58		160	263	74	
114	245	64		161	267	74	
115	067	78		162	267	82	
116	078	60		163	267	46	
117	255	57		164	275	40	AK106-1
118	245	69		165	090	33	
119	247	78		166	090	35	AK106-3
120	230	65		167	265	35	AK106-4
121	244	73		168	090	45	
122	237	76		169	285	45	AK105-2
123	089	60		170	280	40	AK105-3
124	227	86		171	245	45	AK107-1
125	244	69		172	300	77	
126	235	61		173	087	84	
127	353	41		174	020	33	
128	279	77		175	280	30	
129	183	37		176	275	45	AK105-4
130	119	17		177	165	40	
131	032	54		178	230	40	AK110-1
132	349	50		179	070	85	

Measurement #	Strike	Dip	Sample?
180	280	85	AK112-2
181	110	65	
182	045	65	
183	255	85	
184	135	65	
185	250	65	
186	265	85	
187	045	65	
188	310	75	
189	300	67	
190	260	70	
191	262	75	

Table A.5. Offsets observed in the field and in thin section, showing orientation of the offsetting fault, sense of offset, amount of offset, and the feature that was observed to be offset by the fault, if applicable.

Fault Population	Sample/Photo #	Strike	Dip	Dip Direction	Offset Sense	Amount of Offset (cm)	Notes	Method of Observation
P1	111-1B	15	25	SE	Reverse			Microscope
	107-3AL	10	15	SE	LL			Microscope
	107-4AA	9	30	SE	RL			Microscope
	Photo # 420	12	27	SE	Reverse	1	Offset Aplite Dike	Field
	Photo # 767	5	28	SE	LL	2	Offsetting Qtz	Field
P2	105-2B	280	45	NE	Normal			Microscope
	106-1B	275	40	NE	Normal			Microscope
	105-1	280	45	NE	Normal+LL		Weak Foliation	Microscope
	106-2u	270	30	N	Normal+LL		Medium Foliation	Microscope
	106-3	270	35	N	Normal+LL		Medium Foliation	Microscope
	106-4A	270	35	N	LL		Random Fabric	Microscope
	107-1A	245	45	NW	LL		Medium Foliation	Microscope
	108-1	270	45	N	Normal+LL		Random Fabric	Microscope
	110-1	280	30	NE	Normal+LL		Medium Foliation	Microscope
	112-2	280	85	NE	Normal+LL		Strong Foliation	Microscope
	Photo # 440	275	70	NE	Normal		Offsetting P1	Field
	Photo # 378	270	33	N	Normal	35	Offsetting P1	Field
	Photo # 352	275	45	NE	Normal	16	Offsetting P1	Field
	Photo # 484	280	40	NE	Normal	15	Offsetting P1	Field
	Photo # 111	30	60	SE	Normal	11	Aplite Dike offset	Field
	Photo # 439	270	45	N	Normal	19	Offsetting 2 aplite dikes	Field
	Photo # 443	285	45	NE	Normal	2.5	Offsetting P1	Field
	Photo # 504	300	67	NE	Normal	1.5	Offsetting P1	Field
	Photo # 531	260	70	NW	Normal	1.5	Offsetting Qtz and P1	Field
	Photo # 531	262	75	NW	Normal	7	Offsetting Qtz and P1	Field
Photo # 111	30	80	SE	Normal	6.5	Offsetting Qtz and P1	Field	
Photo # 531	280	40	NE	Normal	4.5	Offsetting P1	Field	
Photo # 687	230	40	NW	LL		Offsetting P1	Field	
Photo # 551	300	77	NE	LL	30	Offsetting Qtz	Field	

Fault Population	Sample/Photo #	Strike	Dip	Dip Direction	Offset Sense	Amount of Offset (cm)	Notes	Method of Observation
P2	Photo # 553	87	84	SE	LL	30	Offsetting Qtz	Field
	Photo # 680	275	45	NE	LL	33	Offsetting P1	Field
	Photo # 807	135	65	SW	LL	37	Offsetting Qtz	Field
	Photo # 553	20	33	SE	LL	5	Offsetting Qtz	Field
	Photo # 683	265	40	NW	LL	5	Offsetting P1	Field
	Photo # 803	255	85	NW	LL	5	Offsetting Qtz	Field
	Photo # 795	110	65	SW	LL	23	Offsetting Qtz	Field
	Photo # 783	280	85	NE	LL	17	Offsetting Qtz	Field
	Photo # 815	265	85	NW	LL	11	Offsetting Qtz	Field
	Photo # 632	280	30	NE	RL	13	Offsetting Qtz	Field
	Photo # 799	45	65	SE	RL	5	Offsetting Qtz	Field
	Photo # 811	250	65	NW	RL	4	Offsetting Qtz	Field

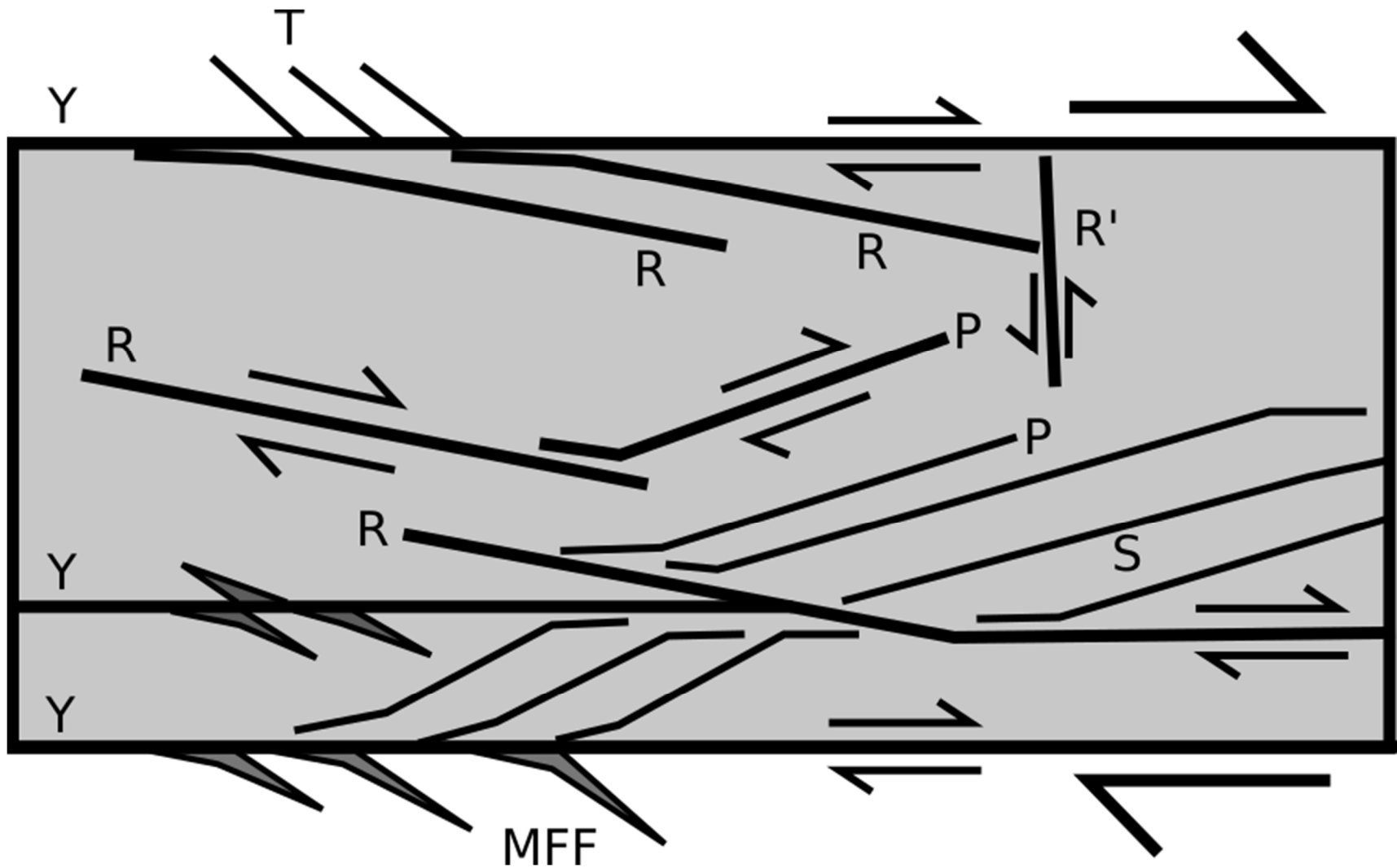


Figure A.1. Schematic of subfractures within brittle faults and their utility as kinematic indicators for slip direction. Modified from Passchier & Trouw (2005).

Appendix B. Geochemical Data

Table B.1. Results from ALS Global whole rock geochemical analysis of two powdered samples of host Foam Creek Stock tonalite.

Wt %	Sample		Analytical Method	
	AK113-4	AK113-5		
SiO ₂	69.3	69.7	Lithium Borate Fusion/ICP-AES	
TiO ₂	0.32	0.4		
Al ₂ O ₃	16.05	15.65		
Fe ₂ O ₃	2.54	3.11		
MnO	0.03	0.04		
MgO	0.9	1.27		
CaO	2.78	3.08		
Na ₂ O	4.7	4.21		
P ₂ O ₅	0.05	0.09		
K ₂ O	2.17	2.02		
Cr ₂ O ₃	<0.01	<0.01		
SrO	0.07	0.08		
BaO	0.17	0.15		
L.O.I.	0.79	0.61		Leco Furnace
Total	99.87	100.41		
C	0.06	0.06	Leco Furnace	
S	0.01	0.01		
ppm			Lithium Borate Fusion/ICP-MS	
Ba	1510	1310		
Ce	9.1	31		
Cr	10	20		
Cs	1.52	1.41		
Dy	0.39	0.51		
Er	0.14	0.14		
Eu	0.64	0.78		
Ga	22.9	21.4		
Gd	0.8	1.63		
Ge	<5	<5		
Hf	2.4	2.5		
Ho	0.08	0.08		
La	4.7	15.8		
Lu	0.02	0.02		
Nb	10.1	8.7		
Nd	4.5	14.9		
Pr	1.1	3.62		
Rb	50.1	46.9		
Sm	1.18	2.89		
Sn	2	1		
Sr	647	692		
Ta	3.3	1.7		
Tb	0.09	0.16		
Th	0.94	3.01		
Tm	0.02	0.02		
U	1.14	1.27		
V	19	29		
W	662	334		
Y	2	2		

Yb	0.13	0.09	Aqua regia digestion/ICP-MS
Zr	69	82	
As	0.1	<0.1	
Bi	0.01	0.01	
Hg	<0.005	<0.005	
In	0.009	0.008	
Re	0.001	0.001	
Sb	<0.05	<0.05	
Se	<0.2	<0.2	
Te	0.01	<0.01	
Tl	0.25	0.32	Four acid digestion/ICP-AES
Ag	<0.5	<0.5	
Cd	<0.5	<0.5	
Co	72	41	
Cu	<1	1	
Li	40	40	
Mo	1	2	
Ni	1	3	
Pb	12	7	
Sc	3	3	
Zn	84	104	

Table B.2. Limits of Detection for the Olympus Delta 6000 Premium Handheld XRF Analyzer, from the Olympus manual.

Element	Range (PPM)
Mg	3000 - 10000
Al	450 - 1400
Si	250 - 800
P	40 - 120
Si	50 - 150
K	20 - 50
Ca	10 - 35
Ti	5 - 10
V	4 - 10
Cr	2 - 9
Mn	3 - 7
Fe	5 - 20
Ni	4 - 10
Cu	2 - 6
Zn	1 - 3
W	4 - 10
Hg	2 - 5
Au	2 - 4
As	1 - 3
Se	1 - 2
Pb	1 - 4
Rb	1 - 2
U	1 - 6
Sr	1 - 2
Y	1 - 2
Zr	1 - 2
Nb	1 - 1
Th	2 - 6
Mo	1 - 2
Ag	5 - 12
Cd	5 - 9
Sn	9 - 14
Sb	10 - 13

Table B.3. Whole rock and PXRF data from the same host powdered samples of unaltered tonalite, plotted against each other in Fig. B.1, used to calibrate the PXRF data for Si. This procedure was performed for all elements that had sufficient data points to determine a linear regression. The correction involves multiplication by the “User Factor”, and addition of the “Offset” to the original data.

Sample #	Whole Rock (wt. %)	PXRF (wt. %)
AK113-4	32.39	29.84
AK113-5	32.58	28.53
N236-1A	33.06	33.74
N289-2	35.97	35.46
WR102-3	32.95	32.40
WR105-16	34.57	36.16
Z-108	34.58	34.06
Z-111	33.41	35.21
Z-118	34.32	35.43
Z-119	30.46	32.51
Z-129	35.91	35.04
Z-138	33.01	30.82
User Factor	0.4046	
Offset	20.145	
R²	0.4101	

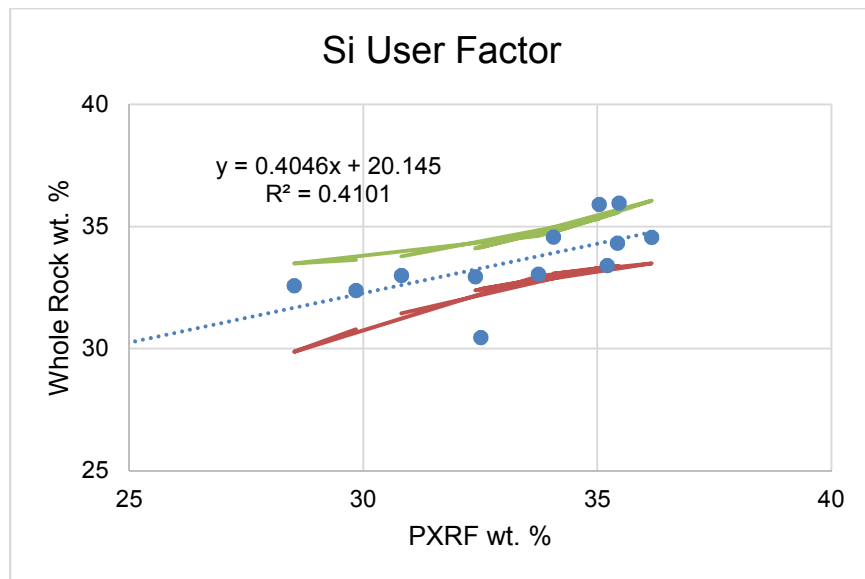


Figure B.1. Whole rock vs. PXRF data for wt. % Si from samples of unaltered tonalite, used to calibrate the PXRF values. 95% confidence bands are shown. Data points shown in Table B.3.

Table B.4. Whole rock and PXRF data from the same host powdered samples of unaltered tonalite, plotted against each other in Fig. B.2, used to calibrate the PXRF data for Ti. This procedure was performed for all elements that had sufficient data points to determine a linear regression. The correction involves multiplication by the “User Factor”, and addition of the “Offset” to the original data.

Sample #	Whole Rock (wt. %)	PXRF (wt. %)
AK113-4	0.192	0.269
AK113-5	0.240	0.335
N236-1A	0.068	0.147
N289-2	0.041	0.068
WR102-3	0.258	0.259
WR105-16	0.011	0.029
Z-108	0.048	0.076
Z-111	0.012	0.034
Z-118	0.024	0.036
Z-119		
Z-129	0.090	0.112
Z-138	0.228	0.273
User Factor	0.8350	
Offset	-0.0142	
R²	0.936	

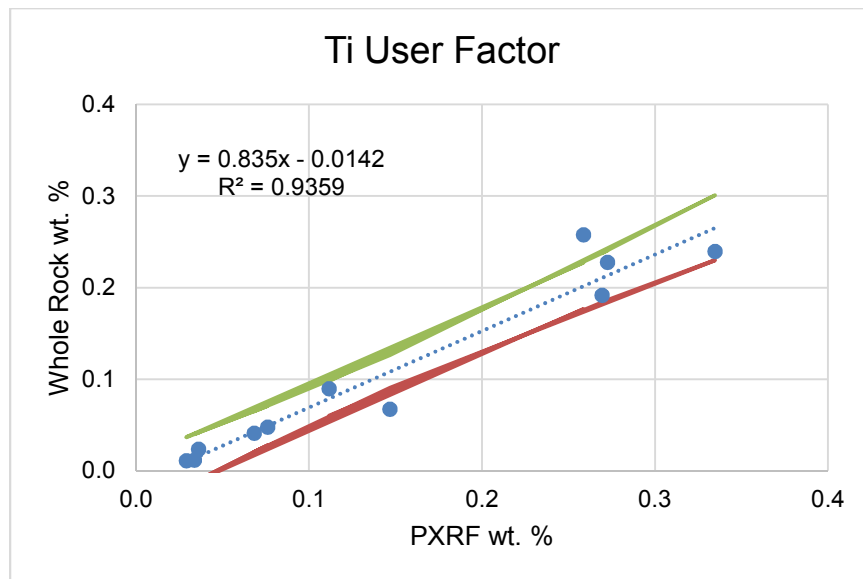


Figure B.2. Whole rock vs. PXRF data for wt. % Ti from samples of unaltered tonalite, used to calibrate the PXRF values. 95% confidence bands are shown. Data points shown in Table B.4.

Table B.5. Whole rock and PXRF data from the same host powdered samples of unaltered tonalite, plotted against each other in Fig. B.3, used to calibrate the PXRF data for Al. This procedure was performed for all elements that had sufficient data points to determine a linear regression. The correction involves multiplication by the “User Factor”, and addition of the “Offset” to the original data.

Sample #	Whole Rock (wt. %)	PXRF (wt. %)
AK113-4	8.49	7.37
AK113-5	8.28	7.08
N236-1A	8.01	8.03
N289-2	8.61	8.49
WR102-3	7.99	7.89
WR105-16	8.45	8.02
Z-108	8.42	8.02
Z-111	9.44	9.10
Z-118	8.71	8.17
Z-119	11.52	10.82
Z-129	7.58	7.2
Z-138	8.57	7.75
User Factor	0.9271	
Offset	1.1073	
R²	0.8555	

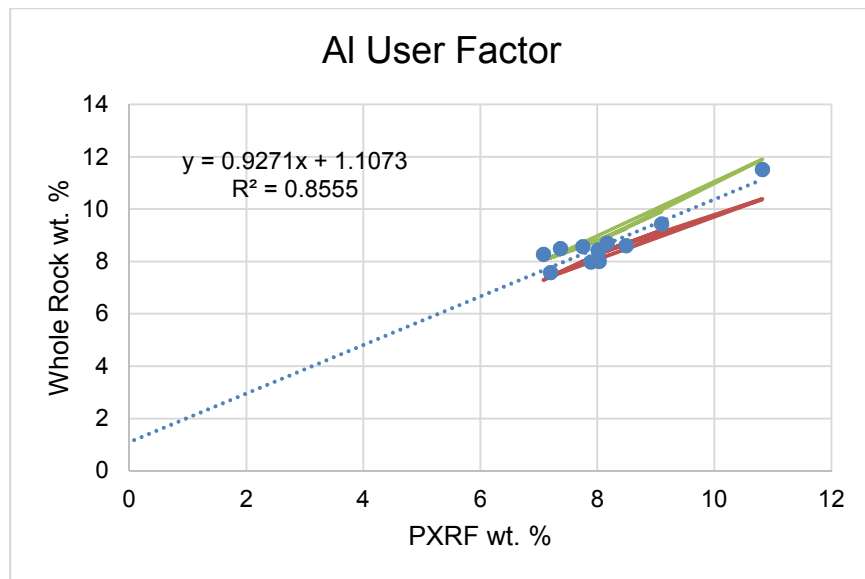


Figure B.3. Whole rock vs. PXRF data for wt. % Al from samples of unaltered tonalite, used to calibrate the PXRF values. 95% confidence bands are shown. Data points shown in Table B.5.

Table B.6. Whole rock and PXRF data from the same host powdered samples of unaltered tonalite, plotted against each other in Fig. B.4, used to calibrate the PXRF data for Fe. This procedure was performed for all elements that had sufficient data points to determine a linear regression. This data shows the PXRF consistently overestimates the amount of iron in a sample. The correction involves multiplication by the “User Factor”, and addition of the “Offset” to the original data.

Sample #	Whole Rock (wt. %)	PXRF (wt. %)
AK113-4	1.78	2.76
AK113-5	2.18	3.43
N236-1A	0.59	1.04
N289-2	0.21	0.34
WR102-3	1.22	1.39
WR105-16	0.15	0.24
Z-108	0.35	0.42
Z-111	0.10	0.13
Z-118	0.16	0.25
Z-119	0.03	0.04
Z-129	0.48	0.75
Z-138	1.34	2.05
User Factor	0.642	
Offset	0.028	
R²	0.981	

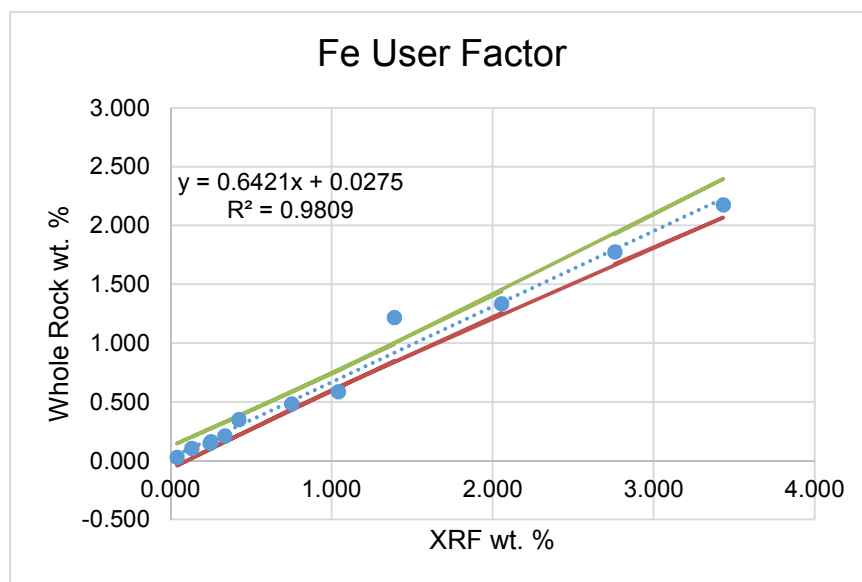


Figure B.4. Whole rock vs. PXRF data for wt. % Fe from samples of unaltered tonalite, used to calibrate the PXRF values. 95% confidence bands are shown. Data points shown in Table B.6.

Table B.7. Whole rock and PXRF data from the same host powdered samples of unaltered tonalite, plotted against each other in Fig. B.5, used to calibrate the PXRF data for Mn. This procedure was performed for all elements that had sufficient data points to determine a linear regression. The correction involves multiplication by the “User Factor”, and addition of the “Offset” to the original data.

Sample #	Whole Rock (wt. %)	PXRF (wt. %)
AK113-4	0.023	0.032
AK113-5	0.031	0.039
N236-1A	0.005	0.008
N289-2	0.002	0.004
WR102-3		
WR105-16	0.003	0.005
Z-108		
Z-111		
Z-118		
Z-119		
Z-129		
Z-138	0.015	0.016
User Factor	0.794	
Offset	0.001	
R ²	0.982	

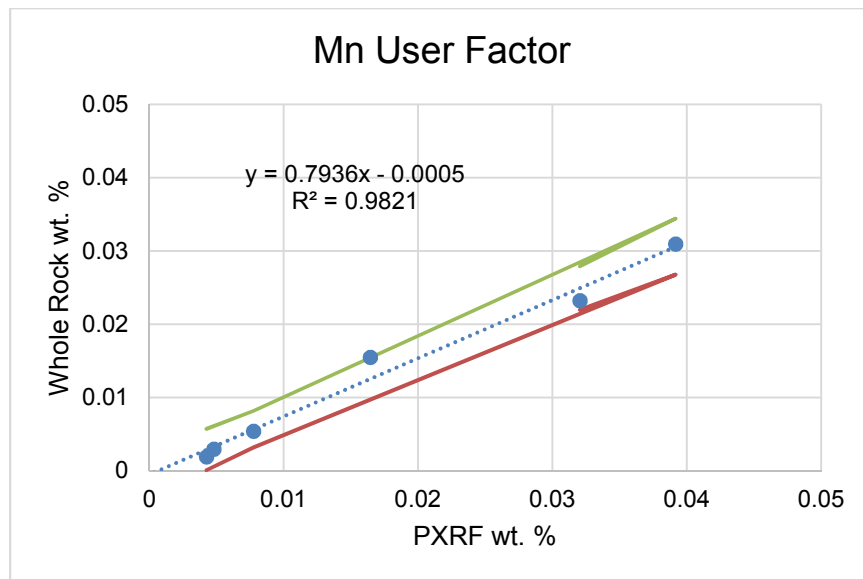


Figure B.5. Whole rock vs. PXRF data for wt. % Mn from samples of unaltered tonalite, used to calibrate the PXRF values. 95% confidence bands are shown. Data points shown in Table B.7.

Table B.8. Whole rock and PXRF data from the same host powdered samples of unaltered tonalite, plotted against each other in Fig. B.6, used to calibrate the PXRF data for Mg. This procedure was performed for all elements that had sufficient data points to determine a linear regression. The correction involves multiplication by the “User Factor”, and addition of the “Offset” to the original data.

Sample #	Whole Rock (wt. %)	PXRF (wt. %)
AK113-4	0.54	1.67
AK113-5	0.77	1.95
N236-1A	0.35	1.53
N289-2	0.15	1.35
WR102-3	0.57	1.89
WR105-16	0.003	1.17
Z-108	0.19	1.32
Z-111	0.04	1.41
Z-118	0.08	1.18
Z-119	0.04	1.45
Z-129	0.25	1.28
Z-138	0.49	1.78
User Factor	0.845	
Offset	-0.975	
R²	0.812	

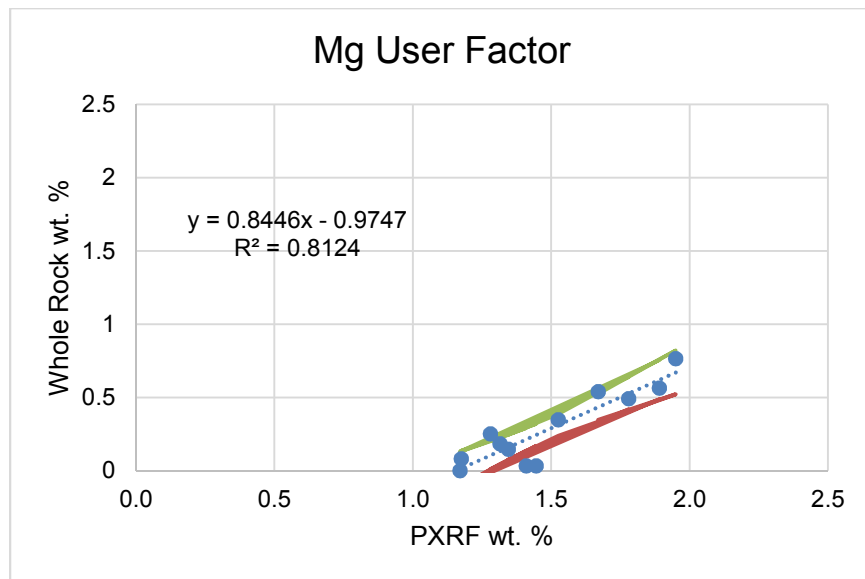


Figure B.6. Whole rock vs. PXRF data for wt. % Mg from samples of unaltered tonalite, used to calibrate the PXRF values. 95% confidence bands are shown. Data points shown in Table B.8.

Table B.9. Whole rock and PXRF data from the same host powdered samples of unaltered tonalite, plotted against each other in Fig. B.7, used to calibrate the PXRF data for Ca. This procedure was performed for all elements that had sufficient data points to determine a linear regression. The correction involves multiplication by the “User Factor”, and addition of the “Offset” to the original data.

Sample #	Whole Rock (wt. %)	PXRF (wt. %)
AK113-4	1.99	1.87
AK113-5	2.20	1.89
N236-1A	1.67	1.54
N289-2	0.90	0.51
WR102-3		
WR105-16	1.18	0.97
Z-108	1.04	0.81
Z-111	1.26	1.10
Z-118	0.78	0.37
Z-119	1.28	0.99
Z-129	1.73	1.76
Z-138	2.23	2.30
User Factor	0.805	
Offset	0.446	
R ²	0.965	

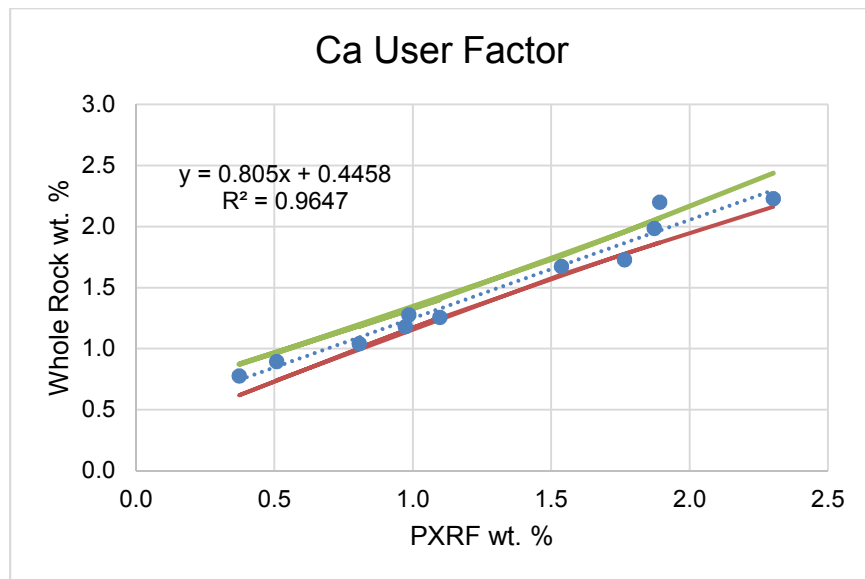


Figure B.7. Whole rock vs. PXRF data for wt. % Ca from samples of unaltered tonalite, used to calibrate the PXRF values. 95% confidence bands are shown. Data points shown in Table B.9.

Table B.10. Whole rock and PXRF data from the same host powdered samples of unaltered tonalite, plotted against each other in Fig. B.8, used to calibrate the PXRF data for K. This procedure was performed for all elements that had sufficient data points to determine a linear regression. The correction involves multiplication by the “User Factor”, and addition of the “Offset” to the original data.

Sample #	Whole Rock (wt. %)	PXRF (wt. %)
AK113-4	1.80	1.90
AK113-5	1.68	2.02
N236-1A	0.78	0.59
N289-2	0.88	0.70
WR102-3	1.74	2.41
WR105-16		
Z-108	0.95	0.77
Z-111	0.61	0.33
Z-118	0.56	0.31
Z-119		
Z-129	0.48	0.21
Z-138	0.95	0.94
User Factor	0.625	
Offset	0.407	
R ²	0.963	

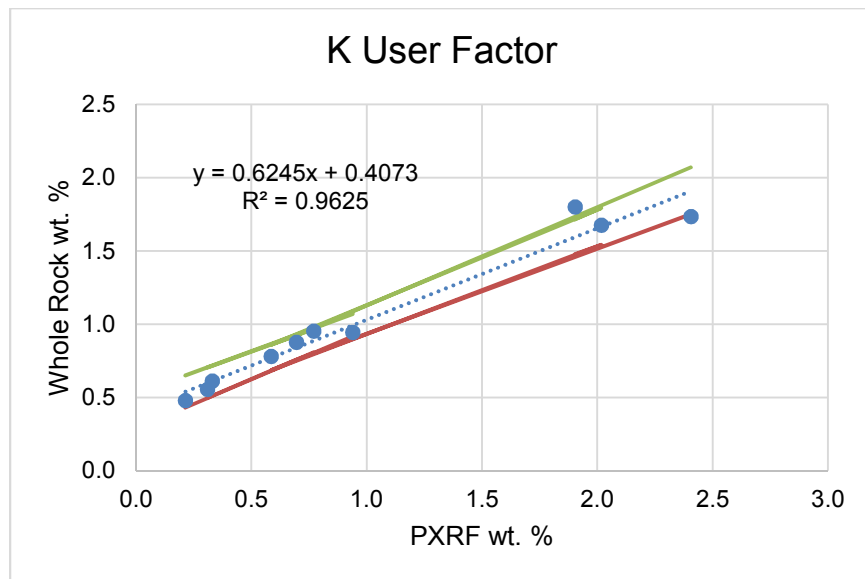


Figure B.8. Whole rock vs. PXRF data for wt. % K from samples of unaltered tonalite, used to calibrate the PXRF values. 95% confidence bands are shown. Data points shown in Table B.10.

Table B.11. Whole rock and PXRF data from the same host powdered samples of unaltered tonalite, plotted against each other in Fig. B.9, used to calibrate the PXRF data for Sr. This procedure was performed for all elements that had sufficient data points to determine a linear regression. The correction involves multiplication by the “User Factor”, and addition of the “Offset” to the original data.

Sample #	Whole Rock (wt. %)	PXRF (wt. %)
AK113-4	0.059	0.061
AK113-5	0.068	0.063
N236-1A	0.050	0.045
N289-2	0.050	0.049
WR102-3	0.068	0.054
WR105-16	0.059	0.060
Z-108	0.051	0.057
Z-111	0.051	0.059
Z-118	0.059	0.057
Z-119	0.144	0.144
Z-129	0.068	0.069
Z-138	0.076	0.073
User Factor	0.970	
Offset	0.003	
R²	0.952	

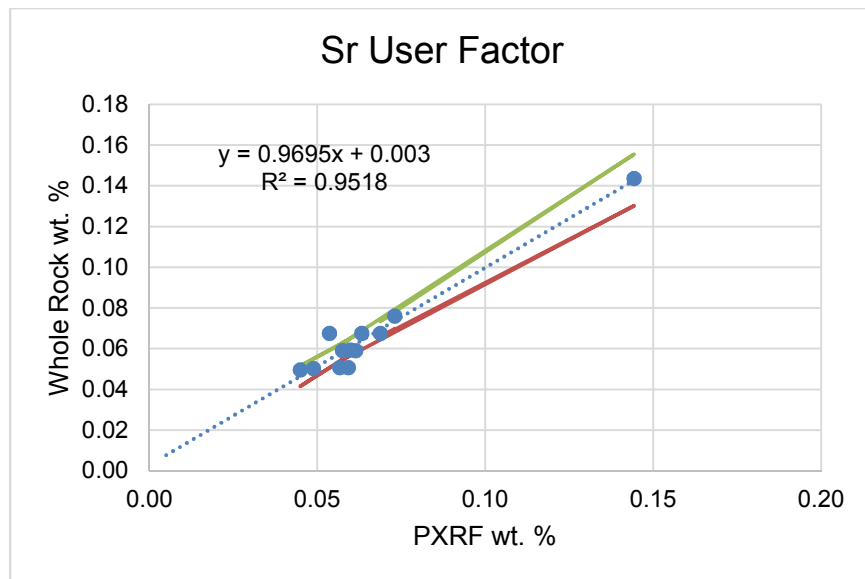


Figure B.9. Whole rock vs. PXRF data for ppm Sr from samples of unaltered tonalite, used to calibrate the PXRF values. 95% confidence bands are shown. Data points shown in Table B.11.

Table B.12. Whole rock and PXRF data from the same host powdered samples of unaltered tonalite, plotted against each other in Fig. B.10, used to calibrate the PXRF data for Rb. This procedure was performed for all elements that had sufficient data points to determine a linear regression. The correction involves multiplication by the “User Factor”, and addition of the “Offset” to the original data.

Sample #	Whole Rock (ppm)	PXRF (ppm)
AK113-4	50	53
AK113-5	47	49
N236-1A	29	28
N289-2	22	23
WR102-3		
WR105-16	7	8
Z-108	20	20
Z-111	7	6
Z-118	6	8
Z-119	4	
Z-129	6	8
Z-138	24	25
User Factor	0.968	
Offset	-0.121	
R ²	0.994	

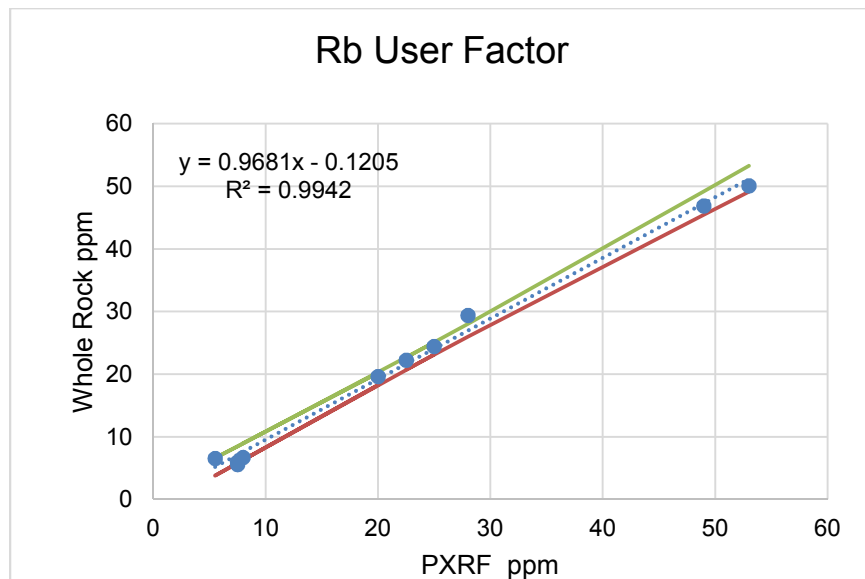


Figure B.10. Whole rock vs. PXRF data for ppm Rb from samples of unaltered tonalite, used to calibrate the PXRF values. 95% confidence bands are shown. Data points shown in Table B.12.

Table B.13. Whole rock and PXRF data from the same host powdered samples of unaltered tonalite, plotted against each other in Fig. B.11, used to calibrate the PXRF data for Pb. This procedure was performed for all elements that had sufficient data points to determine a linear regression. The correction involves multiplication by the “User Factor”, and addition of the “Offset” to the original data.

Sample #	Whole Rock (ppm)	PXRF (ppm)
AK113-4	12	14
AK113-5	7	8
N236-1A	11	15
N289-2	13	16
WR102-3		
WR105-16	7	8
Z-108	6	7
Z-111	5	7
Z-118	5	6
Z-119	15	18
Z-129	4	6
Z-138	7	7
User Factor	0.807	
Offset	0.362	
R²	0.953	

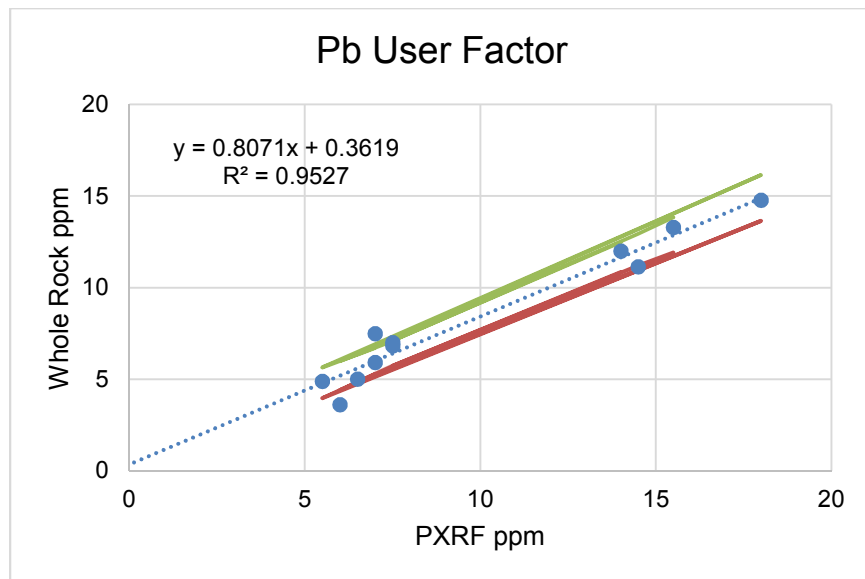


Figure B.11. Whole rock vs. PXRF data for ppm Pb from samples of unaltered tonalite, used to calibrate the PXRF values. 95% confidence bands are shown. Data points shown in Table B.13.

Table B.14. Whole rock and PXRF data from the same host powdered samples of unaltered tonalite, plotted against each other in Fig. B.12, used to calibrate the PXRF data for Zn. This procedure was performed for all elements that had sufficient data points to determine a linear regression. The correction involves multiplication by the “User Factor”, and addition of the “Offset” to the original data.

Sample #	Whole Rock (ppm)	PXRF (ppm)
AK113-4	84	85
AK113-5	104	96
N236-1A	20	21
N289-2	11	12
WR102-3		
WR105-16	1	6
Z-108	20	24
Z-111	11	12
Z-118	19	27
Z-119	1	
Z-129	25	31
Z-138	79	93
User Factor	1.0129	
Offset	-3.8058	
R²	0.9756	

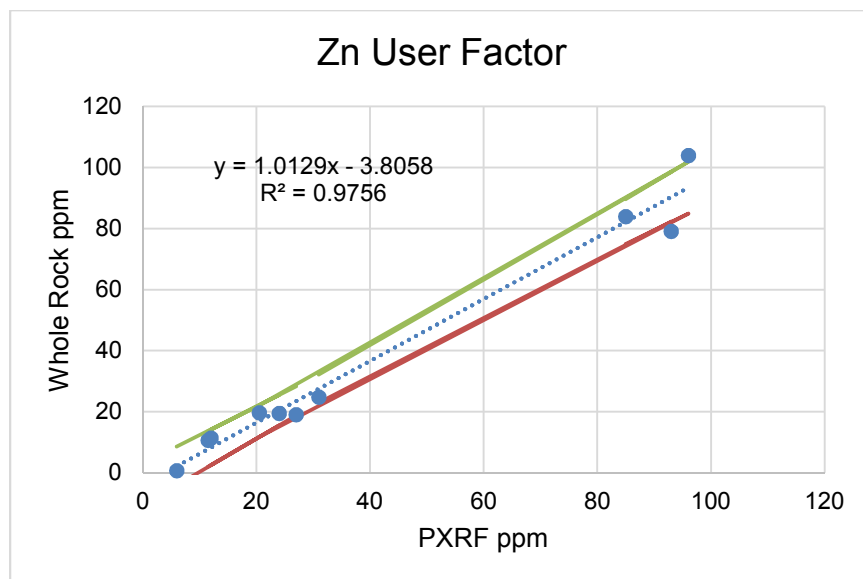


Figure B.12. Whole rock vs. PXRF data for ppm Zn from samples of unaltered tonalite, used to calibrate the PXRF values. 95% confidence bands are shown. Data points shown in Table B.14.

Table B.15. PXRF values for each spot analysis of the P1 fault cores, corrected through the linear regression user factor technique outlined in section 2.4, and shown earlier in Appendix B. The data has also been converted from wt % element to oxides.

Date	12/14/2015	12/14/2015	12/14/2015	12/14/2015	12/14/2015	12/16/2015	12/16/2015	12/16/2015	12/16/2015	12/16/2015	12/16/2015	12/16/2015	12/16/2015	12/16/2015	12/16/2015	12/16/2015
Reading	8	9	10	11	12	3	4	5	6	7	8	9	10	11	12	13
Analysis	P1-7	P1-8	P1-9	P1-10	P1-11	P1-47	P1-48	P1-49	P1-50	P1-51	P1-52	P1-53	P1-54	P1-55	P1-56	P1-57
Sample	107-4	107-4	107-4	107-4	107-4	107-4	107-4	107-4	107-4	107-4	107-3L	107-3L	107-3L	107-3L	107-3L	107-2
Collimated?	C	C	C	C	C	C	C	C	C	C	C	C	C	C	C	C
<i>wt %</i>																
SiO2	71.92	72.69	82.40	70.93	63.78	73.32	72.57	79.83	83.49	70.78	69.63	77.52	74.38	73.24	75.13	66.47
TiO2		0.24	0.65	0.50	0.58	0.09	0.11	0.40	0.67	0.70	0.08	0.29	0.27	0.16	0.21	0.07
Al2O3	19.10	20.01	9.17	18.19	16.12	18.63	19.68	8.22	7.75	15.46	17.35	21.03	19.78	17.28	14.98	14.56
Fe2O3	3.56	2.79	1.20	3.09	2.55	3.29	2.24	2.46	0.97	4.22	1.93	1.64	3.10	3.88	2.23	2.46
MnO	0.04	0.04	0.04	0.10	0.10	0.08	0.03	0.07	0.03	0.12	0.02	0.03	0.02	0.03	0.02	
MgO	0.02	1.10	0.11	0.79	0.75	0.78	0.22	0.67		1.03	1.44	1.10	0.71	2.01	0.22	0.22
CaO		1.02	0.71		0.87			2.78	0.86		1.24		1.56	2.32		
K2O	1.11	1.17	1.29	1.58	2.23	1.18	1.14	0.99	0.89	1.64	2.55	3.25	1.91	2.36	2.82	3.05
SrO	0.05	0.06	0.03	0.05	0.03	0.05	0.05	0.03	0.03	0.04	0.05	0.07	0.07	0.05	0.04	0.03
<i>ppm</i>																
Rb	35	44	37	62	66	44	39	47	32	51	53	81	63	89	81	81
Zr	45	93	60	79	105	43	107	92	65	57	19	187	94	59	93	38
Pb	145	272	79	102	44	241	191	148	54	140						
Zn	105	180	72	141	117	133	141	144	40	221				17		

Date	12/16/2015	12/16/2015	12/16/2015	12/16/2015	12/16/2015	12/16/2015	12/16/2015	12/16/2015	12/16/2015	12/16/2015	12/16/2015	12/16/2015	12/16/2015	12/16/2015	12/16/2015	12/16/2015
Reading	14	15	16	17	18	19	20	21	22	23	24	25	26	27	28	29
Analysis	P1-58	P1-59	P1-60	P1-61	P1-62	P1-63	P1-64	P1-65	P1-66	P1-67	P1-68	P1-69	P1-70	P1-71	P1-72	P1-73
Sample	107-2	107-2	107-2	107-2	107-4	107-4	107-4	107-4	107-4	111-1	111-1	111-1	111-1	111-1	107-5	107-5
Collimated?	C	C	C	C	C	C	C	C	C	C	C	C	C	C	C	C
<i>wt %</i>																
SiO2	73.40	72.96	73.95	69.25	75.43	76.38	78.43	69.08	72.72	70.05	71.27	71.99	71.84	66.99	69.08	74.35
TiO2	0.21	0.16	0.19	0.07	0.17	0.23	0.25	0.21	0.13	0.12	0.24	0.81	0.90	0.32		0.36
Al2O3	11.13	19.75	19.12	15.56	11.39	17.63	13.99	13.18	20.57	17.56	15.16	19.96	20.13	16.91	16.88	13.25
Fe2O3	5.60	4.59	1.93	0.94	3.96	1.97	2.15	7.92	2.12	5.44	4.60	2.59	2.75	5.43	1.87	3.81
MnO	0.02	0.02			0.14	0.03	0.05	0.07	0.03	0.04	0.04	0.04	0.05	0.07	0.05	0.06
MgO	1.41	0.99	0.34	0.67	0.36	0.95	0.43	0.44	0.86	0.92	1.00	0.97	0.29	2.94	0.40	0.09
CaO	1.91						1.21			2.11	2.03	2.00	1.95	3.75	1.67	
K2O	3.77	4.67	3.49	1.34	1.45	2.01	1.28	2.46	1.70	2.02	1.96	1.50	1.35	1.82	1.17	1.98
SrO	0.03	0.05	0.05	0.03	0.03	0.06	0.04	0.02	0.06	0.05	0.05	0.06	0.07	0.05	0.04	0.04
<i>ppm</i>																
Rb	171	108	85	29	53	55	40	69	69	45	46	36	41	51	30	51
Zr	95	29	34	30	113	98	59	17	62	43	113	181	66	246	33	83
Pb					329	194	122	112	56	21	24				28	153
Zn	17	28	21		226	115	152	192	143	25	41	38	52	63	80	300

Date	12/16/2015	12/16/2015	12/16/2015	12/16/2015	12/16/2015	12/16/2015	12/16/2015	12/16/2015
Reading	30	31	32	33	34	35	36	37
Analysis	P1-74	P1-75	P1-76	P1-77	P1-78	P1-79	P1-80	P1-81
Sample	107-5	107-5	107-5	111-1	111-1	111-1	111-1	111-1
Collimated	C	C	C	C	C	C	C	C
wt %								
SiO2	74.64	73.69	68.14	68.87	72.96	74.48	71.77	76.91
TiO2	0.31	0.22	0.10	0.11	0.11	0.08	0.26	0.07
Al2O3	19.92	13.65	16.86	18.35	17.91	17.03	15.00	14.77
Fe2O3	3.11	4.31	2.59	2.73	2.26	1.57	2.52	1.57
MnO	0.03	0.06	0.05	0.03	0.04	0.02	0.04	0.02
MgO	1.11	0.50	0.54	0.62	0.99	1.13		0.22
CaO			1.53	1.41		0.85	1.11	
K2O	1.31	2.53	1.39	1.84	2.56	1.11	3.14	1.64
SrO	0.06	0.03	0.04	0.05	0.05	0.05	0.03	0.04
ppm								
Rb	44	63	38	42	48	29	79	39
Zr	130	63	32	44	44	38	16	29
Pb	56	171	44		12	11		
Zn	222	350	119	23	33	14	34	34

Table B.16. PXRF values for each spot analysis of the P2 fault cores, corrected through the linear regression user factor technique outlined in section 2.4, and shown earlier in Appendix B. The data has also been converted from wt % element to oxides.

Date	12/16/2015	12/16/2015	12/16/2015	12/16/2015	12/16/2015	12/16/2015	12/16/2015	12/16/2015	12/16/2015	12/16/2015	12/16/2015	12/16/2015	12/16/2015	12/16/2015	12/16/2015
Reading	38	39	40	41	42	43	44	45	46	47	50	51	52	53	54
Analysis	P2-1	P2-2	P2-3	P2-4	P2-5	P2-6	P2-7	P2-8	P2-9	P2-10	P2-11	P2-12	P2-13	P2-14	P2-15
Sample	107-1	107-1	107-1	107-1	107-1	107-1	107-1	107-1	107-1	111-4	111-4	111-4	111-4	106-1	106-1
Collimated?	C	C	C	C	C	C	C	C	C	C	C	C	C	C	C
Wt. %															
SiO2	72.076	74.154	71.635	72.094	74.604	73.816	73.141	74.786	72.172	66.796	67.506	67.316	66.744	70.181	73.868
TiO2	0.620	0.545	0.422	0.337	0.402	0.394	0.559	0.412	0.276	0.227	0.300	0.231	0.306	0.384	0.442
Al2O3	16.299	16.684	19.960	19.750	19.557	15.335	16.229	19.452	18.769	25.863	24.584	26.686	27.177	19.487	18.576
Fe2O3	1.553	1.615	3.123	4.106	1.099	3.044	1.655	3.840	4.501	1.773	2.465	1.545	1.699	2.373	2.103
MnO	0.032	0.026	0.046	0.035	0.045	0.083	0.026	0.065	0.034	0.020	0.038	0.022		0.027	0.021
MgO	0.653	0.316	1.549	1.143	0.218	0.485	0.204	1.087	1.717	0.765	0.681	0.723	1.087	1.283	0.415
CaO								0.843	0.914	9.169	7.196	9.512	9.443	1.363	1.218
K2O	7.231	7.178	5.824	4.989	6.170	4.575	7.336	2.863	3.083	0.512	1.305	0.729		5.102	4.613
SrO	0.027	0.032	0.030	0.031	0.037	0.026	0.030	0.044	0.034	0.056	0.067	0.062	0.063	0.040	0.053
ppm															
Rb	203	175	264	235	228	179	195	122	148	22	42	27	16	113	132
Zr	56	84	54	93	67	50	46	74	56	74	57	65	63	62	77
Pb				18				14		4		6			
Zn	44	45	113	128	128	571	34	118	138	30	46	45	82	22	18

Date	12/16/2015	12/16/2015	12/16/2015	12/16/2015	12/16/2015	12/16/2015	12/16/2015	12/16/2015	12/16/2015	12/16/2015	12/16/2015	12/16/2015	12/16/2015	12/16/2015	12/16/2015	12/16/2015
Reading	55	56	57	58	59	60	61	62	63	64	65	66	67	68	69	70
Analysis	P2-16	P2-17	P2-18	P2-19	P2-20	P2-21	P2-22	P2-23	P2-24	P2-25	P2-26	P2-27	P2-28	P2-29	P2-30	P2-31
Sample	106-1	106-1	106-1	106-1	106-1	100-3	100-3	100-3	100-3	100-3	110-1	110-1	110-1	110-1	110-1	108-1
Collimated?	C	C			C						C	C	C	C	C	C
Wt. %																
SiO2	75.608	71.133	71.817	68.103	72.232	73.280	73.808	73.686	74.829	73.695	65.463	71.081	67.974	71.436	69.159	76.093
TiO2	0.256	0.490	0.369	0.213	0.329	0.334	0.364	0.420	0.345	0.359	0.287	0.447	0.513	0.585	0.478	0.285
Al2O3	15.528	19.662	19.259	14.214	16.053	17.560	17.280	18.156	17.245	18.769	16.281	21.571	19.154	21.011	18.979	16.614
Fe2O3	3.473	2.015	2.182	1.667	1.050	1.547	1.102	1.218	1.085	1.439	2.854	1.224	4.639	3.147	3.527	1.689
MnO	0.017	0.016	0.027	0.016	0.023	0.021	0.018	0.022	0.019	0.022	0.036	0.024	0.043	0.041	0.031	0.023
MgO	0.611	1.087	0.779	0.765	0.218	0.471	0.373	0.415	0.597	0.457	1.227	0.667	1.745	2.151	1.339	-0.244
CaO	1.521	2.176	2.543	1.781							3.395	5.978	2.813	4.488	2.927	2.008
K2O	2.463	5.990	5.157	1.861	5.982	4.926	5.385	6.048	5.109	4.972	1.068	2.063	1.571	2.062	1.897	3.472
SrO	0.046	0.043	0.044	0.035	0.042	0.038	0.037	0.038	0.037	0.042	0.039	0.045	0.047	0.045	0.041	0.062
ppm																
Rb	86	141	123	54	188	151	170	183	159	150	43	85	64	112	76	102
Zr	67	65	70	76	37	31	31	39	35	36	102	91	128	119	120	71
Pb				4		7	5	4	6	6				13		
Zn	22		25	15	17	24	17	12	13	15	31	31	42	57	68	41

Date	12/16/2015	12/16/2015	12/16/2015	12/16/2015	12/16/2015	12/16/2015	12/16/2015	12/16/2015	12/18/2015	12/18/2015	12/18/2015	12/18/2015	12/18/2015	12/18/2015	12/18/2015	12/18/2015	12/18/2015
Reading	71	72	73	74	75	77	78	2	3	4	5	6	7	8	9	10	
Analysis	P2-32	P2-33	P2-34	P2-35	P2-36	P2-37	P2-38	P2-39	P2-40	P2-41	P2-42	P2-43	P2-44	P2-45	P2-46	P2-47	
Sample	108-1	103-1	103-1	103-1	103-1	103-1	103-1	101-6	101-6	101-6	101-6	101-6	101-6	106-1	106-1	106-1	106-1
Collimated?	C	C	C	C	C	C	C	C	C	C	C	C	C	C	C	C	C
Wt. %																	
SiO2	72.674	73.513	69.852	66.199	70.198	80.516	71.626	72.985	71.245	68.666	65.654	66.346	68.917	76.413	77.417	77.590	
TiO2	0.392	0.439	0.436	0.998	0.572	0.311	0.651	0.520	0.462	0.414	0.319	0.304	0.472	0.602	0.368	0.246	
Al2O3	20.047	13.846	12.848	18.366	19.101	13.654	20.660	17.490	18.261	16.842	16.036	16.229	17.928	18.769	17.490	16.999	
Fe2O3	2.365	3.364	4.547	4.070	4.097	2.110	3.610	2.563	2.392	1.445	1.067	2.319	2.750	2.367	1.588	1.616	
MnO	0.014	0.046	0.029	0.038	0.043	0.027	0.043	0.025	0.023	0.025	0.015	0.030	0.028	0.024	0.015		
MgO	1.129	1.031	0.569	1.367	1.647	0.401	0.877	1.185	0.120	1.045	0.891	0.583	0.765	0.807	0.260	1.143	
CaO	1.312		1.048		2.517	0.710	2.950	2.473	3.853	1.845	1.160	4.110	3.010	1.893	0.695	0.791	
K2O	4.876	2.305	2.086	3.063	3.164	2.389	3.254	2.374	2.503	2.774	3.924	2.020	2.056	4.915	4.937	4.051	
SrO	0.063	0.027	0.050	0.052	0.070	0.046	0.080	0.048	0.053	0.039	0.031	0.057	0.046	0.051	0.052	0.044	
ppm																	
Rb	163	68	96	93	123	70	126	72	72	49	62	46	61	121	133	115	
Zr	49	58	59	57	75	47	80	66	47	28		41	43	74	63	81	
Pb											8			5			
Zn	42	35	67	43	66	35	106	44	30	28	12	25	32	29	33	28	
Date	12/18/2015	12/18/2015	12/18/2015	12/18/2015	12/18/2015	12/18/2015	12/18/2015	12/18/2015	12/18/2015	12/18/2015	12/18/2015	12/18/2015	12/18/2015	12/18/2015	12/18/2015	12/18/2015	12/18/2015
Reading	11	12	13	14	15	16	17	18	19	20	21	22	23	24	25	26	
Analysis	P2-48	P2-49	P2-50	P2-51	P2-52	P2-53	P2-54	P2-55	P2-56	P2-57	P2-58	P2-59	P2-60	P2-61	P2-62	P2-63	
Sample	110-1	110-1	106-3	106-3	106-3	112-2	112-2	112-2	112-2	100-3	100-3	100-3	100-3	100-3	108-1	108-1	
Collimated?	C	C	C	C	C	C	C	C	C	C	C	C	C	C	C	C	
Wt. %																	
SiO2	69.895	74.361	75.772	76.041	73.158	73.271	76.006	70.735	74.180	72.648	73.972	74.872	75.296	75.478	71.297	79.858	
TiO2	0.209	0.378	0.324	0.295	0.578	0.389	0.307	0.461	0.396	0.319	0.364	0.395	0.369	0.478	0.547	0.265	
Al2O3	17.542	16.194	15.248	16.088	17.507	16.684	13.584	17.560	16.351	18.313	19.504	20.345	18.226	19.697	14.652	10.886	
Fe2O3	2.420	3.029	1.575	1.912	2.381	3.517	2.756	2.742	2.218	1.278	0.999	0.668	0.727	0.607	4.391	2.085	
MnO	0.032	0.029	0.022	0.022	0.023	0.045	0.047	0.058	0.031	0.020	0.016		0.020	0.020	0.039	0.021	
MgO	0.905	0.611	0.667	0.134	0.358	1.297	0.316	0.485	0.905	0.527	0.807	1.255	0.751	0.597	1.241		
CaO	1.412	1.021		1.106	1.314	8.227	5.428	7.427	3.444						1.114		
K2O	2.865	2.909	5.260	4.703	5.463	1.259	1.623	1.374	2.795	3.880	4.231	4.666	5.824	5.426	3.676	3.009	
SrO	0.038	0.037	0.038	0.051	0.043	0.105	0.079	0.094	0.068	0.041	0.042	0.047	0.040	0.040	0.044	0.027	
ppm																	
Rb	74	79	132	122	126	42	53	50	71	116	142	133	174	201	164	71	
Zr	47	58	58	60	83	102	54	101	97	39	24	28	27	34	142	69	
Pb										9							
Zn	19	24	18	33	18	185	219	68	70	19	18			13	46	21	

Date	12/18/2015	12/18/2015	12/18/2015	12/18/2015	12/18/2015	12/18/2015	12/18/2015	12/18/2015	12/18/2015	12/18/2015	12/18/2015	12/18/2015	12/18/2015	12/18/2015	12/18/2015	12/18/2015
Reading	29	30	31	32	33	34	35	36	37	38	39	40	41	42	44	45
Analysis	P2-64	P2-65	P2-66	P2-67	P2-68	P2-69	P2-70	P2-71	P2-72	P2-73	P2-74	P2-75	P2-76	P2-77	P2-79	P2-80
Sample	105-1	105-1	105-1	112-2	112-2	112-2	105-1	105-1	105-1	104-4	104-4	104-4	104-4	104-4	105-2	105-2
Collimated?		C	C	C	C	C	C	C	C	C	C	C	C	C		C
Wt. %																
SiO2	73.686	71.661	73.686	72.509	71.488	70.311	68.363	65.905	74.093	66.667	63.395	67.870	68.155	71.038	72.405	73.011
TiO2	0.259	0.278	0.427	0.289	0.207	0.519	0.171	0.059	0.229	0.306	0.388	0.387	0.136	0.632	0.343	0.325
Al2O3	19.522	20.240	19.942	15.633	16.491	16.789	18.068	16.088	20.117	15.072	14.880	17.735	15.843	18.331	18.436	18.453
Fe2O3	1.251	2.067	1.285	2.759	3.195	2.869	1.090	0.488	0.961	2.156	1.788	1.594	1.199	2.714	1.279	1.214
MnO	0.021	0.022	0.030	0.051	0.062	0.050	0.023		0.023	0.014		0.017		0.018	0.018	0.020
MgO	0.401	1.647	0.316	0.513	0.344	0.947	1.451	1.675	0.779	0.723	0.611	1.325	0.499	1.227	0.499	1.003
CaO	1.992	3.521	2.271	7.810	7.573	7.450	1.661	1.510	2.850	2.418	1.804	1.928	1.989	1.883	1.394	1.792
K2O	3.347	3.263	4.621	1.200	1.289	1.335	2.907	1.715	4.016	2.755	3.261	3.279	2.077	5.478	6.488	6.118
SrO	0.045	0.046	0.041	0.106	0.093	0.089	0.034	0.026	0.043	0.057	0.053	0.064	0.054	0.067	0.040	0.047
ppm																
Rb	106	118	155	39	41	27	102	53	128	83	78	92	44	128	158	160
Zr	67	46	56	80	57	101	44	40	62	166	149	120	81	294	33	32
Pb				18	136	20									4	
Zn	26	28	27	320	500	211	14		26	53		17	22	23	27	30

Date	12/18/2015	12/18/2015	12/18/2015	12/18/2015	12/18/2015	12/18/2015
Reading	46	47	48	49	50	51
Analysis	P2-81	P2-82	P2-83	P2-84	P2-85	P2-86
Sample	105-2	105-2	105-2	105-2	104-1	104-1
Collimated?	C	C	C	C	C	C
Wt. %						
SiO2	67.558	74.110	73.098	72.769	75.772	69.609
TiO2	0.342	0.295	0.304	0.363	0.252	0.246
Al2O3	16.456	19.399	19.750	19.469	12.865	17.034
Fe2O3	1.312	1.394	1.638	1.777	2.282	4.271
MnO	0.020	0.028	0.022	0.036	0.039	0.095
MgO	0.667	-0.412	0.569	1.031	0.583	1.451
CaO	1.465	1.897	2.590	3.008	1.842	4.098
K2O	4.335	6.050	5.140	5.177	2.887	2.758
SrO	0.043	0.043	0.044	0.046	0.056	0.061
ppm						
Rb	135	134	135	143	119	128
Zr	43	50	37	43	38	74
Pb						
Zn	30	29	27	35	46	116

Appendix C. Fluid Inclusion Data

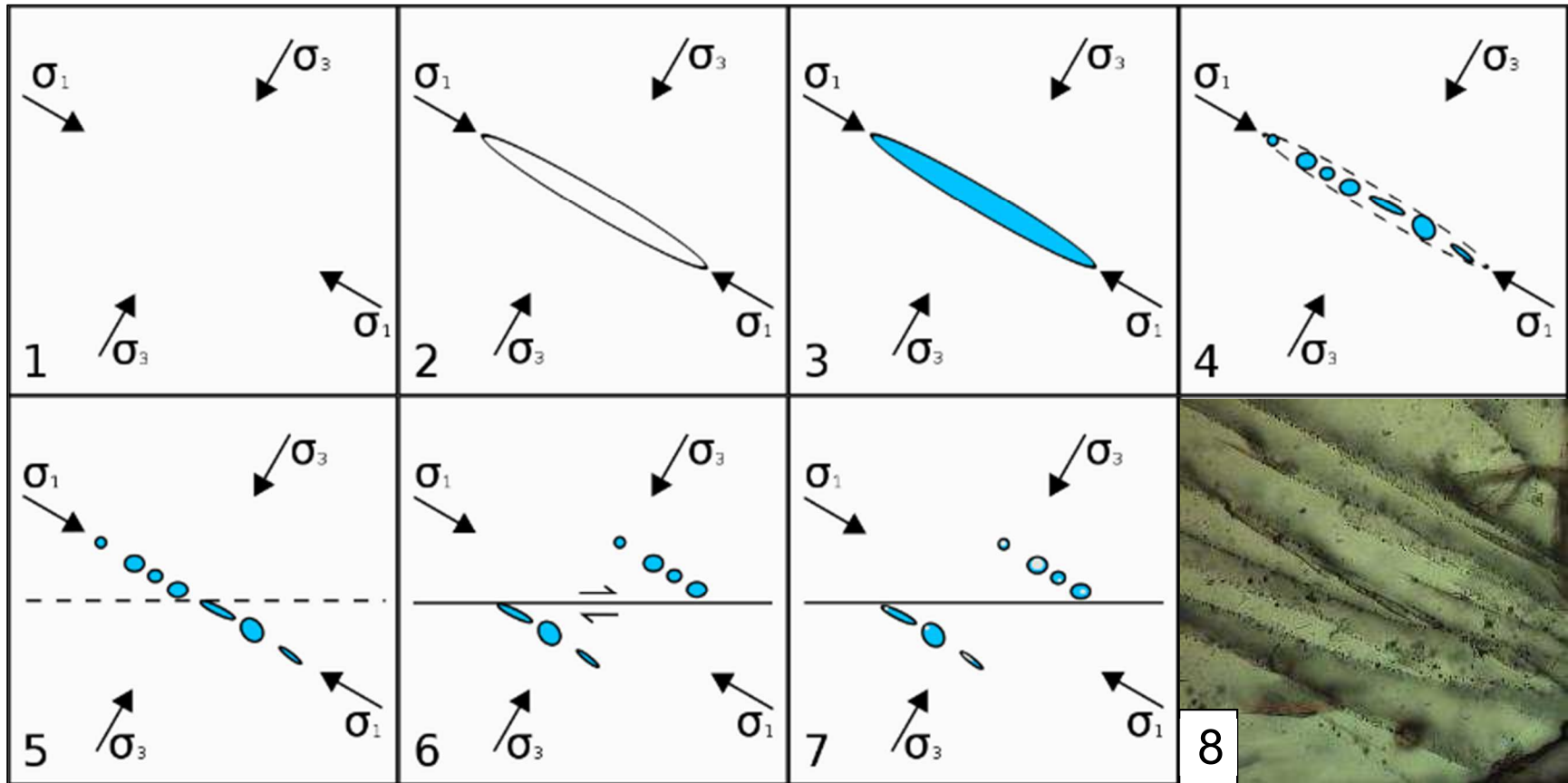


Figure C.1. Schematic of fluid inclusion plane formation, in relation to primary stress directions, showing ideal conditions. 1) A stress field on a homogeneous body of rock (wallrock quartz grains in this study), σ_1 denoting the primary stress vector. 2) Formation of a dilatant fracture in the rock, parallel to the σ_1 - σ_2 plane, normal to σ_3 . 3) Fluids flow through the fracture at depth. 4) The quartz begins to heal, trapping the fluids in planes of fluid inclusions, some elongated along the plane, others irregularly shaped. 5+6) Assuming an unchanged stress field, brittle deformation of the rock results in slip along a fault surface and associated offsetting of fluid inclusion planes. 7) Fluids trapped in the inclusions dissociate into separate components of vapor, liquid, and salt upon cooling and uplift. 8) Photomicrograph of aligned fluid inclusion planes in quartz in the FCS.

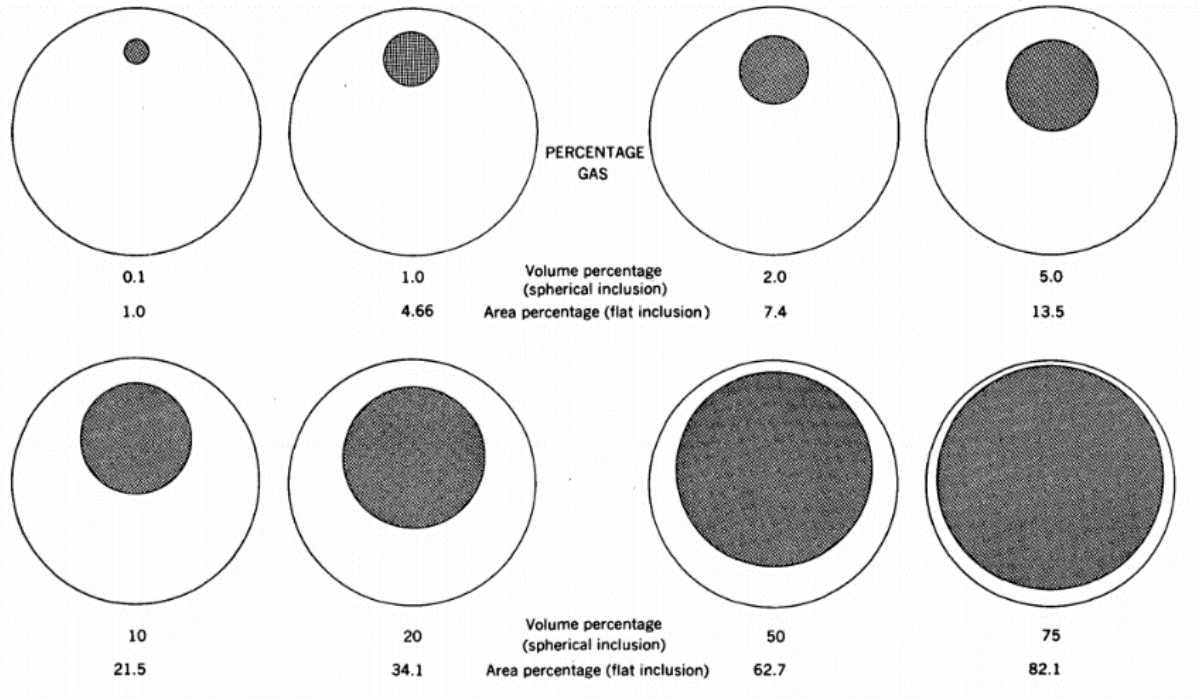


Figure C.2. Schematic for estimation of phase volume percentage in a two-phase liquid-vapor fluid inclusion, assuming a spherical inclusion. From Roedder (1972).

Table C.2. Results of geothermobarometry of fluid inclusions. Liquid volume, initial melting temperature, final melting temperature, and homogenization temperature were all observed on the heating-cooling stage. These observations were used to calculate salinity using the equation outlined in section 2.4, and pressure values were determined using the BULK software package (Section 2.5). Method for measuring the volume of liquid is outlined in section 2.4, and Fig. C.2. The “Pressure CH₄” and “Pressure N₂” columns contain the results output by the BULK system from the vapor component end-members discussed in section 4.3.

Sample	Chip	Run	Vol. Liquid (%)	Initial Melting Temp(°C)	Final Melting Temp(°C)	Homogenization Temp(°C)	Salinity (wt. % eq. NaCl)	Pressure CH ₄ (MPa)	Pressure N ₂ (MPa)
P2 105-3A	2+3	1	90	-30	-6.6	258	9.98	208.5	233.7
	4+5	1	95	-30	-5.5	265	8.55	214.4	237.7
	4+5	2	95		-3.4	337	5.56	274.9	277.3
	4+5	3	95		-10.8	266	14.77	215.1	238.3
	4+5	4	30		-2.5	270.3	4.18	218.9	240.8
	4+5	5	90	-30	-5.8	259.9	8.95	210.1	234.8
	6	2	25		-2.8	271.1	4.65	219.5	241.2
106-1B	1+2	1	90	-27	-11.6	256	15.57	206.9	232.5
	1+2	2	85		-10	307	13.94	249.7	261.3
	1+2	3	95		-8	234	11.70	188.5	219.5
	3	1	95	-25	-11	234	14.97	188.5	219.5
	3	2	98	-26	-7.3	261	10.86	211.1	235.4
	3	3	95	-25	-6.5	268	9.86	216.9	239.5
	3	4	95		-5.2	248	8.14	200.2	227.8
	5	1	90		-6.9	267	10.36	216.1	238.9
	6	1	95	-22	-4.5	262	7.17	211.9	236.0
	6	2	90	-32	-11	311	14.97	253.1	263.5
	6	3	80	-27	-10.3	258	14.25	208.5	233.7
6	4	85		-7.8	259	11.46	209.4	234.3	
110-1B	1	1	90	-25	-0.2	258	0.35	208.5	233.7
	1	2	85	-29	-4.6	267	7.31	216.1	238.9
	1	3	80	-22	-4.7	314	7.45	255.6	265.1
	2	1	90	-25	-2.2	262	3.71	211.9	236.0
	2	2	90		-3.6	279	5.86	226.2	245.7
108-1B	1	1	90		-30.1	258.3	28.72	208.8	233.8
	1	2	90		-24.3	304.8	25.15	247.9	260.1
	1	3	90		-28.5	237.7	27.72	191.6	221.7
	1	4	90		-28.3	261.8	27.60	211.7	235.9

Sample	Chip	Run	Vol. Liquid (%)	Initial Melting Temp(°C)	Final Melting Temp(°C)	Homogenization Temp(°C)	Salinity (wt. % eq. NaCl)	Pressure CH ₄ (MPa)	Pressure N ₂ (MPa)	
108-1B	2	1	85		-27.1	261.3	26.86	211.1	235.6	
	2	2	90		-27.8	262.4	27.29	212.2	236.2	
	4	1	98		-20.1	258.8	22.44	209.2	234.1	
	4	2	95		-20.9	304.2	22.98	247.4	259.8	
	4	3	90		-20.9	245.6	22.98	198.2	226.4	
	4	4	95		-24.6	291	25.33	236.3	252.5	
	4	5	90		-24.8	274.1	25.46	222.1	242.9	
	4	6	95		-32.8	237.4	30.49	191.3	221.5	
	4	7	90		-31.1	285	29.36	231.2	249.1	
	4	8	90		-50	-31	269	29.30	217.8	240.0
	4	9	90		-50	-22	263	23.70	212.7	236.6
P1 107-4BA	1	1	95	-26	-14.5	265.3	18.22	214.7	237.9	
	1	2	90		-13.1	338.6	16.99	276.3	278.1	
	1	3	90		-9.9	281.3	13.83	228.1	247.0	
	1	4	98		-7.3	252	10.86	203.5	230.2	
	2347	1	20		-6.7	289	10.11	237.6	251.3	
	2347	2	95		-9.6	239	13.51	192.7	222.5	
	2347	3	80		-6.7	327	10.11	266.6	272.0	
	2347	4	90	-26	-12.3	297	16.24	241.3	255.8	
	2347	5	80		-11.7	325.2	15.67	265.0	271.1	
	2347	6	80		-9.1	299.5	12.96	243.4	257.2	
	2347	7	90		-10.4	324.5	14.36	264.5	270.7	
	6	1	95		-13.6	271	17.43	219.5	241.2	
	5	1	20		-8	302	11.70	245.7	258.5	
	5	2	80		-4.8	316	7.59	257.3	266.2	
	5	3	80	-25	-2	279	3.39	226.2	245.7	
	5	4	90		-11.8	269	15.76	217.8	240.0	
5	5	95		-12	275	15.96	222.8	243.5		
111-1A	1	1	90		-13.6	299	17.43	243.0	256.9	
	1	2	80		-7	290.6	10.49	235.9	252.2	
	1	3	80		-8.9	301	12.73	244.7	258.0	
	2	1	90		-11.5	289	15.47	234.6	251.3	
	2	2	90		-18.1	261.9	21.04	211.8	235.9	

Sample	Chip	Run	Vol. Liquid (%)	Initial Melting Temp(°C)	Final Melting Temp(°C)	Homogenization Temp(°C)	Salinity (wt. % eq. NaCl)	Pressure CH₄(MPa)	Pressure N₂(MPa)
111-1A	2	3	25		-7.5	305	11.10	247.7	260.2
	3	1	98		-3.6	273.6	5.86	221.6	242.7
	3	2	95		-9.6	261	13.51	211.1	235.4
	3	3	25		-7.1	301	10.61	244.7	258.0
	4	1	95	-30	-14.8	289	18.47	234.6	251.3
	4	2	90	-28	-14.8	301	18.47	244.7	258.0
	4	3	20		-9.7	285	13.62	231.2	249.1
	4	4	90	-26	-11.5	287	15.47	232.9	250.2

Appendix D. Geochronological Data

Table D.1. Select K-Ar dates from Engels *et al.* (1976) of nearby plutons. For locations of the sample locations in this table, see figure 1.5.

Sample Location	Lat	Long	Age (Ma)	Mineral
Foam Creek Stock	-121.108	48.045	77.58 ± 2.1	Musc
			71.11 ± 2.1	Biot
Sloan Creek Plutons	-121.340	48.035	89.9 ± 4.3	Hbl
			75.3 ± 1.2	Biot
Sulphur Mountain Pluton	-121.113	48.247	72.09 ± 2.1	Hbl
			59.14 ± 1.7	Biot
Clark Mountain Stock	-120.937	48.047	60.69 ± 2.4	Musc
			58.49 ± 2.3	Biot
Tenpeak Pluton 1	-121.027	48.048	84.38 ± 2.5	Hbl
			71.81 ± 2.1	Musc
			67.64 ± 2	Biot
Tenpeak Pluton 2	-120.977	48.020	90.36 ± 3.2	Hbl
			72.13 ± 3.4	Musc
			71.79 ± 2.2	Biot
Tenpeak Pluton 3	-120.937	47.953	92.69 ± 3.1	Hbl
			77.17 ± 2.4	Biot

Table D.2. Ar-Ar dates from Matzel (2004) of the Tenpeak Pluton, located adjacent to the Foam Creek Stock (See Fig. 1.5).

Sample #	Age (Ma)	Mineral
TP19B	90.5 ± 0.8	Hbl
TP-749-1	88.5 ± 1.0	Hbl
TP11	67.0 ± 0.6	Biot
TP31	68.1 ± 0.4	Biot
TP-524-1	75.2 ± 0.4	Biot

Appendix E. Geochemical Data

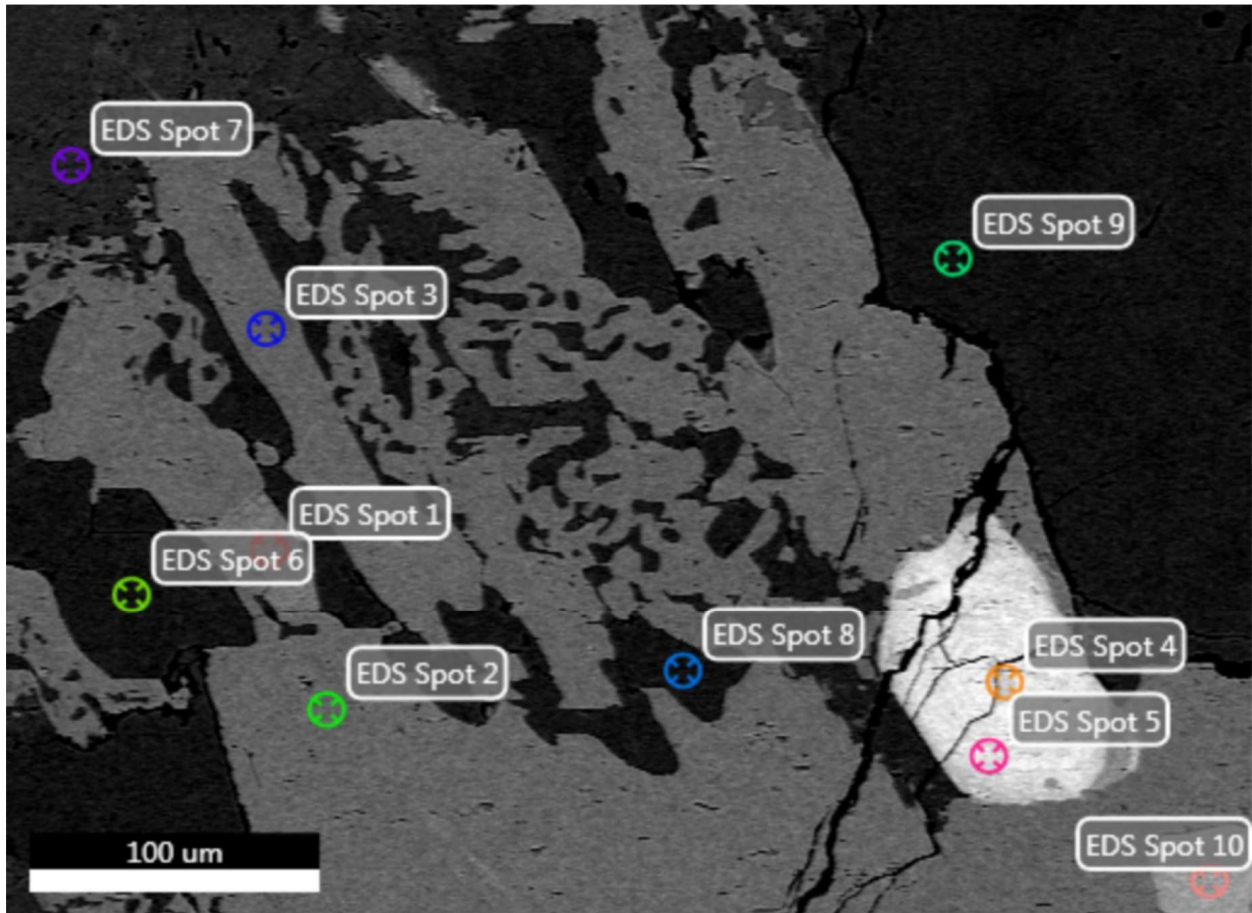
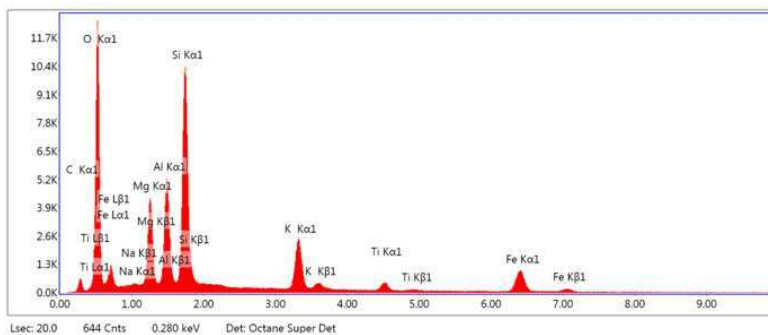


Fig. E.1. SEM BSE image from sample 113-4, also shown in Fig. 3.13, of a highly zoned allanite core hosted in an epidote grain, displaying the “wormy” between plagioclase, quartz, and magmatic epidote in unaltered FCS. This figure shows the display from the TEAM EDAX software, with spots chosen for EDS analysis. Results for each spot are shown in the following pages. Interpretation of the spot analyses are shown in table E.1.

Table E.1. Interpretations of EDS analyses, from Fig. E.1.

	Spot	Interpretation
Sample 113-4	1	Biotite
Area 7	2	Epidote
	3	Epidote
	4	Allanite
	5	Allanite
	6	Quartz
	7	Plagioclase (Andesine)
	8	Qtz
	9	Qtz
	10	Apatite

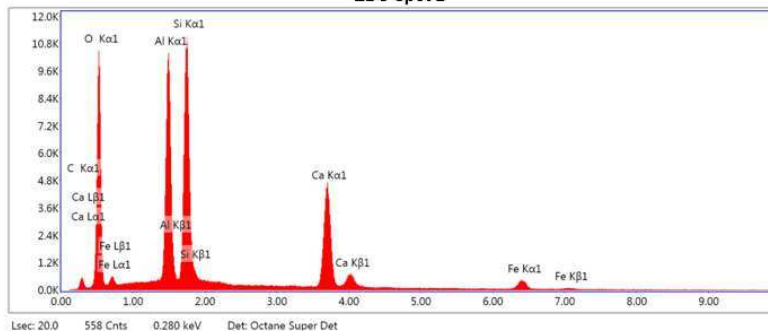
EDS Spot 1



eZAF Smart Quant Results

Element	Weight %	Atomic %	Net Int.	Error %	Kratio	Z	R	A	F
O K	38.7	56.5	3855.7	7.8	0.1585	1.0953	0.9560	0.3817	1.0000
NaK	0.5	0.5	65.2	15.1	0.0022	0.9911	0.9830	0.4411	1.0048
MgK	7.5	7.2	1612.9	6.0	0.0446	1.0070	0.9908	0.5962	1.0070
AlK	9.3	8.0	2108.4	5.2	0.0600	0.9688	0.9981	0.6735	1.0090
SiK	18.8	15.7	4434.6	4.4	0.1333	0.9891	1.0049	0.7258	1.0053
K K	8.2	4.9	1253.4	3.2	0.0704	0.9129	1.0330	0.9402	1.0256
TiK	2.0	1.0	208.2	7.0	0.0172	0.8398	1.0447	0.9745	1.0660
FeK	14.9	6.2	708.5	3.9	0.1260	0.8202	1.0513	0.9980	1.0505

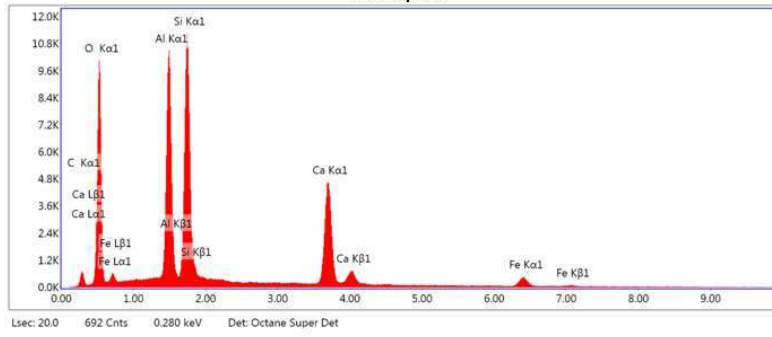
EDS Spot 2



eZAF Smart Quant Results

Element	Weight %	Atomic %	Net Int.	Error %	Kratio	Z	R	A	F
O K	41.6	58.9	3230.5	8.8	0.1258	1.0816	0.9604	0.2842	1.0000
AlK	15.7	13.2	4195.2	4.1	0.1130	0.9562	1.0018	0.7587	1.0102
SiK	18.7	15.1	4750.9	4.2	0.1353	0.9762	1.0085	0.7493	1.0065
CaK	18.9	10.7	2535.7	2.6	0.1676	0.9161	1.0402	0.9668	1.0181
FeK	5.2	2.1	259.9	6.1	0.0438	0.8087	1.0532	0.9927	1.0612

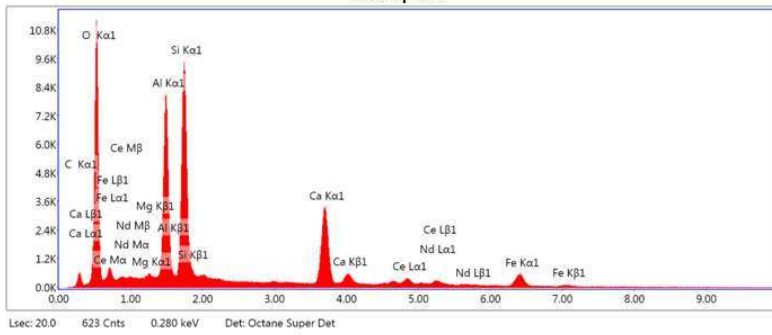
EDS Spot 3



eZAF Smart Quant Results

Element	Weight %	Atomic %	Net Int.	Error %	Kratio	Z	R	A	F
O K	41.0	58.5	3108.3	8.8	0.1223	1.0826	0.9599	0.2813	1.0000
AlK	15.6	13.2	4126.5	4.2	0.1123	0.9571	1.0014	0.7585	1.0103
SiK	18.8	15.2	4708.0	4.2	0.1354	0.9771	1.0081	0.7492	1.0065
CaK	19.2	10.9	2538.6	2.6	0.1694	0.9170	1.0399	0.9665	1.0181
FeK	5.3	2.2	261.6	6.0	0.0445	0.8095	1.0530	0.9925	1.0607

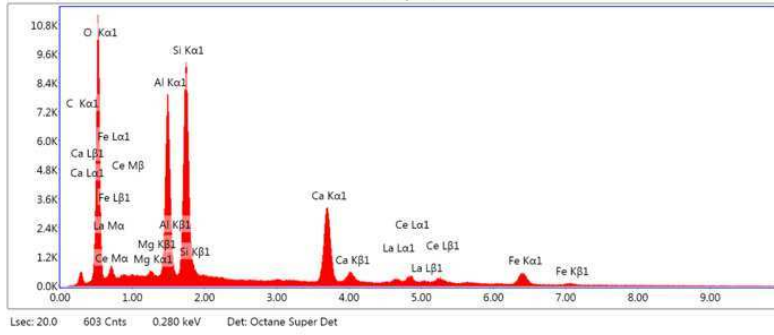
EDS Spot 4



eZAF Smart Quant Results

Element	Weight %	Atomic %	Net Int.	Error %	Kratio	Z	R	A	F
O K	38.3	59.0	3507.3	8.3	0.1402	1.1180	0.9396	0.3333	1.0000
MgK	0.4	0.4	87.2	13.1	0.0023	1.0295	0.9760	0.5557	1.0071
AlK	13.6	12.4	3232.1	5.1	0.0893	0.9908	0.9837	0.6717	1.0081
SiK	16.9	14.9	4037.2	4.8	0.1179	1.0119	0.9910	0.6972	1.0060
CaK	13.6	8.4	1851.7	2.9	0.1256	0.9517	1.0261	0.9557	1.0301
CeL	6.1	1.1	222.7	11.3	0.0439	0.6644	1.1955	1.0382	1.0635
NdL	3.9	0.7	123.8	15.0	0.0280	0.6586	1.1899	1.0392	1.0614
FeK	7.2	3.2	355.0	5.6	0.0614	0.8425	1.0435	0.9842	1.0454

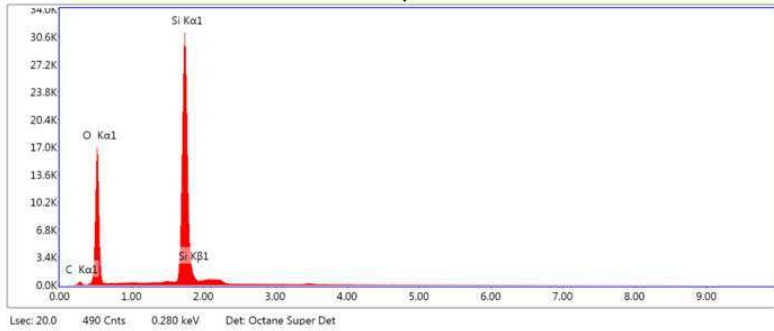
EDS Spot 5



eZAF Smart Quant Results

Element	Weight %	Atomic %	Net Int.	Error %	Kratio	Z	R	A	F
O K	40.2	60.5	3484.5	8.2	0.1465	1.1098	0.9442	0.3348	1.0000
MgK	0.3	0.3	53.5	18.0	0.0015	1.0216	0.9802	0.5613	1.0075
AlK	13.3	11.9	3060.9	4.9	0.0890	0.9831	0.9878	0.6859	1.0084
SiK	17.1	14.6	3907.4	4.6	0.1201	1.0039	0.9949	0.7105	1.0060
CaK	13.6	8.1	1738.3	2.9	0.1240	0.9438	1.0293	0.9591	1.0294
LaL	3.0	0.5	109.5	20.1	0.0212	0.6571	1.2007	1.0387	1.0706
CeL	5.3	0.9	180.2	11.3	0.0374	0.6586	1.1985	1.0397	1.0552
FeK	7.4	3.2	342.2	5.7	0.0622	0.8350	1.0457	0.9855	1.0479

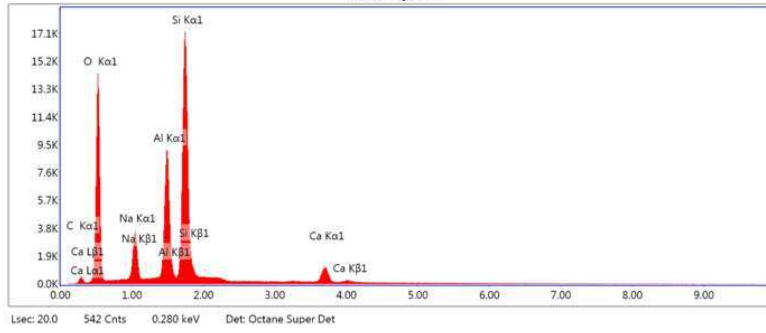
EDS Spot 6



eZAF Smart Quant Results

Element	Weight %	Atomic %	Net Int.	Error %	Kratio	Z	R	A	F
O K	49.8	63.5	5362.2	7.0	0.2323	1.0508	0.9756	0.4523	1.0000
SiK	50.2	36.5	13274.6	2.5	0.4205	0.9465	1.0210	0.9001	1.0023

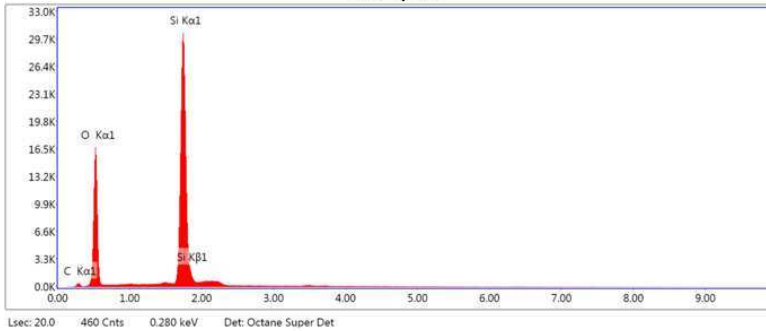
EDS Spot 7



eZAF Smart Quant Results

Element	Weight %	Atomic %	Net Int.	Error %	Kratio	Z	R	A	F
O K	43.5	57.2	4393.9	7.5	0.1854	1.0631	0.9733	0.4083	1.0000
NaK	7.1	6.5	1087.5	6.7	0.0375	0.9608	0.9988	0.5598	1.0067
AlK	14.2	11.1	3544.7	4.0	0.1034	0.9385	1.0128	0.7803	1.0139
SiK	30.6	22.9	7222.2	3.9	0.2227	0.9579	1.0191	0.7713	1.0032
CaK	4.6	2.4	546.0	4.1	0.0391	0.8978	1.0485	0.9549	1.0189

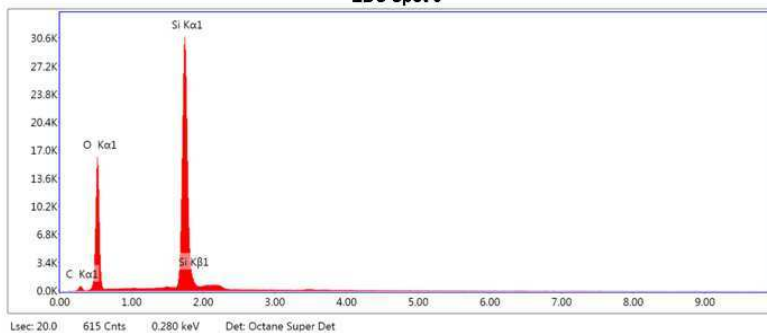
EDS Spot 8



eZAF Smart Quant Results

Element	Weight %	Atomic %	Net Int.	Error %	Kratio	Z	R	A	F
O K	49.7	63.4	5121.3	7.0	0.2322	1.0510	0.9755	0.4513	1.0000
SiK	50.3	36.6	12763.0	2.5	0.4230	0.9467	1.0209	0.9004	1.0023

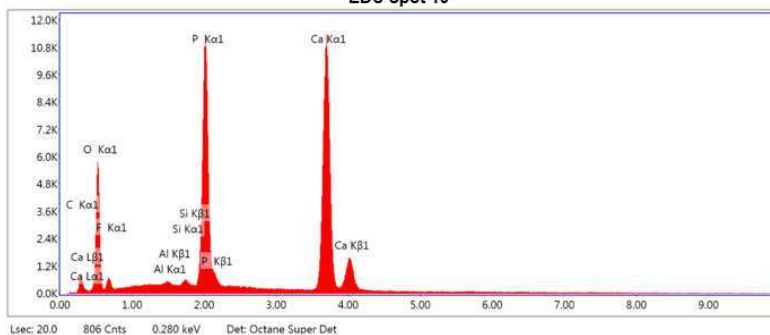
EDS Spot 9



eZAF Smart Quant Results

Element	Weight %	Atomic %	Net Int.	Error %	Kratio	Z	R	A	F
O K	48.9	62.7	4925.8	7.1	0.2248	1.0518	0.9751	0.4470	1.0000
Si K	51.1	37.3	12831.7	2.5	0.4282	0.9475	1.0206	0.9019	1.0023

EDS Spot 10



eZAF Smart Quant Results

Element	Weight %	Atomic %	Net Int.	Error %	Kratio	Z	R	A	F
O K	34.8	53.9	1795.3	10.0	0.0644	1.0985	0.9495	0.1710	1.0000
F K	3.3	4.2	213.3	11.8	0.0058	1.0198	0.9593	0.1766	1.0000
Al K	0.1	0.1	34.1	29.8	0.0008	0.9721	0.9924	0.7299	1.0149
Si K	0.2	0.2	73.9	16.1	0.0019	0.9926	0.9994	0.8288	1.0257
P K	19.2	15.3	5061.4	2.8	0.1644	0.9526	1.0060	0.8964	1.0191
Ca K	42.4	26.2	6293.8	2.2	0.3833	0.9322	1.0330	0.9757	1.0104

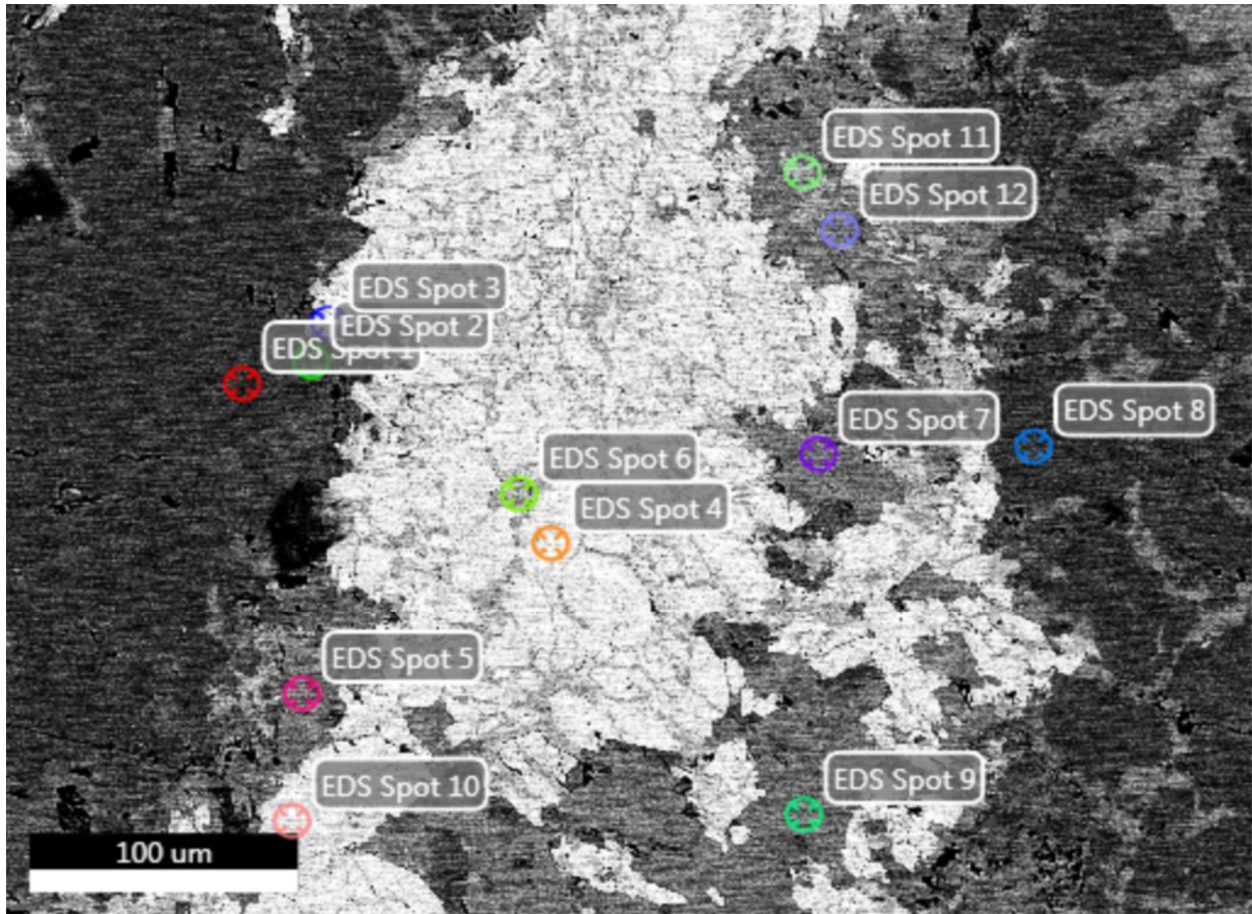
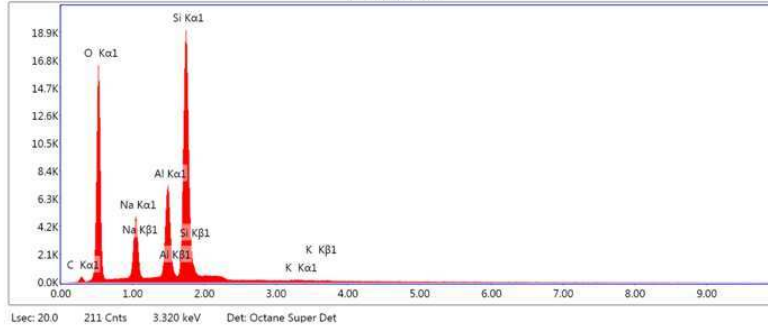


Fig. E.2. SEM BSE image from sample 111-1, the same sample as that show in Fig. 3.19, of a P1 fault core hosting a mass of fine-grained secondary minerals. This figure shows the display on the TEAM EDAX software, with spots chosen for EDS analysis. Results for each spot are shown in the following pages. Interpretation of the spot analyses are shown in table E.2.

Table E.2. Interpretations of EDS analyses, from Fig. E.2.

	Spot	Interpretation
Sample 111-1	1	Albite
Area 18	2	Plagioclase
	3	Chlorine-bearing Amphibole (Hastingsite)
	4	Chlorine-bearing Amphibole (Hastingsite)
	5	Adularia
	6	Actinolite
	7	Adularia
	8	Albite
	9	Adularia
	10	Chlorine-bearing Amphibole (Hastingsite)
	11	Chlorite
	12	Adularia

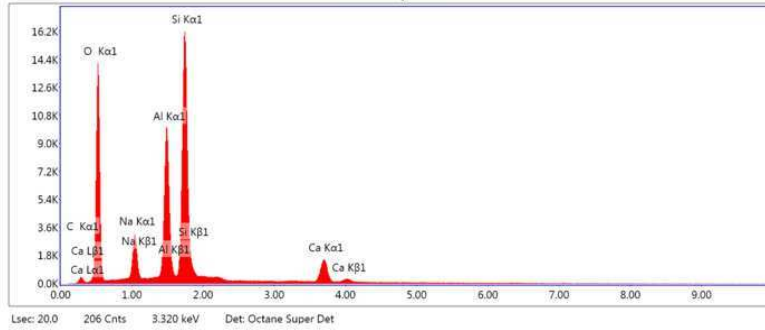
EDS Spot 1



eZAF Smart Quant Results

Element	Weight %	Atomic %	Net Int.	Error %	Kratio	Z	R	A	F
O K	43.1	55.9	5179.6	6.8	0.2104	1.0609	0.9757	0.4682	1.0000
NaK	11.2	10.1	1851.9	6.1	0.0615	0.9586	1.0009	0.5809	1.0064
AlK	12.0	9.2	3050.0	4.2	0.0856	0.9363	1.0148	0.7652	1.0149
SiK	33.3	24.6	8181.5	3.8	0.2426	0.9556	1.0210	0.7747	1.0025
KK	0.5	0.3	69.4	11.7	0.0038	0.8805	1.0462	0.9265	1.0159

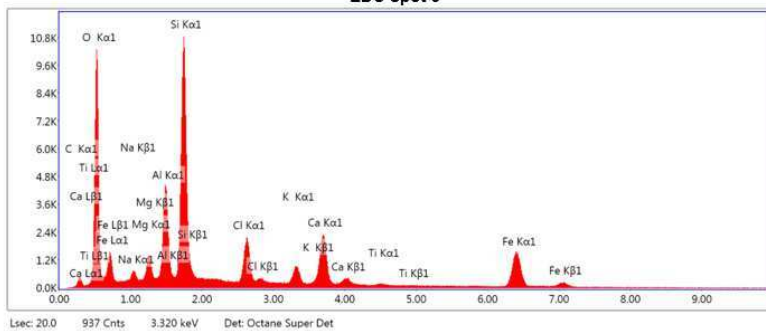
EDS Spot 2



eZAF Smart Quant Results

Element	Weight %	Atomic %	Net Int.	Error %	Kratio	Z	R	A	F
O K	44.0	58.0	4348.4	7.7	0.1781	1.0639	0.9725	0.3870	1.0000
NaK	5.9	5.4	925.4	6.9	0.0310	0.9616	0.9981	0.5486	1.0066
AlK	15.3	11.9	3947.5	4.0	0.1117	0.9393	1.0122	0.7808	1.0129
SiK	28.3	21.3	6855.2	4.0	0.2050	0.9587	1.0185	0.7647	1.0036
CaK	6.5	3.4	802.5	3.5	0.0557	0.8987	1.0480	0.9568	1.0181

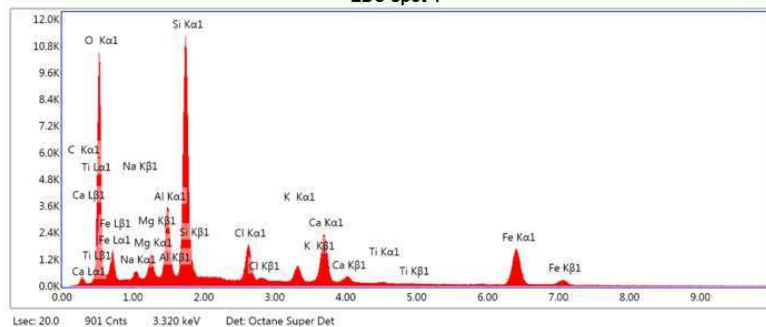
EDS Spot 3



eZAF Smart Quant Results

Element	Weight %	Atomic %	Net Int.	Error %	Kratio	Z	R	A	F
O K	34.8	54.5	3195.5	8.3	0.1284	1.1123	0.9460	0.3349	1.0000
NaK	1.2	1.3	144.9	11.7	0.0048	1.0072	0.9738	0.3997	1.0037
MgK	1.8	1.8	368.5	7.9	0.0099	1.0235	0.9818	0.5488	1.0067
AlK	7.1	6.5	1683.2	5.4	0.0467	0.9848	0.9894	0.6724	1.0094
SiK	17.7	15.8	4481.0	4.4	0.1314	1.0056	0.9965	0.7382	1.0067
ClK	4.7	3.3	917.5	4.2	0.0389	0.9348	1.0153	0.8696	1.0214
KK	2.3	1.5	379.1	6.6	0.0208	0.9288	1.0259	0.9313	1.0429
CaK	8.8	5.5	1190.2	3.4	0.0810	0.9450	1.0306	0.9491	1.0340
TiK	0.2	0.1	18.8	57.9	0.0015	0.8548	1.0386	0.9637	1.0720
FeK	21.4	9.6	1061.0	3.5	0.1840	0.8356	1.0466	0.9951	1.0431

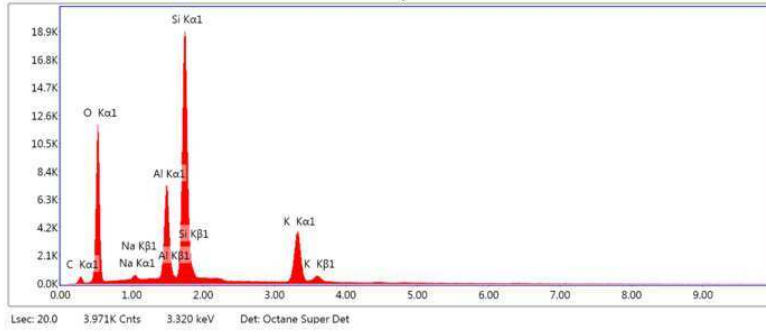
EDS Spot 4



eZAF Smart Quant Results

Element	Weight %	Atomic %	Net Int.	Error %	Kratio	Z	R	A	F
O K	35.1	55.1	3262.7	8.2	0.1319	1.1131	0.9451	0.3406	1.0000
NaK	1.0	1.1	117.3	12.0	0.0039	1.0080	0.9729	0.3919	1.0036
MgK	1.9	1.9	380.5	8.0	0.0103	1.0244	0.9810	0.5418	1.0064
AlK	5.6	5.2	1315.5	5.6	0.0367	0.9856	0.9886	0.6656	1.0096
SiK	18.4	16.5	4646.9	4.3	0.1371	1.0065	0.9957	0.7415	1.0066
ClK	4.0	2.8	765.1	4.6	0.0326	0.9356	1.0146	0.8690	1.0220
KK	2.2	1.4	352.0	6.7	0.0194	0.9297	1.0252	0.9331	1.0446
CaK	9.0	5.6	1212.9	3.3	0.0831	0.9459	1.0300	0.9509	1.0353
TiK	0.1	0.1	13.9	58.9	0.0011	0.8557	1.0380	0.9644	1.0753
FeK	22.8	10.3	1123.0	3.5	0.1960	0.8365	1.0462	0.9954	1.0421

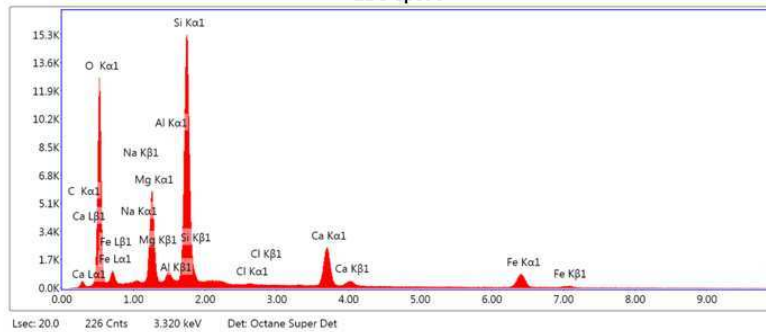
EDS Spot 5



eZAF Smart Quant Results

Element	Weight %	Atomic %	Net Int.	Error %	Kratio	Z	R	A	F
O K	44.2	59.7	3674.2	8.3	0.1508	1.0691	0.9687	0.3248	1.0000
NaK	0.2	0.2	31.7	34.6	0.0011	0.9665	0.9945	0.5253	1.0071
AlK	10.6	8.5	2832.5	3.9	0.0803	0.9442	1.0089	0.8049	1.0171
SiK	31.2	24.0	8040.3	3.5	0.2409	0.9638	1.0153	0.8120	1.0053
K K	13.9	7.7	2051.9	2.8	0.1149	0.8886	1.0416	0.9378	1.0121

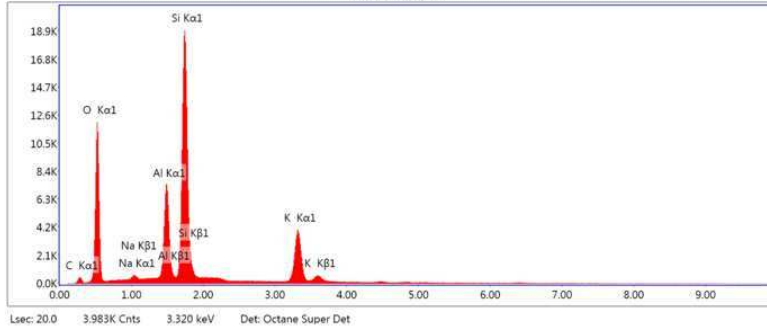
EDS Spot 6



eZAF Smart Quant Results

Element	Weight %	Atomic %	Net Int.	Error %	Kratio	Z	R	A	F
O K	40.6	57.7	3953.6	7.9	0.1589	1.0824	0.9593	0.3643	1.0000
NaK	0.6	0.5	75.1	14.8	0.0025	0.9793	0.9860	0.4544	1.0053
MgK	9.8	9.2	2200.7	5.8	0.0594	0.9949	0.9937	0.6100	1.0071
AlK	1.4	1.2	333.9	7.3	0.0093	0.9571	1.0009	0.6691	1.0125
SiK	25.8	20.9	6602.8	3.9	0.1938	0.9771	1.0076	0.7694	1.0050
ClK	0.2	0.1	37.6	27.6	0.0016	0.9077	1.0254	0.8579	1.0202
CaK	10.0	5.7	1321.5	3.1	0.0900	0.9171	1.0395	0.9608	1.0275
FeK	11.5	4.7	560.8	4.1	0.0973	0.8097	1.0527	0.9973	1.0550

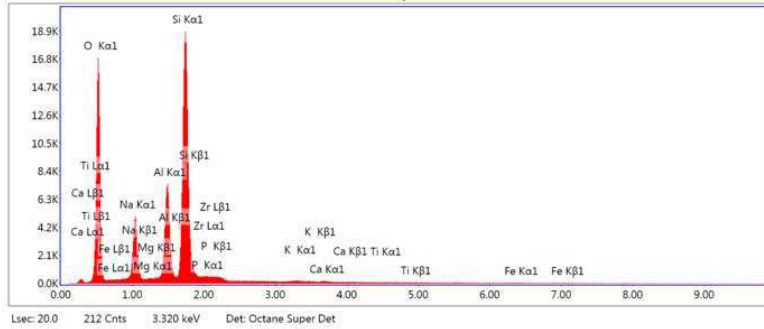
EDS Spot 7



eZAF Smart Quant Results

Element	Weight %	Atomic %	Net Int.	Error %	Kratio	Z	R	A	F
O K	43.8	59.2	3760.0	8.3	0.1503	1.0696	0.9686	0.3252	1.0000
NaK	0.7	0.6	102.7	12.2	0.0034	0.9670	0.9945	0.5275	1.0070
AlK	10.9	8.7	3006.9	3.8	0.0830	0.9447	1.0088	0.8033	1.0168
SiK	30.9	23.8	8185.9	3.5	0.2389	0.9643	1.0153	0.8086	1.0053
KK	13.8	7.6	2104.0	2.8	0.1147	0.8890	1.0415	0.9376	1.0121

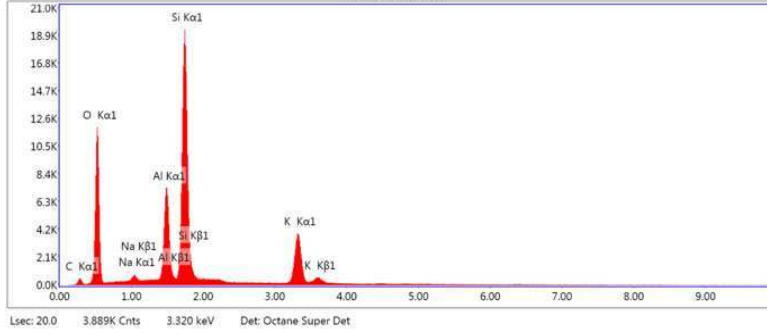
EDS Spot 8



eZAF Smart Quant Results

Element	Weight %	Atomic %	Net Int.	Error %	Kratio	Z	R	A	F
O K	42.6	56.1	5249.5	7.1	0.2007	1.0674	0.9718	0.4419	1.0000
NaK	10.8	9.9	1907.2	6.2	0.0596	0.9648	0.9974	0.5691	1.0061
MgK	0.6	0.5	137.6	9.2	0.0035	0.9800	1.0047	0.6350	1.0116
AlK	11.3	8.8	3085.3	4.3	0.0815	0.9425	1.0115	0.7550	1.0141
SiK	30.6	23.0	8168.0	3.9	0.2280	0.9620	1.0179	0.7718	1.0033
P K	0.5	0.3	94.3	12.7	0.0033	0.9229	1.0238	0.6867	1.0045
ZrL	2.1	0.5	207.6	6.0	0.0124	0.7252	1.1982	0.8230	1.0093
KK	0.7	0.4	115.9	9.8	0.0060	0.8868	1.0437	0.9231	1.0164
CaK	0.4	0.2	55.7	15.3	0.0036	0.9019	1.0476	0.9474	1.0208
TiK	0.2	0.1	17.1	56.4	0.0013	0.8152	1.0540	0.9785	1.0398
FeK	0.3	0.1	17.4	45.3	0.0029	0.7952	1.0582	1.0011	1.1040

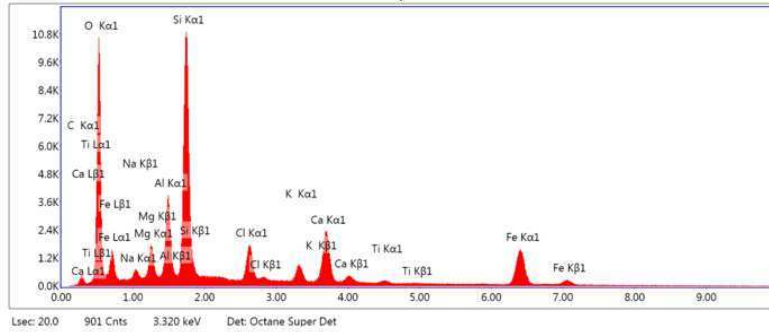
EDS Spot 9



eZAF Smart Quant Results

Element	Weight %	Atomic %	Net Int.	Error %	Kratio	Z	R	A	F
O K	43.4	58.7	3749.4	8.3	0.1496	1.0698	0.9686	0.3267	1.0000
NaK	1.1	1.0	170.2	9.4	0.0056	0.9672	0.9945	0.5303	1.0070
AlK	11.0	8.8	3029.3	3.8	0.0835	0.9449	1.0088	0.8021	1.0168
SiK	31.1	24.0	8247.7	3.5	0.2402	0.9645	1.0153	0.8073	1.0052
KK	13.5	7.5	2063.5	2.9	0.1123	0.8892	1.0415	0.9369	1.0121

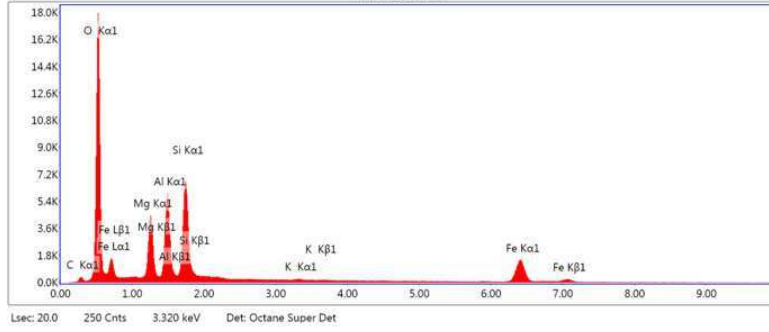
EDS Spot 10



eZAF Smart Quant Results

Element	Weight %	Atomic %	Net Int.	Error %	Kratio	Z	R	A	F
O K	35.6	55.5	3231.4	8.2	0.1334	1.1110	0.9461	0.3413	1.0000
NaK	0.8	0.9	91.8	15.3	0.0031	1.0060	0.9739	0.3956	1.0037
MgK	2.3	2.3	454.7	7.8	0.0126	1.0223	0.9819	0.5470	1.0065
AlK	5.9	5.4	1350.9	5.5	0.0385	0.9836	0.9895	0.6677	1.0096
SiK	18.6	16.5	4572.6	4.3	0.1378	1.0044	0.9966	0.7415	1.0065
ClK	3.6	2.6	686.7	5.2	0.0299	0.9337	1.0154	0.8685	1.0219
KK	2.0	1.3	319.4	8.1	0.0180	0.9277	1.0260	0.9337	1.0447
CaK	9.1	5.6	1191.2	3.5	0.0833	0.9438	1.0307	0.9518	1.0350
TiK	0.3	0.1	26.8	41.3	0.0022	0.8538	1.0387	0.9648	1.0737
FeK	21.9	9.8	1053.2	3.5	0.1877	0.8346	1.0467	0.9955	1.0427

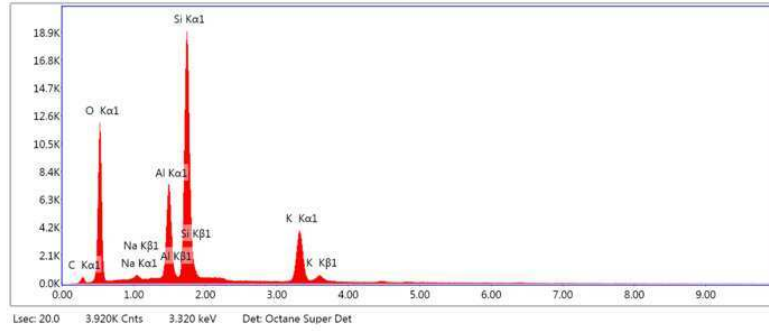
EDS Spot 11



eZAF Smart Quant Results

Element	Weight %	Atomic %	Net Int.	Error %	Kratio	Z	R	A	F
O K	41.8	60.4	5641.4	6.1	0.2462	1.0968	0.9548	0.5446	1.0000
MgK	8.7	8.3	1666.7	6.4	0.0489	1.0086	0.9897	0.5581	1.0058
AlK	11.5	9.9	2342.6	5.6	0.0706	0.9703	0.9971	0.6348	1.0064
SiK	13.9	11.4	2923.3	4.9	0.0931	0.9907	1.0039	0.6842	1.0044
K K	0.3	0.2	40.2	30.0	0.0024	0.9146	1.0321	0.9384	1.0375
FeK	23.8	9.8	1072.6	3.4	0.2021	0.8220	1.0507	1.0037	1.0443

EDS Spot 12



eZAF Smart Quant Results

Element	Weight %	Atomic %	Net Int.	Error %	Kratio	Z	R	A	F
O K	44.5	60.0	3714.9	8.3	0.1528	1.0687	0.9688	0.3260	1.0000
NaK	0.2	0.2	25.2	54.0	0.0008	0.9662	0.9947	0.5242	1.0070
AlK	10.6	8.5	2837.2	3.9	0.0806	0.9439	1.0090	0.8045	1.0170
SiK	30.9	23.7	7971.5	3.5	0.2393	0.9635	1.0155	0.8116	1.0053
K K	13.8	7.6	2048.4	2.8	0.1149	0.8883	1.0417	0.9383	1.0121

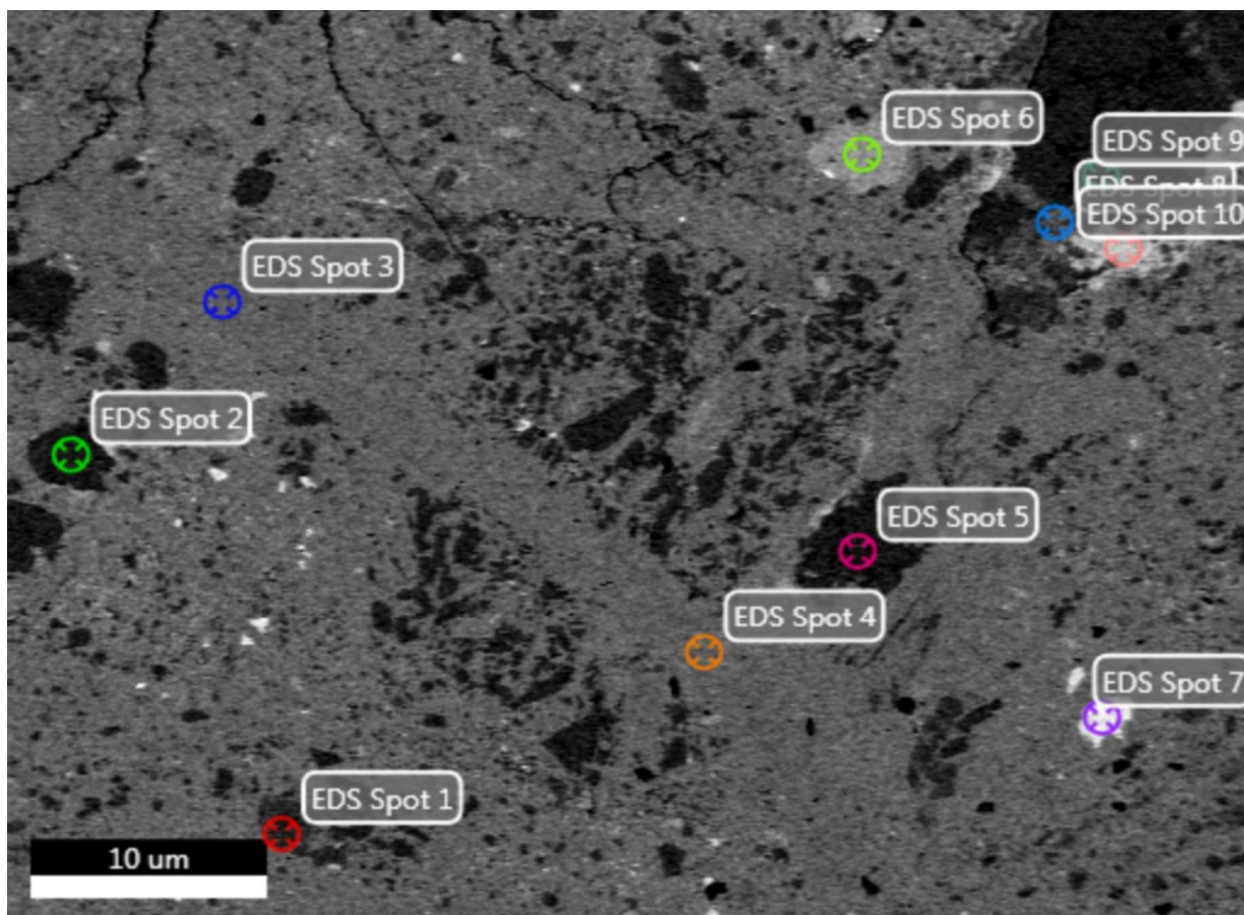
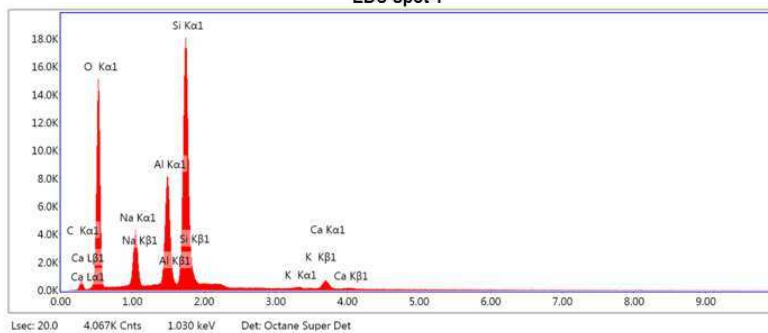


Fig. E.3. SEM BSE image from sample 106-3A, also shown in Fig. 3.25, of a P2 fault core, with a crosscutting vein of adularia, hosting adularia matrix and clasts of quartz and albite. This figure shows the display on the TEAM EDAX software, with spots chosen for EDS analysis. Results for each spot are shown in the following pages. Interpretation of the spot analyses are shown in table E.3.

Table E.3. Interpretations of EDS analyses, from Fig. E.3.

	Spot	Interpretation
Sample 106-3A	1	Albite
Area 10	2	Quartz
	3	Adularia
	4	Adularia
	5	Quartz
	6	Epidote
	7	Titanite
	8	Quartz
	9	Quartz
	10	Biotite (with minor Cl content)

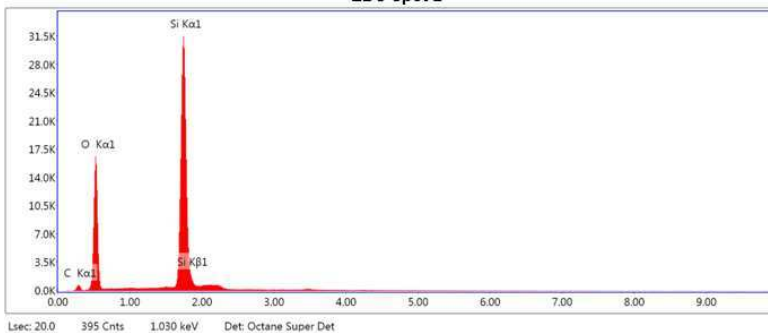
EDS Spot 1



eZAF Smart Quant Results

Element	Weight %	Atomic %	Net Int.	Error %	Kratio	Z	R	A	F
O K	42.8	56.1	4682.4	7.3	0.1904	1.0629	0.9741	0.4281	1.0000
NaK	9.3	8.5	1502.2	6.3	0.0499	0.9606	0.9994	0.5698	1.0065
AlK	13.2	10.2	3365.8	4.1	0.0945	0.9382	1.0134	0.7714	1.0142
SiK	31.7	23.7	7733.8	3.9	0.2296	0.9576	1.0197	0.7714	1.0029
K K	0.5	0.2	68.6	18.8	0.0038	0.8825	1.0451	0.9284	1.0213
CaK	2.6	1.3	319.0	5.1	0.0220	0.8975	1.0490	0.9522	1.0197

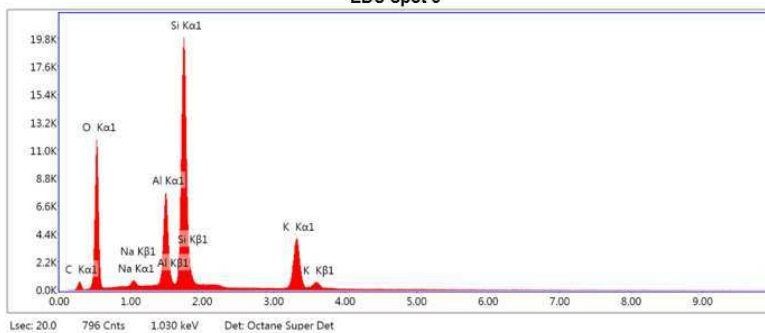
EDS Spot 2



eZAF Smart Quant Results

Element	Weight %	Atomic %	Net Int.	Error %	Kratio	Z	R	A	F
O K	49.1	62.9	5219.6	7.1	0.2243	1.0516	0.9752	0.4471	1.0000
SiK	50.9	37.1	13491.4	2.5	0.4233	0.9473	1.0207	0.9011	1.0023

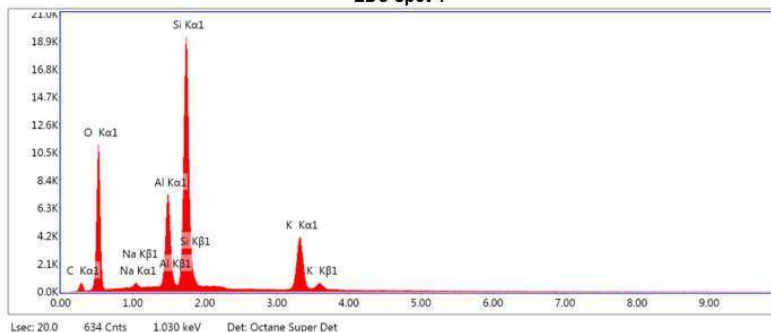
EDS Spot 3



eZAF Smart Quant Results

Element	Weight %	Atomic %	Net Int.	Error %	Kratio	Z	R	A	F
O K	43.4	58.9	3667.1	8.4	0.1459	1.0701	0.9682	0.3215	1.0000
NaK	0.4	0.4	67.5	16.9	0.0022	0.9675	0.9941	0.5279	1.0071
AlK	10.5	8.4	2881.8	3.9	0.0792	0.9452	1.0085	0.8051	1.0173
SiK	31.7	24.5	8406.2	3.5	0.2441	0.9648	1.0150	0.8128	1.0053
KK	14.0	7.8	2135.2	2.8	0.1158	0.8895	1.0413	0.9370	1.0120

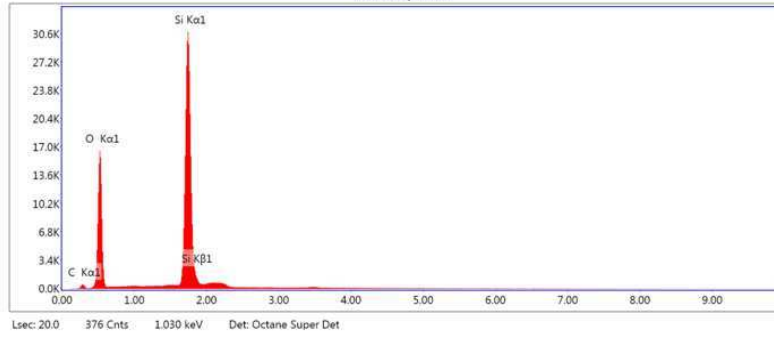
EDS Spot 4



eZAF Smart Quant Results

Element	Weight %	Atomic %	Net Int.	Error %	Kratio	Z	R	A	F
O K	42.8	58.4	3426.1	8.4	0.1418	1.0711	0.9677	0.3166	1.0000
NaK	0.2	0.2	33.0	29.2	0.0011	0.9684	0.9937	0.5284	1.0072
AlK	10.6	8.6	2817.0	3.9	0.0805	0.9461	1.0081	0.8069	1.0174
SiK	31.8	24.7	8107.2	3.5	0.2449	0.9657	1.0146	0.8129	1.0054
KK	14.5	8.1	2120.0	2.8	0.1196	0.8904	1.0409	0.9368	1.0119

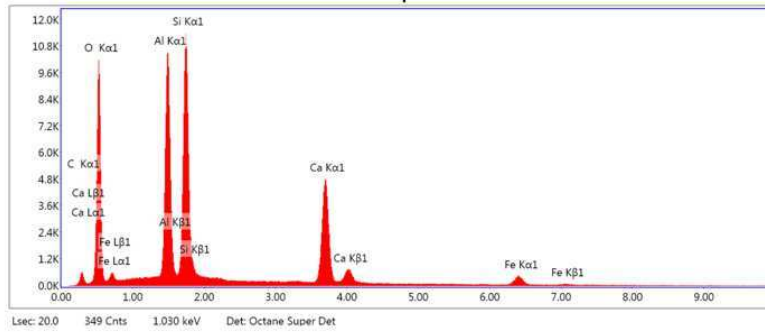
EDS Spot 5



eZAF Smart Quant Results

Element	Weight %	Atomic %	Net Int.	Error %	Kratio	Z	R	A	F
O K	49.3	63.0	5043.7	7.1	0.2277	1.0514	0.9753	0.4480	1.0000
Si K	50.7	37.0	12925.1	2.5	0.4259	0.9471	1.0207	0.9008	1.0023

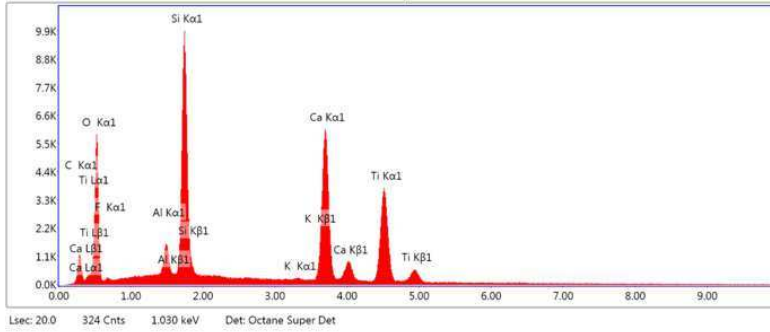
EDS Spot 6



eZAF Smart Quant Results

Element	Weight %	Atomic %	Net Int.	Error %	Kratio	Z	R	A	F
O K	41.0	58.4	3169.2	8.8	0.1220	1.0826	0.9599	0.2798	1.0000
Al K	15.9	13.4	4298.0	4.1	0.1143	0.9571	1.0014	0.7583	1.0102
Si K	18.7	15.2	4800.6	4.2	0.1349	0.9771	1.0082	0.7475	1.0065
Ca K	19.2	10.9	2616.9	2.6	0.1706	0.9169	1.0399	0.9664	1.0180
Fe K	5.2	2.1	263.7	6.4	0.0438	0.8095	1.0530	0.9924	1.0609

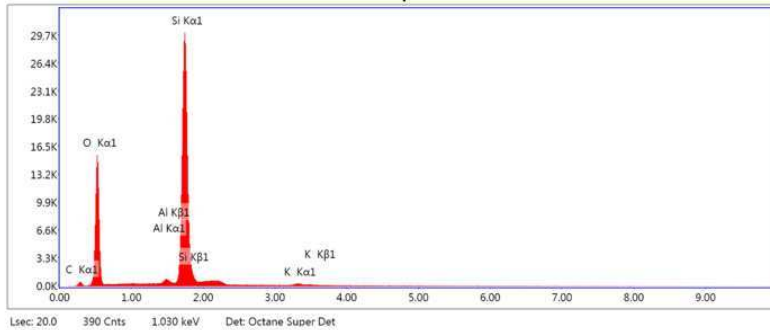
EDS Spot 7



eZAF Smart Quant Results

Element	Weight %	Atomic %	Net Int.	Error %	Kratio	Z	R	A	F
O K	37.6	58.3	1780.6	10.0	0.0690	1.1089	0.9478	0.1718	1.0000
F K	1.3	1.7	71.0	14.5	0.0021	1.0296	0.9576	0.1622	1.0000
AlK	1.8	1.7	457.2	6.4	0.0122	0.9816	0.9909	0.7090	1.0119
SiK	14.5	12.8	4010.1	3.8	0.1134	1.0024	0.9980	0.8007	1.0101
KK	0.1	0.1	22.3	57.7	0.0012	0.9256	1.0272	0.9665	1.1046
CaK	23.2	14.3	3281.8	2.4	0.2154	0.9417	1.0318	0.9816	1.0428
TiK	21.5	11.2	2215.4	2.9	0.1722	0.8518	1.0397	0.9561	1.0184

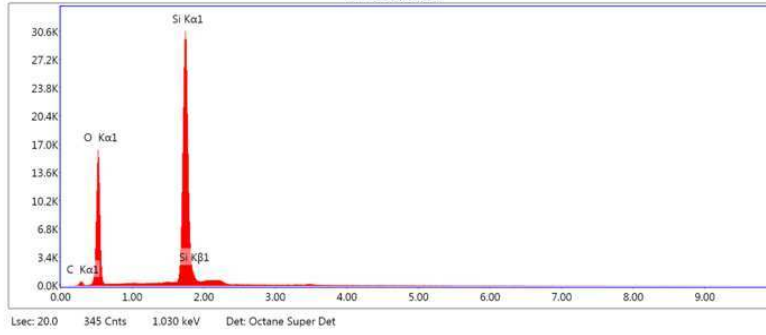
EDS Spot 8



eZAF Smart Quant Results

Element	Weight %	Atomic %	Net Int.	Error %	Kratio	Z	R	A	F
O K	48.0	62.0	4914.3	7.2	0.2133	1.0539	0.9744	0.4309	1.0000
AlK	1.2	0.9	317.0	5.9	0.0095	0.9302	1.0137	0.8217	1.0343
SiK	49.6	36.5	12992.4	2.6	0.4117	0.9494	1.0200	0.8918	1.0025
KK	1.2	0.6	158.3	6.5	0.0094	0.8749	1.0453	0.9214	1.0149

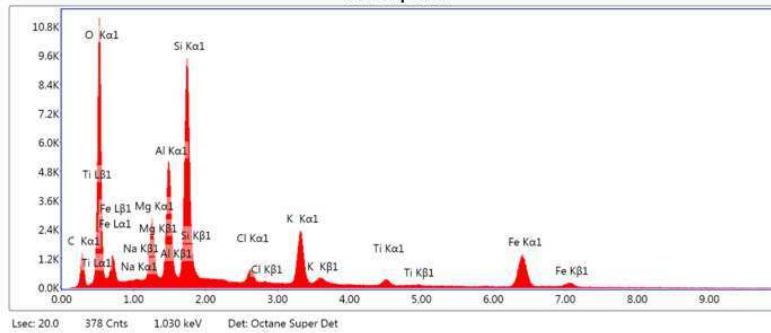
EDS Spot 9



eZAF Smart Quant Results

Element	Weight %	Atomic %	Net Int.	Error %	Kratio	Z	R	A	F
O K	49.1	62.9	4988.5	7.1	0.2267	1.0516	0.9753	0.4474	1.0000
Si K	50.9	37.1	12858.1	2.5	0.4266	0.9472	1.0207	0.9010	1.0023

EDS Spot 10



eZAF Smart Quant Results

Element	Weight %	Atomic %	Net Int.	Error %	Kratio	Z	R	A	F
O K	35.5	54.3	3426.4	7.8	0.1414	1.1084	0.9496	0.3783	1.0000
Na K	0.5	0.5	53.9	18.1	0.0018	1.0034	0.9771	0.4142	1.0042
Mg K	5.1	5.1	1016.3	6.7	0.0282	1.0197	0.9851	0.5683	1.0068
Al K	9.6	8.7	2112.0	5.3	0.0602	0.9810	0.9925	0.6668	1.0087
Si K	17.9	15.6	4082.5	4.5	0.1230	1.0017	0.9995	0.7187	1.0058
Cl K	1.6	1.1	292.8	6.9	0.0127	0.9310	1.0181	0.8604	1.0215
K K	7.9	4.9	1180.4	3.3	0.0664	0.9250	1.0285	0.9348	1.0277
Ti K	1.4	0.7	148.1	9.2	0.0123	0.8512	1.0408	0.9724	1.0770
Fe K	20.4	8.9	942.0	3.5	0.1678	0.8318	1.0483	0.9975	1.0449